Enhancing low-frequency induction heating effect of ferromagnetic composites : Toward medical applications

Ziyin Xiang

N°d'ordre NNT : 2021LYSEI022

THESE de DOCTORAT DE L'UNIVERSITE DE LYON
opérée au sein de
L'Institut National des Sciences Appliquées de Lyon

Ecole Doctorale N° ED160 EEA
ÉLECTRONIQUE, ÉLECTROTECHNIQUE, AUTOMATIQUE

Spécialité/ discipline de doctorat :Génie électrique

Soutenue publiquement le 12/Avril/2021, par :

Ziyin XIANG

Enhancing Low-frequency Induction Heating Effect of Ferromagnetic Composites – toward Medical Applications

---

Devant le jury composé de :

SEBALD Gaël	Professeur des Universités/INSA-LYON/Université de Tohoku	Examinateur
GUIFFARD Benoit	Professeur des Universités/Université de Nantes	Rapporteur
DEMOLY Frédéric	HDR, Maître de Conférences /UTBM	Rapporteur
NARITA Fumio	Professeur /Université de Tohoku	Examinateur
DANIEL Laurent	Professeur des Universités / Centrale Supelec	Examinateur
DUCHARNE Benjamin	HDR, Maître de Conférences/INSA-LYON	Directeur de thèse
LE Minh Quyen	Maître de Conférences/INSA-LYON	Co-directrice de thèse
DeLLA SCHIAVA Nellie	PhD., Praticien hospitalier /HCL Hôpital Edouard Herriot	Co-encadrante

Département FEDORA – INSA Lyon - Ecoles Doctorales – Quinquennal 2016-2020

SIGLE	ECOLE DOCTORALE	NOM ET COORDONNEES DU RESPONSABLE
CHIMIE	**CHIMIE DE LYON** **http://www.edchimie-lyon.fr** Sec. : Renée EL MELHEM Bât. Blaise PASCAL, 3e étage **secretariat@edchimie-lyon.fr** INSA : R. GOURDON	**M. Stéphane DANIELE** Institut de recherches sur la catalyse et l'environnement de Lyon IRCELYON-UMR 5256 Équipe CDFA 2 Avenue Albert EINSTEIN 69 626 Villeurbanne CEDEX **directeur@edchimie-lyon.fr**
E.E.A.	**ÉLECTRONIQUE, ÉLECTROTECHNIQUE, AUTOMATIQUE** **http://edeea.ec-lyon.fr** Sec. : M.C. HAVGOUDOUKIAN **ecole-doctorale.eea@ec-lyon.fr**	**M. Gérard SCORLETTI** École Centrale de Lyon 36 Avenue Guy DE COLLONGUE 69 134 Écully Tél : 04.72.18.60.97 Fax 04.78.43.37.17 **gerard.scorletti@ec-lyon.fr**
E2M2	**ÉVOLUTION, ÉCOSYSTÈME, MICROBIOLOGIE, MODÉLISATION** **http://e2m2.universite-lyon.fr** Sec. : Sylvie ROBERJOT Bât. Atrium, UCB Lyon 1 Tél : 04.72.44.83.62 INSA : H. CHARLES **secretariat.e2m2@univ-lyon1.fr**	**M. Philippe NORMAND** UMR 5557 Lab. d'Ecologie Microbienne Université Claude Bernard Lyon 1 Bâtiment Mendel 43, boulevard du 11 Novembre 1918 69 622 Villeurbanne CEDEX **philippe.normand@univ-lyon1.fr**
EDISS	**INTERDISCIPLINAIRE SCIENCES-SANTÉ** **http://www.ediss-lyon.fr** Sec. : Sylvie ROBERJOT Bât. Atrium, UCB Lyon 1 Tél : 04.72.44.83.62 INSA : M. LAGARDE **secretariat.ediss@univ-lyon1.fr**	**Mme Sylvie RICARD-BLUM** Institut de Chimie et Biochimie Moléculaires et Supramoléculaires (ICBMS) - UMR 5246 CNRS - Université Lyon 1 Bâtiment Curien - 3ème étage Nord 43 Boulevard du 11 novembre 1918 69622 Villeurbanne Cedex Tel : +33(0)4 72 44 82 32 **sylvie.ricard-blum@univ-lyon1.fr**
INFOMATHS	**INFORMATIQUE ET MATHÉMATIQUES** **http://edinfomaths.universite-lyon.fr** Sec. : Renée EL MELHEM Bât. Blaise PASCAL, 3e étage Tél : 04.72.43.80.46 **infomaths@univ-lyon1.fr**	**M. Hamamache KHEDDOUCI** Bât. Nautibus 43, Boulevard du 11 novembre 1918 69 622 Villeurbanne Cedex France Tel : 04.72.44.83.69 **hamamache.kheddouci@univ-lyon1.fr**
Matériaux	**MATÉRIAUX DE LYON** **http://ed34.universite-lyon.fr** Sec. : Stéphanie CAUVIN Tél : 04.72.43.71.70 Bât. Direction **ed.materiaux@insa-lyon.fr**	**M. Jean-Yves BUFFIÈRE** INSA de Lyon MATEIS - Bât. Saint-Exupéry 7 Avenue Jean CAPELLE 69 621 Villeurbanne CEDEX Tél : 04.72.43.71.70 Fax : 04.72.43.85.28 **jean-yves.buffiere@insa-lyon.fr**
MEGA	**MÉCANIQUE, ÉNERGÉTIQUE, GÉNIE CIVIL, ACOUSTIQUE** **http://edmega.universite-lyon.fr** Sec. : Stéphanie CAUVIN Tél : 04.72.43.71.70 Bât. Direction **mega@insa-lyon.fr**	**M. Jocelyn BONJOUR** INSA de Lyon Laboratoire CETHIL Bâtiment Sadi-Carnot 9, rue de la Physique 69 621 Villeurbanne CEDEX **jocelyn.bonjour@insa-lyon.fr**
ScSo	**ScSo*** **http://ed483.univ-lyon2.fr** Sec. : Véronique GUICHARD INSA : J.Y. TOUSSAINT Tél : 04.78.69.72.76 **veronique.cervantes@univ-lyon2.fr**	**M. Christian MONTES** Université Lyon 2 86 Rue Pasteur 69 365 Lyon CEDEX 07 **christian.montes@univ-lyon2.fr**

*ScSo : Histoire, Géographie, Aménagement, Urbanisme, Archéologie, Science politique, Sociologie, Anthropologie

Acknowledgements

I would first like to thank my supervisor, Dr. Benjamin Ducharne, whose expertise is invaluable in formulating the research questions and methodology. He is always there waiting for helping me and answering me at any time. He is a patient, optimistic and responsible supervisor. He always encourages me with a smile and a sentence he used to say: "However, the good thing is…you have made progress!" when I encounter difficulties or make mistakes. Sometimes he is more like a kind friend.

I would like to express my great appreciation to my thesis co-supervisor Dr. Minh Quyen Le. She played a great role in promoting and supervising the completion of my thesis. She is a passionate and creative researcher. Her insightful guide pushed me to sharpen my thinking and brought my work to a higher level. I want to thank her for her patient support and for all of the opportunities I was given to further my thesis.

Besides my advisors, I would like to thank the rest of my thesis committee: Prof. Benoit Guiffard and Dr. Frédéric Demoly for their valuable comments on my thesis; Prof. Gaël Sebald, Prof. Fumio Narita, Prof. Laurent Daniel and Dr. DeLLA SCHIAVA Nellie for taking time reading my thesis and present on the defense, evaluating my work.

I wish to acknowledge my Ph.D. scholarship provided by the Chinese Scholarship Council (CSC), the UT-INSA program. Thank my country (China) for giving me this precious opportunity to study abroad.

My sincere thanks also go to Dr. Laurence Seveyrat, who has helped me a lot with SEM and DSC test with great patient. I am grateful for the assistance given by Dr. Pierre-Jean Cottinet for his help of establishing the LFIH experimental setup. I would like to thank Dr. Jean-Fabien Capsal for helping me with building the thermal transfer modeling in Comsol simulation. I want to thank Dr. Gildas Coativy, he provided me useful suggestions about polymer material at the beginning of my thesis. I whould also like to offer specially thanks to Dr. DELLA SCHIAVA Nellie for her valuable advices in medical applications. I appreciate a lot the experience in hospital where I had the opportunity to observe her performed varicose treatment on a patient.

I would also like to thank staffs and colleagues in LGEF laboratory, Mr. Frederic Deformerie: a skillful technician who always helping me cutting samples or sample holders. A big thanks to and Ms. Evelyne Dorieux: the most patient and responsible secretary I have ever known. My special thanks to Dr. Mickaël Lallart and Dr. Linjuan Yan, for providing me kindly help and useful information about future work.

I would like also to thanks my colleagues and friends, especially Mr. Khao-Iam Jakkpat (Jame) who had been an internship student and worked with me for 6 months. And my special thanks to Mr. Van Cuong Nguyen for helping me with 3D printing stuff, we have done a lot of work together. My thanks also go to my sweet sisters Ms. Yan Zhang, Ms. Xiaoting Zhang, Ms. Kritsadi Thetpraphi and Ms. Yuanyuan Liu, for always sharing the ups and downs of life and work with each other. I wish to thank as well as Ms. Giulia Lombardi, Mr. Bhaawan Gupta, Ms. Hiba Haissoune, Mr. Omar Zahhaf, Ms. Giulia D'Ambrogio and Mr. Amaury Fimbelfor all the happiness and good memories we have been together.

I would also take this opportunity to thank my boyfriend Mr. Bo Chen, always stays with me, encourages me, and takes care of me.

At last, I sincerely thank my family, my parents and my brother, for being my spiritual support. Especially my mother, she is a good listener and always provides me with wise counsels. I really appreciate them for supporting all my decisions. No matter how far away, there is always a place in the deep of the heart, we call it home.

Ziyin XIANG

23/03/2021

Résumé

Les composites ferromagnétiques, matrices polymères renforcées de particules ferromagnétiques présentent un potentiel intéressant dans de nombreuses applications médicales. Dans cette thèse, nous nous concentrons particulièrement autour du Chauffage par Induction Basse Fréquence (CIBF) de cathéters ferromagnétiques, une méthode alternative pour l'ablation des varices. L'effet CIBF apparaît dès lors que le composite est exposé à un champ magnétique alternatif. Ce phénomène est principalement dû aux courants de Foucault dits "microscopiques" générés par les mouvements des parois des domaines magnétiques. En introduisant le cathéter à travers la varice endommagée et en l'excitant par un champ magnétique basse fréquence, haute amplitude, il est concevable d'atteindre une température suffisamment élevée pour guérir correctement la zone endommagée sans perturber les zones saines environnantes. Par comparaison aux traitements existants, la méthode CIBF est précise, économique et simple. En transférant la chaleur sans conduction, l'encombrement du cathéter est réduit et le procédé semble applicable même pour des veines très sinueuses.

Des composites ferromagnétiques de différentes formes et fractions volumiques ont été fabriqués et testés grâce à un dispositif expérimental dédié. Différents paramètres (fréquence, pourcentage de particules…) ont été analysés afin d'établir la combinaison présentant la meilleure réponse thermique. Les propriétés physiques (perméabilité, conductivités électrique et thermique) ont également été caractérisées. Un modèle Comsol® combinant comportement ferromagnétique et thermique a été conçu afin d'améliorer la compréhension des phénomènes.

Pour améliorer la conversion, des échantillons anisotropes ont été développés en imposant un champ magnétique statique dans la phase de solidification.

Finalement, une imprimante 3D de type extrusion a été utilisée pour imprimer des échantillons de formes proches de celle d'un cathéter. Des spécimens isotropes et anisotropes ont été imprimés. Les réponses CIBF distinctes et marquées entre les différentes directions testées chez les échantillons anisotropes ouvrent la voie à d'autres applications médicales comme le suivi électromagnétique (navigation chirurgicale).

Mots clés *: Composites ferromagnétiques; Chauffage par induction basse fréquence (CIBF); Modélisation par transfert thermique; Composites à comportement magnétique anisotrope; La fabrication additive; Magnétophorèse; Applications médicales*

Abstract

Ferromagnetic composites, polymer matrix mixed with ferromagnetic particles show good potential in medical applications. In this thesis, we especially focus on the Low Frequency Induction Heating (LFIH) of ferromagnetic catheters as an alternative process for varicose veins ablation. The LFIH effect appears as soon as the composite is exposed to an alternating magnetic field. This phenomenon is mainly due to the so-called "microscopic" eddy currents generated by the magnetic domain wall motions. By inserting the catheter through a damaged varicose vein, and exciting it with a low frequency, high amplitude magnetic field, it is conceivable to reach a temperature high enough to properly heal the damaged area without injuring the surrounding healthy ones. Compared to the existing treatments, the LFIH method is accurate, cost competitive and simple. By transferring heat in a non-conductive way, the catheter bulkiness is reduced and the method is applicable even in tortuous veins.

Ferromagnetic composites with different shapes and particle volume fractions were built and tested in a specific experimental bench. Different parameters (frequency, particle fraction …) were analyzed to reach the best thermal answer. The physical properties (permeability, electrical and thermal conductivities) were also characterized. A Comsol® model combining ferromagnetic behavior and thermal transfer properties was designed to improve the understanding of the phenomena.

For a better efficiency, specimens with anisotropic magnetic behaviors were built by curing them under the influence of a static magnetic field.

Finally, a commercial extrusion-type 3D printer was used to print samples with catheter shapes. Isotropic and anisotropic specimens were built. Interesting LFIH behavior were observed and for the later ones directional answers potentially interesting in alternative medical applications like the electromagnetic tracking (surgery navigation).

Key words: *Ferromagnetic composites; Low-frequency induction heating (LFIH); Thermal transfer modeling; Anisotropic magnetic behavior composites; Additive manufacturing; Magnetophoresis; Medical applications*

Acronyms

ABS	**A**crylonitrile **B**utadiene **S**tyrene
AM	**A**dditive **M**anufacturing
AMF	**A**lternating **M**agnetic **F**ield
CAD	**C**omputer **A**ssitant **D**esign
CAI	**C**omputer **A**ssisted **I**nterventions
DSC	**D**ifferential **S**canning **C**alorimetry
EMT	**E**lectromagnetic **T**racking
EVSA	**E**ndo**v**enous **S**team **A**blation
EVTA	**E**ndo**v**enous **T**hermal **A**blation
FCGW	**F**erromagnetic **C**omposite **G**uide **W**ire
FDM	**F**used **D**eposition **M**odeling
GEM	**G**eneral **E**ffective **M**edia
IGT	**I**mage-**G**uided **T**herapy
IH	**I**nduction **H**eating
kRPM	**K**ilo **R**evolution **P**er **M**inute
LFIH	**L**ow-**F**requency **I**nduction **H**eating
MFH	**M**agnetic **F**luid **H**yperthermia
MHP	**M**agnetic **H**eating **P**ower
MRI	**M**agnetic **R**esonance **I**maging
PDMS	**P**oly**D**i**M**ethyl**S**iloxane
PLA	**P**oly**l**actic **A**cid
PSS	**P**recision **S**tainless **S**teel tip
RFA	**R**adio**F**requency **A**blation
STT	**S**moothflow **T**apered **t**ip
3D	**T**hree-**D**imensional

Symbols

B	Magnetic flux density
H	Magnetic field strength
f	Magnetic field frequency
E	Induced electromotive force
S	Sample section area
N	Number of coil turns
n	Number of permanent magnet
V	Velocity
μ_0	Permeability in free pace
μ_r	Relative permeability
μ_p	Relative permeability of polymer matrix
μ_f	Relative permeability of particle
$\mu,\ \mu_c$	Relative permeability of composite
$\Delta\mu_r(T)$	Relative permeability variations as a function of temperature
$\Delta\mu_r(T_{amb})$	Relative permeability variation at room temperature
ΔT	Temperature difference
ε	Emissivity
C_p	Specific heat capacity
$C_{p,composite}$	Specific heat capacity of composite
$C_{p,ABS}$	Specific heat capacity of ABS
C_{p,Fe_3O_4}	Specific heat capacity of Fe_3O_4
λ	Thermal conductivity
λ_f	Thermal conductivity of particle
λ_p	Thermal conductivity of polymer matrix
h	Transfer coefficient
$\rho_{composite}$	Density of composite
$\rho_{polymer\ matrix}$	Density of polymer matrix

$\rho_{particle}$	Density of particle
v_f	Particle volume fraction
% vol.	Particle volume fraction
$v_{Fe_3O_4}$	Fe_3O_4 particle volume fraction
$\omega_{Fe_3O_4}$	Fe_3O_4 particle weight fraction
σ_f	Particle phase conductivity
σ_p	Polymer phase conductivity
σ_c	Composite conductivity
$\emptyset_c$	Particle percolation threshold
A	GEM equation constant
$L_{composite}$	Inductance of composite
$L_{polymer}$	Inductance of polymer
Fe_3O_4@ABS	Composite of Fe_3O_4 particles doped into ABS matrix
Mn-Zinc@ABS	Composite of Mn-Zinc particles doped into ABS matrix
Ni@ABS	Composite of Ni particles doped into ABS matrix
Copper@ABS	Composite of Copper particles doped into ABS matrix
Carbon black@ABS	Composite of Carbon black particles doped into ABS matrix
Fe_3O_4@PDMS	Composite of Fe_3O_4 particles doped into PDMS matrix

General Introduction

Magnetic composite materials combine the properties of conventional polymers to those of magnetic materials (Ferri, and/or ferromagnetic particles mixed or embedded in a polymer matrix). Magnetic materials can be found in a wide range of applications in science and technology. Modern medical applications such as varicose treatment, hyperthermia, or even endovenous thermal ablation require to bring heat flux locally through the human body. The challenge behind such techniques resides in converting electrical power into heat flux and transfer it directly to the targeted area without contaminating and damaging the surrounding tissues. Low-frequency induction heating (LFIH) of catheters made out of biocompatible magnetic composites is an elegant solution. By inserting the catheter through the varicose to be treated and by exciting it through LFIH, it seems possible to reach a temperature high enough to properly heal the damaged area while preserving the surrounding healthy ones.

In this thesis, two ferromagnetic composites: the Acrylonitrile Butadiene Styrene (ABS) and the PolyDiMethylSiloxane (PDMS) filled with iron oxide (Fe_3O_4) magnetic particles are studied. We especially focus on the LFIH effect and the potential of these two materials as ferromagnetic catheters toward varicose veins healing applications.

In **Chapter 1**, a background knowledge on magnetism is reminded with a special attention on the ferromagnetic materials and their magnetization processes, including the domain wall theory, the hysteresis behavior, and their applications. The eddy current natures and their potential as heat sources are discussed. The ferromagnetic particles and the polymer matrix selection criteria are described. The potential of the ferromagnetic composites towards medical applications including the varicose veins healing or the electromagnetic tracking are also introduced.

Chapter 2 introduces the fabrication methods and the physical characterization of isotropic Fe_3O_4@ABS composites. The conductivity percolation thresholds of the tested composites are obtained using the general effective media theory. The magnetic permeabilities are studied theoretically and experimentally. Mixing laws are used for their theoretical estimations. Experimental measurements of the permeability as a function of the temperature, the frequency, and the particle content are carried out. Finally, the B(H) hysteresis cycles of

the Fe_3O_4@ABS composites are measured using a home-made hysteresis-graph relying on a laboratory electromagnet.

Chapter 3 focus on the LFIH effect of the isotropic Fe_3O_4@ABS composites. Diverse factors related the intrinsic nature of the composites (composition, nature, particle size, geometrical information, …) and to the magnetic excitation field (amplitude, frequency) are studied. To better highlight the LFIH effect mechanisms, comparisons with conductive but non-ferromagnetic samples are performed. Based on experimental results, macro- and micro-scale thermal transfer models are built with Comsol Multiphysics®. Simulation results, together with experimental tests, confirmed the feasibility of significantly increasing the ferromagnetic composite temperature through LFIH effect.

In **Chapter 4**, ferromagnetic composites are processed under a constant homogeneous magnetic field. This leads to a strong anisotropic behavior due to alignments of the ferromagnetic particles. The casting fabrication method is introduced and characterization results are analyzed. We especially noticed a significant enhancement of the LFIH effect when the anisotropic composite is excited along the alignment direction. We also notice that a structured distribution of the ferromagnetic particle is enough to improve the ferromagnetic properties.

Finally, in **Chapter 5**, a commercial extrusion-type 3D printer is exploited to process a Fe_3O_4@PDMS magnetic paste into desired 3D structures. After multiple attempts, we produced composite pastes compatible with the 3D printer and able to be processed into flexible ferromagnetic composites with either isotropic or anisotropic properties. The resulting 3D printed composites are investigated. The LFIH effect, the magnetic and the thermal properties of both isotropic and anisotropic composites are compared. This development is interesting in multiple medical applications, including endovascular ablation, electromagnetic tracking for surgery navigation, medical imaging, and so on.

Content

List of Figures

List of Tables

Les Résumé de Thèse en Français

Chapitre 1 - État de l'art

1.1 Les matériaux ferromagnétiques

Les matériaux magnétiques peuvent être classés en six catégories: matériaux diamagnétiques, matériaux paramagnétiques, matériaux ferromagnétiques, matériaux ferrimagnétiques, matériaux antiferromagnétiques et matériaux super-paramagnétiques.

Les matériaux ferromagnétiques présentent de grandes dépendances aux champs magnétiques externes. Des propriétés magnétiques rémanentes sont observées une fois le champ externe supprimé. Le fer, le nickel et le cobalt sont des exemples de matériaux ferromagnétiques.

Les matériaux ferromagnétiques sont composés de petites zones appelées domaines magnétiques. Dans un domaine magnétique, tous les moments atomiques sont dirigés selon une même direction et orientation. Dans un état désaimanté, l'aimantation résultante issue de l'ensemble des domaines magnétiques s'annule.

Sou l'effet d'un champ externe, les domaines magnétiques caractérisés par un moment magnétique présentant une direction et une orientation proches de celles du champ externe gagnent en énergie et croient tandis que les autres rétrécissent et disparaissent.

Ce phénomène se prolonge jusqu'à ce que l'aimantation atteigne une valeur seuil dite de saturation ou plus aucune variation n'est observée. Une fois cet état saturé atteint, la réduction du champ d'excitation conduit à une distribution des domaines magnétiques déséquilibrée appelée magnétisation rémanente, ou encore magnétisation résiduelle. Si le champ d'excitation est inversé, le matériau retourne vers une distribution en domaines magnétiques plus équilibrée ou différentes directions et orientations sont observées (coercivité) et ou l'état magnétique moyen et proche de zéro.

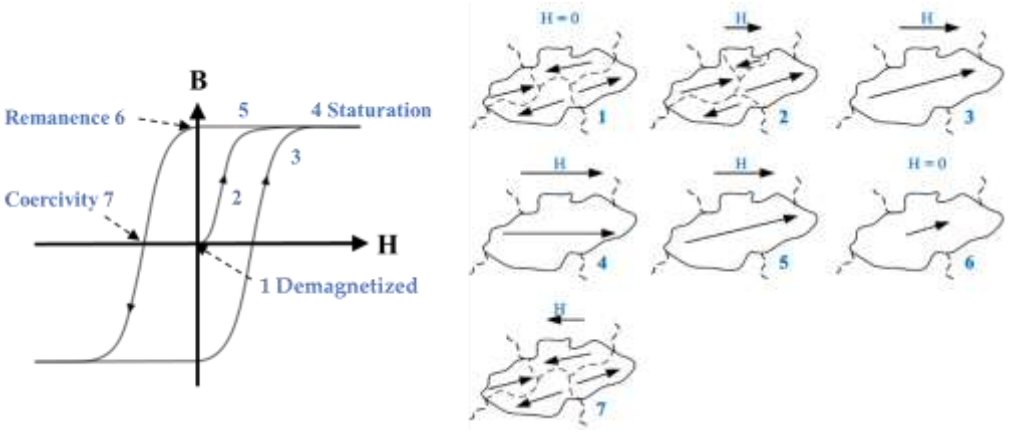

Figure 1. Processus d'aimantation, cinétique des domaines magnétiques.

Le cycle d'hystérésis représente l'évolution du champ d'induction magnétique B en fonction du champ d'excitation magnétique H d'un matériau magnétique (figure 1). Le cycle d'hystérésis est un outil de caractérisation du comportement magnétique. Il est en général attribué aux mouvements des parois des domaines magnétiques. L'aire du cycle d'hystérésis est égale à l'énergie dissipée par un matériau de volume unitaire lors d'un cycle de fonctionnement. La variation ΔB en fonction de ΔH lue sur le cycle d'hystérésis est appelée perméabilité différentielle. Le cycle d'hystérésis est une caractéristique intrinsèque du matériau qui peut varier en taille et en forme.

1.2 Les composites ferromagnétiques

Les matériaux magnétiques sont utilisés dans une large gamme d'applications scientifiques et technologiques. Des particules magnétiques distribuées dans une matrice polymère donnent naissance à un composite magnétique (matériaux multifonctionnels). La nature des particules a une influence significative sur le comportement magnétique du composite. La fraction volumique et l'orientation spatiale ont également un impact significatif.

Dans ce travail de thèse, nous souhaitons développer une méthode de Chauffage par Induction Basse Fréquence (CIBF) de composites ferromagnétiques dans un objectif médical : le traitement des varices. L'objectif final étant médical, le composite que nous allons développer doit être biocompatible. Nous avons identifié des particules d'oxyde de fer (Fe_3O_4) de 5 µm de diamètre comme étant un bon candidat pour ce qui concerne les particules. Pour justifier ce choix, nous avons comparé les performances de ces particules à celles d'autres particules ferromagnétiques (Ni, Mn-Zinc ...).

Les propriétés magnétiques des composites ferromagnétiques dépendent également de façon indirecte à la matrice polymère. En fonction de la distribution et de l'orientation des particules au sein de la matrice, les composites ferromagnétiques peuvent entre autres présenter des

comportements anisotropes. Les composites anisotropes se caractérisent par des propriétés physiques qui dépendent de la direction spatiale. Dans cette thèse, des composites ferromagnétiques isotropes et anisotropes ont été étudiés. Pour ce qui concerne la matrice polymère des composites isotropes, l'ABS thermoplastique a été choisi (ce polymère est très disponible, sa fabrication et ses propriétés physiques sont bien maitrisées). Pour les composites anisotropes nous avons plutôt opté pour le PDMS. Le PDMS permet d'obtenir un composite biocompatible extrêmement flexible, particulièrement bien adapté pour le traitement des varices et la technique CIBF.

1.3 L'effet CIBF

L'effet CIBF peut être défini comme l'élévation de température observée dans un matériau ferromagnétique sous l'influence d'un champ magnétique alternatif basse fréquence. La source de chaleur provient principalement des pertes par hystérésis et de l'effet des courants de Foucault. L'effet CIBF est principalement dû aux courants de Foucault dits "microscopiques".

Des pertes par hystérésis sont observées dès lors qu'un matériau ferromagnétique est exposé à un champ magnétique alternatif. L'excitation magnétique conduit à un arrangement des domaines magnétiques. Etant alternatif, le champ d'excitation induit des mouvements alternés des parois des domaines magnétiques qui s'accompagnent de pertes énergétiques. Ces pertes proviennent des courants de Foucault dits «microscopiques», interactions entre les parois des domaines magnétiques et la microstructure lors de l'aimantation de l'échantillon ferromagnétique.

A hautes fréquences, une conversion magnétothermique élevée peut être atteinte. Cependant, une fréquence trop élevée (> 100 kHz) est bannie dans le domaine médical car des dommages indésirés peuvent être observés sur le corps humain. Selon les directives de la commission internationale de protection contre les rayonnements non ionisants (ICNIRP), la gamme dite des « basses fréquences » s'étend de 1 Hz à 100 kHz. Au-delà des 100 kHz, des effets de chauffage indésirés doivent être pris en compte.

Jusqu'à présent, les champs magnétiques basses fréquences ont rarement été exploités pour des applications médicales. Dans cette thèse, deux applications potentielles sont particulièrement ciblées:

_ le traitement des varices

_ le suivi électromagnétique.

1) Le traitement des varices

La traitement des varices par ablation thermique consiste à insérer un composite ferromagnétique biocompatible dans la veine à traiter. Puis de le chauffer par un champ magnétique externe alternatif basses fréquences (moins de 50 kHz) et d'induire la cicatrisation de la veine à traiter. L'effet CIBF commence dès lors que l'échantillon ferromagnétique est exposé au champ magnétique alternatif. Etant basse fréquence, le champ magnétique alternatif est censé chauffer uniquement le composite ferromagnétique. La destruction de la veine malade peut intervenir sans endommagement des tissus sains environnants. Selon nos analyses de calorimétrie différentielle à balayage (DSC) effectuées sur des varices provenant du corps d'un patient, le point de fusion de la veine est proche des 120 ° C.

Dans cette thèse nous proposons une méthode alternative pour le traitement des varices basée sur le mécanisme CIBF. Notre méthode est proche de la technique d'ablation thermique endoveineuse (EVTA). Notre objectif n'est pas de la concurrencer mais plutôt d'exposer les bénéfices de la méthode CIBF. Nos résultats de simulation et expérimentaux sont prometteurs, ils montrent un fort potentiel de la méthode proposée. La méthode CIBF repose sur les courants de Foucault dits microscopiques, générés à l'intérieur des particules magnétiques sous l'influence d'une source magnétique alternative. Comme l'excitation magnétique reste à l'extérieur du patient et qu'aucune connexion physique n'existe entre le cathéter ferromagnétique et la source énergétique, la méthode CIBF conduit à une procédure beaucoup plus confortable pour le chirurgien. La sélectivité de l'effet CIBF qui n'agit que sur le matériau ferromagnétique rend quasi impossible la brûlure de tissus voisins. De plus, la méthode CIBF est moins coûteuse. Finalement, le cathéter ferromagnétique peut être imprimé en 3D avec des formes et des tailles adaptées et variables d'un patient à l'autre.

2) Les capteurs électromagnétiques: système de suivi

Les interventions chirurgicales assistées par ordinateur (IAO) se caractérisent par une grande précision, ainsi qu'un temps d'intervention réduit. Elles font désormais partie intégrante de la médecine moderne. Une localisation spatiale des outils d'intervention est indispensable pour un contrôle en temps réel. La localisation de l'appareil dans le corps du patient est appelée «tracking», c'est une technologie clé pour l'IAO.

La localisation par suivi électromagnétique (LSE) repose sur de petits capteurs/récepteurs qui circulent à travers un champ magnétique généré par un électroaimant émetteur (Figure 2). Cet émetteur est chargé de produire des champs magnétiques alternatifs ou quasi-statiques. Ces champs vont induire des courants dans les capteurs embarqués qui vont agir comme des détecteurs. Le phénomène physique derrière ces systèmes de poursuite repose principalement sur l'induction magnétique.

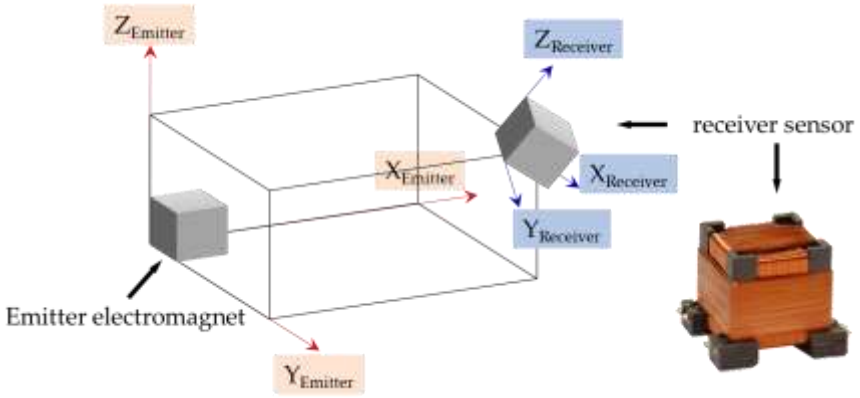

Figure 2. Schéma de principe d'un système de localisation par suivi électromagnétique.

Jusqu'à présent, les systèmes LSE souffrent de deux inconvénients majeurs:

_ Ils sont trop volumiques pour pouvoir intégrer des instruments chirurgicaux;

_ Ils présentent des sensibilités importantes aux objets métalliques de proximité (équipement médical …) qui peuvent déformer ou perturber le champ magnétique source et induire des divergences dans la précision du système.

Pour améliorer cette précision, des composites ferromagnétiques anisotropes avec une perméabilité dépendante de la direction peuvent être une bonne solution. Qu'ils soient sous forme de capteurs ou de récepteurs, l'utilisation de composites ferromagnétiques anisotropes peut être envisagée. Dans les chapitres suivants, nous nous concentrerons sur la caractérisation et la validation de composites ferromagnétiques développés pendant ces travaux de thèse, la faisabilité et les performances de l'effet CIBF sur des composites de type anisotropes et isotropes. Nous nous intéresseront également au traitement des varices. Finalement, l'utilisation de composites ferromagnétiques pour les systèmes LSE sera décrite dans le chapitre 4.

Chapitre 2 - Caractérisation des composites ferromagnétiques isotropes

La caractérisation des composites ferromagnétiques développés dans cette thèse est une étape cruciale. Elle nous aidera à comprendre les propriétés des composites et à améliorer leurs performances. Dans ce chapitre, les méthodes de fabrication et de caractérisation de composites isotropes seront décrites. Les évaluations théoriques et mesures expérimentales de la conductivité, la perméabilité et des propriétés thermiques seront proposées. Nous nous concentrerons particulièrement sur le comportement de l'hystérésis magnétique et sa relation étroite avec l'effet CIBF.

2.1 Fabrication de composites ferromagnétiques

Notre objectif est de fabriquer des composites avec un pourcentage élevé de particules ferromagnétiques (offrant des perméabilités et des réponses thermiques importantes). Nous avons opté pour une méthode robuste de «pressage à chaud» utilisant une presse à chaud.

Grâce à la méthode du «pressage à chaud», nous avons construit avec succès des échantillons de différents pourcentages de particules magnétiques (de 3 à 30% vol.), de formes rectangulaires (60 × 14 × 4 mm, figure 3 (a)) et de formes cylindriques (Ø30 mm, épaisseur 15 mm, figure 3 (b)). Outre les composites Fe_3O_4@ABS, des composites non-ferromagnétiques mais dopés de particules conductrices: 15% vol. de cuivre et 3% vol. de noir de carbone ont également été fabriqués pour vérifier l'effet CIBF sur des composites formés de particules conductrices mais non ferromagnétiques. Finalement d'autres composites ferromagnétiques (10%, 23% et 40% vol. Fe_3O_4, 15% vol. Ni et 30% vol. Mn-Zinc) ont également été fabriqués pour tester d'autres paramètres.

L'échantillon présenté sur la figure 3(a) est trop grand pour une utilisation endo-veineuse. De ce fait, une autre série d'échantillons en forme d'aiguille a été développée. Deux tailles différentes ont été testées: la grande taille 40 × 3,1 × 3,2 mm^3, et la petite taille 27 × 2,5 × 3,2 mm^3 (Figure 3 (d)). Ces deux tailles peuvent être utilisées pour le traitement endo-veineux, elles sont en bonne adéquation avec les diamètres habituels des veines du corps humain (4 à 5 mm).

De façon classique pour les composites biphasés, il existe une fraction volumique de particules critique appelée seuil de percolation $\emptyset c$ définissant la limite entre l'état électrique non conducteur et l'état conducteur. Dans ce travail, pour prédire $\emptyset c$, nous avons utilisé la théorie des milieux effectifs. Nous avons estimé à 47% vol. la fraction volumique critique (seuil de percolation) pour le Fe_3O_4@ABS. Pour un pourcentage inférieur au seuil de percolation, la conductivité électrique est de l'ordre de 10^{-6} S/m et le composite peut être classé comme isolant. Pour le Fe_3O_4@PDMS le seuil de percolation se rapproche des 50% vol.

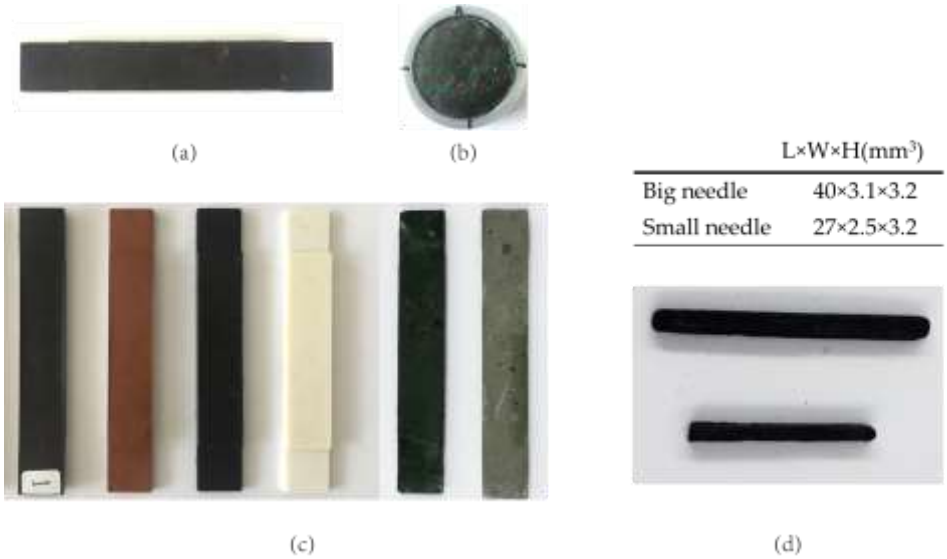

	L×W×H(mm³)
Big needle	40×3.1×3.2
Small needle	27×2.5×3.2

Figure 3. (a) Échantillon de forme rectangulaire; (b) un échantillon de forme cylindrique; (c) échantillons rectangulaires de différentes natures (de gauche à droite): Fe_3O_4@ABS, cuivre@ABS, noir de carbone@ABS, ABS pur, Mn-Zinc@ABS, Ni@ABS; (d) échantillons en forme d'aiguille.

2.2 Caractérisation magnétique

Pour la caractérisation magnétique de nos composites ferromagnétiques nous nous sommes concentrés dans l'estimation de leurs perméabilités. Différentes méthodes ont été testées:

_ En simulation à l'aide d'un outil numérique.

_ Par mesure spectroscopique d'inductance.

_ A l'aide d'un modèle analytique.

_ A partir de cycles d'hystérésis expérimentaux.

1) Outil numérique

Une simulation par éléments finis à l'aide du logiciel Comsol® a été réalisée pour l'estimation de la perméabilité relative μr. La perméabilité relative des composites magnétiques obtenue en fonction de la fraction volumique de particules est représentée sur la figure 4. Comme anticipé de façon intuitive, la matrice polymère mélangée à une plus grande quantité de particules magnétiques conduit à des propriétés magnétiques améliorées (perméabilité plus élevée).

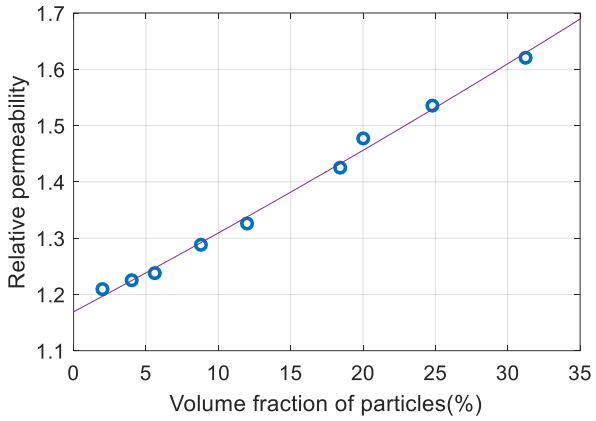

Figure 4. Evolution de la perméabilité relative en fonction du pourcentage de particules (issue de la simulation Comsol®).

2) Mesure spectroscopique de l'inductance

Pour caractériser l'évolution de la perméabilité sur une large plage de fréquences (20 Hz à 1 MHz), des mesures d'inductances ont été effectuées à l'aide d'un impédancemètre.

La perméabilité magnétique est mesurée à l'aide de la mesure de l'inductance d'une bobine enroulée autour de l'échantillon de composite magnétique. La perméabilité effective est dérivée de la mesure d'inductance. Tous les échantillons de forme cylindrique (y compris l'ABS pur) ont été encerclés par une bobine de 100 spires. La perméabilité relative (μr) a été obtenue en utilisant l'équation 1 (ci-dessous) et en supposant toutes les bobines identiques:

$$\mu_r = \frac{L_{composite}}{L_{polymer}} \qquad \text{Equation 1}$$

$L_{composite}$ et $L_{polymer}$ désignent respectivement l'inductance du composite ferromagnétique et celle du polymère pur.

On peut voir sur la figure 5 que les perméabilités relatives résultantes des composites de Fe_3O_4@ABS varient de 1 pour les 3% vol. de particules à 1,8 pour le 30% vol.. μr augmente régulièrement en fonction de la fraction volumique.

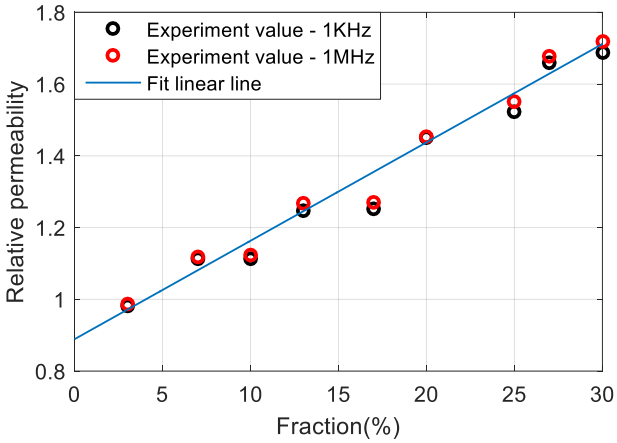

Figure 5. Evolution de la perméabilité relative des composites de Fe_3O_4@ABS mesurée à l'aide de l'impédancemètre.

3) Loi de mélange, utilisation d'un modèle analytique

La prédiction de la perméabilité magnétique effective (perméabilité moyenne d'un milieu non homogène) d'un composite ferromagnétique est à l'origine de nombreux travaux académiques et industriels. Au cours des dernières décennies, de nombreux progrès ont été accomplis autour des théories efficaces de mélanges, comme la formule de Maxwell-Garnett, la formule de Bruggeman, la formule du potentiel cohérent et bien d'autres. Parmi tous ces modèles prédictifs, le modèle non sphérique de Bruggeman est celui qui semble donner les meilleurs résultats de simulation pour nos composites isotropes Fe_3O_4@ABS (particules de 5 µm). Comme on peut le vérifier sur la figure 6, les valeurs expérimentales suivent parfaitement la courbe théorique.

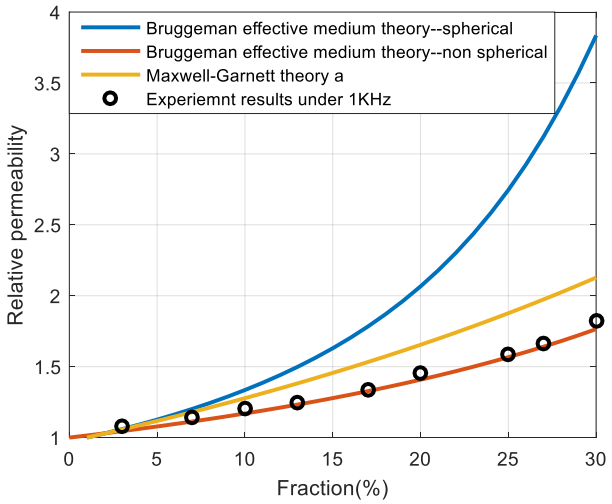

Figure 6. Comparaison de l'évolution théorique et expérimentale de la perméabilité relative de composites Fe_3O_4@ABS en fonction du pourcentage de particules.

4) Courbe d'hystérésis

Les cycles d'hystérésis de tous nos composites ferromagnétiques ont été mesurés à l'aide d'un dispositif expérimental dédié incluant un électroaimant de laboratoire. Les spécimens de forme cylindrique (figure 3 (b)) sont bien adaptés et ont fait l'objet de cette caractérisation. La figure 7 représente les cycles d'hystérésis des composites ferromagnétiques obtenus sous une excitation magnétique sinusoïdale de 1 Hz, 17 kA.m^{-1}.

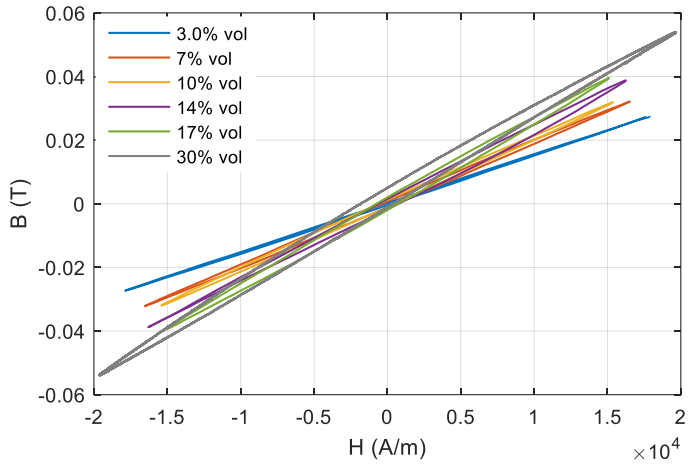

Figure 7 Cycle d'hystérésis des composites Fe_3O_4@ABS dopés de différentes fractions de particules (1Hz).

Comme prévu, une teneur plus élevée en Fe3O4 conduit à des cycles d'hystérésis plus raides et donc des valeurs de perméabilité plus élevées. La surface du cycle d'hystérésis augmente également légèrement en fonction de la fraction des particules.

2.3 Caractérisation thermique

L'étude de l'influence de la température sur les propriétés magnétiques est une étape obligatoire dans la conception de notre composite.

Pour vérifier l'influence de la température, de nouvelles mesures d'inductance et indirectement de perméabilités des échantillons composites Fe_3O_4@ABS (figure 3 (a)) ont été effectuées à l'aide de l'impédancemètre. La largeur de la bande de fréquence testée a été réglée à 1 kHz - 1 MHz (en concordance avec les applications typiques de chauffage par induction). Ces tests expérimentaux ont été réalisés en plaçant les composites à l'intérieur du four pour des températures variants de –20 ° C à 100 ° C.

Finalement, nous avons pu constater qu'indépendamment des variations de fréquences, les composites testés présentent des propriétés magnétiques relativement stables. La perméabilité magnétique d'un échantillon donné pour une fréquence donnée est quasiment constante dans la plage de températures testée. (Figure 8)

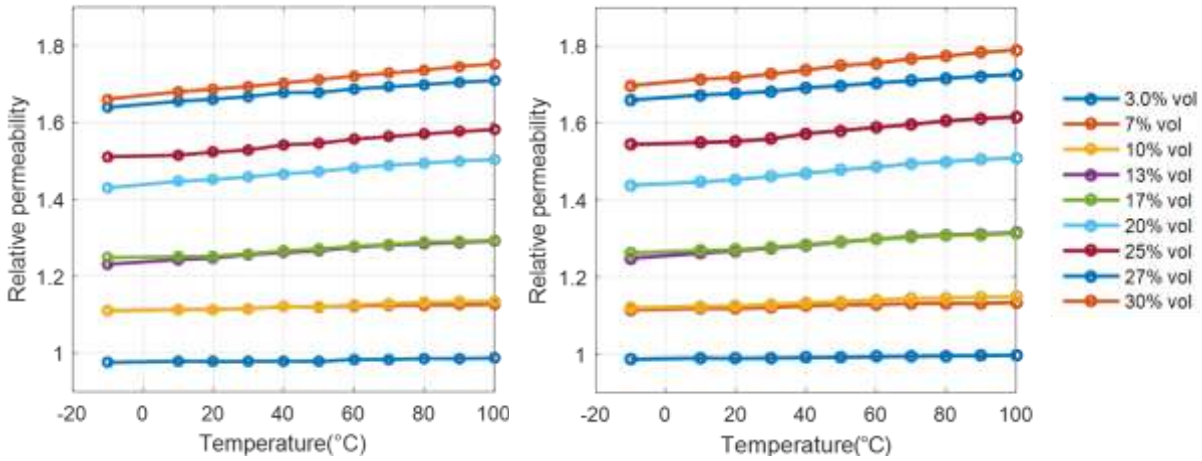

(a) (b)

Figure 8 Variation de la perméabilité en fonction de la température pour des composites de Fe_3O_4@ABS à (a) 1 KHz; et à (b) 1 MHz.

De plus, un dispositif de caractérisation dédié a été utilisé pour mesurer la conductivité thermique des composites. Les composites Fe_3O_4@ABS (3, 8 et 17% vol. de particules), les composites Ni@ABS (10, 23, 40% vol. de particules), ainsi que l'ABS pur ont été caractérisés. Les résultats expérimentaux se sont révélés en bonne adéquation des résultats théoriques.

Dans le chapitre suivant, l'effet CIBF pour des composites ferromagnétiques isotropes est étudié. Une analyse complète des paramètres impliqués dans le mécanisme CIBF est proposée.

Chapitre 3 - Effet CIBF des composites ferromagnétiques isotropes

Dans cette partie, nous nous concentrons sur l'effet de chauffage par induction basse fréquence (CIBF). Celui-ci est appliqué à des composites ferromagnétiques isotropes constitués d'un polymère thermoplastique (acrylonitrile butadiène styrène, ABS) dopé de particules magnétiques d'oxyde de fer (Fe_3O_4). L'effet CIBF apparaît dès lors que l'échantillon est exposé à un champ d'excitation magnétique alternatif et est principalement dû aux courants de Foucault dits «microscopiques» associés aux mouvements des parois des domaines magnétiques. Ce phénomène (CIBF) peut être influencé par divers facteurs, incluant des paramètres liés aux composites (son contenu, sa nature, la taille des particules magnétiques, sa dimension …) mais également la forme d'onde de l'excitation magnétique (fréquence, amplitude …). Une simulation Comsol® basée sur le transfert thermique et associée à des résultats expérimentaux, a permis de démontrer la possibilité de chauffer par induction notre composite ferromagnétique jusqu'à des températures supérieures à 100 ° C. Une optimisation de la source magnétique et de la fraction particulaire du matériau doit permettre de nouveaux progrès. Ces résultats sont particulièrement encourageants et prometteurs pour le traitement endo veineux thermique par méthode CIBF.

3.1 Configuration CIBF

Pour la validation expérimentale de l'effet CIBF, un banc de caractérisation expérimental spécifique a été développé (Figure 9). Pour générer une excitation de champ magnétique alternative significative, un inducteur magnétique comprenant plusieurs paires d'aimants permanents cylindriques a été fixé sur l'arbre moteur d'une machine tournante haute vitesse. Comme nous pouvons le voir figure 10, la distribution polaire de ces aimants permanents est alternativement sud/nord, ceci permet de générer une excitation magnétique sinusoïdale dont la fréquence est directement liée à la vitesse de rotation du moteur grande vitesse. En pratique, avec une vitesse de rotation maximale (supposée de 35000 tr/min, donnée constructeur), l'inducteur 8 aimants permet d'atteindre un champ magnétique alternatif de 2300 Hz, celui à 16 aimants nous donne une excitation à 4200 Hz. Pour contrôler l'amplitude du champ magnétique, nous pouvons contrôler la distance entre l'inducteur magnétique et le composite. Les variations de température sont mesurées à l'aide de deux thermocouples. Le premier thermocouple mesure la température dans la zone chaude (au plus près du passage des aimants), l'autre est utilisée pour déterminer la température du centre de l'échantillon. Les données mesurées sont enregistrées en temps réel à l'aide une carte DEWE®. Pour obtenir une image de température plus intuitive, une caméra thermique est également utilisée sur toute la durée de l'expérience.

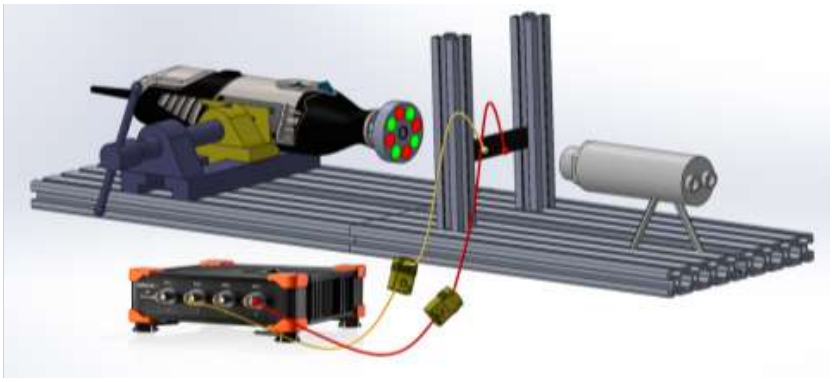

Figure 9 Banc de caractérisation expérimentale pour l'étude du chauffage par induction basse fréquence des composites ferromagnétiques.

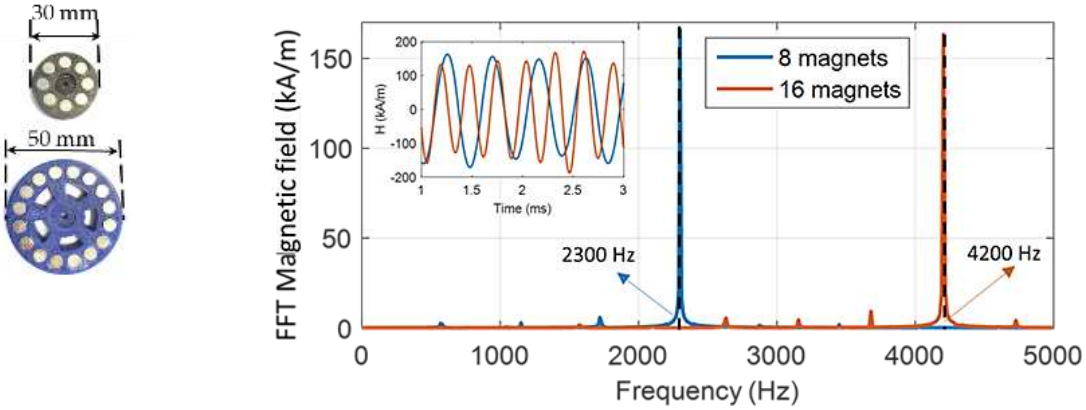

(a) (b)

Figure 10. (a) Inducteur à 8 aimants et à 16 aimants. (b) FFT du champ magnétique généré par les deux types d'inducteurs à la vitesse maximale du moteur. Encadré: évolution temporelle des champs d'excitations magnétiques (8 aimants en rouge, 16 en bleu).

3.2 Paramètres d'influence du CIBF

Afin de mettre en évidence le chauffage par induction des composites ferromagnétiques proposés, une comparaison avec des échantillons fabriqués à partir de particules conductrices mais non ferromagnétiques (noir de carbone, cuivre ..) est proposée. Pour cette comparaison nous nous intéressons en particulier aux images thermiques. Par opposition aux composites ferromagnétiques, les échantillons formés de particules conductrices présentent une réponse très faible sous l'influence du champ d'excitation magnétique, et aucune élévation de température n'est observée. Ceci s'explique par l'absence des courants de Foucault dits «microscopiques» et confirme que le mouvement des parois des domaines magnétiques est le mécanisme de chauffage prédominant à basse fréquence. Ces mouvements magnétiques et les courants de Foucault associés induisent des variations de températures locales à travers les

particules ferromagnétiques qui à leurs tours réchauffent le composite. Ces résultats expérimentaux confirment également la dépendance en fréquence des pertes par hystérésis dans les composites ferromagnétiques, en revanche aucune influence de la fréquence n'est observée sur les composites à particules conductrices.

Les premiers essais expérimentaux valident la faisabilité de générer des pertes magnétiques suffisantes pour observer une augmentation significative de la température des échantillons ferromagnétiques exposés à un champ magnétique alternatif.

L'efficacité du chauffage par induction dépend de divers facteurs, y compris l'excitation magnétique (forme d'onde, fréquence, amplitude …) ainsi que des paramètres intrinsèques aux composites (concentration des particules, taille des particules, géométrie du composite, nature des particules …)

1) Influence de l'effet de fréquence

L'échantillon utilisé pour vérifier l'influence de la fréquence est de forme rectangulaire (figure 3 (a)), il est fabriqué à partir d'ABS mélangé à 17% vol. de particules de Fe_3O_4. Le moteur à courant continu associé à l'inducteur 8 aimants présente une vitesse variable de 5 à 35 ktr.min^{-1}. La figure 11 montre l'évolution de la température du composite pour les différentes vitesses testées, la fréquence de l'excitation magnétique correspondante varie de 300 à 2300 Hz. Comme prévu, l'effet de chauffage est clairement dépendant de la fréquence.

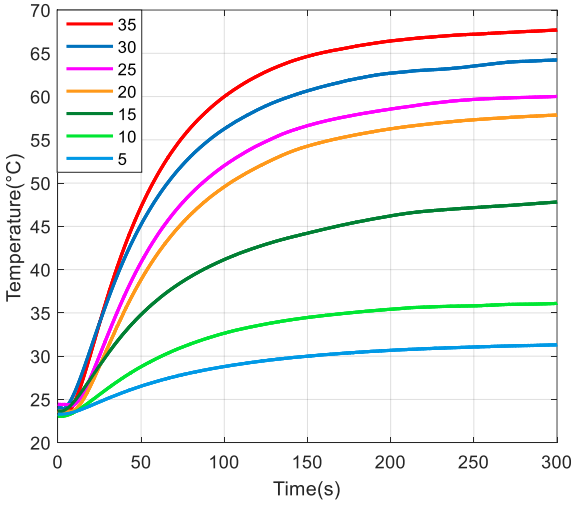

(a)

Figure 11. Température en fonction du temps pour différentes vitesses du moteur (k.tr/min).

2) Influence de l'effet d'amplitude

Les tests ci-dessus ont mis en évidence la dépendance en fréquence de l'effet de chauffage par induction. Il est évident que l'énergie transférée dépend également fortement de la force du champ magnétique. Celle-ci peut être contrôlée en modifiant la distance entre la source magnétique et l'échantillon. La figure 12 (a) montre l'évolution temporelle de la température pour différentes distances inducteur/échantillon et ceci pour une fréquence de l'excitation magnétique de 2300 Hz. Comme prévu, la température diminue fortement lorsque la distance augmente. Cette diminution est quasi-linéaire.

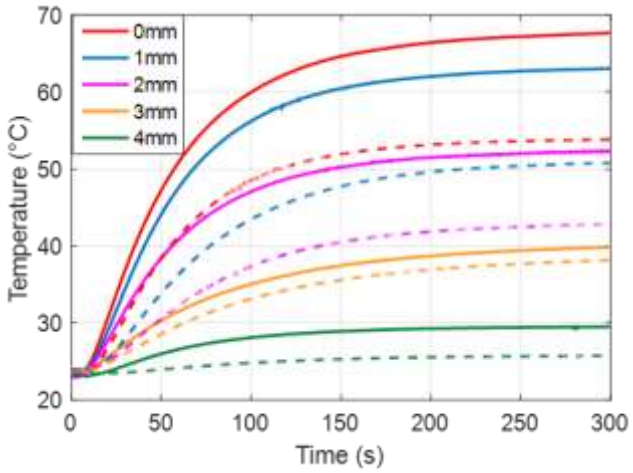

Figure 12. Évolution temporelle de la température pour différentes distances composite / inducteur magnétique. Les lignes continues sont associées à la température de la zone chaude tandis que les lignes pointillées présentent l'évolution de la température au centre de l'échantillon.

3) Influence de la concentration des particules

Des tests expérimentaux sont effectués sur des composites Fe_3O_4@ABS de forme rectangulaire (figure 3 (a)). Les figures 13 (a) et (b) donnent les variations temporelles de la température. Des échantillons formés de diverses fractions volumiques de particules (de 0% à 30%) sont excités par la source magnétique et deux fréquences sont testées: 2300 Hz et 4200 Hz. Pour chaque fraction de particule, une augmentation de la fréquence se traduit par une élévation de la température. Aucune variation n'est observée dans le cas du thermoplastique ABS pur, en revanche la température augmente régulièrement pour les échantillons présentant des perméabilités plus élevées. Les polymères dopés de particules ferromagnétiques présentent des perméabilités améliorées et des pertes par hystérésis générant une élévation de température conséquente.

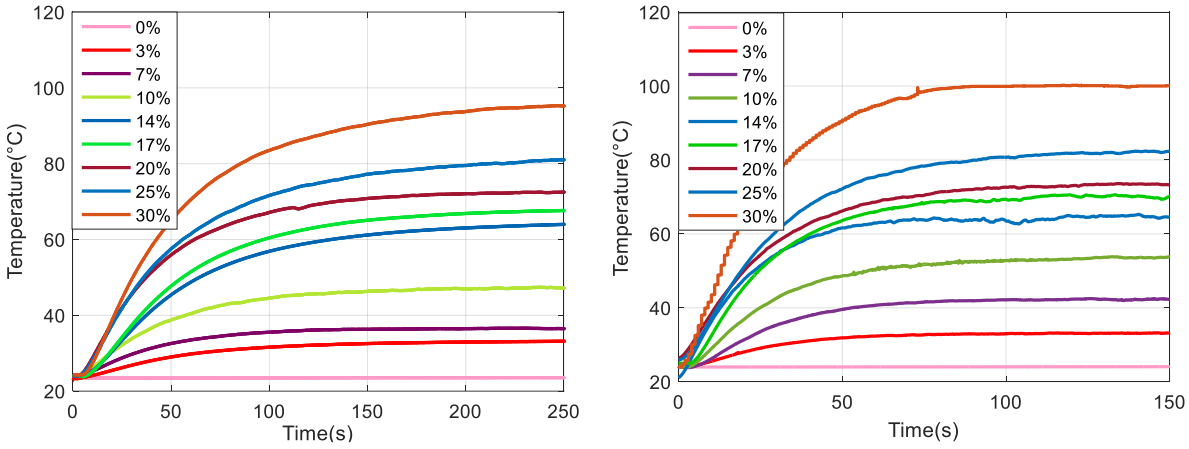

Figure 13 Évolution temporelle de la température des composites Fe_3O_4@ABS obtenue à partir de différentes fractions de particules et sous influence de l'inducteur à 8 aimants (a) et de l'inducteur à 16 aimants (b).

La constante de temps de la réponse thermique constitue un autre facteur clé dans le succès du traitement des varices. Si l'on considère notre système comme un système du premier ordre, cette constante de temps correspond au temps requis pour atteindre une température égale à 63% de la valeur finale. Cette constante de temps dépend de la fraction volumique de particules, ainsi que de la fréquence et de l'amplitude du champ magnétique (voir section 3.2).

4) Influence de la taille des particules

Des échantillons isotropes rectangulaires de base polymère ABS mélangée à différentes tailles de particules de Fe_3O_4 (50-100 nm, 5 um, 50 um) ont été préparés (figure 3 (a)). Nous cherchons à vérifier que la taille des particules a une influence significative sur les propriétés magnétiques des composites. La perméabilité des échantillons est déterminée indirectement à travers la mesure des inductances correspondantes. Les résultats montrent que l'échantillon formé de particules de 50 µm de diamètre présente la perméabilité relative la plus élevée.

Ces mêmes échantillons sont par la suite soumis à un champ magnétique d'amplitude 160 $kA.m^{-1}$ et de fréquence 2300 Hz. Les résultats révèlent que le composite dopé de particules de 5 µm de diamètre conduit à une élévation de température supérieure, et ceci quelle que soit la fraction de particules testée.

Le mécanisme CIBF des composites magnétiques est clairement dépendant de l'aire des cycles d'hystérésis magnétiques qui représente indirectement la chaleur générée à travers le matériau. L'observation de ces cycles pour les matériaux testés montre à nouveau que les composites dopés de particules de 5 µm présentent la plus grande surface, confirmant les conclusions établies par les mesures de perméabilités et de températures.

5) Influence de la géométrie des échantillons

a) Influence de l'épaisseur

Dans cette étude, des composites Fe_3O_4@ABS formés de 30% vol. de particules, de surfaces supérieures et inférieures rectangulaires (60 × 14 mm2) et d'épaisseurs variables (de 0,3 mm à 4,0 mm) sont fabriqués. L'élévation de température sous l'effet CIFB est modérée pour le film composite mince (0,3 mm), où une relativement faible augmentation de 10 ° C est observée. En revanche, les échantillons de 3 et de 4 mm d'épaisseur présentent une variation de température beaucoup plus importante, ceci confirme que le succès de l'effet CIBF dépend fortement de la forme de l'échantillon. Un rapport volume/surface plus élevé entraîne clairement une augmentation de la vitesse du temps de réponse (paramètres critiques à minimiser pour répondre aux exigences médicales [29]).

b) Influence de la forme

Nous cherchons à vérifier ici que l'effet CIBF peut être influencé par la forme du matériau. Pour comparer aux échantillons de forme rectangulaire déjà testés, des grands et des petits échantillons supplémentaires en forme d'aiguille (figure 3 (d)) formés de 25% vol. et de 30% vol. de particules de Fe_3O_4 sont réalisés.

Les tests CIBF des composites Fe_3O_4@ABS en forme d'aiguille montrent que la variation de température ne dépend pas de la forme mais uniquement du rapport volume/surface de l'échantillon. La comparaison entre les réponses des deux échantillons en forme d'aiguille permet de conclure que plus ce rapport est élevé, plus l'élévation de température résultante sera importante.

6) Influence de la nature des particules

Afin de valider le choix de l'oxyde de fer, nous avons comparé ses performances à celles d'autres types de particules magnétiques (Ni, Mn-Zinc). Les résultats confirment que le Fe_3O_4 présente de meilleures performances magnétiques et par conséquence une meilleure réponse thermique. La bonne perméabilité du Fe_3O_4 permet de conduire efficacement le flux magnétique à travers le composite, générant une augmentation significative de l'effet de chauffage par induction.

3.3 Modèle Comsol® pour l'étude des transferts thermiques

Pour une analyse plus approfondie du comportement thermique des composites ferromagnétiques, un modèle Comsol® éléments finis a été développé et étudié.

Deux niveaux d'échelles ont été étudiés (échelle macroscopique, échelle microscopique):

1) Echelle macroscopique

Un échantillon homogène, présentant des échanges par rayonnement et par convection a été simulé pour obtenir la puissance de chauffage magnétique moyenne (MHP). La valeur MHP réelle de l'échantillon a été estimée en ajustant la distribution de températures moyennes simulées aux mesures de températures expérimentales dans la zone la plus chaude de l'échantillon.

Le résultat met en évidence l'excellent accord entre les températures expérimentales et simulées dans la zone chaude. Il permet de confirmer la grande fidélité de notre modèle.

Le tableau 1 résume les paramètres de réglage utilisés pour des composites magnétiques constitués de différentes fractions volumiques de particules. L'émissivité ε, la chaleur spécifique Cp ($J.kg^{-1}.K^{-1}$), la conductivité thermique λ ($Wm^{-1}.K^{-1}$) et le coefficient de transfert h ($Wm^{-2}.K^{-1}$) sont des paramètres du composite qui ne dépendent que de la fraction volumique des particules et ne varient pas avec la fréquence du champ d'excitation magnétique. En revanche, la fréquence influe de manière significative sur la réponse thermique des composites.

Tableau 1. Paramètres thermiques pour la modélisation des composites macroscopiques constitués de différentes fractions de particules et modélisés à des fréquences de champ magnétique de 2300Hz et 4200Hz.

	3% vol.	**10% vol.**	**17% vol.**	**30% vol.**
Surface emission ε	0.9	0.9	0.9	0.9
Specific heat Cp (J.kg–1.K–1)	1260	1040	900	744
Thermal conductivity λ ($W.m^{-1}.K^{-1}$)	0.32	0.36	0.4	0.54
Transfer coefficient h ($W.m^{-2}.K^{-1}$)	20	20	20	20
Heat power density P($W.m^{-3}$) – 2300Hz	0.2×10^6	0.7×10^6	1.3×10^6	2x 106
Heat power density P($W.m^{-3}$) – 4200Hz	0.4×10^6	1.05×10^6	1.8×10^6	3.7 x 106

2) Echelle microscopique

Pour mieux comprendre l'effet CIBF, de la modélisation à l'échelle microscopique a également été développée. La figure 14 illustre les transferts thermiques entre particules ferromagnétiques à l'intérieur de la matrice polymère. Trois fractions volumiques différentes (3%, 10% et 17%) sont testées. Comme illustré figure 14, l'échantillon présentant la fraction volumique la plus élevée (17%) présente une très petite distance inter-particule, ceci conduit à un effet de chauffage par induction plus régulier et une augmentation considérable de la température de l'ensemble du composite. En revanche, dans le cas du composite à faible contenu magnétique (3%), la distance inter-particules est très importante, les transferts thermiques sont beaucoup moins homogènes, ce qui entraîne une diminution générale de la température de l'ensemble de l'échantillon.

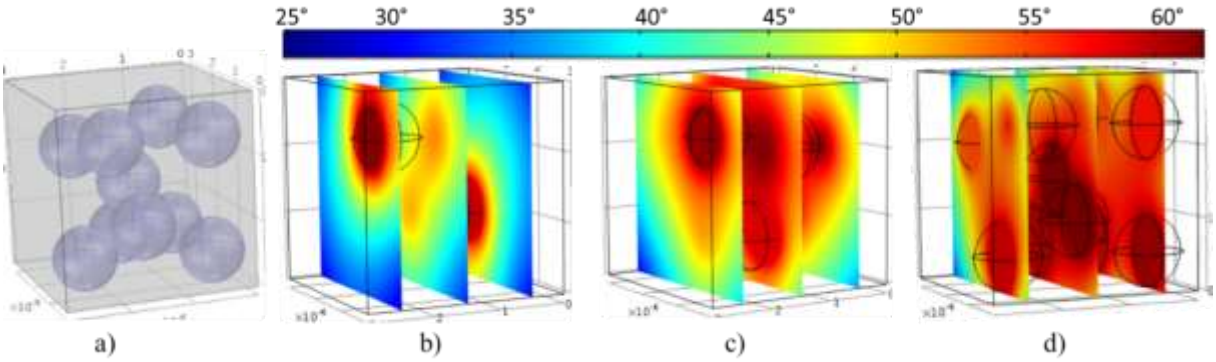

Figure 14. (a) Illustration de la distribution à l'échelle microscopique du composite ferromagnétique. Répartition de la température (b) 3% vol. fraction, (c) 10% vol. fraction, et (d) 17% vol. fraction.

Les résultats de modélisation indiquent que dans la configuration actuelle des composites testés, une température maximale d'environ 100 ° C peut être atteinte à la fin de la première minute. Ce résultat confirme la viabilité de la méthode. Cependant, les performances de nos composites et du système d'induction doivent être considérablement améliorées pour répondre aux contraintes imposées pour le traitement des varices (la température doit monter jusqu'à 100-120 ° C pendant un temps très court (généralement moins de 5 s) pour éviter des brûlures cutanées, des hématomes voir des lésions nerveuses). L'outil de simulation développé fourni une analyse approfondie des paramètres principaux de la méthode CIBF.

La figure 15 (a) illustre l'évolution temporelle de la température en fonction de la fraction volumique sous une intensité magnétique de 2300 Hz. Comme observé précédemment, le composite dopé à 30% vol. atteint une élévation de température proche des 100 ° C. La figure 15 (b) montre que les résultats de simulation de ce même composite anticipe une température finale de 220 ° C pour une excitation magnétique à 7000 Hz, bien supérieure aux exigences médicales. De plus, cette température serait considérablement plus élevée en augmentant la

fraction de particules. Même si cette fraction ne peut dépasser les 30 à 40% vol. correspondant au seuil de percolation.

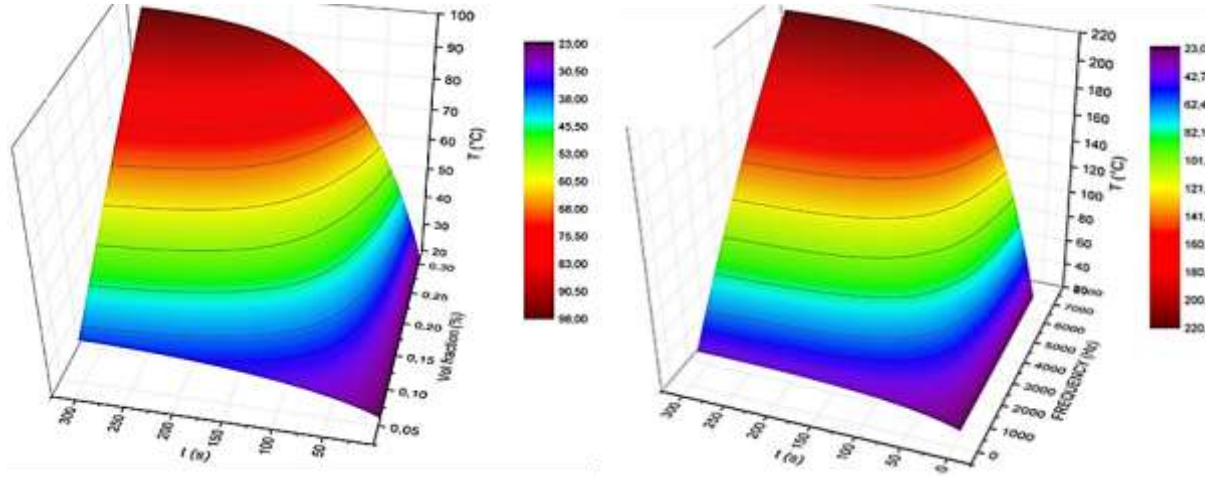

(a) (b)

Figure 15. Performance du chauffage par induction en termes de (a) fraction volumique et (b) fréquence du champ magnétique.

Ce chapitre a fourni une analyse complète des différents paramètres impliqués dans le mécanisme CIBF. Pour améliorer de manière significative l'efficacité de chauffage par induction, l'excitation magnétique AC (amplitude et fréquence) ainsi que la fraction de particules Fe_3O_4 représentent les paramètres les plus sensibles. Des résultats expérimentaux et des résultats de simulation ont montré la viabilité du chauffage par induction. 100 ° C a déjà était atteint, ce qui est proche de la température cible imposée par la procédure d'ablation veineuse. Nous avons également mis en évidence que l'effet de chauffage dépend également dans une second mesure de la nature et de la taille des particules, finalement les dimensions de l'échantillon présentent également une influence relative. Pour s'adapter aux contraintes médicales, des composites ferromagnétiques ont été élaborés en forme d'aiguille. Une grande amélioration de l'effet CIBF a été obtenue en doublant le nombre d'aimants permanents de l'inducteur et donc la fréquence de l'excitation. Dans le chapitre suivant nous nous intéressons à l'optimisation du processus de fabrication du matériau.

Chapitre 4 - Composites ferromagnétiques anisotropes

4.1 Fabrication de composites anisotropes

Les particules magnétiques peuvent être incorporées dans la matrice polymère de manière aléatoire ou de façon ordonnée (figure 16). Une structure ordonnée conduira à des propriétés anisotropes de l'échantillon résultant. Cette anisotropie donne naissance à des directions préférentielles où les propriétés physiques sont améliorées. Une distribution structurée des particules magnétiques peut être obtenue en fabriquant le composite sous l'influence d'un champ magnétique externe (magnétophorèse). Ceci conduit à la formation de chaînes de particules et à un composite présentant de fortes propriétés d'anisotropie.

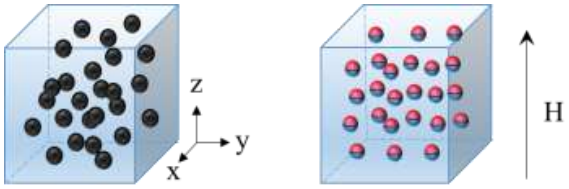

Figure 16 Représentation schématique des particules: (a) distribution aléatoire; (b) distribution structurée

Les élastomères à base de PDMS présentent un comportement extensible à haute température et une stabilité mécanique sur une plage de température allant de -45 à 200 ° C, ils constituent donc la meilleure option de matrice polymère pour nos composites anisotropes.

Nous avons opté pour l'utilisation d'un moule pour la fabrication de notre composite anisotrope. De la poudre de particules Fe_3O_4 est mélangée à l'élastomère silicone. Pour créer un alignement dans la distribution des particules, le moule de forme cubique de $5 \times 5 \times 5$ mm^3 rempli de la solution résultante du mélange est placé entre deux aimants permanents comme illustré sur la Figure 17. En raison du fort champ magnétique, des chaînes de particules se forment et se figent dans l'élastomère (le long de la direction z, parallèle aux lignes de champs magnétiques). Des résultats expérimentaux et des résultats de simulation sont proposés pour vérifier l'amplitude et l'uniformité du champ magnétique générées par les aimants permanents dans la zone de l'échantillon.

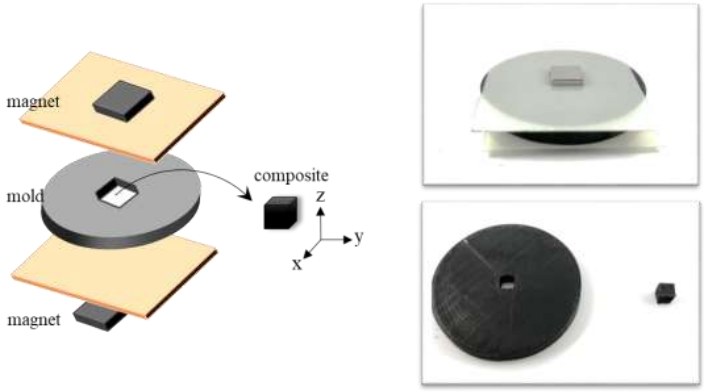

Figure 17. Vue 3D globale et photos du moule cubique et de l'échantillon cubique.

4.2 Caractérisation des composites anisotropes

Des images au microscope électronique à balayage (MEB) sont utilisées pour étudier la distribution des particules des composites ferromagnétiques. Figure 18, les points blancs représentent les particules de Fe_3O_4 tandis que le fond noir est la matrice de PDMS. Les premières observations montrent clairement de forts alignements (le long de l'axe z) dans la direction du champ magnétique.

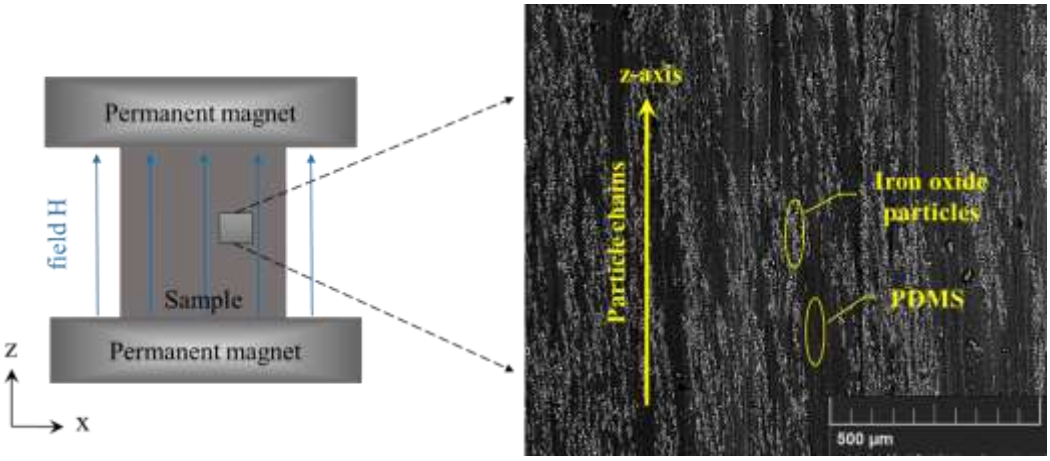

Figure 18. Image MEB d'un composite anisotrope.

Des composites orientés et non orientés de 5% vol. Fe_3O_4 ont été observés au MEB. L'observation des images SEM et de leurs histogrammes de directivité montrent clairement une forte distribution structurée des particules ferromagnétiques, confirmant nos attentes.

La perméabilité magnétique d'échantillons de forme cubique peut être obtenue à partir de la mesure de l'inductance. Comme prévu sur la figure 19 (b), le cube anisotrope présente une perméabilité relative plus élevée sur l'axe z que sur l'axe x et y (amélioration de 25%). Il est

intéressant d'observer que les échantillons orientés ont toujours une perméabilité plus élevée que les échantillons non orientés.

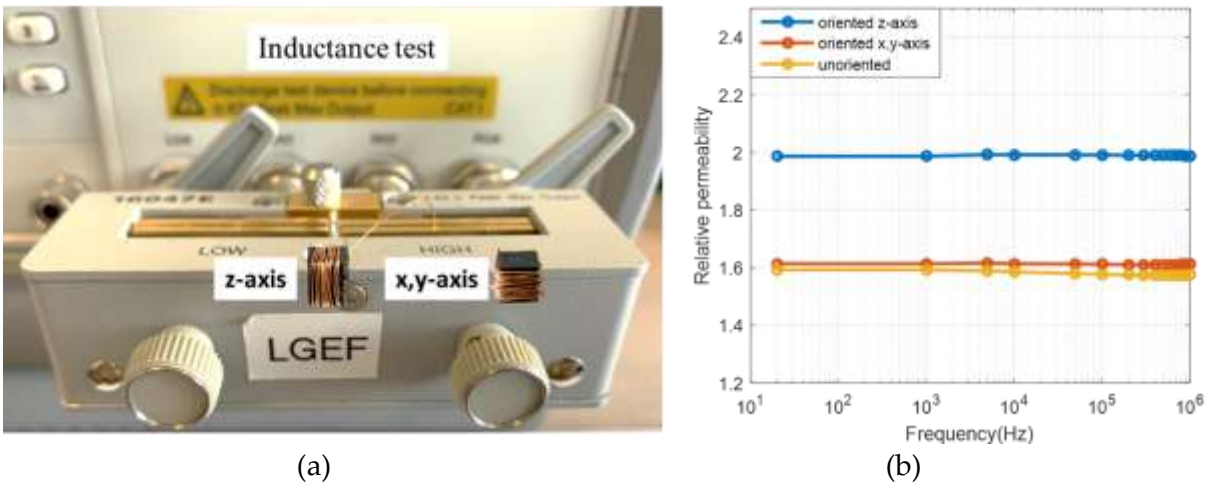

(a) (b)

Figure 19. Banc d'essai utilisé pour la détermination de la perméabilité: (a) Compteur LCR basé sur la mesure de l'inductance. (b) Perméabilité relative de l'échantillon aléatoire et des échantillons orientés (axe z et axe x, y) en fonction de la fréquence.

Les cycles d'hystérésis des composites Fe3O4@PDMS isotropes et anisotropes (particules de 5 μm de diamètre, fraction de 30% vol. de particules) ont été mesurés dans le banc de caractérisation de notre laboratoire. Ces cycles d'hystérésis sont présentés sur la figure 20, l'excitation magnétique est orientée dans la direction de l'alignement. Dans les mêmes conditions expérimentales, l'aire du cycle d'hystérésis des composites anisotropes est clairement plus grande que celle du composite isotrope (réponse magnétique plus forte), l'induction rémanente est également plus élevée, ces résultats confirment la réponse magnétothermique supérieure du composite anisotrope.

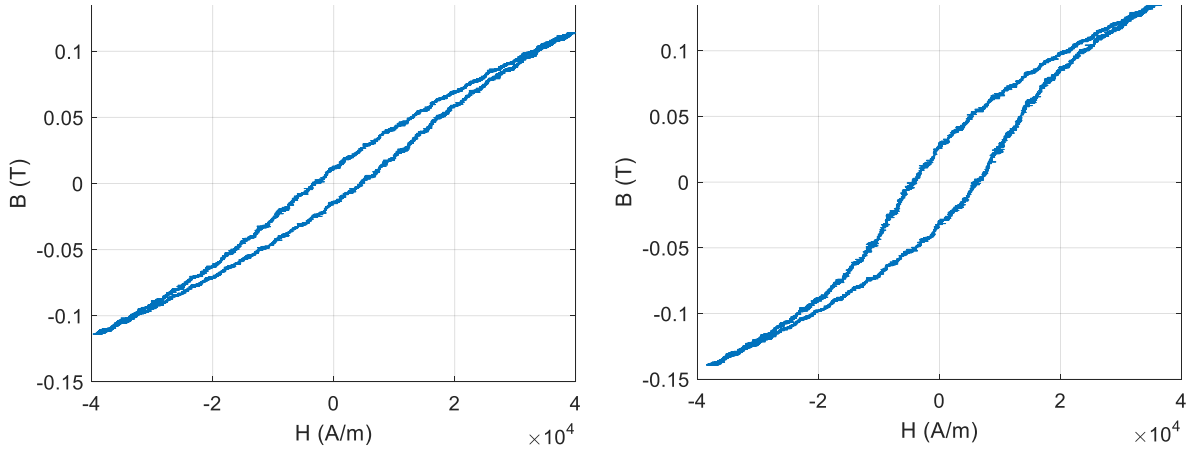

(**a**) (**b**)

Figure 20 Cycle d'hystérésis de (a) composite Fe3O4@PDMS non orienté, et (b) composite Fe3O4@PDMS orienté sous champ magnétique de fréquence 1Hz et 40 kA.m-1.

La figure 21 donne les variations temporelles de température pour les échantillons orientés et non orientés, induites par une excitation magnétique alternative le long de l'axe z (axe de facile aimantation des composites anisotropes). Quelle que soit la fraction de particules, les échantillons orientés génèrent systématiquement une élévation de température supérieure. A l'échelle microscopique, les chaînes de particules alignées canalisent les lignes de champ magnétique et donnent lieu à une réponse CIBF améliorée. Que ce soient les composites isotropes ou les anisotropes, les réponses thermiques s'assimilent clairement à des réponses du type premier ordre.

En comparant la température finale obtenue dans chacune des directions (x, y et z) nous observons que les échantillons anisotropes présentent systématiquement une réponse thermique plus importante que les échantillons isotropes. De plus, la constante de temps de l'effet CIBF selon l'axe z (axe de facile aimantation) est trois fois inférieure à celle des x et y.

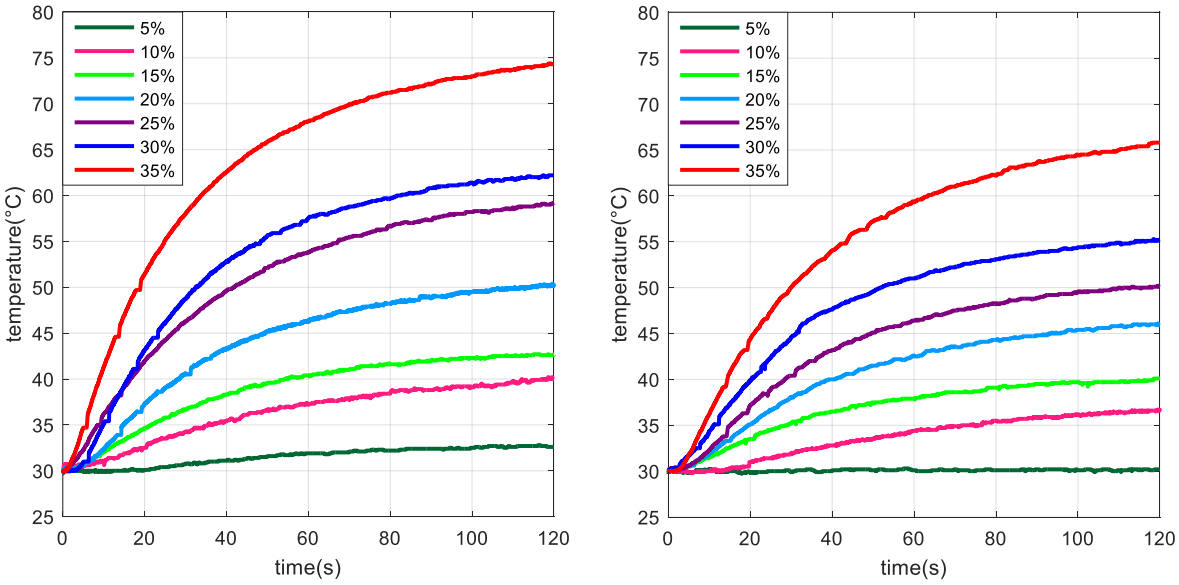

Figure 21. Diagramme de température en fonction du temps pour augmenter les échantillons de fraction de volume de particules. a) axe Z du composite orienté; b) Axe Z du composite non orienté.

Les différences fortes de perméabilité magnétique observées d'une direction à l'autre des échantillons anisotropes ouvrent d'autres perspectives, telle que la conception de capteurs

intelligents pour les applications médicales, capteurs qui peuvent être utilisés pour le système de suivi électromagnétique (LSE) particulièrement utile dans les procédures endovasculaires.

Dans ce chapitre nous avons vérifié que des comportements anisotropes avec des propriétés magnifiés ont été obtenus grâce au principe de magnétophorèse. Dans le chapitre suivant nous nous concentrons sur l'optimisation de la formulation des matériaux afin d'être adaptable à l'impression 3D.

Chapitre 5 - Composites flexibles imprimés 3D

Dans ce dernier chapitre, l'ensemble des résultats présentés provient de l'utilisation d'une imprimante 3D commerciale de type extrusion. Des pâtes magnétiques préparées dans notre laboratoire (mélange de microparticules de Fe_3O_4 et matrice PDMS) ont été testées. L'ensemble du processus expérimental se résume en deux étapes:

_ mélange de la poudre magnétique et du polymère pour constituer une pâte adaptée à l'impression 3D,

_ extrusion de la pâte, couche par couche jusqu'à l'obtention de l'objet désiré.

Un comportement anisotrope peut être obtenu sous l'effet d'un champ externe pendant l'opération d'impression. La figure 22 donne une illustration du procédé d'impression 3D. Le dispositif de génération du champ magnétique externe est positionné sous la buse de l'extrudeuse de manière à fournir un champ homogène lors de l'impression des échantillons testés.

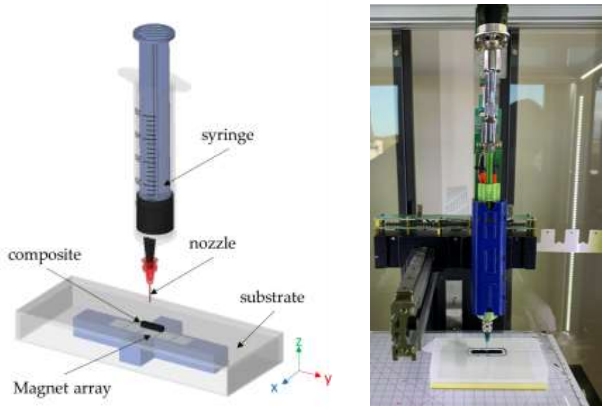

(a) (b)

Figure 22 (a) Schéma et (b) image physique de la configuration d'impression 3D.

Des aimants permanents sont utilisés comme source magnétique. L'ensemble inducteur est construit sur la base d'un réseau de cinq aimants cubiques identiques. Trois configurations ont été testées :

_ le réseau vertical,

_ le réseau horizontal

_ le réseau de type Halbach.

La distribution du champ magnétique résultant a été simulée à l'aide des éléments finis à partir du logiciel Comsol®. Les résultats de simulation donnant la densité de l'induction magnétique

(B) le long de l'axe z de symétrie pour les trois configurations testées sont présentés sur la figure 23. Une bonne cohérence entre la vérification expérimentale (sonde à effet Hall) et les résultats théoriques a été observée. Il est important d'imprimer l'échantillon aussi près que possible du centre du réseau d'aimants car les gradients de champ augmentent avec la distance à l'axe de symétrie.

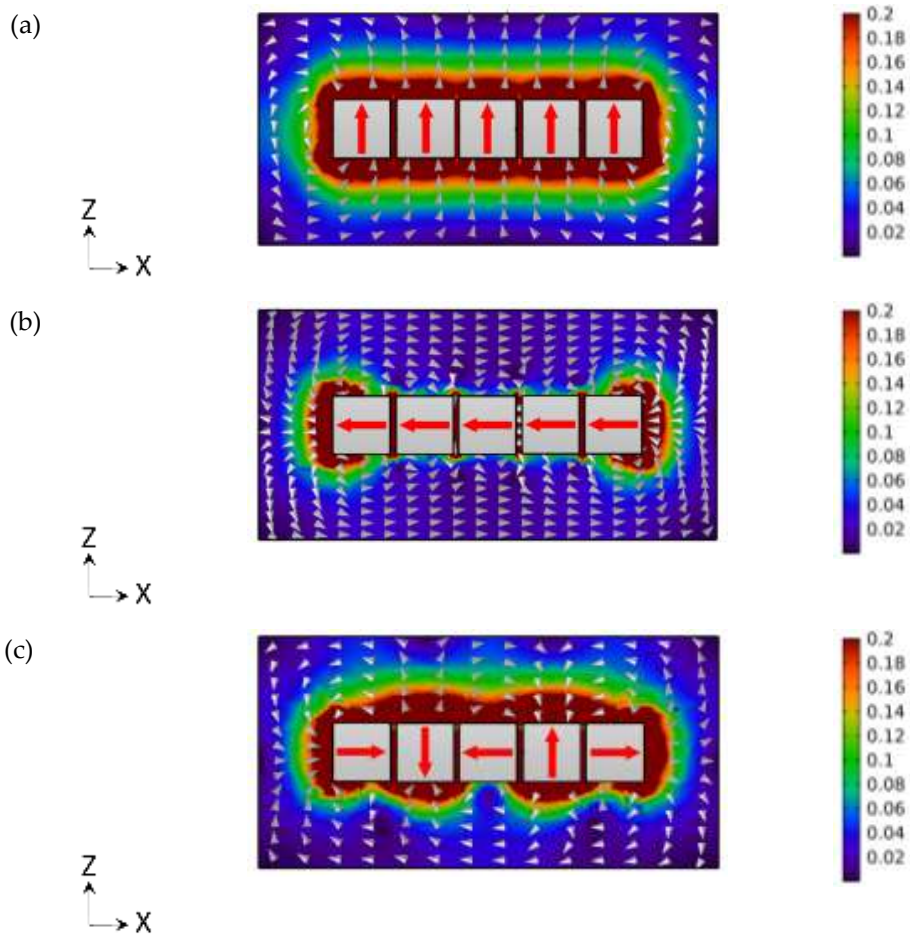

Figure 23 Répartition du champ magnétique (a) du réseau vertical; (b) réseau horizontal; et (c) matrice de Halbach.

Des composites Fe_3O_4@PDMS (30% vol. de particules) sont imprimés avec ou sans l'influence d'un champ magnétique statique. Le niveau du champ ne dépend pas uniquement du réseau d'aimant mais également de la distance entre la source magnétique et l'échantillon imprimé. Nous avons testé trois distances (4 mm, 8 mm et 12 mm) et imprimé des composites en forme d'aiguille de dimensions 33 × 5 × 4 mm^3.

On peut voir (figure 24 (b)) l'influence de la distance sur la masse des composites imprimés dans les 3 configurations testées. Quelle que soit la distance, le réseau vertical conduit systématiquement à une force magnétique supérieure (figure 24 (a)). Enfin, pour obtenir le meilleur compromis entre performances magnétiques et qualité d'impression, nous avons opté pour une distance de 8 mm entre le réseau magnétique et le plateau d'impression..

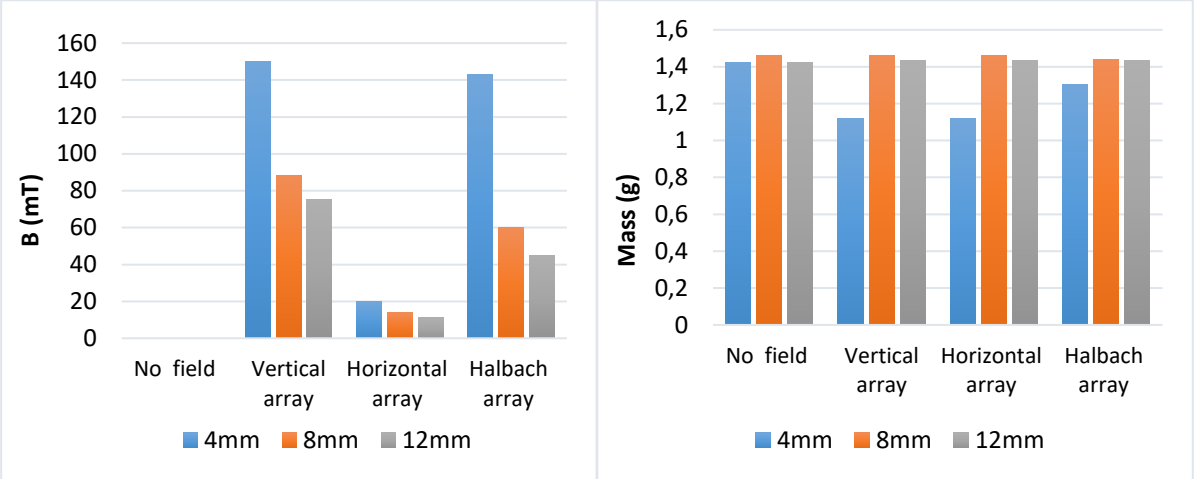

Figure 24 Influence de la distance a) de la densité de flux magnétique; et b) la masse des composites imprimés sous 4 configurations d'installation.

La figure 25 ci-dessous montre les composites imprimés en forme d'aiguille soumis à différentes configurations du champ magnétique externe. Tous les échantillons exposés ici, ont été imprimés à partir d'un extrudeur en plastique, et ont été placés à la même distance (8 mm) du réseau d'aimants. Clairement, les trois sources magnétiques donnent des échantillons avec des apparences très inhomogènes. La qualité d'impression dépend définitivement de la direction du champ. Un champ magnétique horizontal est définitivement la configuration la plus adéquate pour obtenir une forme fidèle à l'objectif de l'échantillon.

(**a**) (**b**) (**c**) (d)

Figure 25 Échantillons imprimés avec une pointe STT sous 4 configurations: (a) sans magnétophorèse; et avec une magnétophorèse consistant en (b) un réseau vertical; (c) réseau horizontal; et (d) matrice de Halbach.

La perméabilité de ces quatre échantillons en forme d'aiguille est mesurée le long de l'axe y. Le critère anisotrope est particulièrement important dans le cas du réseau Halbach où l'on constate une augmentation d'environ 30% par comparaison aux échantillons non orientés. Le test CIBF montre également que l'échantillon orienté par le réseau Halbach possède la plus forte variation de température en revanche l'échantillon soumis au réseau vertical présente la plus faible.

Pour mettre en évidence le comportement anisotrope des échantillons de formes cubiques (5 × 5 × 5 mm^3) sont préparés. Le réseau horizontal et le réseau Halbach sont testés, ceux-ci génèrent un champ magnétique important le long de l'axe y.

Les résultats de mesure de perméabilité (figure 26) montrent que l'échantillon non orienté présente comme prévu un comportement magnétique globalement isotrope. En revanche l'orientation des particules magnétiques générée par le champ statique améliore clairement la perméabilité le long des axes x et z et une augmentation encore plus significative peut être observée dans la direction de facile aimantation (axe y). On observe également que le réseau Halbach conduit à une perméabilité relative plus élevée sur l'axe y que le réseau horizontal.

La figure 27 montre les résultats des tests CIBF des parallélépipèdes orientés par les réseaux horizontal et Halbach. Ces résultats confirment le comportement anisotrope et ceci même si l'amplitude de champ à l'origine de la magnétophorèse est relativement faible. D'autre part, un faible niveau de champ semble suffire pour aimanter avec succès les composites anisotropes dans la direction de facile aimantation. Finalement, la direction du champ externe est le facteur clé pour favoriser l'anisotropie, que ce soient pour les tests magnétiques ou thermiques.

Les échantillons excités dans la direction de facile aimantation présentent une amélioration significative de la perméabilité relative (augmentation de 50%) et de la température (augmentation de 30%).

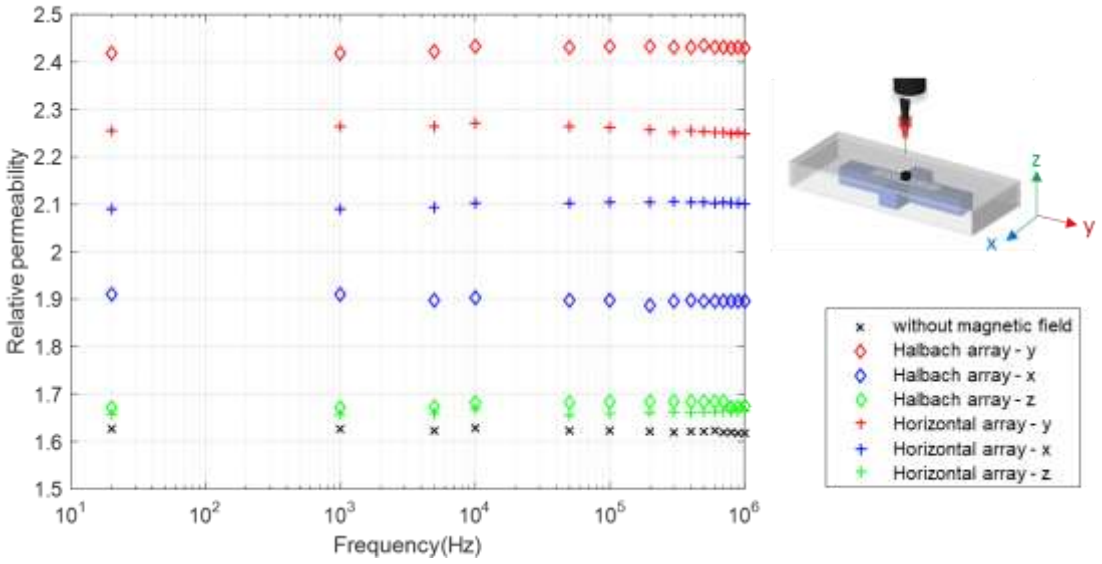

Figure 26 Perméabilité relative de l'échantillon cubique imprimé dans différents axes.

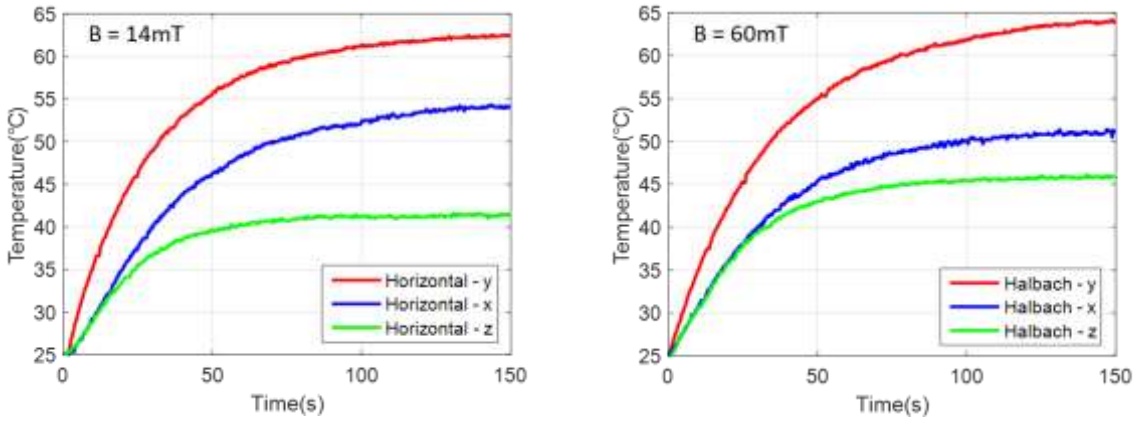

(**a**) (**b**)

Figure 0-27 Time evolution of temperature measured on cubic samples subjected to magnetophoresis using (a) horizontal array; and (b) Halbach array.

La conductivité thermique des composites magnétiques dépend fortement de la distribution des particules au sein de la matrice polymère. Pour l'échantillon orienté, la conductivité thermique augmente d'environ 58% dans la direction de facile aimantation. L'augmentation de la conductivité thermique provient de l'alignement des chaînes de particules dont la conductivité thermique est bien supérieure à celle de la matrice polymère. En ce qui concerne la capacité thermique, une légère augmentation d'environ 10% dans la direction de facile aimantation est observée.

Dans ce chapitre nous avons développé un processus de magnétophorèse couplé à de l'impression 3D qui permet d'obtenir des formes et des tailles adaptées de composites Fe_3O_4@PDMS présentant des comportements magnétiques anisotropes. Les particules magnétiques s'alignent sous l'effet du champ magnétique pendant l'étape d'impression. Une amélioration importante de la perméabilité relative et de l'effet CIBF est observée. Ces premiers résultats d'impression 3D sous influence sont particulièrement encourageants, ils ouvrent la voie à de nombreuses utilisations médicales (comme le suivi électromagnétique ou encore le traitement des varices étudié dans cette thèse).

Chapter 1 State of Arts

In this chapter, a background knowledge on magnetism is reminded with a special attention on the ferromagnetic materials and their magnetization processes, including the domain wall theory, the hysteresis behavior, and their applications. The eddy current natures and their potential as heat sources are discussed. Next, we presents the selection criteria of particles and the polymer matrix in order to get high magnetic performance. The potential of the ferromagnetic composites towards medical applications including the varicose veins healing or the electromagnetic tracking are also introduced.

1.1 Background on magnetism

1.1.1 Magnetism

The source of magnetism lies in the basic building block of all matter: the atom. A magnetic field is produced whenever an electrical charge (electron) is in motion. The strength of this field is called the magnetic moment. The macroscopic magnetism as observed at the human scale comes from the atomic magnetic moments (one is the motion of the electrons in an orbit around the nucleus, and the other is the spin of the electrons around its axis). No resulting magnetic field exists in paired electrons as they cancel each other. According to their interactions with a magnetic field, materials can be classified as [1]: diamagnetic materials, paramagnetic materials, ferromagnetic materials, ferrimagnetic materials, antiferromagnetic materials, and super-paramagnetic material.

Diamagnetic materials have a weak, negative susceptibility to magnetic fields. A magnetic field slightly repels diamagnetic materials. Diamagnetic materials do not show magnetic remanence when the external field is removed. Only paired electrons exist in diamagnetic materials. Examples include copper, silver, and gold.

Paramagnetic materials have a small, positive susceptibility to magnetic fields. A magnetic field slightly attracts paramagnetic materials. Paramagnetic materials do not show magnetic remanence when the external field is removed. Paramagnetic materials have some unpaired electrons, but their alignments become defused due to thermal energy randomization. For this reason, its magnetization cannot be retained in the absence of an external magnetic field [6]. Examples include magnesium, molybdenum, and lithium.

Ferromagnetic materials have a large, positive susceptibility to external magnetic fields. They exhibit a strong attraction to the magnetic field and show remanent magnetic properties once an external field is removed. Ferromagnetic materials have some unpaired electrons and their atoms have a net magnetic moment. Iron, Nickel, and cobalt are examples of ferromagnetic materials.

The magnetic moments distribution and properties depend on the temperature. The Curie temperature is a critical point where phase changing can be observed The Curie point of a ferromagnetic material is the temperature above which it loses its ferromagnetic properties. For lower temperatures, the magnetic moments are aligned within the magnetic domains. As the temperature is increasing towards the Curie point, the alignment within each domain is decreasing. Above the Curie point, the material becomes paramagnetic.

A ferrimagnetic material has populations of atoms with opposing magnetic moments (same direction but opposite orientation). The moment amplitudes are unequal resulting in a spontaneous magnetization. Ferrimagnetic materials are weakly attracted to magnetic fields. Ferrimagnetic materials are like ferromagnets as they hold a spontaneous magnetization

below the Curie temperature and show no magnetic order (paramagnetic) above this temperature. The oldest known magnetic substance “magnetite” (iron(II,III) oxide; Fe3O4) is a ferrimagnet. Zinc and Magnesium are examples of ferrimagnetic materials.

In antiferromagnetic materials, the exchange interaction between neighboring atoms leads to an antiparallel alignment of the atomic magnetic moments. The resulting magnetization is null. In the periodic table, the only element with antiferromagnetic properties at room temperature is chromium. Figure 1-1 shows the atomic arrangement of the different magnetic phases:

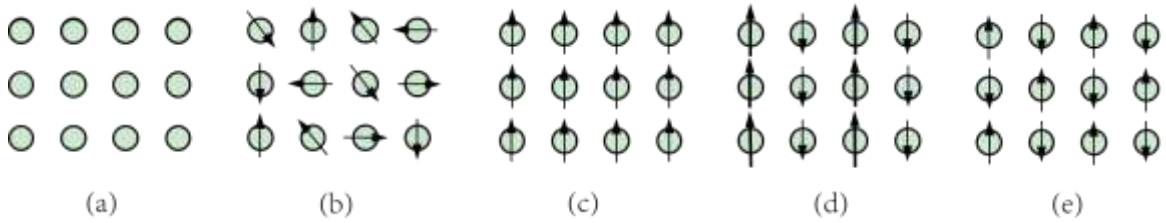

Figure 1-1. Five different atomic magnetic moments arrangement: (a) Demagnetization; (b) Paramagnetism; (c) Ferromagnetism; (d)Ferrimagnetism; (e) Antiferromagnetism.

1.1.2 Domain theory and magnetization processes

When a ferromagnetic material is subjected to a gradually increasing magnetic field, its magnetization increases discontinuously (small jumps). When a jump occurs, electromagnetic noise is generated. If the noise is monitored and amplified, a series of "clicks" can be heard. This phenomena is known as the “Barkhausen effect”. Non-magnetic inclusions, or dislocations in the crystallographic structure, can cause "pinning" of the domain walls at the origin of this behavior. In the absence of magnetic field, domain walls form to minimize the internal potential energy [2]. When these magnetic domains are subjected to a magnetic field, the domain walls are "unpinned" and start to move [3][4]. These sudden movements of the domain walls generate sudden changes in the volume of the neighboring domains and Barkhausen noise is generated. The Barkhausen activity was the first confirmation of the magnetic domain existance [5].

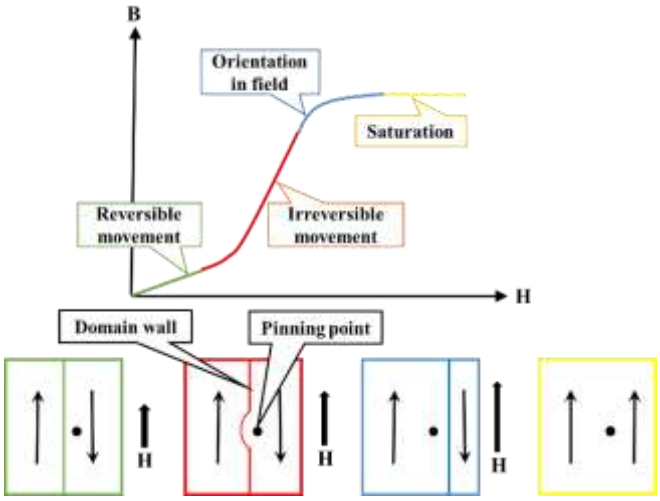

Figure 1-2. Domain wall motions during the magnetization process

Ferromagnetic materials are composed of small areas called domains. In each domain, all the atomic moment are aligned in the same orientation (cf. Figure 1-1(c)). In an un-magnetized state the magnetic domains cancel each other (Figure 1-3). The magnetic moment direction within a given domain is constant in areas distant from the boundaries (also known as the domain wall). Typically, the magnetic domains are of a 1-100 μm size.

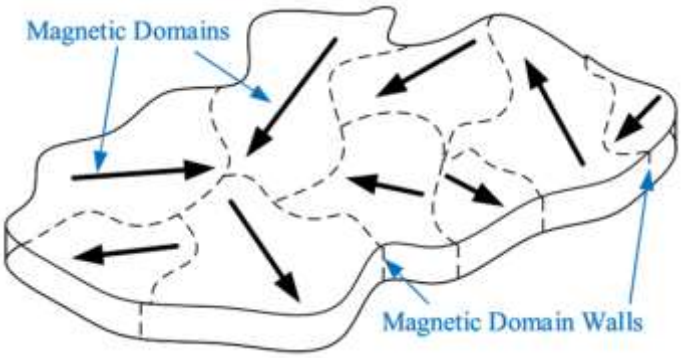

Figure 1-3. Magnetic domains and magnetic walls visualization[6]

The domains characterized by a magnetic moment with a close direction and orientation of the external field gain in energy and grow while the others shrink and disappear. The size of the favorably oriented domains increases while the size of the other domains decreases and this in order to minimize a sum of internal energy. Until the magnetization reaches a saturation value and no more variation is observed. Afterward, if the excitation field is reduced down to zero, the alignment of the magnetic domains is disrupted. A considerable magnetization level is retained, which is designated as the remanent magnetization, also known as the residual magnetization. When the applied field reverses its direction, the material is again split up into magnetic domains of different directions and orientations. Now, if the field keeps increasing in the reverse direction, domains with residual magnetization direction gradually and eventually surrender to other domains. Finally, the total average magnetization reaches an

equilibrium state as zero. The magnetic field required is called the coercive field, its value is an intrinsic property used to distinguish the "soft" and "hard" ferromagnetic materials.

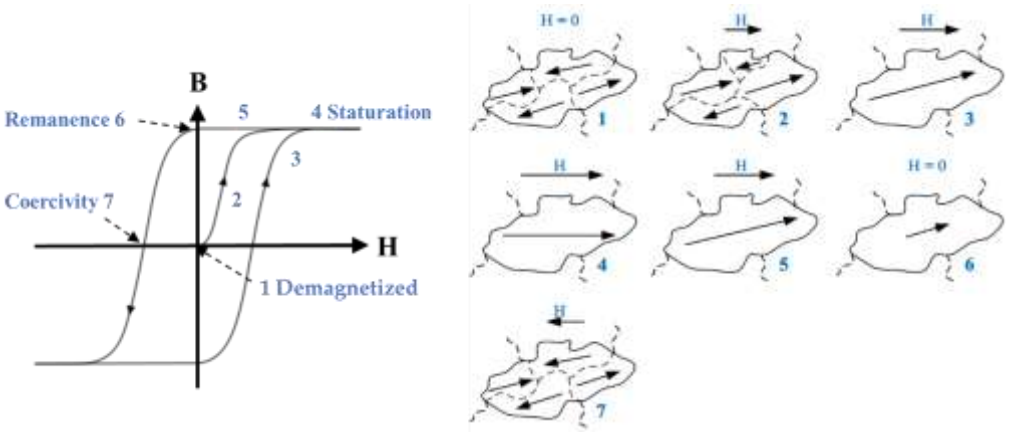

Figure 1-4. Magnetization process and magnetic domain evolution [7]

The exchange energy (E_{ex}), the demagnetizing field energy (E_D), the magnetocrystalline anisotropy energy (E_λ), the magnetoelastic energy (E_k) and the Zeeman energy determines the magnetic domain structure (size and orientation). The magnetic domain structure in the equilibrium state minimized the resulting energy:

$$E = E_{ex} + E_D + E_\lambda + E_k + E_H \qquad \text{Equation 1-1}$$

1.1.3 Magnetic hysteresis

The hysteresis loop is the representation of the magnetic induction (B) vs the magnetizing force (H) of a ferromagnetic material (see Figure 1-4 on the left). Hysteresis loops are generated from the characterization of ferromagnetic materials. Hysteresis in magnetism is generally attributed to the impediment of domain wall movement by material inclusions and stress inhomogeneities inherent to the materials. The hysteresis loop's total area equals the energy dissipated when a material of unit volume is magnetized during a cycle of operation. The slope of B as a function of H is the magnetic permeability. The curvature of the hysteresis loop is a characteristic of the material nature and can vary in size and shape [8].

According to its hysteresis loop, a magnetic material can be classified as a soft magnetic material or as a hard magnetic material (Figure 1-5). A narrow hysteresis loop is linked to a soft magnetic material (small amount of dissipated energy). Narrower hysteresis loops exhibit high permeability and low coercivity. Soft magnetic materials can be easily magnetized and demagnetized, little energy is needed. Coercivity is lower than 1000A/m [9].

Wider hysteresis loops (high remanent induction and coercivity) are typically observed for hard magnetic materials. The initial permeability is low and the magnetization cycle requires large energy dissipation. Demagnetization is challenging to achieve, there is a larger area to cover when reversing the hysteresis loop to its original un-magnetized state.

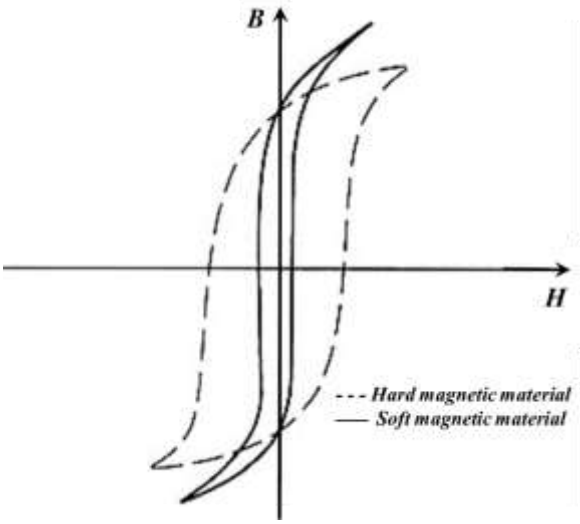

Figure 1-5. Schematic representation of hard and soft ferromagnetic material

Hysteresis is magnetism is frequency dependent. If the maximum *H* value of the magnetic field is lower than *Hs*, minor hysteresis loops will be obtained (Figure 1-6).

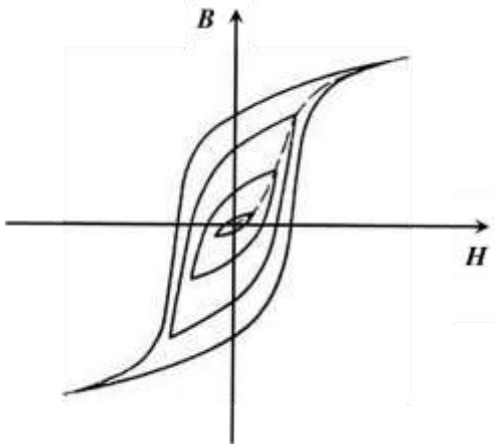

Figure 1-6. Schematic representation of quasi-static hysteresis loop

The hysteresis cycle is the standard magnetic signature, it displays the evolution of the magnetic state M as a function of the magnetic excitation H, assuming both these vector quantities in a collinear situation. Below a given frequency known as the quasi-static threshold, the frequency dependence of the hysteresis cycle is insignificant and the hysteresis shape remains unchanged. Beyond the quasi-static threshold under maximal H imposed conditions, the hysteresis area (also known as the hysteresis losses) follows the trajectory depicted in Figure 1-7 below:

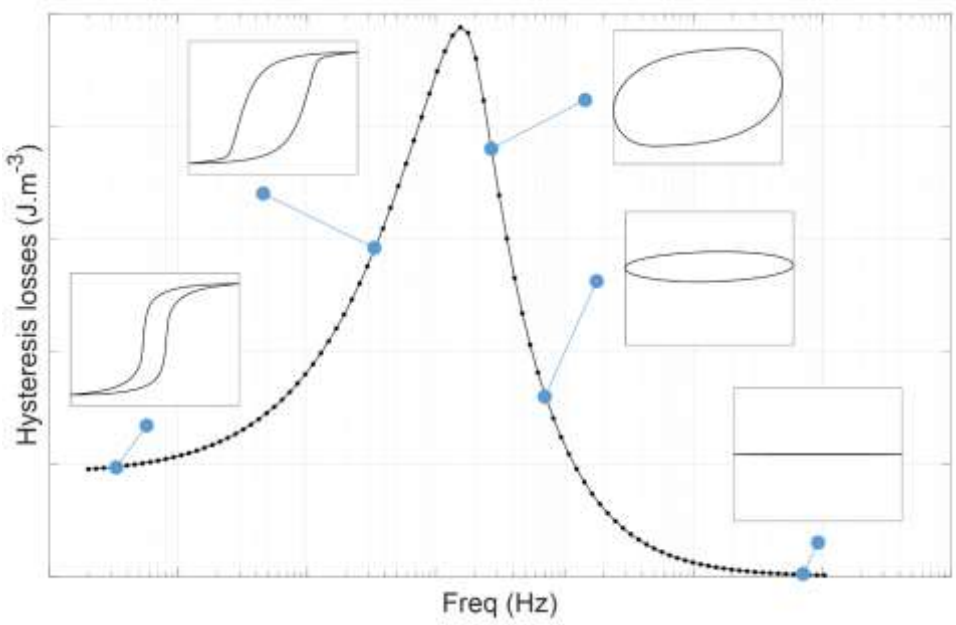

Figure 1-7 Hysteresis area as a function of the frequency

The hysteresis area grows first, up to a maximum value then decreases continuously until a full disappearance under extreme frequency levels when a shield of macroscopic eddy currents prevents magnetic penetration in the tested specimen. In a one hand, the sequence of this two phases is always true, in the other hand due to the complexity of hysteresis and ferromagnetism, this trajectory is always a little different from one sample to another [10]. Magnetic permeability is the property used to evaluate the capability of driving a magnetic field. It gives an indication of the attraction strength to a permanent magnet.

Magnetic permeability is defined as the ratio between the magnetic induction (B) and the magnetic excitation (H) variations:

$$\mu = \frac{\Delta B}{\Delta H} \qquad \text{Equation 1-2}$$

Permeability in free pace is denoted μ_0. Its value is $4\pi \times 10^{-7}$ H/m. This value is a standard value known as the vacuum permeability. Permeability of other mediums or substances are simply denoted μ. Relative permeability is the ratio of permeability of any substance to that of free space, it is denoted μ_r,

$$\mu_r = \frac{\mu}{\mu_0} \qquad \text{Equation 1-3}$$

A magnetic material can be characterized by its relative permeability. The magnetic permeability of diamagnetic materials is less than the permeability of vacuum, μ_0.When μ_r is less than 1. When μ_r is slightly larger than 1, the material is weakly attracted by an external magnetic field like the paramagnetic material. When μ_r is greatly larger than 1, on the other

hand, the material is strongly attracted by external magnetic fields and known as a ferromagnetic material.

Soft magnetic composite materials consist of magnetic particles scattered in non-magnetic matrix. The properties such as permeability and conductivity of these materials can be modeled using different theories, like the well-known “practical medium theory”. These theories and models will be introduced in the second Chapter of this thesis. The ferromagnetic composites' characterization will be described as well.

1.2 Magnetic composites

1.2.1 Introduction of magnetic composites

Magnetic materials can be found in a wide range of applications in science and technology. Magnetic particles mixed in a polymer are used to create magnetic composite, which opens a new generation of multifunctional materials. They combine the properties of conventional polymers to those of magnetic materials (Ferri, and/or ferromagnetic particles mixed or embedded in a polymer matrix). These composites are classified as magneto-polymeric materials [11].

The nature of the magnetic particles has a significant influence on the magnetic behavior of the composite materials. By nature we mean, the type (e.g., Iron, Iron oxide, Nickel, etc.), the size (nano, micro, etc.), and the shape (e.g., spherical, cubic, rod-shaped, etc.). The volume fraction and the spatial orientation is also significantly impacting the magnetic composites' property.

The magnetic properties of the ferromagnetic composites depend also indirectly on the polymer matrix. Composite materials consisting of a relatively rigid polymeric matrices filled with magnetic particles have been known for a long time. Rigid magnetic composites have been successfully used as permanent magnets, magnetic cores, etc. These rigid magnetic composites keep the same size, shape, and elastic properties under the influence of an external magnetic field.

Elastomer constitute another option for the polymer matrix. Several attempts have been made to build soft actuators, micromanipulators, artificial muscles, and suspension devices using magnetic elastomers

Recently, gels matrix have created significant interest as novel intelligent or smart materials. Gels have been developed and studied for biomedical and industrial field applications, e.g., controlled drug delivery systems, muscle-like soft linear actuators, biomimetic energy transducing devices, and separation techniques.

Different types of magnetic polymers are depicted in Figure 1-8. In this thesis, the ABS based ferromagnetic composite has been studied. The flexible PDMS based ferromagnetic composites have also been investigated.

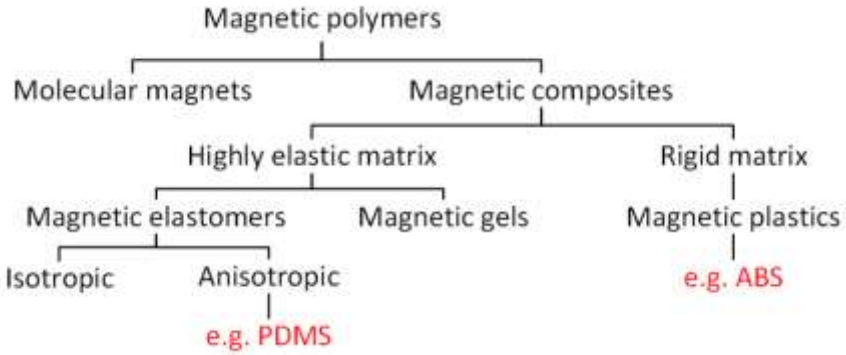

Figure 1-8. Classification of magnetic polymers [12]

According to the arrangement of particles within the matrix, ferromagnetic composites can be divided into isotropy and anisotropy. Anisotropic composites are materials whose properties are directionally dependent, while those of isotropic composites are not varying according to the direction of measurement. In this thesis, both isotropic and anisotropic ferromagnetic composite have been studied. A deeper investigation on anisotropic structure will be detailed in chapter 4.

1.2.2 Application of magnetic composites

Ferromagnetic composites are generating intense research innovation due to their high potential for applications in the biomedical, coatings, microfluidics, and microelectronics fields. By merging magnetic and polymer materials, composites with exceptional magnetic answers can be obtained.

Adjusting the polymeric matrix is essential for improving the mechanical properties of the composites especially in flexible applications. Examples are macroscopic deformation in field gradients for Ferrogels [13], deformation of Magneto-Active Elastomers in magnetic field [14][15]. These materials are called smart ferroelastic composites thanks to their original properties like large magneto deformational effects, high elastic modulus and magnetic shape memory. Recently, ferroelastic composites have even drawn more attention due to their potential for new applications including multifunctional devices, ultrasonic imaging, and acoustic devices (transducers, sensors, etc.) [16].

A significant advantage of the magnetic induction heating (IH) method is the possibility to have a non-contact control of the temperature variations. The heat generated by the magnetic particles under an external field is triggering a phase or conformational transition of the polymer, leading ultimately to a programmed response. As seen in Figure 1-9, IH effect has been found in various systems like :

- Drug delivery

Inductive heating can be used as a stimulus by promoting structural changes in a thermosensitive material, accompanied by the concomitant release of entrapped molecules. This strategy has been applied to design on-demand controlled drug delivery systems, mainly for cancer therapy, called "magneto-chemotherapy" [17].

- Shape memory material

The typical sequence for thermally stimulated shape memory polymers is the application of an initial deformation to the polymer at an elevated temperature (pre-deformation), fixing the shape by cooling the pre-deformed shape memory material under strain to a lower temperature (storage), and then heat the material to recover the original shape (recovery) [18].

- Self-healing material

The addition of induction-heated particles allows local repair of parts without disassembling the entire body. Local heating of the composite is done with an external alternating magnetic field [19]. The thermoplastic matrix ensures the self-healing through a shape memory mechanism. The magnetic particle can trigger actuation first, followed by self-healing. Application of an external temperature stimulus triggers the shape memory property, resulting in healing [20]. The resulting temperature elevation triggers the original dye aggregates' recovery, enabling the reparation [21].

- Magnetic fluid hyperthermia

Magnetic fluid hyperthermia cancer treatment involves injecting a fluid containing magnetic nanoparticles directly into tumors. Under the influence of an alternating magnetic field, the nanoparticles dissipate enough energy to raise the local temperature up to 42-45°C, high enough to destroy the tumors. Various candidate materials have been suggested, such as manganese/zinc ferrites, iron/platinum alloys, and more recently, substituted manganese oxides [22]. As magnetic field hyperthermia is the most advanced induction heating technology application in the medical field, a fine description of this method will be done in the introduction of section 1.3.2.

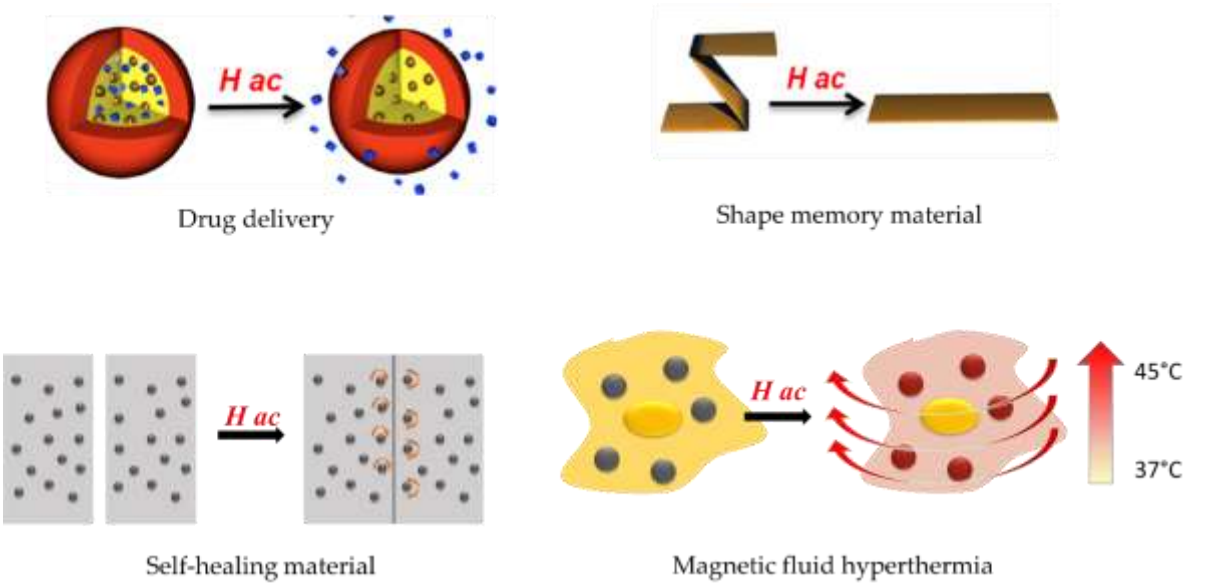

Figure 1-9. Illustration of the different applications of magnetic composites in the IH effect.

1.3 Induction heating (IH) effect

The induction heat (IH) effect can be described as the temperature elevation observed in a ferromagnetic material under the influence of an alternating magnetic field. The heat-generating mechanism under low frequency mainly stems from the hysteresis losses and the eddy current effect when a ferromagnetic material is in a micrometer size or in a nanometer size. Others heat-generating mechanisms can be observed including the Brown and the Néel relaxation. The IH mechanisms can be differentiated by the material size. There is no precise definition between the heat-generating mechanisms with particle size but approximation:

- According to [23], the mechanisms of heat losses when a high frequency ac magnetic field is applied to nanoparticles smaller than 20 nm are the moment relaxation (Néel), the particle relaxation (Brown), and hysteresis losses. The Néel mechanism dominates in particles with sizes below 7.5 nm, whereas Brownian mechanism prevails above this diameter, while hysteresis losses beyond superparamagnetic transition.
- Researchers in [24] suggest a domination region below 20 nm for Néel mechanism and above 20 nm for Brown mechanism.
- More recent studies support that both Néel and Brown relaxations are overestimated, and actually even weak hysteresis effects may govern the heating procedure[25].

Our main study ferromagnetic particle will be micrometer particles (5um Fe_3O_4, the selection explanation and motivation will be clarified in the following section 1.5.1. The Brown and the Néel relaxation mechanism may not be the IH dominant generating reason of our studied ferromagnetic material. In the following content, we will make a distinction between the eddy current and magnetic hysteresis loss.

1.3.1 Eddy currents and magnetic hysteresis loss

The IH effect of ferromagnetic composites under the influence of low frequency alternating (AC) magnetic field can be due to the so-called "macroscopic" eddy currents or to the so-called "microscopic" eddy currents.

- Macroscopic –eddy currents

According to the Faraday's law, the so-called "macroscopic" eddy currents are formed within a closed loop in a conductive material through an alternating electromagnetic field or the alternating movement of an electric conductor in a static magnetic field.

In the following Figure 1-10, the magnet displacement induces a magnetic field in the conducting surface below and macroscopic eddy currents. There is no return path to these currents, their energy dissipates in the form of heat.

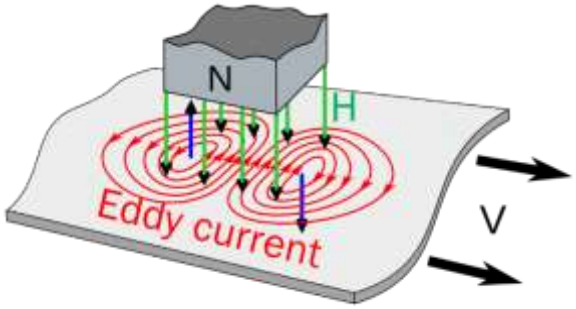

Figure 1-10. Macroscopic eddy current

The loss expression of the macroscopic eddy current in a specimen is:

$$P_e = K_e \cdot B_{max}^2 \cdot f^2 \cdot t^2 \cdot Vol \qquad \text{Equation 1-4}$$

where P_e is the eddy current loss (W), K_e is the proportional constant depending on the material geometry, B_{max} is the maximum flux density ($Wb/m2$), f is the frequency (Hz), and Vol is the magnetic material volume (m^3).

- Microscopic eddy currents

Hysteresis losses occur when ferromagnetic materials are placed within a coil supplied with an alternating electric current. The magnetic force leads to a parallel arrangement of the Weiss domains within the ferromagnetic material, which results in a temporary magnetic dipole within the ferromagnetic particle. Being alternative, the excitation field induces alternating magnetic dipoles which are accompanied by an energy loss. This kind of energy loss is produced by the so-called "microscopic" eddy currents which originate from the interactions between the walls of the magnetic domains and the microstructure during the magnetization of the ferromagnetic specimen [26].

1.3.2 Application of the IH effect

Induction heating technology has been chosen in many industrial, domestic, and medical applications[27]. Its advantages includes efficiency, fast heating, safety, cleanness, and accurate control. Thanks to its contactless nature, it is becoming one of the most popular heating technologies. It is replacing older heating techniques such as flame heating, resistance heating, or traditional ovens or furnaces. The advantages of induction heating are developed below[28]:

- Controlled heating:

The energy transferred by the induction heating system, such as its position can be accurately controlled through an appropriate design. In other words, we can easily and accurately adjust the heating temperature by controlling the frequency and the amplitude of the magnetic field. The heating process can be localized, constant, and accurate by controlling the coil's position.

- Contactless:

Since induction heating is a contactless process, the target is not affected by the heating device. In the medical field, the induction heating process is less invasive. The temperature of the surroundings environment is lower, avoiding undesired issues, (including spilled food in domestic induction heating …).

- High efficiency:

Induction heating is characterized by short time constants. It directly heats the induction target, reducing wasted heat. It significantly reduces the heating times thanks to its high power densities and its weak thermal inertia. Efficient coil and power converter designs allow to reach efficiency values higher than 90%, significantly improving conventional heating techniques. Moreover, just the target is heated, the heat loss is minimized and high temperatures can be reached. Thus, induction heating is environment friendly.

Induction heating technology is a mature technology and it is already widely used: household, industrial, medical applications. However, this technology is still under investigation. Some of these applications are detailed below:

a) Domestic applications

Induction heating technology is well-known for induction cooking. Induction cooking heats a cooking vessel by magnetic induction instead of thermal conduction from a flame or an electrical heating element. In an induction cooker, a coil of copper wire is placed under the cooking pot, and an alternating electric current (e.g., 24 kHz) is passing through. The resulting oscillating magnetic field induces a magnetic flux that repeatedly magnetizes the pot. It produces large eddy currents in the pot and Joule losses converted into heat. The cooking vessel must be made of, or contain a ferromagnetic metal such as cast iron or some stainless steels. Considering the power efficiency and cost restrictions, excitation frequencies usually

range from 20 kHz up to 100 kHz. The lower limit is set to avoid undesired acoustic noise emissions. The higher limit is imposed by the switching losses of the power devices[29].

b) Industrial applications

Induction heating is used to bond, harden, or soften metals or other conductive materials. Iron and its alloys are good candidates to induction heating due to their ferromagnetic nature. Induction heating offers an attractive combination of speed, consistency, and control. Induction heating can be used to harden a part, to prevent wear, make the metal-plastic for forging or hot-forming into a desired shape. It can also be used to braze or solder, melt and mix ingredients[30].

c) Medical applications

A new area of induction heating technology applications can be found in the medical field. Since the very beginning and due to its clean, fast, and portable characteristics, induction heating was used to manufacture and sterilize surgical instruments. More recently, it has also been used to some minimally invasive therapies [31].

Induction heating technology is a good alternative for hyperthermia treatment. It provides a non-contacting heat source and an accurate control of the temperature. Hyperthermia means to convert heat from a magnetic material via magnetic energy losses in the presence of an external alternating magnetic field. The produced heat can be used to kill cancer cells and destroy tumors.

Hyperthermia is a local treatment used to remove cancer tissue while minimizing the damage of the surrounding healthy cells. According to the temperature variation, hyperthermia therapy can be classified into three types: diathermia (41 C), hyperthermia (41-45 C), and thermal ablation (greater than 45 C) [32]. Cancer cells are more sensitive to temperature variations than healthy tissues, and they can be killed at a temperature above 46 °C (cell necrosis). Moderate hyperthermia involves cancer treatment in a temperature range of 41–46 °C (denaturation and aggregation of intracellular proteins are killing the cancer cells). Diathermia occurs at a temperature below 41 °C and is useful for treating rheumatic diseases by physiotherapy. Magnetic fluid hyperthermia usually refers to local hyperthermia. Nanoparticles are used as heat mediators. The use of fluids with ferromagnetic nanoparticles (e.g., iron oxide nanoparticles) to obtain precise heat distributions is still under investigation. This treatment consists in locally injecting magnetic nanoparticles into the tumor site and exposing the site to an oscillating magnetic field (100 kHz-100 MHz, 10 - 100 kA/m).

In magnetic fluid hyperthermia, two mechanisms, are responsible for heat generation: The Brownian-Néel relaxation and the hysteresis losses. Unlike laser and microwave hyperthermia, this minimally invasive procedure prevents undesired damage of the healthy tissues as just the magnetic nanoparticles absorb the magnetic field energy. This treatment is still under development, and the challenges is now in the properties of the ferromagnetic composites.

This limitation hinders the ability to concentrate the nanoparticles within the targeted tumor site, negatively affecting the homogeneous heat distribution [21,34].

1.3.3 Frequency range of IH effect

Under the influence of an alternating magnetic field, a ferromagnetic composite will be the source of the so-called "macroscopic" eddy currents and/or the so-called "microscopic" eddy currents. At high frequency magnetic field, high magnetothermal conversion can be reached. However, too high frequency (300 kHz to 1 MHz) is banish in the medical field as harm can be generated on the human body.

According to the International Commission On Non-Ionizing Radiation Protection (ICNIRP) Guidelines, the low-frequency range extends from 1 Hz to 100 kHz. After epidemiological and biological data concerning chronic conditions were carefully reviewed, it has been concluded that there is no compelling evidence of a direct damage to the human body of a low-frequency magnetic field exposure. Power lines, transport systems, electrical appliances produce artificial magnetic fields (sometimes alternative, in the low-frequency range), and we are commonly exposed to magnetic fields. Through these sources, an average person is exposed to magnetic fields up to 0.1 μT daily. By comparison to the Earth's magnetic field, it is about 500 times stronger.

Above 100 kHz, heating effect has to be considered [34]. The duration of exposure and energy absorbed in a safety range are defined precisely in Europe. From 100 kHz to 10 MHz, protection from magnetic fields depends on the exposure conditions. The most significant one is the exposition time. Undesired long time exposition to frequencies over 100 kHz could produce high energy absorption.

Figure 1-11 depicted the spectrum of frequencies. Radio to microwave frequencies are used for hyperthermia and ablation technology. Up to now, low-frequency magnetic fields have been rarely exploited in medical applications. This issue is therefore the main purpose of my thesis work. Two potential applications will be proposed in the following section 1.4.2, consisting of varicose vein treatment and tracking system based electromagnetic sensor. The application towards varicose vein treatment is based on the low-frequency induction heating (LFIH) effect mechanism, which will be the key point of this thesis.

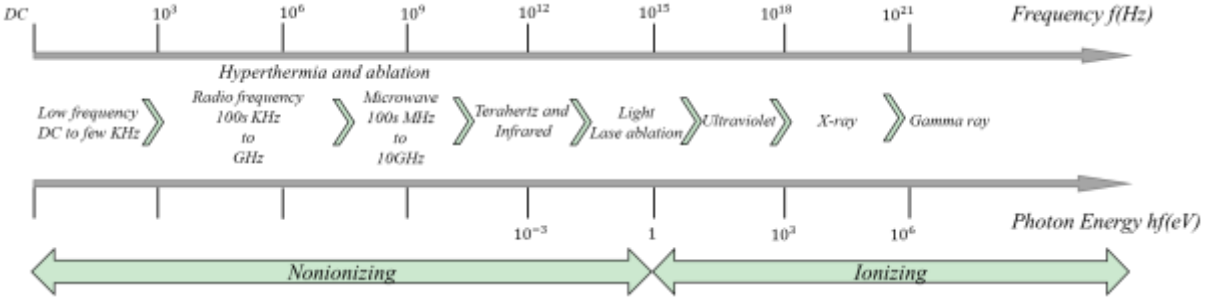

Figure 1-11. Spectrum of frequencies[35]

1.4 Research background and objective

1.4.1 Research key point – LFIH effect

As described in the subsection1.3.1, The induction heating effect of ferromagnetic materials, which appears when such materials are exposed to an alternating (AC) magnetic field, is based on the so-called "macroscopic" eddy currents and "microscopic" eddy currents (i.e., hysteresis loss).

In the case of low-frequency induction heating (LFIH) we proposed, when our polymer based particulate ferromagnetic composites are exposed to low-frequency range AC magnetic field, only the so-called "microscopic" eddy currents exist inside the composites. In this thesis (Chapter 3.2) will demonstrate such an effect through experimental investigation. Induction heating phenomena will be highlighted and validated via both empirical tests and thermal transfer modeling via COMSOL simulation.

Thanks the low frequency characteristics of the excited magnetic field, the impact of the alternating magnetic field on the human body during the medical operating process will be greatly reduced. Only ferromagnetic particles under low-frequnecy magnetic excitation would be active.

There has been pretty limited investigation of LFIH effect. B. Knauf *et al*. studied the LFIH on the application of plastic packaging for microfluidic systems, with a working frequency of 220KHz [36][37]. The heat generate mechanism has been explained by so-called "macroscopic" eddy currents. The company Inductoheat.Inc has developed a complex system for LFIH with a low-frequency of 50-60Hz, the system is able to heat up till 870°C within a short time, which makes it an attractive alternative to furnace/oven heating[38]. Similar LFIH heater with a low-frequency of 50-60Hz has been introduced in the patent[39].To the best of our knowledge, none of these investigations has yet related to LFIH catheter for medical applications. Our work comes up with the most novel idea of applying the LFIH effect which is based on the so-called "microscopic" eddy currents to the medical field.

1.4.2 Research -based medical applications

1.4.2.1 Varicose veins healing

Varicose veins healing using thermal ablation consists in inserting a biocompatibility ferromagnetic composite into sick veins. Then heat them by an external AC low frequency magnetic field (less than 100 kHz) and generate the apoptosis of the sick vein. The LFIH effect starts as soon as the treated sample is exposed to the alternating magnetic excitation field [40]. Human body tissues can be considered as electrical conductive materials since the skin contains 64% water, muscles and kidneys 79%, and the bones 31% [41]. At low-frequency, the

alternating magnetic field is supposed to heat solely the ferromagnetic composite. Thus, destroying the sick vein without damaging the surrounding healthy tissues.

In the Ph. D. work, differential Scanning Calorimetry(DSC)(DSC131 Evo Setaram) analyses have been performed on varicose veins coming from a patient's body. To confirm the varicose veins melting temperature, analyses have been repeated 3 times in different parts of the vein. As illustrated in Figure 1-12, the melting point is around 120°C.

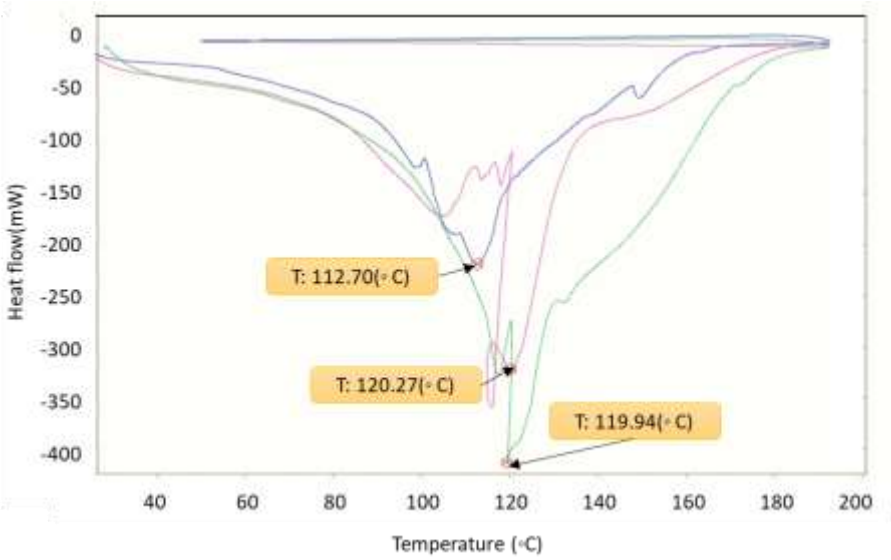

Figure 1-12 DSC analysis of varicose veins.

Two way can be used clinically to heal varicose veins:

- The surgical treatment: It involves an incision to find the varicose veins. Then, the damage vein can be tied off (ligated) or removed (stripped) if the vein is located close to the skin's surface [42].
- A minimally invasive (MI) treatment: sclerotherapy, microphlebectomy, and endovenous thermal ablation (EVTA). EVTA includes endovenous laser ablation (EVLA), endovenous steam ablation (EVSA), and radiofrequency ablation (RFA) (Figure 1-13). Compared to surgical treatment, MI treatments are efficient with less pain and an overall easier recovery [43]. EVLA is the most frequently used technique, followed by RFA. EVSA is a new technique that has not yet been extensively studied. To effectively destroy varicose veins, most of the endovenous ablation methods needs to reach a maximum temperature of 120°C [44], except for the RFA procedures (VNUS® Closure Plus system [45]), which heats local tissue to an only 85–90°C in direct contact. Such lower temperature probably results in less postoperative pain. However, the main drawback of RFA is its impracticality to certain "special" cases. Segmental RFA cannot treat veins smaller than 7 cm [44]. Furthermore, this technique does not allow for varying the energy delivered, as opposed to EVLA where the total amount of supplied energy per centimeter can be altered by adjusting the pullback speed/power.

Only 20 J/cm is used for small veins, whereas higher energy (60 J/cm) is needed when treating large veins. Despite this, EVLA has also some severe weaknesses. Indeed, implanting the guidewire is delicate, and perforation of the vein is possible, especially in very tortuous veins [44]. Another disadvantage of EVLA is the whole healing system introduction in multiple consecutive steps (the guidewire first, the sheath, and the laser fiber). Each additional step increases the risk of errors.

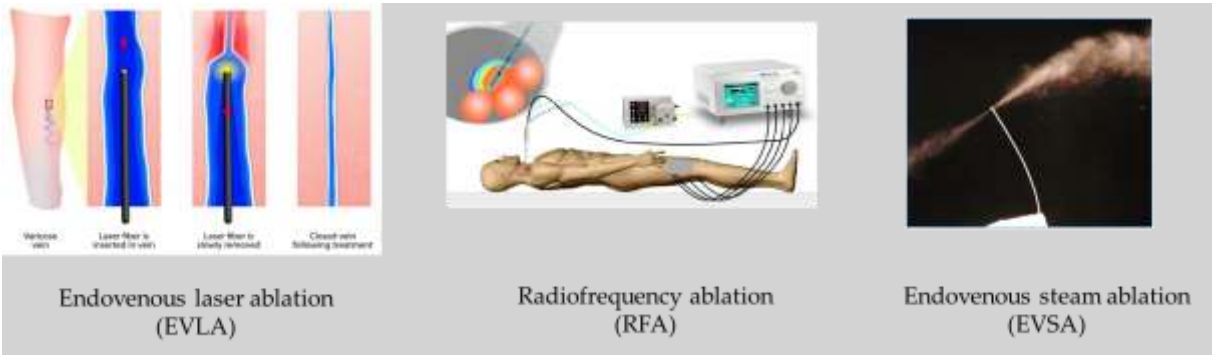

Figure 1-13. Endovenous thermal ablation (EVTA) treatments for varicose veins healing.

In this Ph.D. work, we propose an alternative method to destroy varicose veins based on the LFIH mechanism. The method is close to the EVTA technique. Our purpose is not to compete with the EVTA methods but rather to exposed benefits that can be made using the LFIH method, as well as demonstrating the feasibility of heating the ferromagnetic composite using an alternative low-frequency magnetic field. Our simulation and experimental results are promising, showing a high potential of the proposed method. The LFIH principle relies on the so-called microscopic eddy currents, generated inside the magnetic particles under the influence of an alternative magnetic source. As the magnetic excitation remains outside the patient and no physical connection exist with the composite introduced into the vessel, LFIH leads to a much more comfortable procedure. However, the distance between the source and the heated target has to be carefully controlled as it can significantly affect the magnetic intensity. Another advantage of LFIH is its "selectivity", affecting just the ferromagnetic material, making it impossible to burn or hurt neighboring tissues.

LFIH method will probably be safer for the patients, avoiding postoperative complications (nerve damage or bleeding as already observed with EVLA) [46]. Moreover, as this technique uses ferromagnetic composites (such as additively manufacturable polymer matrix doped with magnetic filler), 3D printing process can be envisaged [47], [48] (3D-printing of smart materials, special shapes and sizes suitable for different types of veins …). Such technical breakthrough can overcome the RFA drawbacks.

In an era of health technology assessment and cost-effectiveness analyses, treatment-related costs become increasingly important. EVLA is the less expensive endothermal treatment, even if the cheapest laser disposables cost approximately 120 Euros [44]. Patients must wear special

goggles or eyeglasses throughout the treatment to protect their eyes from the laser light. The RFA Procedure-related costs are higher due to the higher cost of the catheter [49]. Generally, the additional cost of $110–$220 per patient is mainly related to consumables [50]. Although it is too early to estimate the total costs of LFIH, we believe that this method will be cost-effective due to cheap commercially available materials, together with its simple fabrication process. In conclusion, based on the LFIH effect, the proposed approach can be an interesting solution for endovenous thermal ablation, which might enable a safer and easier procedure than EVLA; thereby lowering costs and increasing the applicability compared to RFA.

1.4.2.2 Tracking system based electromagnetic sensor

Computer assisted interventions (CAI) relying on the benefits of high accuracy, freehand operation and less intervention time on patient body, has becoming an integral part of modern medical treatment. Within the field of CAI, image-guided therapy (IGT) is based on the registration of pre-operative patient data to the actual operative field. IGT can provide guidance for mechatronic positioning of medical instruments. Real-time control of the IGT device's localization in the patient's body is very important. 3D space localization is referred as "tracking", it is a key technology for CAI.

The most established tracking method is optical tracking. It uses cameras and special markers. Due to the requirement for a free line-of-sight to the markers, it is not feasible for minimally invasive surgical procedures, instruments such as flexible endoscopes, catheters and needle tips, since they must be tracked inside the human body. Indeed, the traditional method provide only bi-dimensional images that lacks of depth perception, making it difficult for surgeons to estimate the spatial relationships between the endovascular instruments (e.g., catheters and guidewires) and the patient's anatomy. As a result, in cases of difficult angulations and tortuous anatomies, even a conceptually simple task, such as vessel cannulation, can become challenging and time-consuming, thus requiring prolonged fluoroscopic exposure time and the injection of large volumes of contrast medium [51].

In an attempt to overcome some of the aforementioned limitations and reduce the perceptual difficulties, the electromagnetic tracking (EMT) technology came out. EMT system localization rely on small EMT receiver sensors (also known as "inductive coil" or "search coil") in a given EMT field provided by an emitter electromagnet (Figure 1-14). This emitter responsible for producing changing (AC) or quasi-static (DC) magnetic fields, which induce currents in the receiver sensors embedded in the detectors. The phenomenon responsible for the operation of these tracking systems relies solely on magnetic induction.

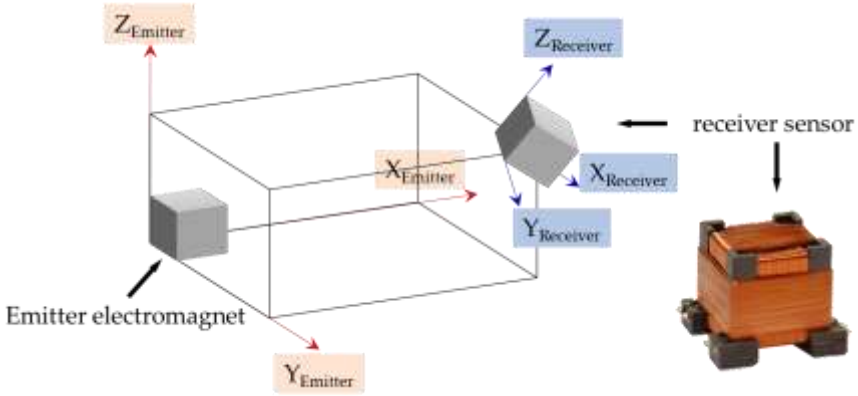

Figure 1-14 Schematic diagram of EMT system

Aurora® system from Northern Digital, Inc. (Waterloo, Ontario, Canada) and microBIRD™ system from Ascension Technology Corp. (Burlington, VT, USA) are commercially available EMT subsystems equipped with a software programming interface that can be integrated by researchers into an image-guided surgery tool [52]–[54]. These systems have been commercially available for many years, but have suffered from two major drawbacks: 1) the sensors have been too large to incorporate surgical instruments; and 2) they have been sensitive to metal objects in the vicinity (medical equipment) that can distort the electromagnetic field. Lately, smaller sensors have become available and can be incorporated into the tips of medical tools [55]. The sensing device less than 1 mm in diameter is placed at the distal end of instruments such as needles or catheters, rather than relying on a tracking array mounted on the proximal end of a rigid instrument. The newer electromagnetic tracking systems are also more robust to small metal objects in the operating field [56], [57].

To enhance the tracking accuracy of EMT system, anisotropic ferromagnetic composites with permeability varying according to the direction can be designed. A combination of the receiving sensor and the anisotropic ferromagnetic composites can be envisaged. As EMT technology will employ the receiving sensor tracking inside the human body, a requirement of soft deformable material should be meet. What's more, similar to the varicose vein treatment, desired shapes should be fabricated in the condition of both material and cost-efficient. Thus the ferromagnetic composites should be additively manufacturable.

Throughout the thesis, we essentially focus on application of varicose vein treatment. The EMT system based ferromagnetic composites will be described in Chapter 4. However, only a design concept is provided. Experimental test together with validation of such a device will be explored in future work.

1.4.3 Research objectives

In this Ph.D. work, we propose to develop ferromagnetic composites for medical applications. Based on the medical applications introduced above, the properties of these developed

ferromagnetic composites should meet with several specific requirement. Such as: 1). biocompatibility; 2). additively manufacturable and 3). low cost. The ferromagnetic composites will be particulate polymer based composites. Compared with metallic ferromagnetic materials, the ferromagnetic composites have less mechanical brittleness and more are flexible. It will be easier for ferromagnetic composites to form complex shapes of desired sample.

To achieve the application of varicose veins treatment, efforts on enhance the LFIH effect of developed ferromagnetic composites will be top objective of my thesis. The target of induced heating temperature to destroy varicose veins is 120°C. A quick time response (less than 5 seconds to reached 120°C) of developed ferromagnetic composites under magnetic field should be achieved at the same time. From the composites property point of view, varicose parameters such as particle nature, size, shape, volume ratio and spatial orientation of ferromagnetic particles in a polymeric matrix will have a strong influence on LFIH effect. The characteristic of low-frequency magnetic excitation such as: amplitude and frequency also matters a lot the LFIH effect on another point of view.

With the assistant of magnetophoresis during fabrication process, anisotropic ferromagnetic composites can be obtained due to the particle alignment inside of polymer matrix. This anisotropic behavior can not only further enhance the LFIH effect, but open a gate for the application of electromagnetic tracking technology, magnetic-responsive sensors as well. In this thesis, the second objective will be develop the high performance anisotropic ferromagnetic composites.

The thirdly objective is, by employing the 3D printing technology, desired shapes of samples are looking forward to fabricate. A combination of 3D printing technology and magnetophoresis makes it possible to get high performance anisotropic ferromagnetic composites in complex shape.

1.5 Research material selection

1.5.1 Particle material selection

The magnetic properties of the magnetic composites rely mostly on the magnetic particles. Iron oxide (Fe_3O_4, γ-Fe_2O_3…), “soft” metallic iron, but also “hard” magnetic materials (Co, Ni, FeN, FePt, FePd…) can be used to produce highly efficient magnetic-responsive materials [58]. Iron oxide (Fe_3O_4) is a popular magnetic material. Due to its substantial magnetic property and its low toxicity, it has been used in biotechnology and medicine applications, including:

- More than 60 years ago, researchers in [59] expanded on microparticles embedded within slime molds and cellular cytoplasm to probe their rheological properties using well-characterized iron oxide microparticles.

- Iron oxide magnetic particles are now used routinely as contrast agents in Magnetic Resonance Imaging (MRI), and new applications are expected in the field of thermal cancer treatment, magnetic targeting and remotely triggered drug release [60].
- The inductive heat property of Fe_3O_4@polyaniline composite nanoparticles in an alternating current (ac) magnetic field was investigated in [61]. This composite would be useful as good thermoseeds for localized hyperthermia treatment of cancers.

Since the final objective of this Ph. D. work was medical applications, the developed magnetically reinforced material should be biocompatible. We identified iron oxide (Fe_3O_4) powder with 5μm of diameter (SIGMA-ALDRICH) to be a promising candidate. To better justify the choice of iron oxide, we compared its performances to those of other magnetic particles, such as Ni and Mn-Zinc. These two materials are commonly used as inductor components due to their low cost, commercial availability, and high magnetic properties.

Researchers working on IH effect of Fe_3O_4 particles further focused on nano-size particles under high frequency alternating magnetic field (AMF):

- In [62], 10 nm Fe_3O_4 nanoparticles were by instance excitated under a 35KHz, 0.06 mT 0.06mT magnetic field (AMF).
- In [63], quite similarly, 20nm Fe_3O_4 nanoparticles are used under the influence of a 500 KHz, 60mT in a AMF-type application.

In this work, we want to develop a low-frequency induction heating (LFIH) of ferromagnetic composites with the objective of using it in the medical field, especially for the treatment of the varicose veins. The aim here is to enhance the LFIH effect through different factors such as the magnetic excitation waveform, the polymer matrix, and the magnetic particles natures [40][64]. Three different particle sizes of commercially available iron oxide powder were tested (50-100nm, 5μm, and 50μm from Aldrich Corporation).

1.5.2 Matrix material selection

1.5.2.1 The isotropic composites

Polymer matrix doped with micro-particles have a high ability to be used in 3D printing technology. Adapting 3D-printing to additive manufacturing (AM) offers the possibility of designing smart material with unconventional shapes.

ABS (acrylonitrile butadiene styrene) is a commune commercial 3D printing material. It is a widely used engineering thermoplastic characterized by a high durability. Printed ABS can reach up to 80% of injection-molded ABS strength, making it highly suitable for functional applications [65]. In [66], a better mechanical properties of ABS has been obtained thanks to the innovative 3D printing strategy they proposed. Many researchers are studying ABS-base magnetic composites manufactured by 3D printing technology:

- In [67], authors investigate the thermal and mechanical properties of new metal-particle filled ABS composites for 3D printing applications. Iron@ABS and Copper@ABS composites of 40% vol. are built.
- Y. Wang et al. successfully used Fused Deposition Modeling (FDM) 3D printing technology to fabricate Ni, Zn ferrite powder@ABS composites [68].
- In [69], authors chose ABS as the polymer matrix and filled it with 40% vol. stainless steel micro powder. These composites are used as magnetic sensors or magnetic–non-magnetic bistrips.

Finally, the thermoplastic ABS can be considered as a suitable choice, it is widespread commercially speaking, and it can be used in injection molding or 3D printing.

1.5.2.2 The anisotropic composites

To obtain arrangements of the ferromagnetic particles inside the polymer matrix under the influence of an external magnetic field, the polymer base must be fluid enough before polymerization. Ideally, the polymer is liquid in its original state (low molecular weight and/or low glass transition temperature) with a limited viscosity, enabling particle diffusion and alignment (including under low amplitude magnetic field) during the fabrication process, just before curing. The elastomers are especially good candidates. The material viscosity and magnetic field strength will set the time constant of the particle chains alignment dynamic [70]. The ideal polymer must also be thermosetting. Once the thermal processes over, the material has to end up in a solid state. Considering all these requirements, Polydimethylsiloxane (PDMS, SYLGARD™184 Silicone Elastomer) has been chosen as the other polymer matrix tested. PDMS is a well-known and widely used viscoelastic biomaterial with applications across the tissue engineering and biomedical fields. It has the original viscosity of 5100cP in a liquid state before curing, which allowed particles alignments and this even under the action of a reasonable magnetic field. Such a material can be easily transformed into a solid elastomer form. It can be cured combined with additional encapsulants at room temperature or under higher temperature without these additives (100°C within 35 minutes). PDMS thermal conductivity of around 0.15 W/m*K is lower than the 0.225 W/m*K for the ABS thermoplastic polymer previously used [40][71]. PDMS elastomers are mechanically stable over a temperature range of -45 to 200°C, and have highly soft, stretchable properties. Applications on epidermal electronics in wearable healthcare have been achieved [72]. Based on the above reasons, PDMS may give super flexible bio-compatible composite, especially well adapted to the healing of varicose veins. Furthermore, this elastomer is cost-effective, commercially available, widely used in industry, and leads to a simple fabrication process.

1.6 Summary

In chapter 1, we have introduced the ferromagnetic composites and the mechanism of low-frequency induction heating (LFIH) effect. By introducing the potential medical applications, the objectives of this research have been declared. The material suitable for this research have been selected. In the following chapters, we report on characterizations and validation of ferromagnetic composites. Feasibility and performance concerning LFIH of both anisotropic and isotropic materials are then discussed.

Chapter 2
Isotropic Ferromagnetic Composites Characterization

The composite materials characterization is a crucial step. It will helps us understanding the composites' properties and improving their performances. In this chapter, the fabrication methods will be introduced such as the equipment and the methods used for the characterization of the isotropic ferromagnetic composites. Theoretical and experimental results giving the conductivity, permeability, and thermal properties of the composites will be described. We will especially focus on the Hysteresis behavior and its close relationship with the IH effect.

2.1 Fabrication process

At the very beginning of our research, we tried to fabricate magnetic composites using the commercially available thermoplastic polymer-based composite PLA (Polylactic acid) - Rustable Magnetic Iron (Proto-Pasta). We used a fused deposition modeling (FDM) 3D printer. However, the commercial composite containing only 7% vol. of iron particles, exhibited very weak magnetic properties and extremely low relative permeability (≈1.1).

To get higher Fe_3O_4 fraction, an extrusion machine has been tried to fabricate ABS-based composite filament. However, the resulting filaments were brittle and discontinuous (mechanically speaking). Similarly, Khatri *et al*. in [69] prepared filaments with ABS as the host polymer and stainless steel micro powder as the functional filler. Compared to the pure ABS polymer, the tensile strength of their printed stainless steel-ABS composites dropped proportionally to the filler content. They observed a dramatic Young's modulus and flexural strength drop for higher filler ratios.

Our objective is to fabricate composite with a high percentage of ferromagnetic content (with an improved permeability and thermal responses). However, to build composites with fused deposition modeling (FDM) type 3D printing is a veritable challenge and a time-consuming operation. The filaments production with the extruder increases greatly the difficulties. Furthermore, many parameters needs special attention (the substrate temperature, the print head speed, the solution viscosity, etc.) to get a satisfactory result. So brittle composites can easily break during the printing process, resulting in a blocked print head and a deterioration of the 3D printer [73]. We finally opted for a much robust "hot-pressing" method using a hot press machine. We called low volume fraction magnetic composites, composite of particle volume fraction in the polymer matrix varying from 3% to 17%. The fabrication procedure of low volume fraction Fe_3O_4@ABS composite is illustrated in Figure 2-1, it comes in 5 steps:

- (a) The ABS granule are poured into the acetone solvent and stirred at room temperature for 2 hours. Once the ABS completely dissolved in the solvent, Fe_3O_4 powders are added to the solution and stirred again for 1 hour to get a perfectly homogeneous solution.
- (b) To improve the dispersion of the Fe_3O_4 powder into the ABS matrix, the solution is scattered via ultrasounds (Hielscher Ultrasonic Processor UP400S, Teltow, Germany) Powerful impulsion are imposed during 10 minutes in an ice bath.
- (c) After that, the frozen solution is transferred into an evaporating dish.
- (d) The mixture is finally placed in an oven (Memmert Typ: V0 400) at 56°C (corresponding to the acetone volatilization temperature) within 2 hours for a full evaporation of the solvent.
- (e) Once the solvent fully removed, the mixture reaches a solid-state. The mixture is cut into small pieces, disposed into a home-made "I "shape mold (60 × 14 × 4 mm), and

in a cylinder shape mold (30 mm diameter, and 15 mm thickness). To reach the best results, the mixture was placed in the mold and then slowly compressed under a maximum pressure of 1300 Psi by a "heat-press" machine. This operation was repeated many times until the obtention of a perfectly compact specimen. On a one hand the tuning temperature must be larger than the glass transition to reach a sufficiently "viscous" state and be easily molded. On the other hand, this temperature has to be smaller than the melting point to avoid deterioration of the composite properties. The final temperature of the hot press possess was set at 150°, close to the average value between the glass transition temperature (105°) and the melting point (230°) of the ABS polymer.

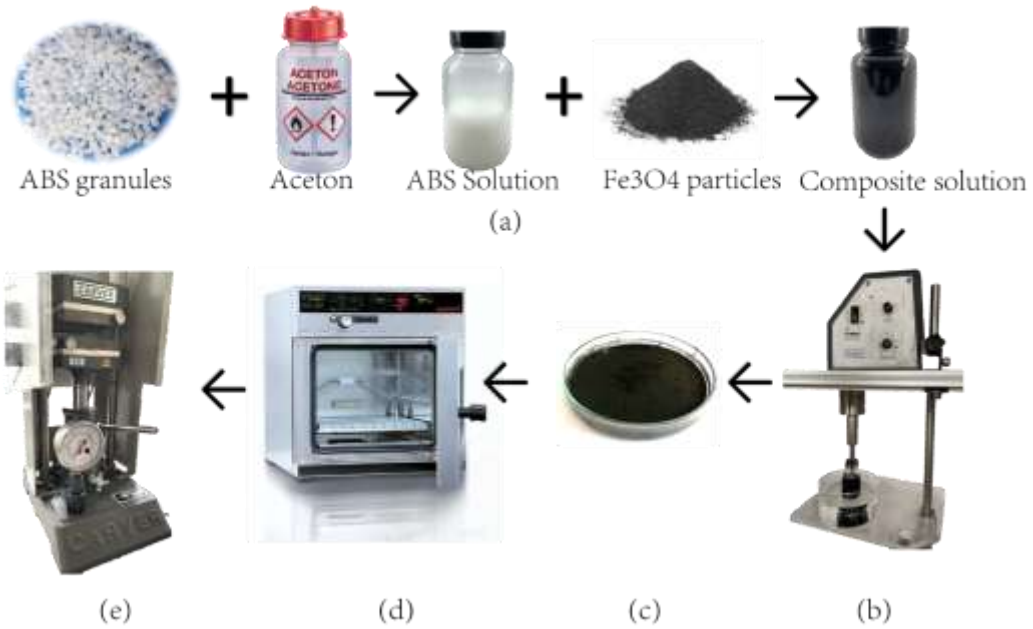

Figure 2-1 The fabrication process of the ABS-based ferromagnetic composite includes 5 steps.

For higher volume fraction composites including 20 to 30% vol. Fe_3O_4 particles, the particle sedimentation due to the higher particle content cannot be ignored and the preparation method needs improvements.

Stages (a) and (b) are conserved. The resulting solution is mixed to cold water right after the ultrasound stirring, it freezes all the particles into the polymer structure. Once the supernatant liquid withdrawn, a rubber state mixture is obtained. Next, the obtained rubber state mixture was transferred into an evaporating dish and placed in the oven at 56°C for 2 hours to fully evaporate the solvent. Then, the hot-press machine is used as a final stage. The particle percentage is limited to 30% to avoid heterogeneity and percolation.

By using the "hot-pressing" method, we successfully built specimen of different magnetic particles content (from 3% vol. to 30% vol.), in rectangular (60 × 14 × 4 mm, Figure 2-2(a)) and

cylinder shape (Ø30mm, thickness 15mm, Figure 2-2 (b)). Besides the Fe_3O_4@ABS composites, two conductive composites: 15% vol. of Copper@ABS and 3% vol. of Carbon black@ABS were fabricated to check the LFIH effect on conductive but non-ferromagnetic specimens. Finally other ferromagnetic composites 10% vol., 23% vol., and 40% vol. Ni@ABS composites, and 30% vol., Mn-Zinc@ABS composites were built with the same manufacturing process to determine which one produces the highest LFIH answer.

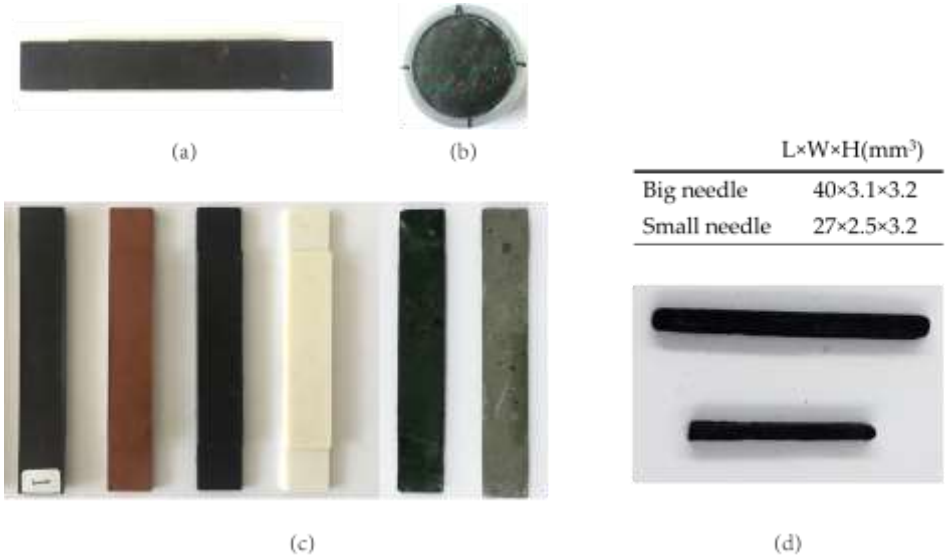

Figure 2-2 (a)Rectangular-shape sample; (b) cylinder-shape sample; (c) different content of rectangular samples (from left to right): Fe_3O_4@ABS, copper@ABS, carbon black@ABS, pure ABS, Mn-Zinc@ABS, Ni@ABS; (d) needle-shaped samples.

The specimen depicted in Figure 2-2 (a) is too big for the endovenous procedure. Thus, another series of needle-shaped specimens was built, two different sizes were tested: the big one 40 × 3.1 × 3.2 mm^3, and the small one 27 × 2.5 × 3.2 mm^3 (Figure 2-2 (d)). Both types of needle samples can be used for the endovenous treatment as they match the typical vein diameters (4–5 mm).

The quality of the fabrication process can be verified by measuring the sample density and comparing it to the theoretical value (Equation 2-1). The absence of "air hole" must be verified as micro cavities can strongly alter the magnetic properties.

$$\rho_{composite} = (1 - v_f)\rho_{polymer\ matrix} + \rho_{particle} \qquad \text{Equation 2-1}$$

where v_f is the particle volume fraction; $\rho_{composite}$, $\rho_{polymer\ matrix}$ (ABS - 1.05 g·cm^{-3}), and $\rho_{particle}$ (Fe_3O_4 - 5.17 g·cm^{-3}) denote the composite , the ABS thermoplastic, and the Fe_3O_4 microparticle volumic masses, respectively.

2.2 Electric characterization

In two phases composite, the fraction of particles has a strong influence on the physical properties. There is a critical particle volume fraction called the percolation threshold $\emptyset_c$

defining a limit between an electrical non-conductive to a conductive state. There are several theoretical methods to predict$\emptyset_c$, including the Maxwell-Garnett theory; and the Bruggeman theory usually referenced to as the general effective media (GEM). In this work, the GEM method based Equation 22 is used to fit with experimental data.

$$v_f \frac{\sigma_p^{1/t} - \sigma_c^{1/t}}{\sigma_p^{1/t} + A\sigma_c^{1/t}} + (1 - v_f)\frac{\sigma_f^{1/t} - \sigma_c^{1/t}}{\sigma_f^{1/t} + A\sigma_c^{1/t}} = 0 \qquad \text{Equation 2-2}$$

where v_f is the particle volume fraction, σ_f is the high-conductivity phase conductivity, σ_p is the low-conductivity phase conductivity, , σ_c is the conductivity of composite, $\emptyset_c$ is the percolation threshold of the higher conductivity phase, A is a constant defined as $A = (1 - \emptyset_c)/\emptyset_c$, and t the critical exponent of percolation conductivity.

In [74], an specimen of Fe_3O_4@epoxy has been investigated. Physically speaking, this composite is close to our Fe_3O_4@ABS and Fe_3O_4@PDMS. In this study, they used the demagnetization coefficient $L_\emptyset = \emptyset_c/t$ (i.e. characterizes the high-conductivity phase $L_\emptyset$). This coefficient is worth 0.331 for the Fe_3O_4. Such value means that the Fe_3O_4 grains behaves closely to a random spheres configuration. Since $\emptyset_c$= 0.496, it can be assumed that not all the nearest-neighbor bonds are electrically contacted. The combination of parameters used for the Fe_3O_4@ epoxy resin composite were: $\sigma_{Fe_3O_4}$= 0.6173 S/m, $\sigma_{polymer}$=1.122 x 10^{-8} S/m, and t = 1.50.

The evolution of the Fe_3O_4@ABS and of the Fe_3O_4@PDMS conductivity as a function of the particle volume fraction obtained with the GEM equation are shown in Figure 2-3. The combination of parameters used for the Fe_3O_4@ABS were: $\sigma_{Fe_3O_4}$= 0.6173 S/m, $\sigma_{polymer}$=1x 10^{-8} S/m, $\emptyset_c$=0.496, and t= 1.50. Same parameters were used for the Fe_3O_4@PDMS composites, just the PDMS conductivity was set to σ_{PDMS}= 0.25 x 10^{-13} S/m.

In a composite made out of a dielectric matrix and metallic particles, the conductivity σ shows a critical behavior when the fraction of the metallic component reaches the percolation threshold. Below the percolation threshold the composite shows no conductivity. By observing Figure 2-3 we estimate at 47% vol. the critical volume fraction (percolation threshold) for the Fe_3O_4@ABS. Below 47% vol. the electrical conductivity will be lower than 10^{-6} S/m, and the composite can be classified as an insulator. Similarly, the critical volume fraction of the Fe_3O_4@PDMS composites is around 50% vol.

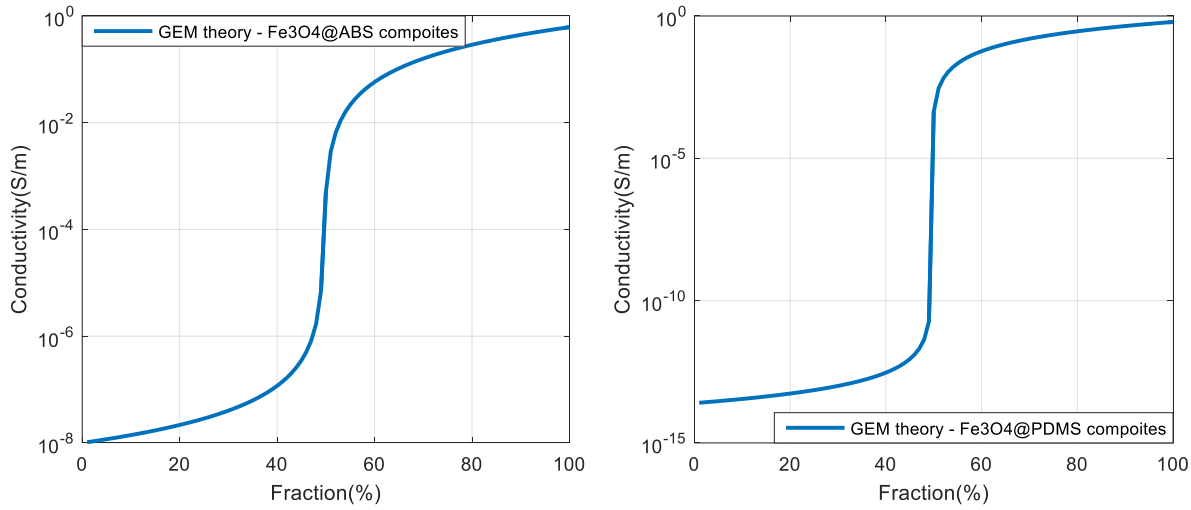

(a) (b)

Figure 2-3 Conductivity as a function of particle volume fraction based on GEM theory: (a) curve for Fe_3O_4@ABS composite; (b) curve for Fe_3O_4@PDMS composite.

In order to check the exact conductivity of our composites, thin gold layers were deposited on both surfaces of our specimen using a Cressington 208HR sputter coater. The gold thickness measured by the sputtering quartz balance, was around 20 nm. The resistivity $\rho_{Fe_3O_4}$ of the 3% vol. to the 30% vol. composite particle fraction Fe_3O_4@ABS were obtained with the LCR Meter (Keysight E4980AL, Agilent) (Figure 2-7).

As illustrated in Figure 2-4, the experimental results fits the GEM theory.

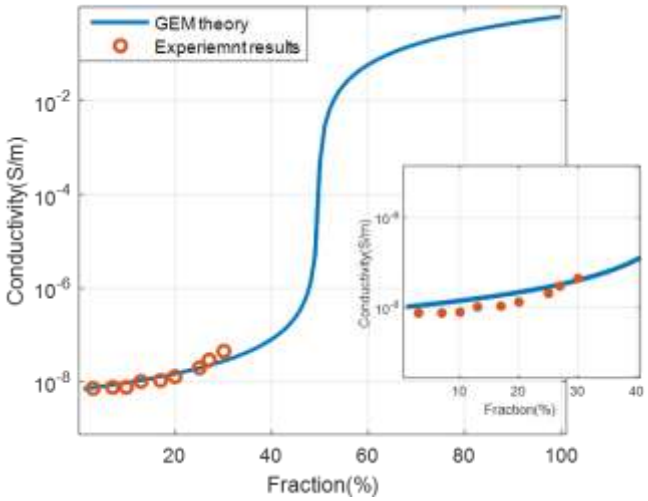

Figure 2-4 GEM theory model and the measurement results of $\sigma_{Fe_3O_4}$

2.3 Magnetic characterization

The magnetic characterization of the composites consists of determining its permeability using different methods: 1) Comsol simulation, 2) empirical measurement of inductance, 3) analytical model, and 4) experimental hysteresis curve.

2.3.1 Simulation model

A finite element simulation using the @Comsol software has been performed for the estimation of the relative permeability μ_r. Figure 2-5 below gives an illustration of the magnetic field distribution inside a polymer matrix homogeneously filled with Fe_3O_4 cubic particles.

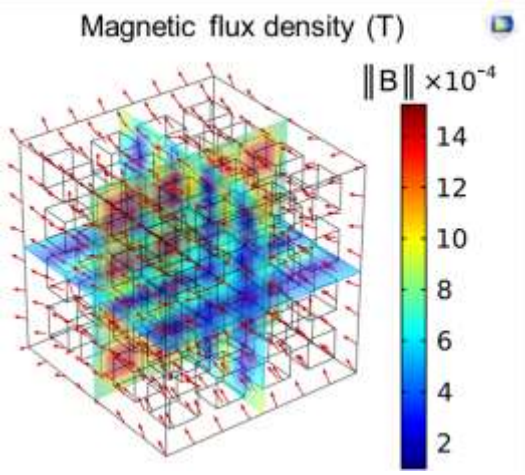

Figure 2-5 Magnetic induction distribution in a magnetic polymer composite homogeneously filled with magnetic particles.

The composite relative permeability can be obtained through Equation 2-4 below:

$$\mu_r = \frac{B_{volume}}{H_{section}} \qquad \text{Equation 2-3}$$

where B_{volume} is the induced magnetic flux density, and $H_{section}$ is the excitation magnetic field through the composite cross-section.

The magnetic particles relative permeability as a function of the volume fraction is displayed in Figure 2-6. As expected, the polymer matrix filled with a larger magnetic particles quantity leads to improved magnetic properties, (higher permeability).

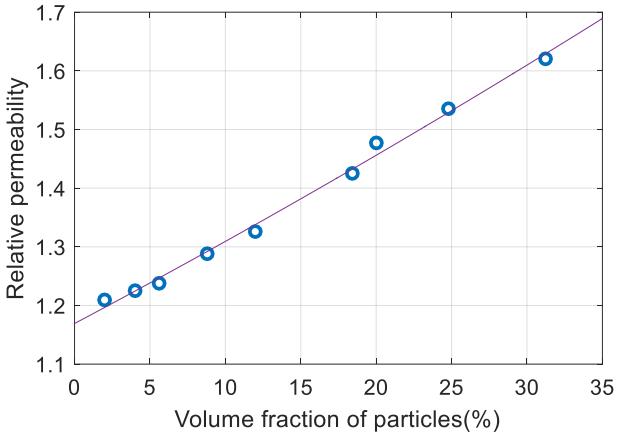

Figure 2-6 Permeability simulation predicted value versus particle percentage

2.3.2 Inductance mesurement

To characterize the permeability changes over a larger frequency range (i.e. 20Hz to 1MHz), inductance measurements of the composite were carried out using a LCR (inductance, capacitance , and resistance) meter (Keysight E4980AL, Agilent)(Figure 2-7).

Figure 2-7 Photo of LCR Meter (Keysight E4980AL, Agilent)

Conventionally, the magnetic permeability is measured using a wound coil around the magnetic core, then the effective permeability is derived from the inductance measurement. All the cylindrical shape samples (including the pure ABS) were winded with a 100 turns coil.

According to [75], the inductance L of multilayer solenoid has a relationship with The relative permeability μ_r:

$$L = \frac{\mu_0 \mu_r}{4\pi}\left(FN^2 2R - \frac{12.57}{10^4} N^2 R \frac{w}{l}(0.693 + Y)\right) \qquad \text{Equation 2-4}$$

Where "F-factor" and thickness correction factor Y are computed automatically. N is the number of the coils, l is the length of the coil covered on the surface of specimen, w is the coil thickness on one side of specimen, R is the diameter from specimen center to a half thickness of the wounded coil.

As the other parameters for measure the inductance of composite and polymer are all the same, only the relative permeability (μ_r) is different, so it can be obtained using Equation 2-5 assuming all the wound coil as similar:

$$\mu_r = \frac{L_{composite}}{L_{polymer}} \qquad \text{Equation 2-5}$$

where $L_{composite}$ and $L_{polymer}$ denote the inductance of the ferromagnetic composite and of the pure polymer, respectively.

It can be seen in Figure 2-8 that the resulting relative permeabilities (μ_r) of Fe_3O_4@ABS composites varies from approximately 1 for the 3% vol. to 1.8 for the 30% vol. As observe, μ_r is increasing steadily as a function of the volume fraction. Experimental test were done at 1 KHz and 1 MHz, and the composites 's magnetic permeabilities showed a high consistency.

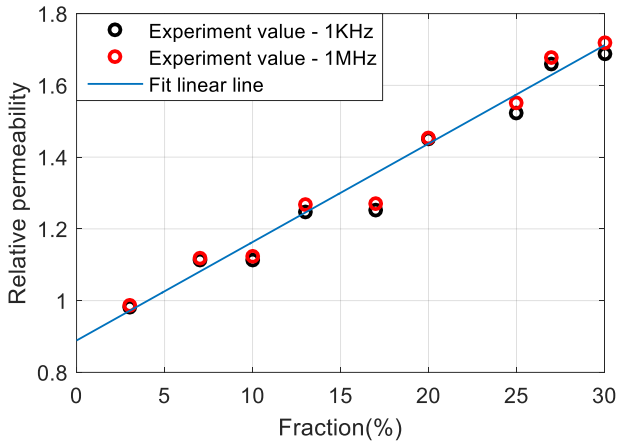

Figure 2-8 The relative permeability of Fe_3O_4@ABS composites measured by LCR Meter

2.3.3 Analytical model based mixing law

Predicting the effective magnetic permeability (average permeability of an inhomogeneous medium) of ferromagnetic composites is important in both academic and industrial researches. In the last decades, large progresses were achieved in effective medium theories, this includes the Maxwell- Garnett's formula, the Bruggeman's formula, the coherent potential's formula and other mixing rules [76]–[78]. Most mixing rules are based on the assumption that inclusions are randomly distributed in the matrix, and very few of them are taking into account the effect of spatial orientation of aligned particles. For a magnetic composite made from two material phases, the interaction between particles/matrix together with its effect on the permeability and the ferromagnetic resonance must also be taken into consideration. The composite permeability depends on the volume fraction of the magnetic particles. Assuming the magnetic particles as separated, physically and electrically (below the percolation limit), the composite's permeability can be enhanced by increasing the particle volume fraction.

The effective medium theory is widely used for calculating the effective properties of composites. According to the Bruggeman effective medium theory, for uniformly distributed spherical particles, the effective permeability of a composite (μ_c) can be calculated using the following formula:

$$v_f \frac{\mu_f - \mu_c}{\mu_f + 2\mu_c} + (1 - v_f) \frac{\mu_p - \mu_c}{\mu_p + 2\mu_c} = 0 \qquad \text{Equation 2-6}$$

where v_f is the particles volume fraction, $\mu_f$is the ferromagnetic particle permeability, and μ_p represents the nonmagnetic polymer matrix permeability ($\mu_p = 1$).

For non-spherical particles, the Bruggeman effective medium theory equation for the permeability calculus is modified as follow:

$$v_f \frac{\mu_f - \mu_c}{\mu_c + (\mu_f - \mu_c)N} + (1 - v_f) \frac{\mu_p - \mu_c}{\mu_c + (\mu_p - \mu_c)N} = 0 \qquad \text{Equation 2-7}$$

For non-spherical particles *N* is set empirically equal to 1/3.

The Bruggeman theory gives good results for medium volume fractions [79]. For low or high volume fractions, the Maxwell-Garnett (MGa) theory [79][80] gives much better predictions.

In case of low volume fraction ($< 10\%$ vol.), the MGa model is written as:

$$\frac{\mu_c - \mu_p}{\mu_c + 2\mu_p} + v_f \frac{\mu_p - \mu_f}{\mu_f + 2\mu_p} = 0 \qquad \text{Equation 2-8}$$

Oppositely, in case of high volume fraction ($> 50\%$ vol.), the formula becomes:

$$\frac{\mu_c - \mu_f}{\mu_c + 2\mu_f} + (1 - v_f) \frac{\mu_f - \mu_p}{\mu_p + 2\mu_f} = 0 \qquad \text{Equation 2-9}$$

Figure 2-9 curves give the relative permeability variation as a function of the particle fraction for 4 different models. The permeability of the Fe_3O_4 particles is set to μ_f = 50. For the Bruggeman theory in a non-spherical configuration, *N* is set to 2/3. Among all these predicting model, the Bruggeman non-spherical model gives the best simulation results of the isotropic Fe_3O_4@ABS composites (particle of 5 μm average size). As shown in Figure 2-10, the experimental values perfectly fit the theoretical curve.

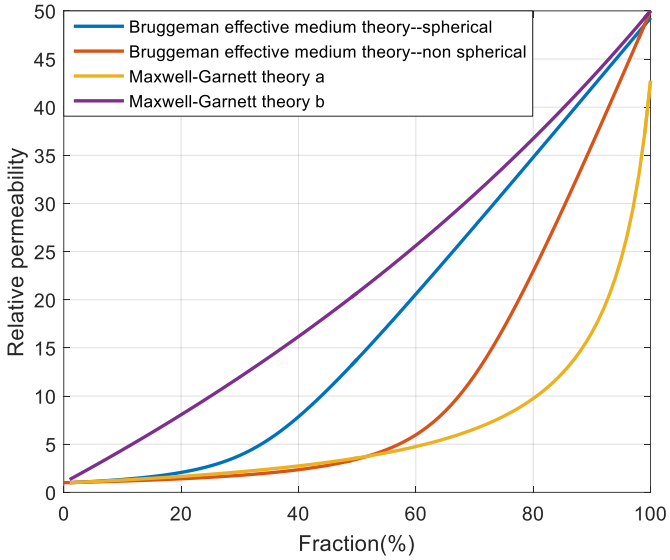

Figure 2-9 Effective medium theory of permeability as a function of particle fraction in 4 different models

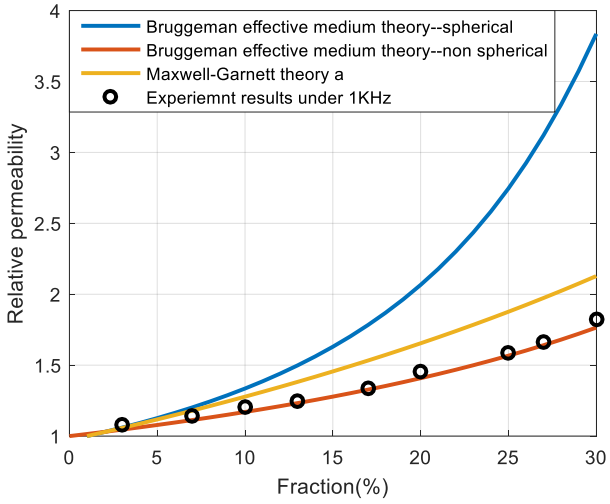

Figure 2-10 The experimental values (Fe_3O_4@ABS) fit with mixing law

Three different fractions of Ni@ABS composites (10, 23, 40% vol.) have also been characterized and simulated using the same process. Again, good simulation results were obtained with the Bruggeman effective medium theory as shown in Figure 2-11.

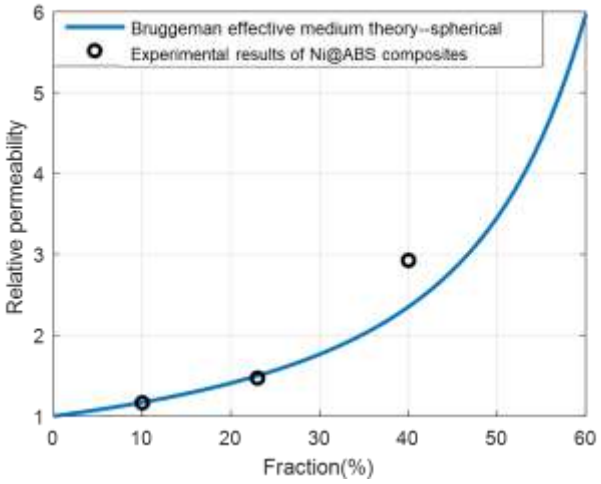

Figure 2-11 The experimental values (Ni@ABS) fit with the Bruggeman effective medium theory

The size of the magnetic particles is a key parameter in the evolution of the composite magnetic properties. According to the Bruggeman effective medium theory and to the Maxwell-Garnett theory [79][80], the composite's permeability depends on the particle shapes and on the particle volume fraction but none of these expressions takes into account the particle sizes. However, some researchers have already modified the Bruggeman equation to consider the particle size [81]. In the literature, experimental results show a steady increase of the permeability under a steady increase of the particle sizes (from the micrometer to the millimeter range) [82][83]. For nanometer magnetic particles, a higher permeability and reduced hysteresis losses are observed with a decrease of the particle size [84][85].

In the next step of this investigation, inductances measurement for the permeability estimation were done on three isotropic ABS-based polymer mixed to different sizes of Fe_3O_4 particles (50-100nm, 5μm, 50μm). More detail will be investigated in Chapter 3, the section of material properties influenced by particle size.

2.3.4 Hysteresis curve

A laboratory electromagnet supplied by a power amplifier (BHM AMP700) was used to provide a magnetic field excitation H. H was monitored by a tesla-meter (FW-Bell 5080 transverse probe, Part Number: STD58-0404). To ensure a homogeneous magnetization, the cylindrical-shape specimens (Figure 2-2 (b)) were placed inside the 15 mm thick air-gap. The induction B was calculated by integrating the induced electromotive force E of a wound coil:

$$B = \frac{1}{NS}\int Edt \qquad \text{Equation 2-10}$$

where N is the number of turns, and S the specimen cross-section.

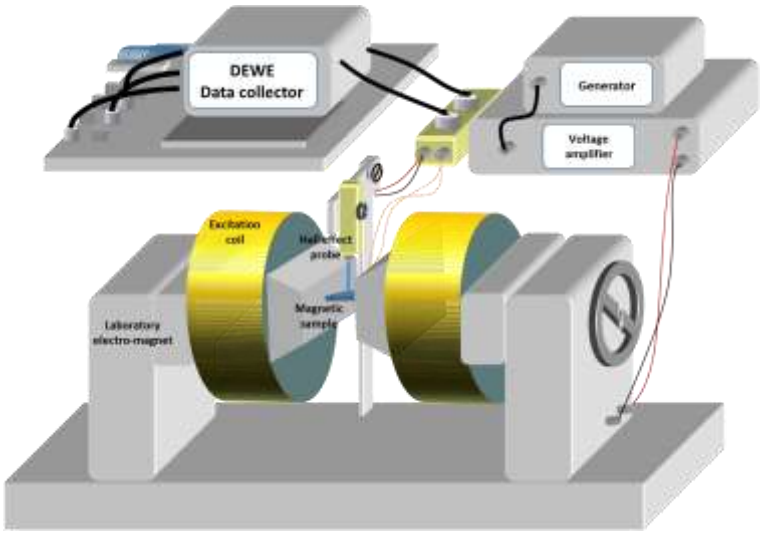

Figure 2-12 Electromagnet setup for hysteresis behavior characterization of magnetic composites.

A real-time data acquisitions of H and E were recorded using a DEWE® acquisition card. The experimental data were treated in post-processing with Matlab® software to plot the B(H) hysteresis cycles. It is worth mentioning that the frequency used for the magnetic excitation ranged from 1 Hz to 100 Hz. On a one hand, we observed a high frequency limitation, due to the strong inductive behavior. On the other hand, tests under extremely low frequencies resulted in small ratio of the induced voltage to noise, which is difficult to process.

The hysteresis behavior of all our composites were plotted using the electromagnet setup. The composites were all cylindrical-shape (Ø30mm, thickness 15mm) and wound by a 100 turns coil. Figure 2-13 depicted the hysteresis cycles of the different particle volume fraction Fe_3O_4@ABS composites obtained under a 1Hz, 20kA/m sinusoidal magnetic excitation.

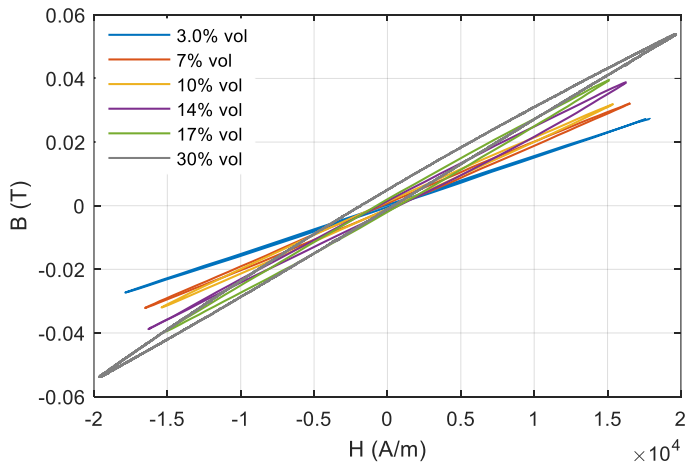

Figure 2-13 Fe_3O_4@ABS composites hysteresis loop in different particle fractions under frequency of 1Hz and voltage excitation of 5V.

As expected, a higher Fe_3O_4 content led to steeper hysteresis loops and thus higher permeability values. The hysteresis loop area is also slightly increasing as a function of the particle fraction. The density energy in Tableau 2-1 represents the hysteresis loss during one period of excitation. These variations are consistent to our expectations, confirming the relation between the magnetic particle content and the ferromagnetic losses.

Tableau 2-1 The coefficient of hysteresis loop in one cycle period for Fe3O4@ABS composites in different fraction.

Volume fraction	Density energy(J/m3)	Relative permeability μr
3%	2.3252e-04	1.2229
7%	5.4078e-04	1.5513
10%	6.0638e-04	1.6501
14%	9.1581e-04	1.8870
17%	1.0403e-03	2.0813
30%	2.1e-03	2.8602

ABS-based composites elaborated with 30% vol. of other ferromagnetic particles were also tested, i.e. comprising pure iron Fe, Nickel, and Mn-Zinc. Their characterization were done at 1Hz and 40 kA/m. The resulting hysteresis plot are depicted in Figure 2-14.

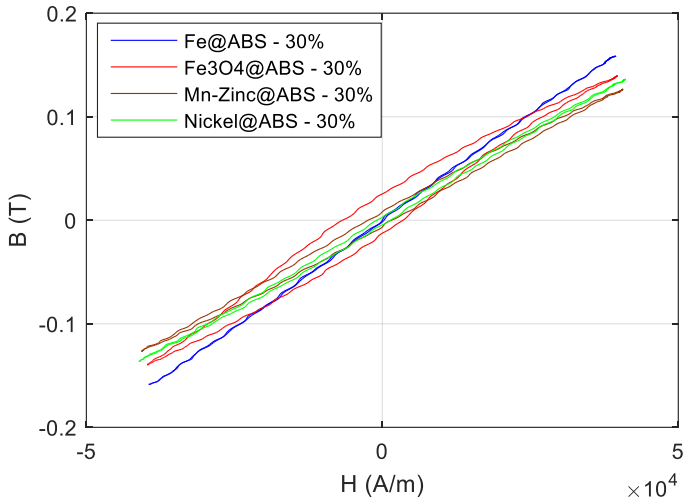

Figure 2-14 Hysteresis loop of different ABS-base magnetic composites at a frequency of 1Hz and voltage excitation of 20V.

After comparing these 4 types of ABS-base ferromagnetic composites, we can conclude that Fe_3O_4 exhibits the largest hysteresis area (highest density energy). The pure Fe has the highest relative permeability, but its energy density is weak, almost 4 times lower than the Fe_3O_4 composite with a same particle fraction (see Tableau 2-2).

Tableau 2-2 Coefficient of hysteresis cycle samples with different ABS-base magnetic composites.

Composites	Density energy(J/m3)	Relative permeability μr
Fe_3O_4	0.0021	2.8602
Fe	7.5840e-05	3.2540
Ni	4.4721e-04	2.6755
Mn-Zinc	8.4201e-04	2.5138

2.4 Thermal characterization

2.4.1 Thermal stability

In all solids, including magnetic materials, a temperature rise increases the atomic thermal vibration. This vibration tends to randomize the directions of the magnetic moments and to modify the overall magnetic behavior. By increasing the temperature, the saturation magnetization decreases gradually and reaches zero at Curie temperature (585°C for the iron oxide (Fe_3O_4)). Permeability is affected differently according to the nature of the material [86]. Thus, the thermal effects must be taken into account before testing a new material in real-life application. To predict the temperature dependence and the variation trend of the magnetic parameters, experimental characterizations are necessary. In this work, a fine study of the thermal influence on the magnetic properties is a mandatory stage before designing a new component (especially true for medical applications)

Rectangular shape (60 × 14 × 4 mm, Figure 2-2(a)) Fe_3O_4@ABS composite specimens were manually wired with a 150 turns coil in a single layer. Inductance measurements were performed with a LCR meter. The tested frequency bandwidth was set to 1 kHz - 1 MHz (close to the typical induction heating applications). Assuming the relative magnetic permeability of the pure ABS as unchanged regardless the temperature and/or frequency variations, Equation 2-5 was used to calculate the specimen's permeability. Experimental tests were carried out with the wired composites placed inside an oven (VOTSCH Industrietechnik VT 7004) with varying temperature from –10°C to 120°C.

Figure 2-15 Thermal properties characterization setup for Fe_3O_4@ABS composites

The relative permeability variations (i.e., $\Delta\mu_r(T)$) as a function of the temperature is expressed in Equation 2-11:

$$\Delta\mu_r(T) = \frac{\Delta\mu_r(T) - \Delta\mu_r(T_{amb})}{\Delta\mu_r(T_{amb})} \qquad \text{Equation 2-11}$$

Here, $\Delta\mu_r(T_{amb})$ is the permeability variation at room temperature. The room temperature is set to 20 °C.

The permeability variations as a function of the temperature for different filler contents is plotted in Figure 2-16 at 1 KHz and 1 MHz. Whatever the frequency tested, all the composites show stable properties. Interestingly, a higher magnetic particle fraction leads to a higher permeability variation with temperature; e.g., 5% changes for the 30% vol. specimen as opposed to 1% for the 3% vol. specimen. The magnetic permeability of the same sample at the same frequency is almost constant in the temperature field from – 20 °C to 100 °C, which proves that the thermal performance of the Fe_3O_4@ABS composite is stable.

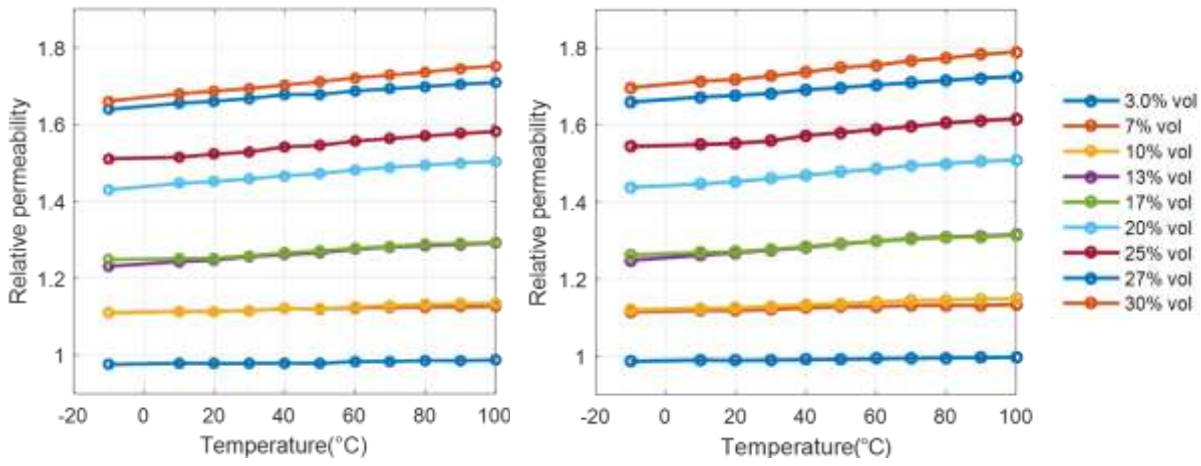

(a) (b)

Figure 2-16 Changes in permeability over temperature for different fraction Fe_3O_4@ABS composites act under (a) 1 KHz; and (b) 1 MHz.

Figure 2-17 shows that for all the frequencies tested, the relative permeability variation of the 10% vol. and the 30% vol. samples is relatively small, approximately 2% and 5%, respectively.

Figure 2-18 (a) shows the variations of the magnetic permeability for the 30% vol. Fe_3O_4@ABS composite. This permeability is almost constant until 100 kHz, confirming a high LFIH potential. A small permeability increase was observed for all the tested samples above 100 kHz (i.e., around 1%–2%). This increase was not due to the intrinsic magnetic properties but rather caused by the self-resonant-frequency (SRF) effect of the coil. This phenomenon is due to the parasitic capacitance in parallel to the inductor, which is a result of the individual turns geometrically close to each other. Another method using a different model (RLC instead of RL) was tested to improve the permeability estimation under very high frequencies. For the varicose treatment, we set the maximum frequency around 5 kHz, therefore no further investigation were done.

Whatever the frequency tested, Figure 2-18 (b) shows relatively weak variations of the 30% vol. Fe_3O_4 composite permeability (no more than several percent), even at 100 °C.

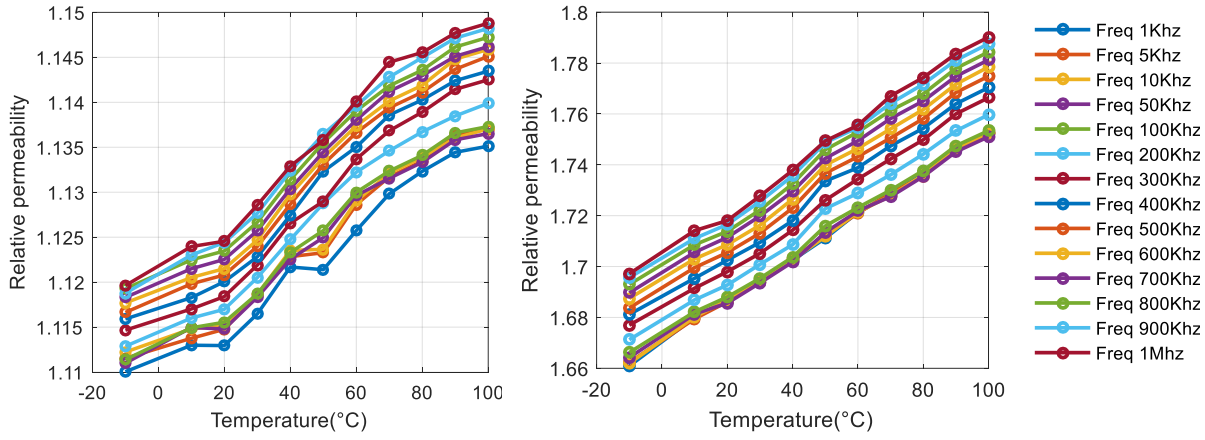

(a) (b)

Figure 2-17 The relative permeability variation under the each frequency: (a) 10% vol. Fe_3O_4@ABS; (b) 30% vol. Fe_3O_4@ABS composites.

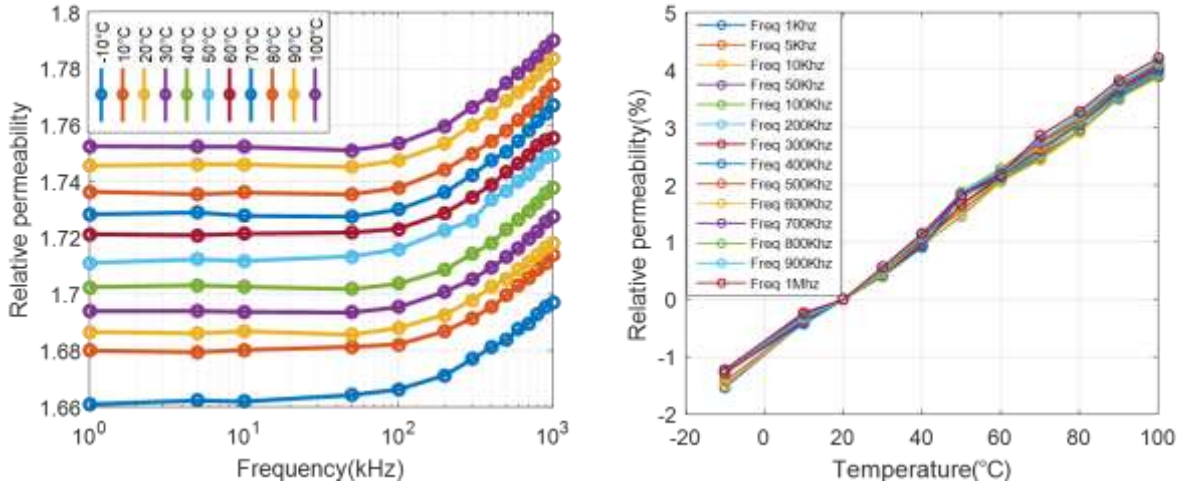

(a) (b)

Figure 2-18 (a) Relative permeability spectra of the 30% vol. Fe_3O_4 composite under different temperatures. (b) Relative permeability change (%) of the 30% vol. Fe_3O_4 composite as a function of temperature.

2.4.2 Thermal conductivity and specific heat capacity

As reported in [87], the specific heat capacity (C_p) of a composite below 50% wt. (~ 20% vol.) can be obtained using Equation 2-12. In the case of isotropic materials under constant pressure and volume variation (no local strain and stress), C_p is equal to the weighted average of each constituent heat capacities ($C_{p,composite}$) [88].

$$C_{p,composite} = (1 - \omega_{Fe_3O_4})C_{p,ABS} + \omega_{Fe_3O_4}C_{p,Fe_3O_4} \quad \text{Equation 2-12}$$

where $\omega_{Fe_3O_4}$ denotes the Fe_3O_4 weight fraction, $C_{p,ABS}$ and C_{p,Fe_3O_4} are the specific heat capacity of the ABS polymer (~ 1800 $J.kg^{-1}.K^{-1}$) and of the Fe_3O_4 particles (~ 450 $J.kg^{-1}.K^{-1}$), respectively.

The relation between the weight fraction $\omega_{Fe_3O_4}$ and the volume fraction $v_{Fe_3O_4}$ is provided in Equation 2-13 below:

$$\omega_{Fe_3O_4} = \frac{v_{Fe_3O_4}}{v_{Fe_3O_4} + (1 - v_{Fe_3O_4})\frac{\rho_{ABS}}{\rho_{Fe_3O_4}}} \quad \text{Equation 2-13}$$

Here, the ABS matrix and the iron oxide power density are $\rho_{ABS} = 1.04\ g/cm^3$ and $\rho_{Fe_3O_4} = 5\ g/cm^3$, respectively.

A material thermal conductivity is its ability to conduct heat. The thermal conductivity of a two phases composite can be calculated using the Maxwell-Eucken's model [89]. The Maxwell-

Eucken model assumes that the additional particles are homogeneously distributed in the polymer matrix, non-interacting, and roughly spherical.

$$\lambda = \frac{\lambda_p v_{f+} \lambda_f (1 - v_f) \frac{3\lambda_p}{2\lambda_p + \lambda_f}}{v_f + (1 - v_f) \frac{3\lambda_p}{2\lambda_p + \lambda_f}} \qquad \text{Equation 2-14}$$

where v_f is the particle volume fraction; λ, λ_f, and λ_p are the thermal conductivity of the composites, the ferromagnetic particles, and the polymer matrix, respectively.

Figure 2-19 shows the thermal conductivity and specific heat capacity of Fe_3O_4@ABS composites obtained with the theoretical model. The model parameters are $\lambda_{ABS} = 0.225 w/mK$, $\lambda_{Fe_3O_4} = 0.9 w/mK$.

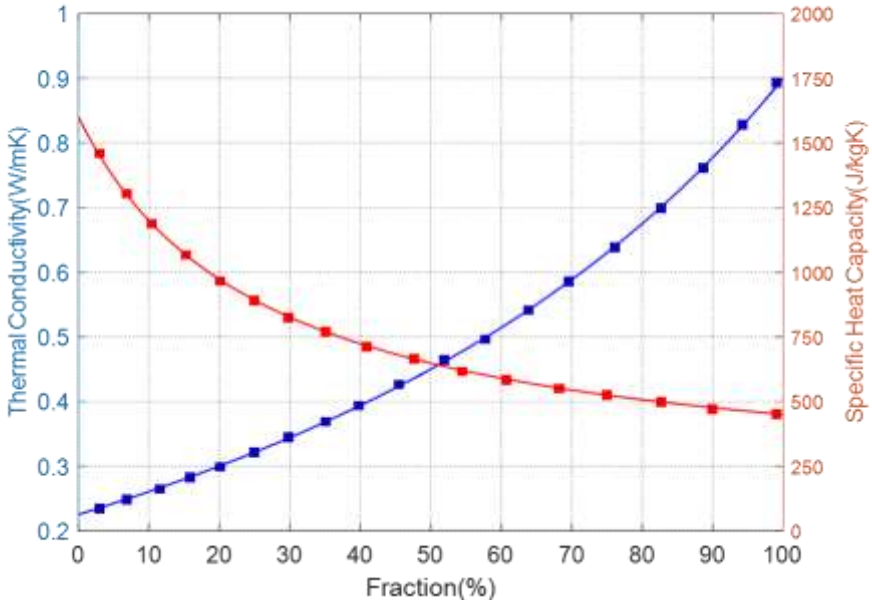

Figure 2-19 Fe_3O_4@ABS composites theoretical thermal conductivity (red line) and specific heat (blue line) as a function of iron oxide content.

A characterization device JEULIN (Ref: 253118) was used to measure the thermal conductivity of the composites, which were placed between two metal blocks of the controlled temperature variation. We measured the thermal resistance of the specimen in a steady state. The tested samples were fabricated with the specific size of 40 x 40 mm and less than 10 mm thick.

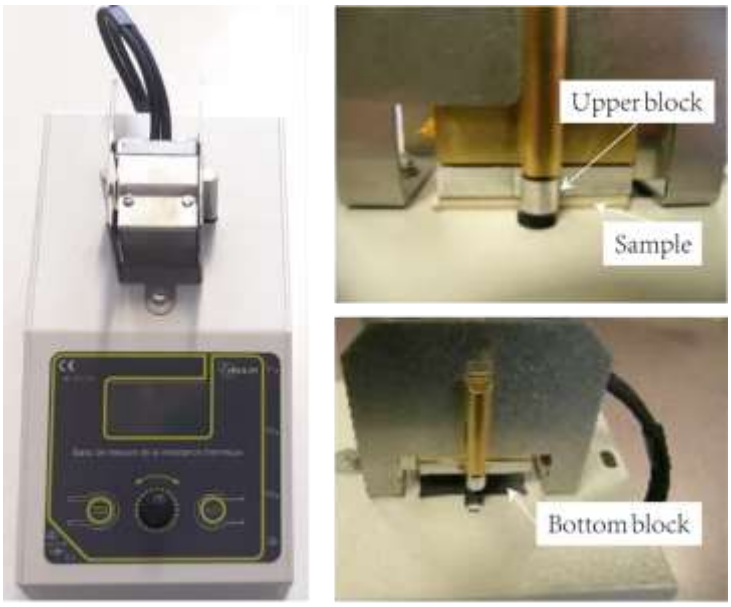

Figure 2-20 Thermal conductivity test bench JEULIN

Fe_3O_4@ABS composites (3, 8 and 17% vol.) , Ni@ABS composites (10, 23, 40% vol.), and pure ABS have all been manufactured in a specific size of 40 x 40 x5 mm^3. The theoretical and experimental results are listed in Tableau 2-3.

We observe a multiplication factor $c = 0.65$ between the experimental results and the theoretical prevision. This experimental bias can be due to the specimens geometry. Our specimens have been made with the hot press machine and their surface is not completely flat as expected. Therefore, they don't fitted perfectly the measurement surface during the test. In other words, there is a 35% air gap factor, meaning that all our experimental results have to be divided by 0.65. As shown in Figure 2-21, once this adjustment done, the results fit correctly the Maxwell-Eucken model. These figures shows the thermal conductivity variations of Fe_3O_4@ABS and Ni@ABS composites obtained with the Maxwell-Eucken's model. The model parameters are $\lambda_{ABS} = 0.225 w/mK$,$\lambda_{Fe_3O_4} = 0.9 w/mK$ and $\lambda_{Ni} = 1.5\, w/mK$.

Tableau 2-3 The theoretical and experimental thermal conductivity of composites.

λ (W/m.K)	Fe_3O_4			Ni			ABS
	3%	7%	17%	10%	23%	40%	-
Theoretical value	0.235	0.253	0.288	0.272	0.345	0.464	0.225
Experimental value	0.154	0.166	0.187	0.187	0.223	0.296	0.146
Experimental value/c	0.237	0.255	0.288	0.288	0.343	0.455	0.225

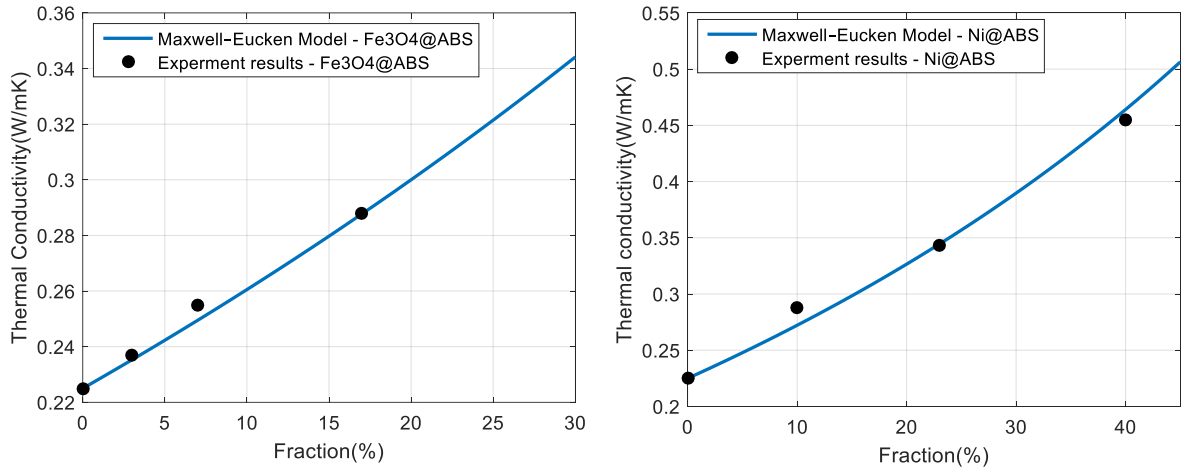

(a) (b)

Figure 2-21 Thermal conductivity of (a) Fe_3O_4@ABS composites; (b) Nickel@ABS composites.

2.5 Summary

This Chapter introduces the fabrication method of isotropic ferromagnetic composites (Fe_3O_4@ABS). The electric properties (e.g., conductivity and percolation threshold), magnetic properties (e.g., permeability and hysteresis behavior), and thermal properties (e.g., thermal conductivity and specific heat) have been studied. Fe_3O_4@ABS composite remains non-conductive state when the particle volume fraction is below its percolation threshold of 47% vol. The permeability has been characterized based on Comsol simulation, analytical model, and experimental test. All these results are pretty coherent. The stability of the permeability's composite has been confirmed in the frequency range of [1kHz–1MHz] and under the temperature from –10° to 100°. The thermal conductivity and the specific heat of composites with different types of magnetic particles have been analyzed.

In the next following chapter, the LFIH effect of isotropic ferromagnetic composites will be performed. A complete analysis of various pertinent parameters involved in the LFIH mechanism will be provided.

Chapter 3
LFIH Effect of Isotropic Ferromagnetic Composites

Chapter 3 focusses on a low-frequency induction heating (LFIH) effect in the isotropic ferromagnetic composites elaborated with thermoplastic polymer (acrylonitrile butadiene styrene, ABS) doped by iron oxide (Fe_3O_4) magnetic particles. The LFIH effect in such ferromagnetic composites appears as soon as the sample is exposed to an alternating magnetic excitation field and is mainly due to the so-called "microscopic" eddy currents linked to the motions of the magnetic domain wall. The heating behavior could be affected by diverse factors, including parameters related to the composites (e.g. content, nature, size of the magnetic particles; dimension of composite, etc.). And also could be affected by the external magnetic excitation such as frequency and amplitude. Thermal transfer based Comsol simulation together with experimental tests, demonstrated a feasibility to inductively heat the ferromagnetic composite up to 100°C -120°C by optimizing the magnetic source and the particle fraction of the material. Those results are encouraging for application in thermal endovenous treatments based on the LFIH effect.

3.1 LFIH experimental setup and control of magnetic field excitation

3.1.1 Description of test bench

For the validation of the induction heating effect, a specific experimental test-bench was developed (Figure 3-1). To generate a significant AC magnetic field excitation, a magnetic inductor, including several pairs of cylinder permanent magnets, was assembled to the DC drill motor. As shown in Figure 3-2, the pole distribution of those permanent magnets was alternatively south and north, a sinusoidal magnetic excitation whose frequency is related to the rotational speed which is driven by the drill motor. Since the sample was fixed on the removable support, it is possible to vary the distance to the magnetic inductor. Two thermal couples were coated on the sample via an adhesive; one allowed to measure the temperature of heat area corresponding to magnet's passage, and the other used to determine the temperature of the sample's center. Both data sets were recorded in real time through a DEWE card (Krypton). To obtain a more intuitive temperature image, a thermal camera (Optris Xi400) was used during the experiment.

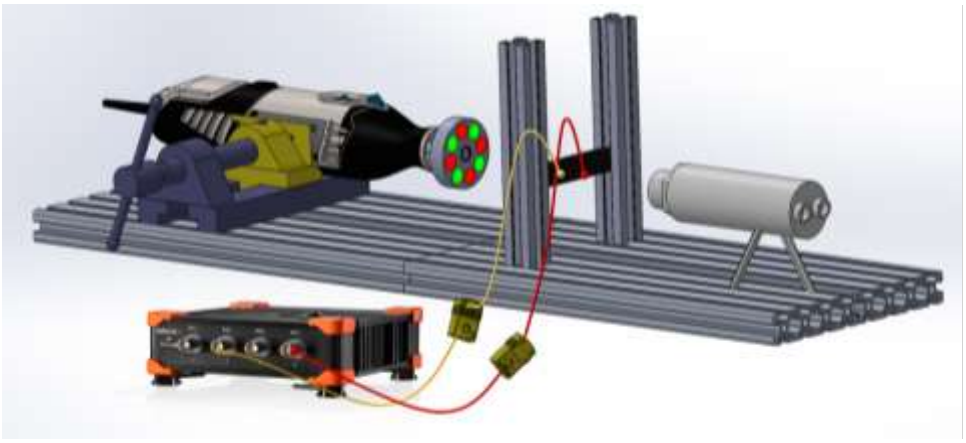

Figure 3-1 Experimental setup schematic diagram of the induction heating effect.

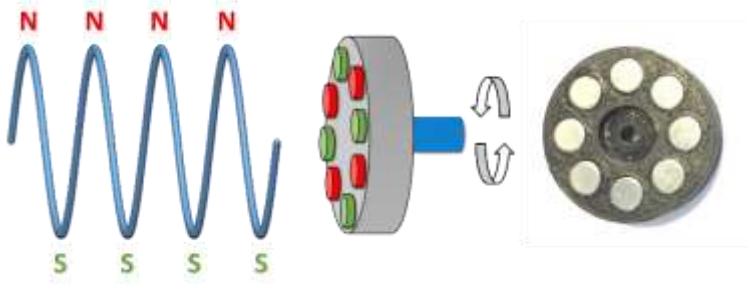

Figure 3-2 Design of the magnetic inductor with permanent magnets

3.1.2 Frequency control of magnetic field excitation

Equation 3-1 enables to deduce the relationship between the motor's velocity (denoted V (RPM)) and the frequency (denoted $f(Hz)$) of the magnetic field excitation. n is the number of permanent magnets assembled to the magnetic inductor.

$$f = \frac{V}{60} \times \frac{n}{2} \qquad \text{Equation 3-1}$$

Based on the Fourier transformer of the measured magnetic field as displayed in Figure 3-3 (a), it is possible to precisely determine its frequency (Figure 3-3 (b)). An emprical measure of the motor's velocity together with the spectra analysis of Figure 3-4 allowed to confirm the expression of Equation 3-1. This test bench can drive variable velocity and with a maximum rotating speed of 35 kRPM. Using 8-magnet inductor, the highest frequency of the magnetic field is approximately 2300 Hz. The amplitude filed is not much affected by the motor's speed, and can reach 160kA/m. Interestingly, the result revealed that the magnetic excitation signal is purely sinusoidal as parasite harmonics are negligible compared to the principal harmonics.

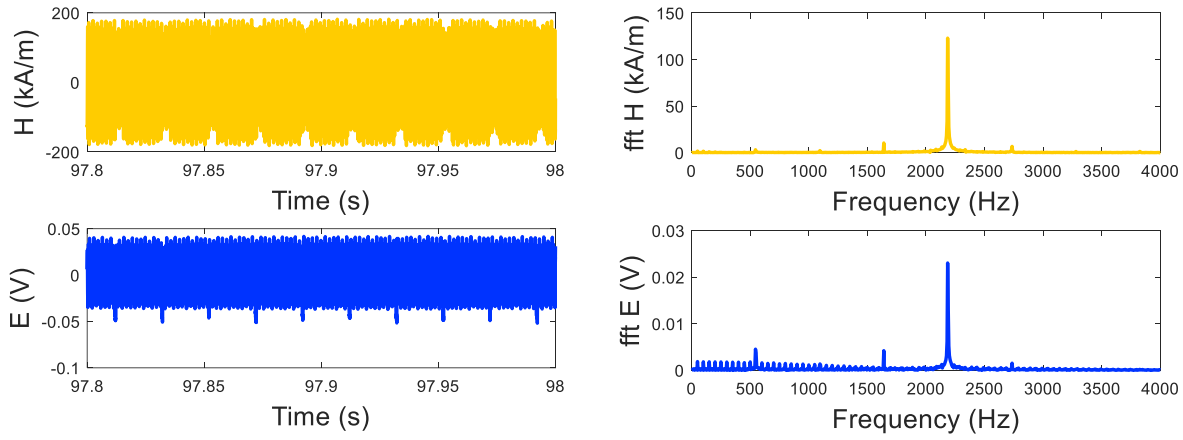

(a) (b)

Figure 3-3 (a) the magnetic strength and induced voltage of the magnetic field created by the 8-magnets inductor (b) the Fourier transformer of frequency

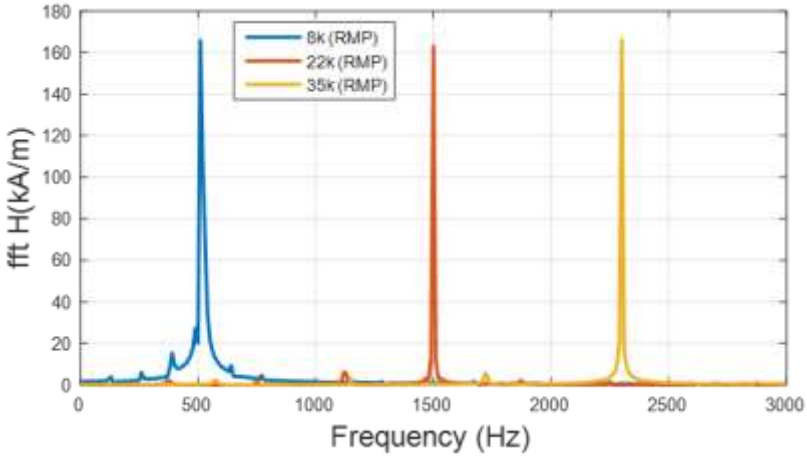

Figure 3-4 FFT spectra of magnetic field

The quantification of the heating effect was either done by an analysis of the linear heating rate or by a direct evaluation of the temperature profile. The linear heating rate was obtained from each measured temperature profile. The temperature rise and the response time should be improved to meet requirement of varicose vein surgery. The idea here is to improve the frequency of excited magnetic field. Thus a new magnetic inductor with a double of identical permanent magnets (i.e., 16) has been developed in this study, see the real photo of the set up in Figure 3-5 below.

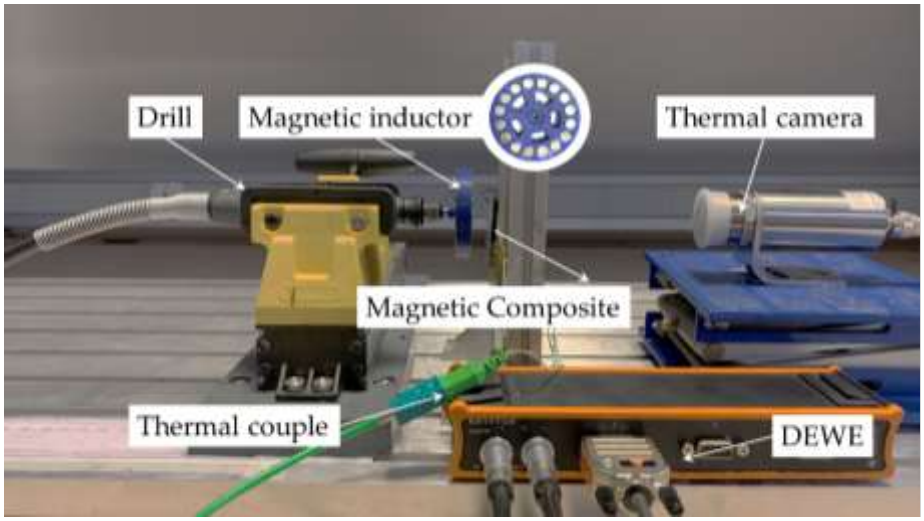

Figure 3-5 Real shot pictures of induction heating test setup.

In practice, with a maximum rotating speed of 35 kRPM, the 8-magnet source can reach an AC magnetic field of 2300Hz, and the 16-magnet source leads to 4200 Hz (see the spectra in Figure 3-6). This value was slightly lower than the estimated value (i.e. 4600 Hz) according to Equation 3-1. The fact is that the new inductor containing a double of permanent magnets becomes heavier, leading to the increase rotational inertia. As a result, more torque was exerted on the motor, somehow reducing the speed.

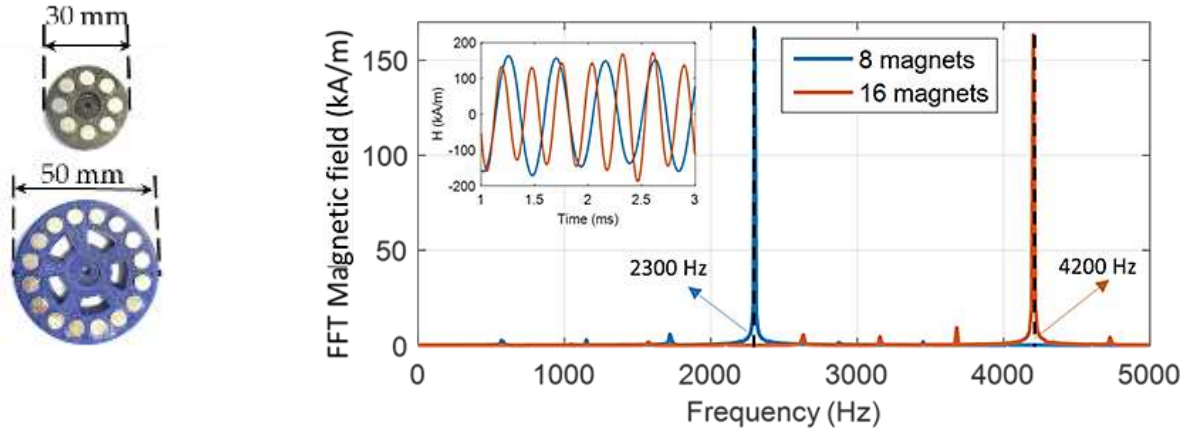

(a) (b)

Figure 3-6. (a) 8-magnet and 16-magnet inductors. (b) FFT spectra of magnetic field driven by the two types of inductors under 35 kRPM motor speed. Inset: Time evolution of the magnetic excitation induced from measurement with the H-coil.

3.1.3 Amplitude control of magnetic field excitation

To control the amplitude of magnetic field, we can control the distance between the magnetic inductor and the composite as described just now. Figure 3-7 (a) and (c) display the alternative voltage signal induced by a hand-made coil sensor at different distances, in case of 8-magnets and 16 magnets, respectively. In both cases, the data are monitored and recorded by an Oscilloscope. The voltage amplitude (e) can be calculated according to the Lenz's law:

$$e = \frac{d\emptyset}{dt} = NBS\omega = N\mu_0 HS\omega \qquad \text{Equation 3-2}$$

where N is the turn numbers of the coil sensor(N = 10), S denotes the cross section of the coil sensor, $\omega = 2\pi f$, H is the filed amplitude that is determined from Figure 3-7 (b) and (d).

The results highlighted that the magnetic strength (H) decreases with the increasing distance between the magnetic inductor and the coil sensor. As expected, the amplitude of H is the same for the case of 8-magnets and 16 magnets. This explains why similar level of Len's voltage (~ 1V) are obtained in Figure 3-7 (a) and (c). Nonetheless, the frequency is double with the 16 magnets, which is coherent to the FFT analysis in subsection 3.1.2.

(a)

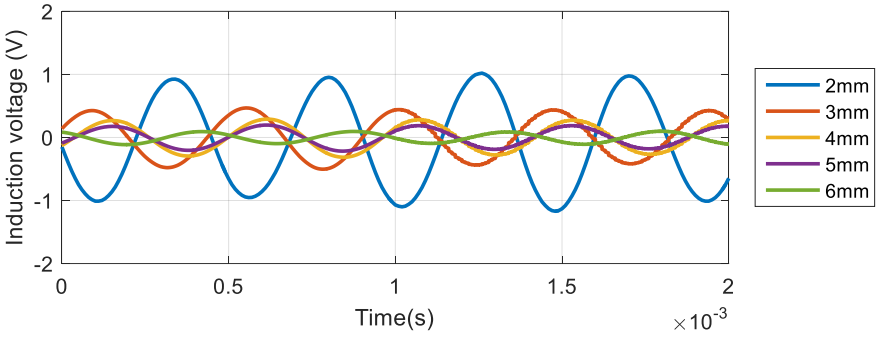

(b)

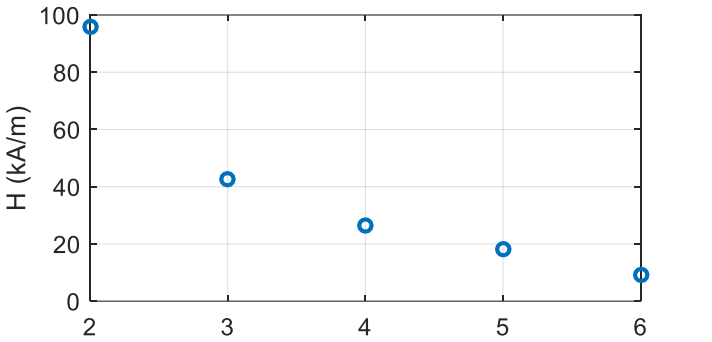

(c)

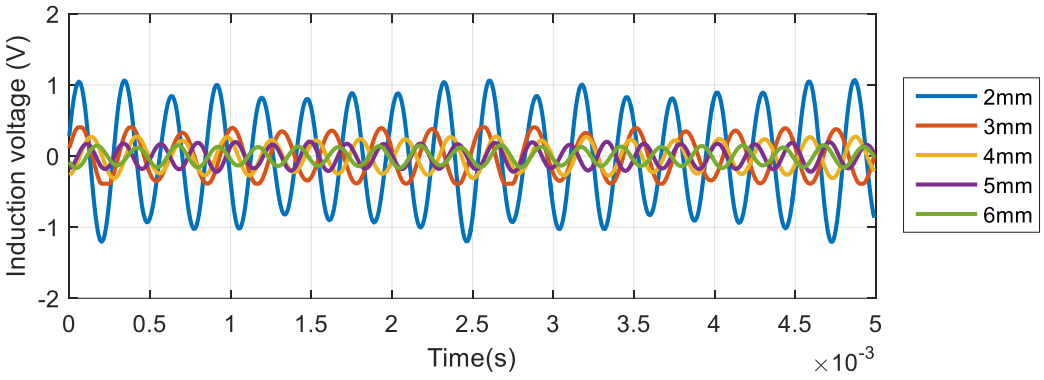

(d)

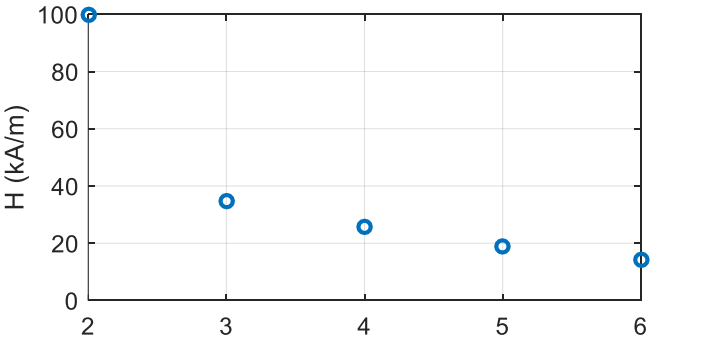

Figure 3-7 The induced voltage from the secondary coil acting on the (a) 8-magnets inductor; (c) 16-magnets inductor. The amplitudes changes with the distance between the coil sensor and (b) 8-magnets inductor; (d) 16-magnets inductor.

3.2 Validation of LFIH mechanism

To better highlight the induction heating effect of the proposed ferromagnetic composites, a comparison with respect to conductive but non-ferromagnetic samples (e.g., carbon black or copper) was performed based on the thermal images of Figure 3-8. As opposed to the ferromagnetic composite, the conductive sample exhibited a very weak response to the magnetic field excitation, and no temperature effect was achieved. This observation was explained by the "microscopic" eddy-current consideration (i.e., domain wall motions were the predominant mechanisms under low frequency), leading to local temperature variations inside the ferromagnetic particles. Finally, experimental results revealed that the frequency dependence of the hysteresis losses only appeared through the ferromagnetic composite, but no reaction was observed on the conductive composites. Similar conclusions have also been reported in [90].

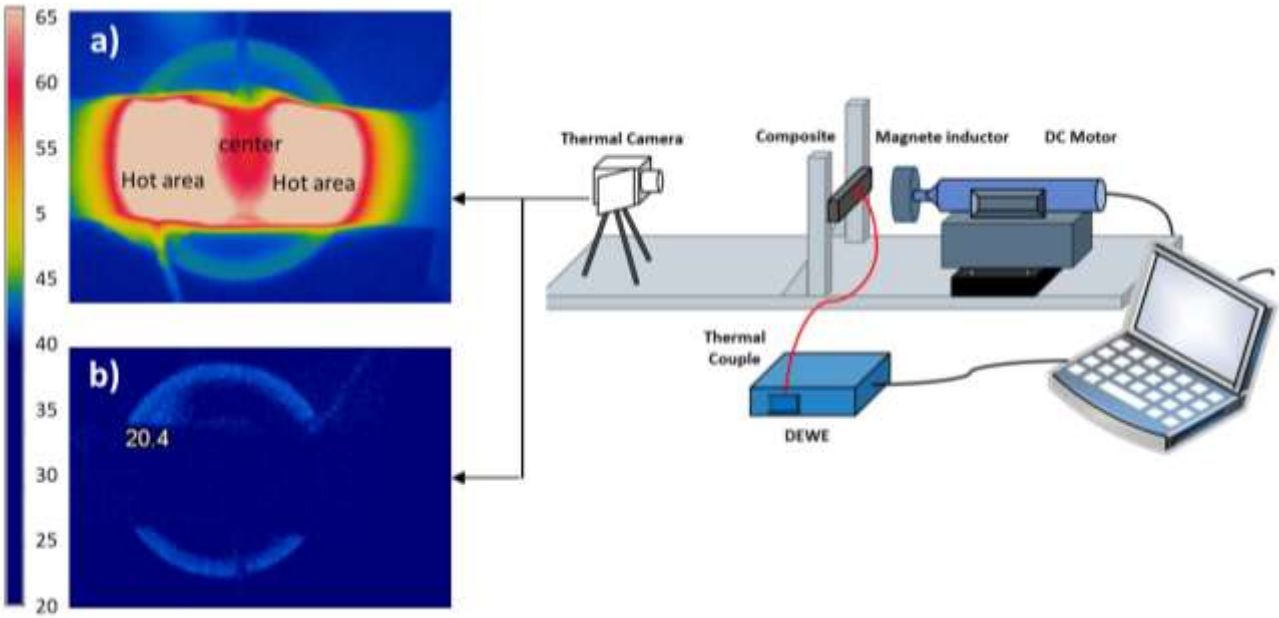

Figure 3-8 LFIH observation under 2.3 kHz AC magnetic field excitation. a) Ferromagnetic composite with17% vol. of iron oxide; b) conductive composite with 15% of copper oxide.

3.3 Influence from magnetic excitation

3.3.1 Frequency effect

The heating experiments confirmed the feasibility to create a hysteresis loss by an electromagnetic field of low frequency using polymers filled with micro-sized magnetic particles. The results demonstrate a significant temperature increase of the ferromagnetic samples when they were exposed to an alternating magnetic field.

The sample used for testing LFIH is rectangular shape (60 × 14 × 4 mm^3, Figure 2-2(a)), fabricated with ABS incorporated by 17% vol. Fe_3O_4 filler. The DC motor carrying the 8-magnets inductor have controllable speed varies from 5 to 35 kRPM. Figure 3-9 shows the temperature evolution of the composite for the whole velocity range, resulting in variation of the magnetic frequency from 300 to 2300 Hz (cf. Equation 3-1.). As expected, the heating effect was found to be greatly frequency dependent. For instance, under the frequency of 2300 Hz, the temperature in steady state rose up to 65°C, whereas only 30°C was attained in the case of 300 Hz. Actually, the heat created from microscopic eddy-current occurs within Fe_3O_4 particles, allowing to transfer the energy of alternating magnetic field to electromagnetic loss. Obviously, the transformation efficiency is strongly depended on the frequency of the external field.

Based on the result of Figure 3-9 (a), a simple linear regression can be used to fit well the experimental data comprising heating temperature versus magnetic frequency, see Figure 3-10. Such a relationship was modeled in accordance with the linear predictor function whose rising slope was estimated to be approximately 1°C/60 Hz. To reach the maximum temperature required for the varicose treatment (i.e., 120°C [44]), it was essential to excite the composite with a magnetic field of about 7200 Hz, which was almost two-fold higher than the maximum frequency generated by our current setup. Two solutions can be envisaged in future work to enhance device performance. First, increasing the pole number of the permanent magnet (although the size and weight of the inductor should be considered so as not to disturb the motor rotation). Second, using a two-fold higher motor speed (e.g., 70 kRPM), which is probably feasible because a few companies have already achieved speeds of approximately 200 kRPM[91]. Many factors are involved in designing and achieving various speeds that now makes these kinds of motors extremely costly. For instance, the expensive dental handpiece is very high speed and can spin at more than 100 kRPM, with some even boasting speeds over 400 kRPM[92]. The highest speed from electrical motors can be achieved by reducing their size to very small and drive negligible loads.

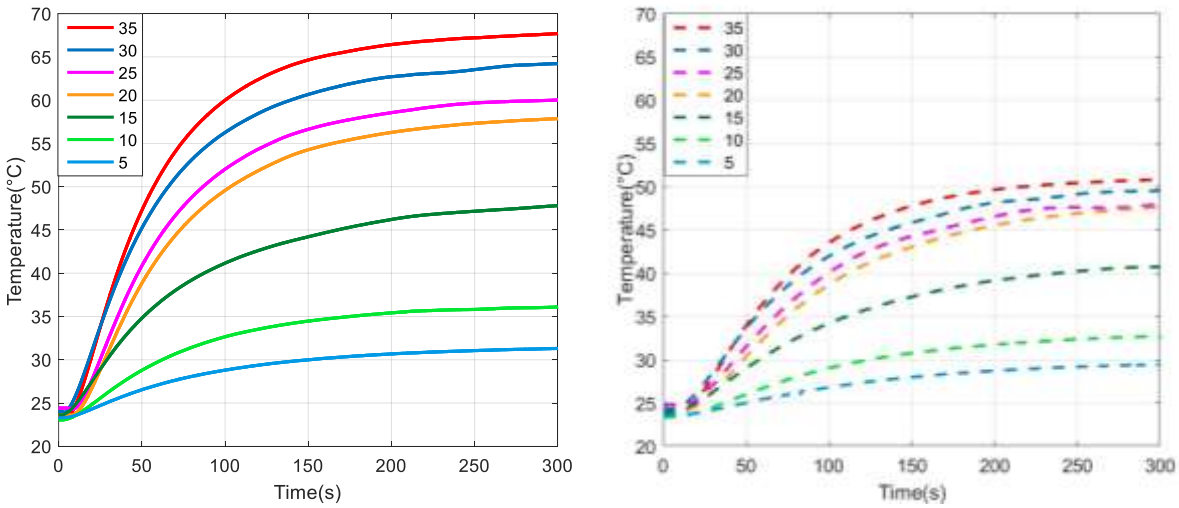

(a) (b)

Figure 3-9 Temperature versus time at different motor speeds (kRPM). (a) Continuous lines relate to the T° of hot source; (b) dotted lines referred to the T° at the center.

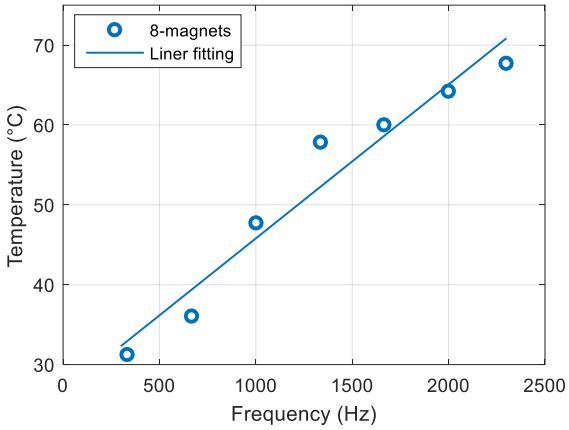

Figure 3-10 Temperature versus frequency of alternative magnetic excitation.

It is interesting to note that the temperature at the center of the ferromagnetic composite is lower compared to those at the two sides (Figure 3-11). This result was consistent with the circular design of the magnetic inductor where the magnetic field was stronger at the periphery (position of permanent magnets) than the one at the center (containing no magnet as the thermal camera observation shown in Figure 3-11(b).

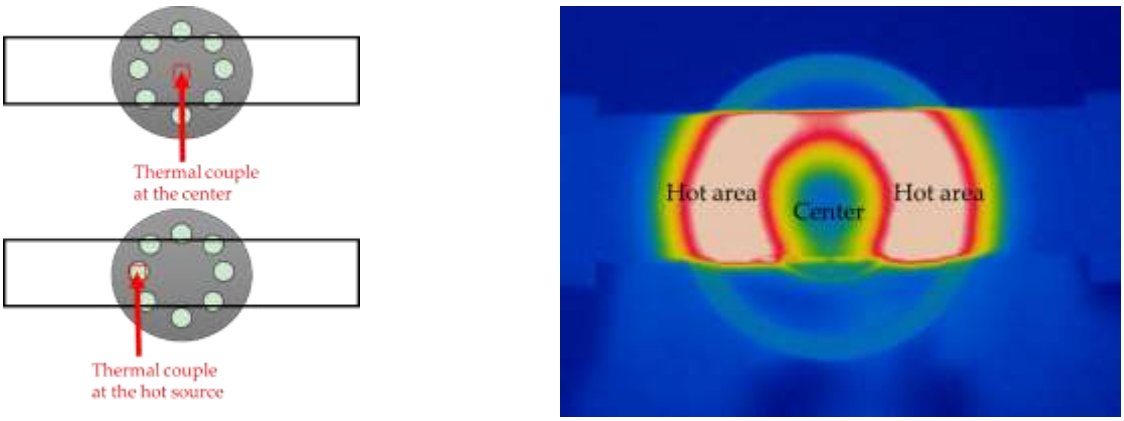

(a) (b)

Figure 3-11 (a) Schematic diagram of thermal couple position; (b) LFIH thermal camera observation under 2.3 kHz AC magnetic field excitation.

3.3.2 Amplitude effect

The above experiments highlighted the frequency dependence of the induction heating effect and determined how to improve it. It was clear that such an effect also depended on the strength of the magnetic field. To vary the magnetic intensity driven to the sample, it is not necessary to change the permanent magnets. Instead, an easier way was to modify the distance between the magnetic source and the sample. Figure 3-12 (a) shows the time evolution in temperature for several distances under 2300 Hz magnetic excitation. As expected, the temperature drastically dropped when the distance increased, which was because the strength of the magnetic field decreased quadratically with increasing distance, as described in Figure 3-12 (b). Figure 3-12 (c) the final temperature in term of the field amplitude, showing how important it is to bring the magnetic source close to the target object.

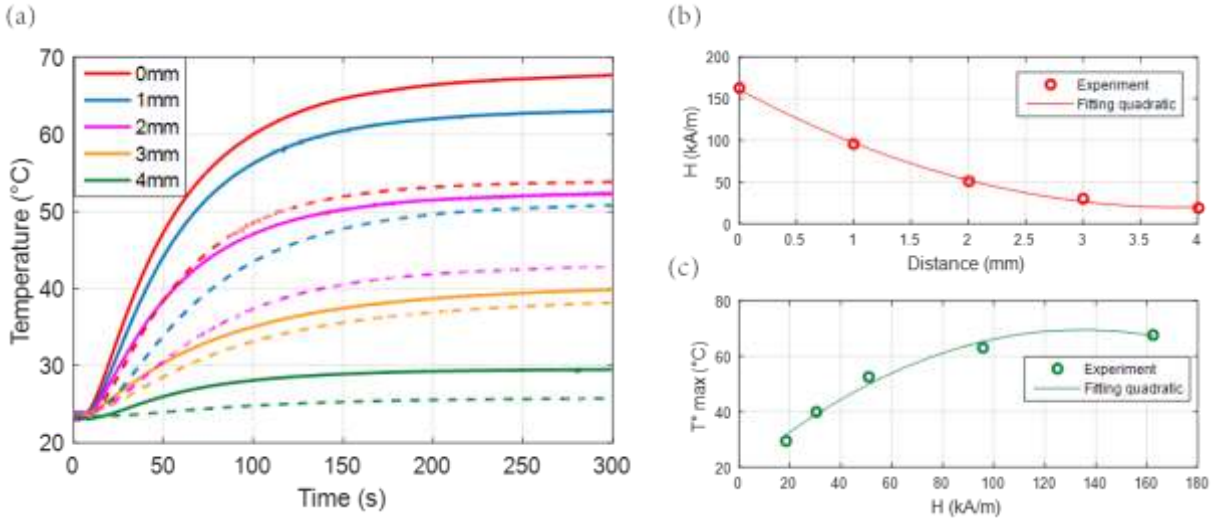

Figure 3-12 (a) Time evolution of temperature at different distances between the composite and the magnetic inductor. Continuous lines show to the T° of hot source whereas dotted lines show the T° at the center. (b) The amplitude of the magnetic field as a function of distance. (c) Final temperature versus magnetic intensity.

3.4 Influence from material properties

The above section clearly highlighted that IH strongly depends on the magnetic excitation. This part aims to show that the material properties play an important role as well. Several relevant parameters are investigated, including composite geometry, together with fraction, size, and nature of ferromagnetic particles. The polymer matrix can affect to the mechanical property, but not to the magnetic behavior of the composite, and therefore probably no influence to the IH effect.

3.4.1 Particle concentration

Experimental test are performed on Fe_3O_4@ABS composites with rectangular shape (60 × 14 × 4 mm^3, Figure 2-2(a)).

3.4.1.1 Temperature response

Figure 3-13 (a) and (b) display the temperature vs. time variations of Fe_3O_4@ABS composites with various particle volume fractions from 0% to 30% under magnetic sources with two different frequency excitations, i.e. 2300Hz, and 4200Hz, respectively. For each particle fraction, the higher the frequency excitation, the higher the temperature variation. While in both cases, the temperature remained constant for the pure ABS thermoplastic, but it increases for samples with higher magnetic content. Indeed, a polymer filled with sufficient ferromagnetic particles not only lead to substantially improved permeability but also hysteresis losses. This results in a significant increase in the magnetic power density, and therefore, boosting the induction heating effect.

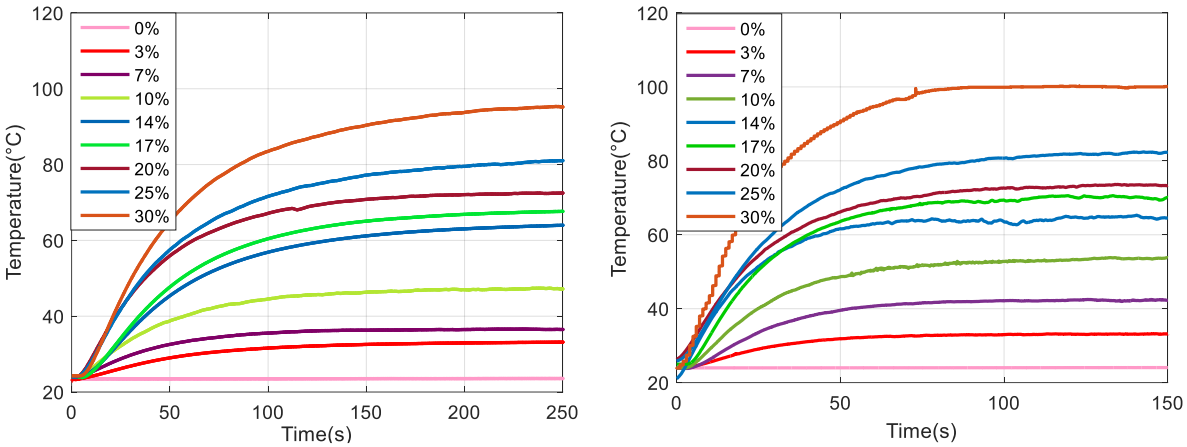

Figure 3-13 Time evolution of the temperature of Fe_3O_4@ABS composites at different particle fraction excited by (a) the 8-magnet inductor and (b) the 16-magnet inductor.

Figure 3-14 (a) shows a composite doped with 30% vol. Fe_3O_4, which was heated at 67 °C and 90 °C after 50 s via the 8-magnet source and 16-magnet source, respectively. Furthermore, to reach the target temperature (e.g., 90 °C), the 16-magnet inductor only take 50 s, which is three-fold faster than the other one. Figure 3-14 (b) displayed the temperature variation ($\Delta T_{16/8} = T_{16\ magnets} - T_{8\ magnets}$) of three samples (i.e., 20% vol., 25% vol., 30% vol.) driven by the two magnetic sources as a function of the exposure time. The value of $\Delta T_{16/8}$ becomes significant under short operation times (25–50 s). The results confirmed the decreasing behavior of $\Delta T_{16/8}$ with longer heating durations (above 50 s). It then quickly drops after more than 100 s. Consequently, the 16-magnets inductor shows a further advantage over the 8-magnets one — especially in medical applications where a fast response time is mandatory.

Figure 3-15 illustrates the temperature behavior in terms of volume fraction of the composite under two different magnetic frequency excitations with recording after 50 s and after 250s. The results show a linear relationship between the heating temperature and the magnetic

particle content. Interestingly, the gap between the two curves in Figure 3-15(a) has a trend to increases as a function of the iron oxide ratio, showing the benefit of using high filler content ferromagnetic composite to improve hysteresis losses inside each particle. What's more worthy to mention here is in Figure 3-15(b) after 250s, although the 16-magnet inductor results in higher temperature variation than the 8-magnet inductor, the final temperature are pretty close. In general, 16-magnets inductor could provide a quicker response, but when the excited time is long enough, 8-magnets and 16-magnets would get the small gap difference temperature evolution (< 6°C).

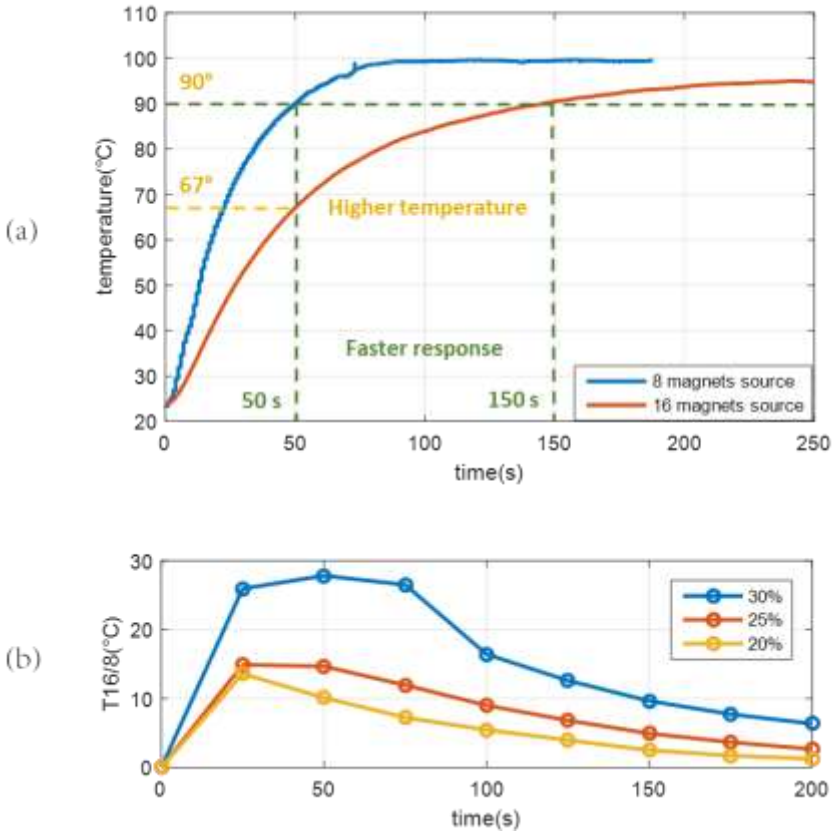

Figure 3-14 (a) Temperature evolution of the 30% Fe3O4 composite using two different inductor excitations; (b) Temperature variation of two magnetic sources $\Delta T_{16/8}$ as a function of duration.

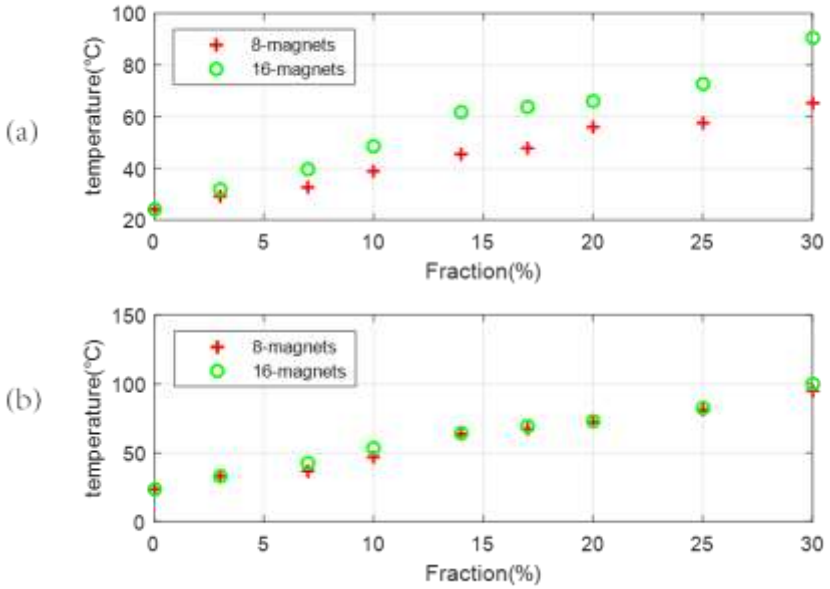

Figure 3-15 Temperature of all Fe_3O_4@ABS composites with different fractions after (a) 50 s; (b) 250s

3.4.1.2 Time constant

Accordingly, all previous analyses demonstrated the feasibility to attain a high enough temperature for endovenous thermal ablation that depends on relevant parameters, such as fraction content of fillers, frequency, and strength of the magnetic field. Beside the temperature value, another factor plays a key role in varicose treatment success is the response time of the device, which should not exceed a few seconds in order not to deteriorate the vessel and limit procedure duration. Actually, endovenous procedure obliged that the heating device should deliver an impulsion at maximum amplitude of 120° for less than 5s when treating one segment of varicose vein. In reality, the main limitation of current endovascular therapy is that it cannot heat portion of veins larger than 11 mm for radiofrequency (RFA) and 20 mm for laser (EVLA), leading to increasing treatment time.

In practice, we say that the time constant is the time for the fist-order system to reach $\approx$ 63 % of its final value. Figure 3-16 displays the evolution of the time constant, where the system has changed about 63% toward its steady-state value. It is noteworthy that the time constant slightly changed as a function of the filler's volume fraction, as well as the frequency and the amplitude of the magnetic field. However, this value is still high relative to the one imposed by varicose vein treatment. A discussion on this issue will be addressed in section 3.6.

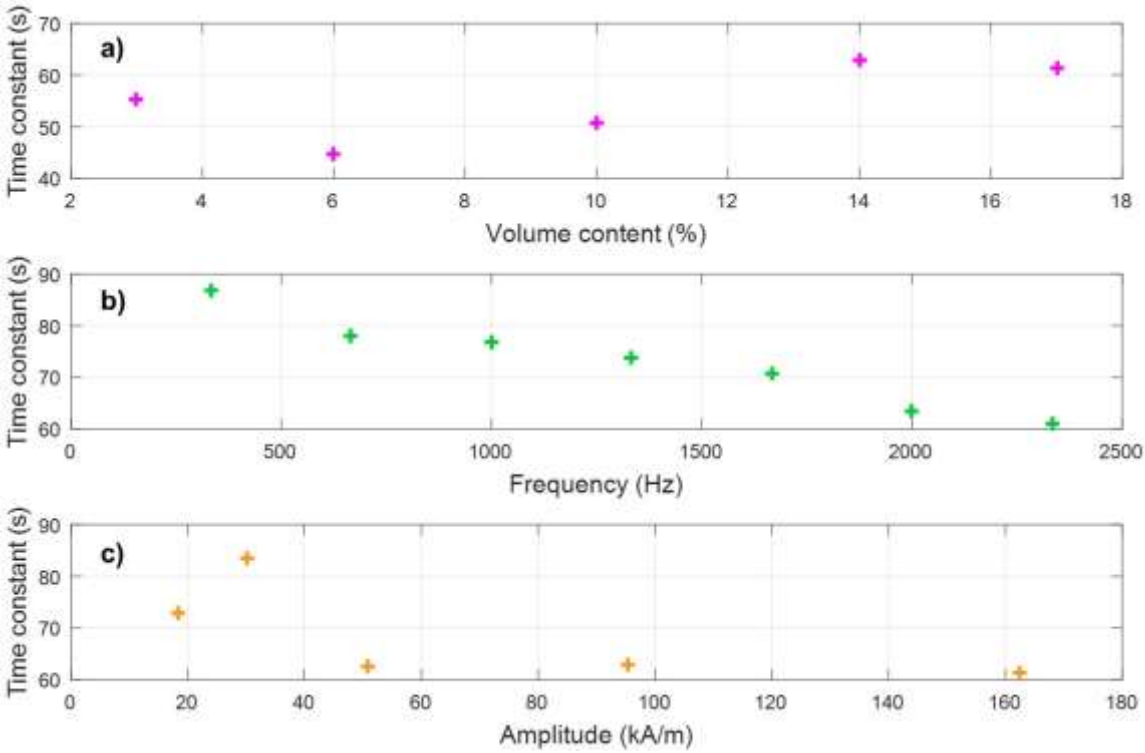

Figure 3-16 The time constant as a function of a) volume content, b) frequency of magnetic field, and c) amplitude of magnetic field.

3.4.2 Particle size

Isotropic ABS-based composites with different sizes of Fe_3O_4 particle (50-100nm, 5um, 50um) were prepared in rectangular shape (60 × 14 × 4 mm^3, Figure 2-2(a)). Particle size will have significant influence on the magnetic properties of composites. The permeability of three kinds of particle size Fe_3O_4@ABS composite with the fraction of 30% vol. have been tested by inductances measurement. As observed in Figure 3-17, the 50 μm size particle Fe_3O_4@ABS composite exhibits the highest relative permeability.

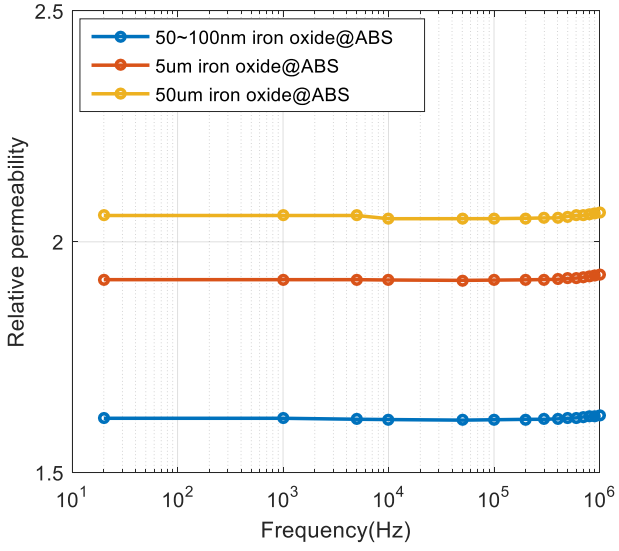

Figure 3-17 Effect of particle size on isotropic Fe_3O_4@ABS composites permeability

Samples with different sizes of Fe_3O_4 particle with various fraction of 10% vol., 20% vol., and 30% vol. have been fabricated for IH test. Figure 3-18 illustrated the temperature variations of all samples applied under magnetic field of 160kA/m amplitude and 2300 Hz frequency. The results revealed the 5µm composite leads to the best temperature level compared to the other, regardless of which particle fraction. As expected, the temperature has quasi linear relationship with the particle volume content. To further explain the influence of particle's size to the IH effect, an approached based on energy density of hysteresis curve is investigated in the follows.

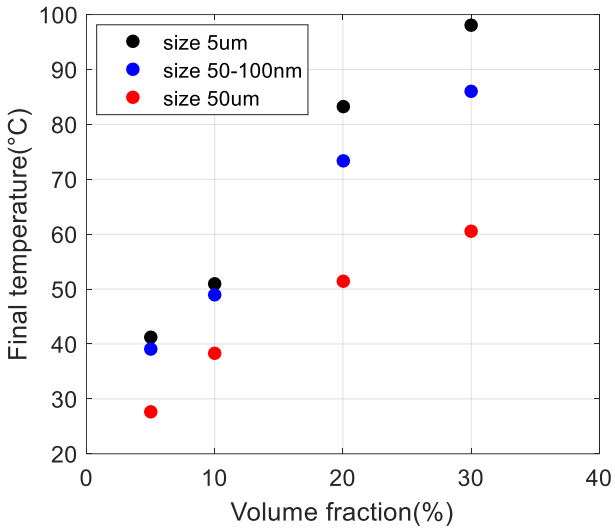

Figure 3-18 Final temperature of Fe_3O_4@ABS composites with particle size of 50-100nm, 5µm, and 50µm on low frequency induction heating effects.

As mention in the section 2.3.4, the hysteresis loss was mainly caused by the domain wall motion, relating to the area of the hysteresis loop B-H. The results as shown in Figure 3-19, for 1 period hysteresis cycle, the 5um particle composites has the largest hysteresis loop area.

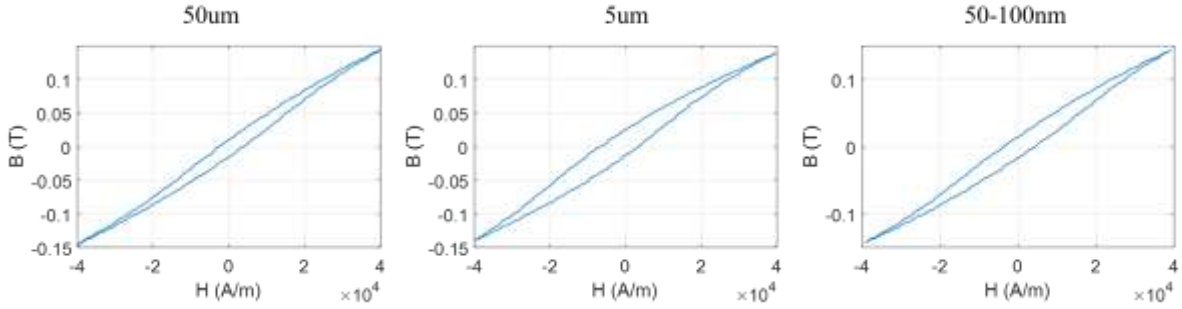

Figure 3-19 Hysteresis curves of 30% vol. Fe_3O_4@ABS composites with the size of 50 µm, 5 µm and 50-100 nm (from top to bottom) measured at a frequency of 1 Hz with voltage excitation of 20V.

Density energy of 30% vol. Fe_3O_4@ABS composites with the size of 50 μm, 5 μm and 50-100 nm have been measured at a frequency of 1 Hz with three different voltage excitation of 20V, 100V and 310V. Figure 3-20 shows the density energy of 1 period hysteresis cycle for these 3 type size Fe_3O_4 @ABS- composites, calculate by integrating the B-H curve. Regardless of the magnetic field amplitude, the 5um size particle composite has the highest density energy.

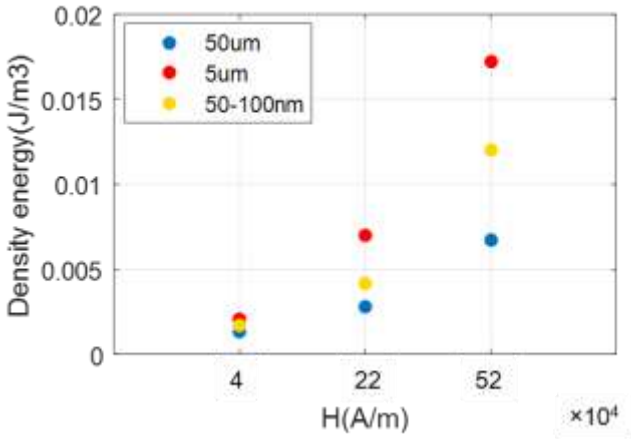

Figure 3-20 Density energy-versus-magnetic field amplitude of Fe_3O_4@ABS composites with particle size of 50 μm, 5 μm and 50-100 nm.

The IH mechanism of magnetic composites could find the answer from behavior of ferromagnetic particles whose area of the hysteresis loop represents the heat generation of the material. Hysteresis properties including saturation magnetization (M_s), coercivity (H_c), and hysteresis loop area are often used as a measure of material's quality. It has been reported on [93][94] that with the increase of the particle size from nano-size to micro-size, the coercivity quickly rises until reaching a maximum value, then gradually decreases and finally falls to zero. Based on the behavior of H_c, it is possible to distinguish multi domain, single domain, and superparamagnetic regions. Typically, for iron oxide particles, the critical diameter of being single domain is approximately 10–20nm [95]. In case of less than 10nm particles, the averaged magnetization is closed to zero, and thus the Fe_3O_4 particle exhibits zero hysteresis/coercivity, which is commonly called superparamagnetism phenomenon [85]. The exact location of the transition from single domain to multiple domain of Fe_3O_4 depends on both size and shape. For Fe_3O_4 particles, the theoretical critical diameter was reported variously from particle morphology. For instance, it was found to be 128nm for the spherical shape and more than 160nm for the cubic shape [96][97]. Considering our experimental results, the coercivity as a function of particle size for Fe_3O_4 particles could be predicted as Figure 3-21. When the magnetic size is larger than 100nm, generation of the eddy currents in the particles is responsible for heat generation. For multi-domain magnetic particles, the heating is mainly due to hysteresis loss. Larger particles have a number of sub-domains with well-defined magnetization direction. When such particles are exposed to the alternative magnetic field, the domain with the magnetization direction along the magnetic field axis grows and the others

shrink. This phenomenon is called domain wall displacement. When the size of particle decreases to single-domain regime, generation of heat due to hysteresis loss is not possible since there are no domain walls, and thus the domain wall displacement is not possible. Even then, these nano particles (NPs) cans produce heat under the influence of the alternating magnetic field [98], but with very high frequency (i.e. around hundreds of kHz to few MHz). The generation of heat by single domain NPs under high dynamic is due to relaxation loss, which is based on two distinct mechanisms, i.e. Néel relaxation and Brownian relaxation [99].

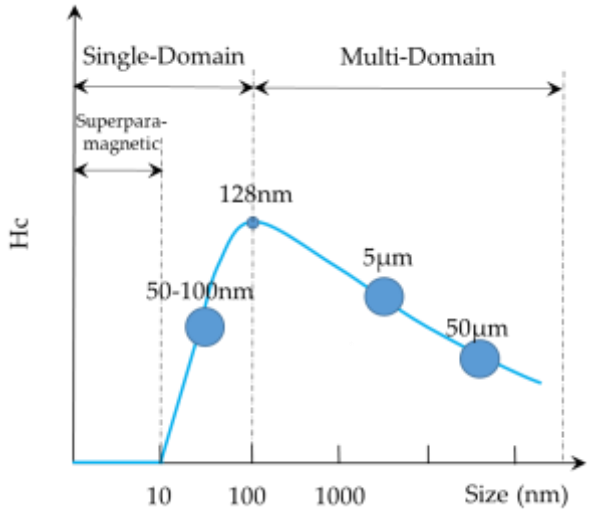

Figure 3-21 Coercivity dependence of magnetic particle size.

In this research, the particle size was chosen equal 5 μm to achieve the best trade-off among material dispersion, mechanical property, and magnetic response of composite. Actually, too small size of particles like nano-scale can lead to critical dispersion when elaborating polymer solution with magnetic powder, particular in case of high filler content (e.g., greater than 20% volume). Therefore, nanoparticles are generally used in fabrication of low particle content. On the other hand, too big particle size can make composite more rigid and fragile, leading to significant change in mechanical behavior of the whole sample. Furthermore, according to the magnetic point of view shown in Figure 3-21, using of particle's size greater than 100 nm allows to create multi-domain wall movement, improving hysteresis loss and thus heating energy. Indeed, single domain NPs can induce heat by another loss mechanisms (Néel and Brownian relaxations) by which the magnetization of magnetic nanoparticles can relax back to their equilibrium position after the application of magnetic field is removed. As a result, single domain NPs have large specific absorption rates and possibly produce heat under low magnetic field amplitude, but very high frequency is needed to favor relaxation losses. Contrarily, multi-domain particles requires larger field amplitude for extensive heating, but can be heated under much lower dynamic. In this study, we focus only on low frequency IH effect of around few kHz. Therefore, the use of magnetic particles at the order of few μm is more adequate to facilitate hysteresis losses caused by multi-domain wall movement.

3.4.3 Composite geometry

3.4.3.1 Thickness effect

In this study, composites with the same rectangular surfaces (60 × 14 mm²) but different thicknesses from 0.3 mm to 4.0 mm are performed. Figure 3-22 (a) shows the temperature evolution versus time of these samples doped with 30% vol. Fe_3O_4. As expected, the temperature change is moderate for the thin composite film (0.3 mm), where only a 10 °C increase has been recorded. In contrast, samples with 3 mm or 4 mm thickness have a much thicker temperature variation, showing that the IH effect strongly depends on the material's volume (or thickness). Considering that the magnetic power density of a given composite is constant (see Figure 3-22(b)), an increase in volume leads to enhanced heating power, and the temperature as well. This result was highlighted based on the increasing trend between the temperature and the sample's thickness, as displayed on Figure 3-22(b). However, a higher volume (or thickness) can result in an increase in the response time, which is one of the critical parameters that should be minimized to meet the medical requirements [40].

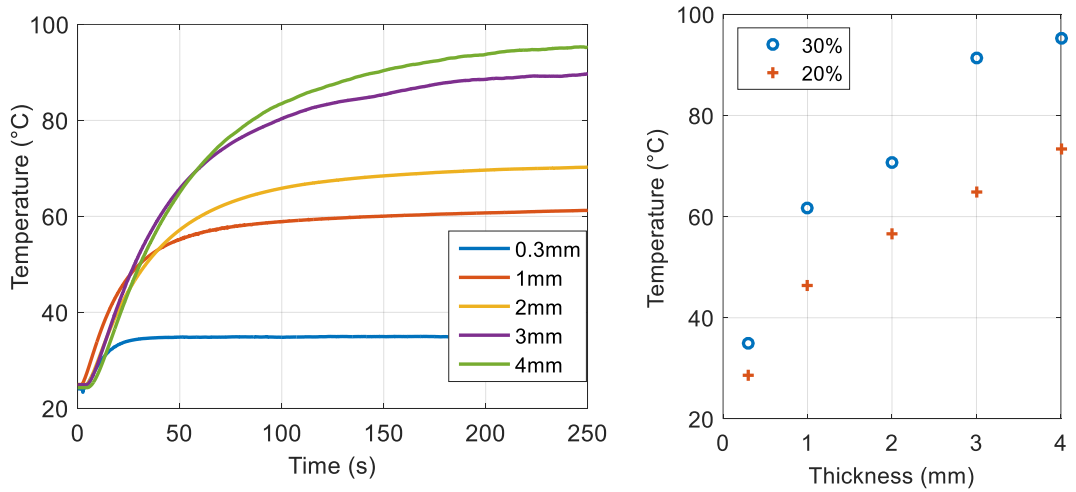

(a) (b)

Figure 3-22. (a) Temperature versus time of 30% vol. Fe_3O_4 composites with different thicknesses. (b) Maximum temperature of the 20% vol. and 30% vol. samples as a function of thickness for the 8-magnet sources.

3.4.3.2 Shape effect

This subsection aims to show that LFIH can be influenced by the shape of the material. To compare with the rectangular-shaped composites used above, the big (40×3.1×3.2 mm³) and small (27×2.5×3.2 mm³) needle-shaped composites elaborated with 25% vol. and 30% vol. Fe_3O_4particles are performed. Test are carried out using two inductors to generate the magnetic field (8-magnets and 16-magnets), again, demonstrating high benefit of being subjected to superior magnetic frequency.

Figure 3-23 shows the temperature evolution for the two needle samples powered by two types of inductors. Besides the frequency excitation and the particle content, the temperature variation of a ferromagnetic composite depends on the shape and the volume of the sample. Actually, the comparison between the two needle samples allows to conclude that the higher the volume, the higher the heating temperature. Furthermore, the results shown in Figure 3-22 and Figure 3-23 reveals that with the same fraction (30% vol.) and the same magnetic field frequency (2300kHz), the rectangular shape leads to superior IH response than the needle shape. Considering these two samples have similar thickness (~ 3mm), the rectangular reaches a temperature of 90°C, which is twofold higher than the one of the big needle. This implies that the surface of the sample exposed to the magnetic field has strong effect to the IH mechanism.

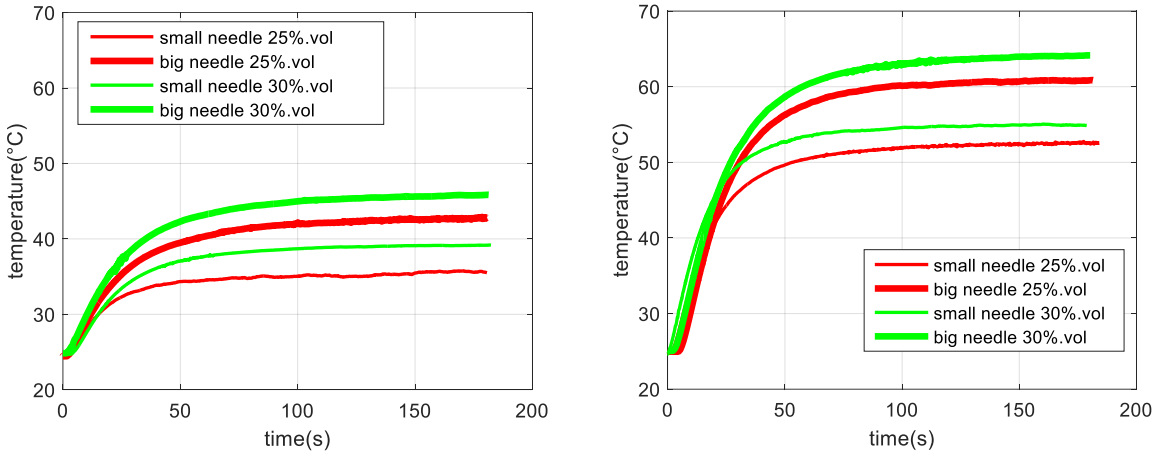

Figure 3-23 Temperature versus time for needle composites filled with 25% vol. and 30% vol. Fe_3O_4using an (a) 8-magnet inductor and a (b) 16-magnet inductor.

For better analysis a set of relevant parameters including fraction content, frequency excitation, and sample's volume, Tableau 3-1 summarizes the temperature change (ΔT), where $\Delta T = T_{final} - T_{ambiant}$ based on the results of Figure 3-23. Interestingly, the 16-magnet inductor leads to a two-fold higher value of ΔT versus the 8-magnet one, which is coherent with the improvement in the 1.8-fold in frequency of the applied magnetic field. As expected, the 30% samples give a higher ΔT with respect to the 25% where the temperature ratio between these two cases reaches approximately 1.2. This value perfectly matches the proportion of the composite fraction (i.e., equal to 30 divided by 25). This result again demonstrates the linear relationship between the temperature variation as a function of the particle content (see also Figure 3-27).

Tableau 3-1 Temperature change (ΔT) of the big and small needles doped with 25% and 30% iron oxide based two different magnetic sources.

	8-Magnet Inductor		16-Magnet Inductor	
Big Needle	18 °C	21 °C	35 °C	40 °C
Small Need	11 °C	14 °C	25 °C	30 °C

Finally, the volume of the big needle is 1.8 time higher than the small needle's volume. This leads to a 1.8-fold increase in ΔT because the magnetic heat power (MHP) described in Figure 3-27 is considered to be dependent merely on the excitation frequency, the nature, and the content of the magnetic particles, but not on the geometry of composite. The experimental results showed a ratio of ΔT of around 1.4 to 1.6 times, which is lower than the expected theoretical value. This is likely due to a higher surface exchange with air of the bigger needle. This exchange leads to heat dissipation, resulting in slightly lower temperature.

3.4.4 Particle nature

In order to better justify the choice of iron oxide, we compared the results with other magnetic particles, such as Ni and MnZn. These two materials are commonly used for inductor components due to their low cost, commercial availability, and high magnetic properties. The samples here are composites in rectangular shape (60 × 14 × 4 mm, Figure 2-2(a)). Figure 3-24(a) displays the temperature evolution over 250 s for different composites of 30% vol. Fe_3O_4; 30% vol. Mn-Zinc; and 10% vol., 23% vol., and 40% vol. Ni. The results confirmed that the iron oxide material—thanks to its important hysteresis area—leads to the best temperature response with respect to the Ni and Mn Zinc. Indeed, the higher magnetic properties of the Fe_3O_4 allow it to efficiently drive magnetic flux inside the particles, thereby allowing for a significant increase in the induction heating effect. Figure 3-24(b) shows the density heat power under a magnetic field of 160 kA/m amplitude and 2300 Hz frequency estimated based on COMSOL. This result has a maximum value for the composite filled with 30% vol.Fe_3O_4; i.e., corresponding to 2.4 MW/m^3 as opposed to 1.7 MW/m^3 for the 30% vol. Mn Zinc and 0.7 MW/m^3 for the 40% vol. Ni. More details about the thermal transfer via COMSOL modeling will be described in the following section 3.5.

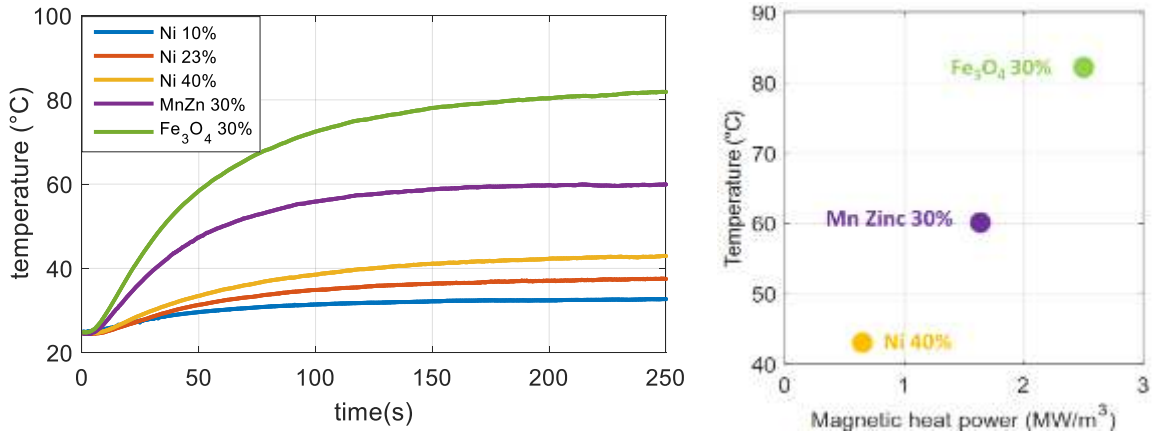

(a) (b)

Figure 3-24 (a) Temperature versus time for composites filled with different types of ferromagnetic particles. (b) Temperature in terms of modeled magnetic heat power for Fe_3O_4, Ni, and Mn Zinc composites at a magnetic field of 160 kA/m amplitude and 2300 Hz frequency.

Tableau 3-2 provides the properties of ABS based composites with 30% vol. magnetic particles. These data have been verified by experimental results and/or theoretical models. For thermal properties, the higher the specific heat capacity of the material, the more energy can be stored with a given temperature difference. 30% vol. Mn-Zinc composite has the highest heat capacity, however, it also owns a highest thermal conductivity. Materials with a high thermal conductivity can effectively transfer heat and readily exchange heat with their environment. 30% vol. Fe_3O_4 composite has the highest relative permeability and density energy for 1 period hysteresis cycle. Mn-Zic composite has a relative permeability slightly lower than Nickel composite but the density permeability is approximately double times than Nickel composite. The hysteresis behavior of these magnetic composites have been investigated in subsection 2.5. The properties discussed here can have an effect to the temperature variation of composites.

Tableau 3-2 Resume of other ABS based magnetic composites' properties

	30% vol. Fe_3O_4@ABS	30% vol. Nikel@ABS	30% vol. Mn-Zinc
Thermal conductivity (W/mK)	0.344	0.389	0.454
Specific heat capacity (J/kgK)	825.8	819.0	1229.7
Relative permeability μ_r	2.8602	2.6755	2.5138
Density energy (J/m^3)	2.10e-3	4.47e-4	8.42e-4

3.5 Thermal transfer based Comsol model

3.5.1 Macro-scale simulation

For a deeper analysis of the pertinent parameters affecting the thermal behavior of the ferromagnetic composite, this subsection investigates the finite element modeling-based Comsol Multiphysics simulation. The imaging result from the thermal camera of Figure 3-11 (b) revealed that the thermal transfer phenomenon could be considered to be symmetric with respect to the center of the sample. In other words, it can be assumed that both sides of the composite were driven by two identical heat sources, as displayed in Figure 3-25, for the different particle fraction of 3% vol., 10% vol., and 17vol. %. Before investigating each pixel

region at a microscopic scale, the whole homogeneous sample with radiation and air convection surfaces were simulated to obtain the average magnetic heating power (MHP) and temperature distribution in the length direction of the sample. The MHP value of the heat source at both sides was estimated by fitting the theoretical average temperature distribution to the experimental temperature measurements at the hottest area of the sample. Indeed, the MHP of the 17% vol. sample was equal to 1.3×10^6 W.m^{-3}, which was determined by parameter scanning until the average surface temperature at both sides approximately equals 65°C, as detected by the thermal camera (rf. Figure 3-9 (a)).

The result in Figure 3-26 highlights the excellent agreement between the theoretical and the empirical temperatures at the center, as well as at the heating zone on both sides, achieved for the polymer doped with 17% vol. of Fe_3O_4powder. It allows to confirm the high reliability of the proposed simulation model together with the calculation of the MHP. A similar behavior was obtained with the 3% vol. and 10% vol. samples.

The thermal radiation effect of the surface was taken into account, where the emissivity ε is equivalent to 0.9. The heat transfer coefficient of convection in the air was maintained equal to 20 W.m^{-2}.K^{-1}[100]. The specific heat capacity (C_p) of a composite can be fitted by Equation 2-12, by considering that C_p of the ABS polymer and the Fe_3O_4 particles are ~ 1800 J.kg^{-1}.K^{-1} and 450 J.kg^{-1}.K^{-1}, respectively. Accordingly, the C_p coefficient decreases with the increasing magnetic fraction in the polymer while the thermal conductivity show an increase trend. The thermal conductivity of the composite ($\lambda_{composite}$) can be obtained according to the Maxwell model (Equation 2-14), by using $\lambda_{polymer}$ = 0.2 W.m^{-1}.K^{-1} and λ_{Fe3O4} = 0.9 W.m^{-1}.K^{-1}. Tableau 3-3 summarizes the setting parameters used for the macroscopic composite model with different volume fractions. The material was subjected to a magnetic intensity of 160 kA/m at 2300 Hz (excited by the 8-magnets inductor) and at 4200 Hz (excited by the 16-magnets inductor). Surface emission ε, Specific heat Cp (J.kg^{-1}.K^{-1}), Thermal conductivity λ (W.m^{-1}.K^{-1}) and Transfer coefficient h (W.m^{-2}.K^{-1}) are the nature parameters of composite which only depend of the particle volume fraction and would not change with the frequency of excitation magnetic field. However, the excitation frequency significantly decide the MHP of composites. In Figure 3-27, two linear fitting lines display the MHP as function of particle volume fraction at 2300 and 4200Hz respectively. The higher the particle volume fraction, the larger the difference of MHP between excited at 2300 and 4200Hz magnetic field.

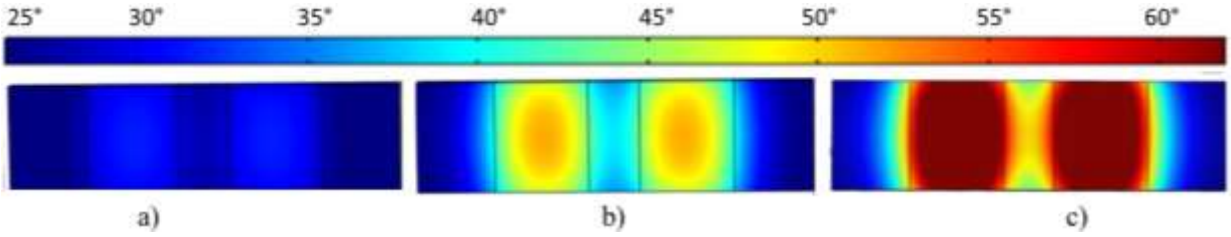

Figure 3-25. Spatial evolution of temperature for the macroscopic scale of the ferromagnetic composite with a) 3% vol. fraction, c) 10% vol. fraction and c) 17% vol. fraction under 2300Hz magnetic field excitaion

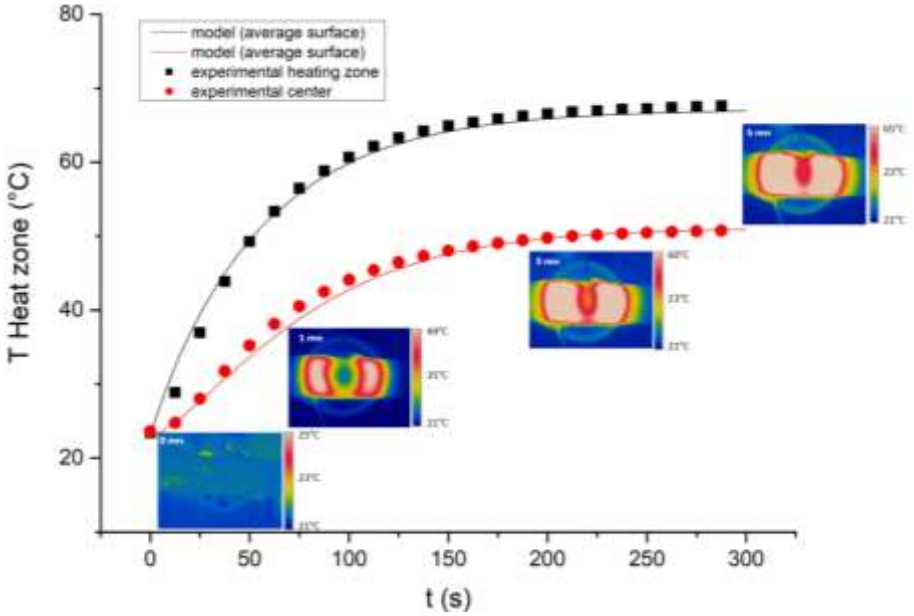

Figure 3-26. Theoretical and experimental temperatures as a function of time for the 17% vol.. fraction composite under 2300Hz magnetic field excitation.

Tableau 3-3 Simulation thermal parameters of the macroscopic composite model with different contents of the particle at magnetic field frequency of 2300Hz and 4200Hz.

	3% vol.	10% vol.	17% vol.	30% vol.
Surface emission ε	0.9	0.9	0.9	0.9
Specific heat Cp (J.kg–1.K–1)	1260	1040	900	744
Thermal conductivity λ ($W.m^{-1}.K^{-1}$)	0.32	0.36	0.4	0.54
Transfer coefficient h ($W.m^{-2}.K^{-1}$)	20	20	20	20
Heat power density P($W.m^{-3}$) – 2300Hz	0.2×10^6	0.7×10^6	1.3×10^6	2x 106
Heat power density P($W.m^{-3}$) – 4200Hz	0.4×10^6	1.05×10^6	1.8×10^6	3.7 x 106

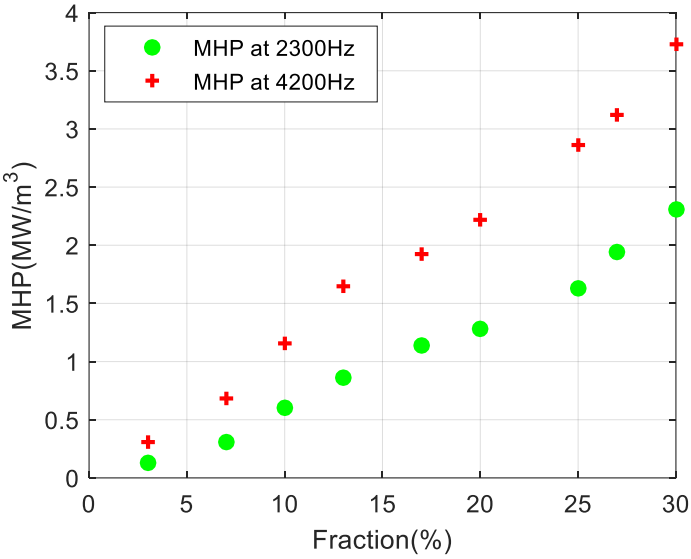

Figure 3-27 Magnetic heating power density of different partical volume fraction Fe3O4@ABS composites at excitation frequency of 2300, 4200Hz

3.5.2 Micro-scale simulation

To better understand the IH in a microscopic scale, Figure 3-28 illustrated the thermal transfer of ferromagnetic particles inside a polymer matrix with three different volume fraction of 3%, 10%, and 17%. Assuming that each particle behaved as a heat micro-source with a constant power density (MHP) whose value can be estimated based on the average surface temperature (which was determined previously in the macro model of Figure 3-25. Consequently, the temperature distribution in the scale of several microns can be mapped by the finite element modeling of thermal transmission and the theoretical estimation of the MHP. As expected in Figure 3-28, the sample with high volume fraction (i.e., 17%) possessed a very small inter-particle distance compared to the other, leading to a more regular induction heating effect and thus significantly increase temperature of the whole composite. On the other hand, in case of the composite with low magnetic content (i.e., 3%), the inter-particle distance is too important with respect to the particle size, thus thermal transfer among heat sources cannot be assumed to be homogenous, resulting in decrease temperature of the entire sample.

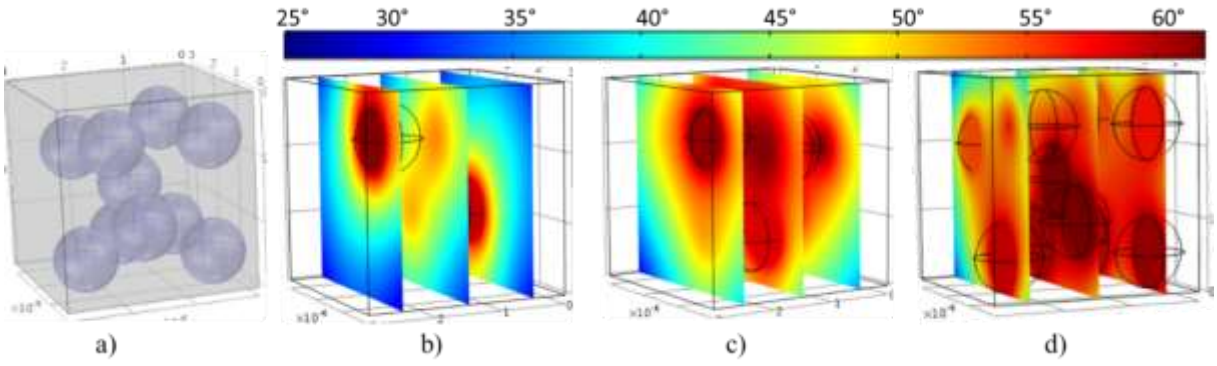

Figure 3-28. (a) Microscopic scale of the ferromagnetic composite. Heat transfer of particles with (b) 3% vol. fraction, (c) 10% vol. fraction, and (d) 17% vol. fraction.

Figure 3-29 (a) displays the simulating MHP driven by a ferromagnetic particle in a low-frequency excitation. A perfectly linear relationship between the MHP and the frequency was observed, confirming that the energy density corresponding to the hysteresis cycle of the particle is almost constant (around 20–25 $kJ.m^{-3}$) in such a frequency range. A similar behavior was also obtained in the case of homogenous composite where its MHP value linearly increases as a function of the frequency (Figure 3-29(b)).

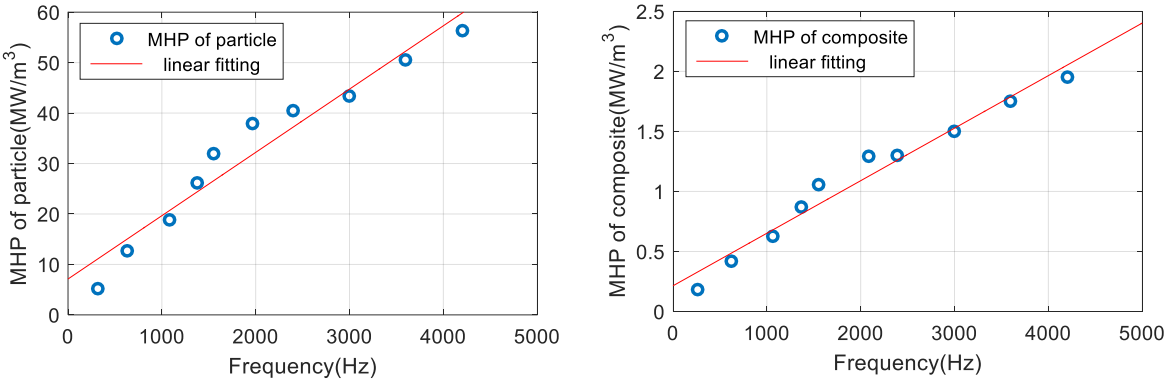

(a) (b)

Figure 3-29. Magnetic heat power (MHP) versus frequency (a) of Fe_3O_4 particle and (b) of composite doped with 17% vol.

3.5.3 Model enhancement

So far, with the experiment result of sections 3.3 and 3.4, it can be concluded that the current setup together with the proposed composite leads to an achievement of maximum temperature around 100°C within approximately 1 min. This result confirms the feasibility of heating the composite elaborated with magnetic particles through the use of a rotating magnetic excitation under somewhat low frequency. However, our system performance needed to be considerably improved to meet the medical requirement for varicose vein operation, where the temperature should rise to 100–120°C for a very short elapse time (usually less than 5 s) to avoid skin burns, hematoma, and nerve injury. Typically, the diameters of varicose veins vary widely due to diversities in individuals like the types of sick veins, the different location of the human body, etc. Diameters data of varicose veins stated in Refs [101][102][103] were collected from the records of several groups of patients. According to these data, we can assume that the maximum varicose veins are about 8 mm. The amount of energy necessary to obliterate the vein was empirically determined by [104], based on previous experience, to be a maximum of 80 J per linear centimeter for a duration not exceeding 4–5 s. Thus, the heating source should generate an average power of about 20 W.

According to our simulation result in Figure 3-29 (b), the equivalent MHP released by a 30% vol. composite under 4200 Hz frequency was equal to 3.7 W/cm^3. Consequently, to drive enough energy to destroy a 1 cm long vein, the necessary volume of the material is nearly 5 cm^3. This dimension, which is clearly too important compared to the vein's diameter and the incision's size of minimally-invasive procedure, seems to be unrealizable in practice. Another option is to enhance the composite's MHP by increasing its magnetic fraction and/or the alternating frequency of the magnetic source. The following simulation provided a deeper analysis of these relevant parameters that strongly affect the induction heating behavior.

Figure 3-30 (a) illustrated the time evolution in temperature as a function of volume fraction under 2300 Hz magnetic intensity. As expected, the composite doped with 30% vol.fraction allowed us to boost the temperature to close to 100°C, compare to 17% vol. sample where only 65°C was achieved. Figure 3-30 (b) shows that the 30% vol. composite gives rise to a final temperature of 220°C at an input magnetic excitation of 7000 Hz, which is higher than the medical need. Obviously, the temperature can be drastically enhanced by increasing the particle fraction and frequency of the magnetic field. However, the filler content of the material should not be above 30–40% vol. to neither exceed the percolation threshold nor favor heterogeneity of the polymer matrix. As mentioned previously in subsection Chapter 1 the frequency of the magnetic field was controlled by a DC motor whose speed was limited to a few hundred kRPM.

Figure 3-31 (a) depicted the time evolution of the heating temperature with different sample thicknesses, from 0.2 to 3.2 mm. All composites were supposed to be filled with 30% vol. of Fe_3O_4 powder and were exposed to an alternating magnetic field of 7000 Hz and 160 kA/m amplitude. Interestingly, both final temperature value and its time constant increased as a function of the thickness. After the elapse of three time constants, which corresponds to a 95% change in state, the system is considered to practically achieve its final heating temperature. To get the heating temperature value from 100° to 120° (see Figure 3-31 (b)), the optimal thickness of the composite should be between 0.7 and 1.2 mm, leading to a response time of about 60 to 90 s (i.e., equivalent to the three-fold time constant). Therefore, by choosing an appropriate sample thickness, as well as improved fraction content and magnetic source frequency, it is possible to drastically speed up the temperature change. Other pertinent parameters could affect the heating time constant, and these should be effectively exploited in the next step of this work. For instance, larger volumic masse ρ and larger heat capacity (C_P) lead to slower changes in temperature, while a larger exchange surface area and better heat transfer (h) lead to faster temperature changes.

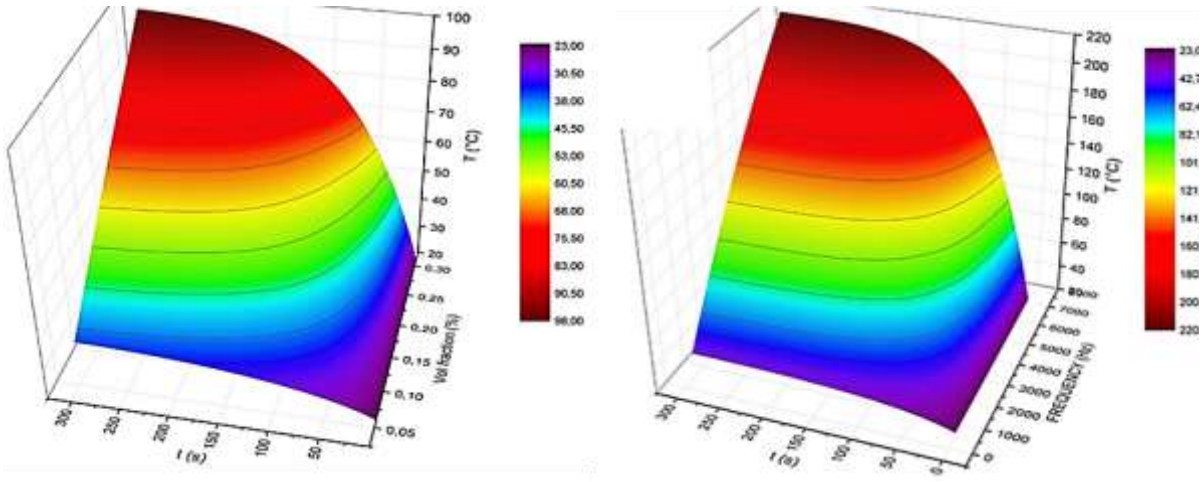

(a) (b)

Figure 3-30. Performance of induction heating in terms of (a) volume fraction and (b) frequency of the magnetic field.

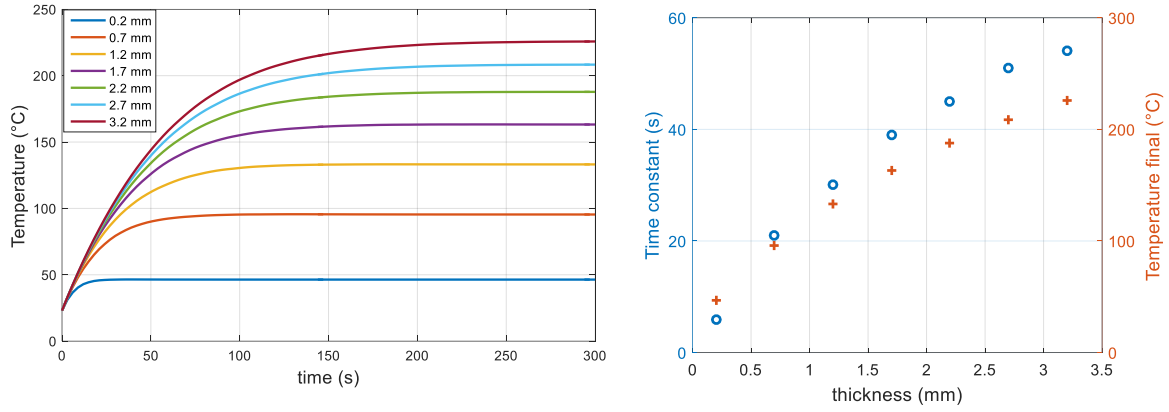

(a) (b)

Figure 3-31. (a) Time evolution of temperature with different sample thickness at optimal fraction and frequency of the magnetic field. (b) Time constant versus heating temperature for various thickness values.

Finally, further enhancement in terms of experimental setup, as well as material design, should be investigated. This work should aim to meet medical requirements so that varicose veins could be efficiently heated within a very short time.

3.6 Application towards varicose veins healing

Figure 3-32 (a) illustrates the working principal of ferromagnetic composite guide wire (FCGW) for endovenous thermal ablation (EVTA). This is an outpatient procedure and an alternative to surgical ligation and stripping for varicose veins. Here, magnetic excitation is applied through the patient's epidermis to deliver heat and seal off targeted blood vessels. The

development of such a concept for EVTA therapy offers many advantages to patients compared to the traditional surgery, such as a shortened recovery period, less pain, and no scarring. The procedure consists of three principal steps, as described on Figure 3-32 (a). First, after using ultrasound to map the course of the treated vein, the surgeon inserts the FCGW through a small incision into the diseased vein, threading it through the blood vessel into the groin area. Second, a magnetic field is delivered to a target element heating and contracting the collagen within the walls of the vein until they shrink and disappear. The vein is thus treated in segments as the FCGW is gradually inched back down towards the incision. Finally, when the entire vein has been ablated, the blood flow is automatically rerouted through healthier adjacent veins, restoring healthy circulation and reducing swelling. The ablated vein becomes scar tissue and is absorbed by the body [105]. Figure 3-32 (b) shows the guide wire design where the tip is made up of ferromagnetic-composite-based Fe_3O_4 particles embedded in a thermoplastic ABS matrix.

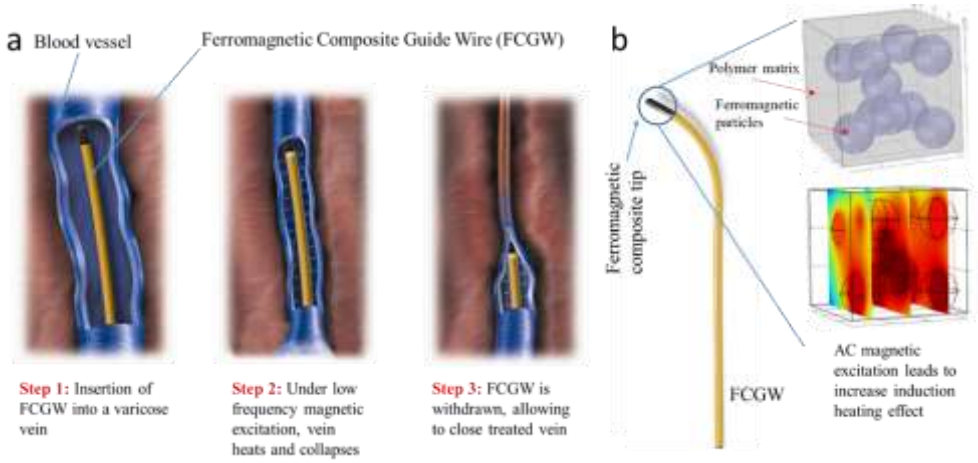

Figure 3-32 Working principal of ferromagnetic composite guide wire (FCGW) for varicose vein treatment. (a) Three principal steps in the procedure; (b) FCGW-design-based Fe_3O_4composite.

In order to integrate them with medical tools, the ferromagnetic devices were elaborated into a needle-like shape (Figure 2-2(d)). Two kinds of samples with identical thicknesses (3.2 mm) but different surface exposures to magnetic sources were selected to better analyze the LFIH performance in terms of the material's geometry. The selected dimensions of these two samples are adaptable to varicose vein diameters (4 and 5 mm).

Figure 3-33 illustrates thermal camera imaging (in both colored and black and white resolutions) of the big needle doped with 30% ferromagnetic particles—these panels were powered by the 8- and the 16-magnet inductors, respectively. The target temperature of the composite was 46 °C under an AC magnetic field of 160 kA/m amplitude and 2300 Hz frequency via the 8-magnet source. The same magnetic strength with higher applied frequency (4200 Hz) was delivered from the 16-magnet. A significant increase in temperature was recorded of 65 °C.

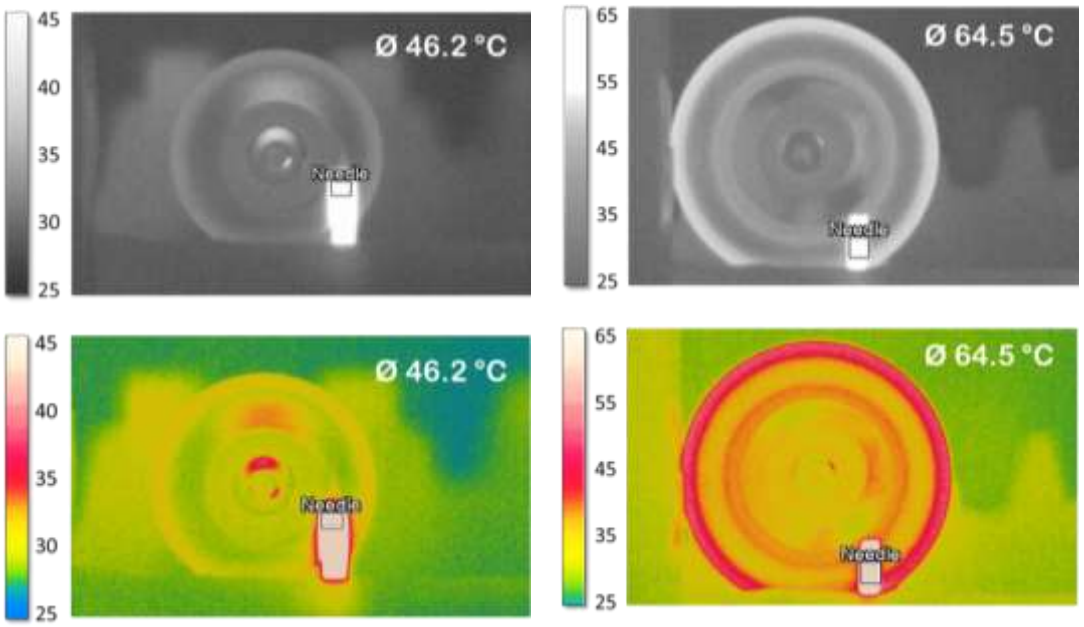

(a) (b)

Figure 3-33 LFIH observation based thermal camera for big needle composite filled with 30% vol. Fe_3O_4 particles using (**a**) the 8-magnet inductor, and (**b**) the 16-magnet inductor.

Figure 3-34 shows the spatial evolution temperature of these two samples incorporated with 30% vol. Fe_3O_4excited by the 8- and 16-magnet inductors, respectively. Both needle-shaped composites have analog thermal transfer profiles where the temperature at the center close to the permanent magnet reached a maximum value and gradually decreased towards both sides further from the center. As expected, the 16-magnet inductor leads to a higher heating temperature than the 8-magnet system. Similar behavior has been obtained for the other samples doped with different Fe_3O_4 contents. Figure 3-35 described the simulation and experimental temperatures of the big needle composites driven under 2300 Hz and 4200 Hz AC magnetic power. The same trend was recorded in the case of the small needle. Excellent agreement between the theoretical and the empirical temperatures has been achieved, reflecting high reliability of the proposed thermal transfer model together with an estimation of the magnetic heat power (MHP) that is quasi-linear to the excitation frequency as well as the magnetic fraction of the fabricated material (Figure 3-29(b)).

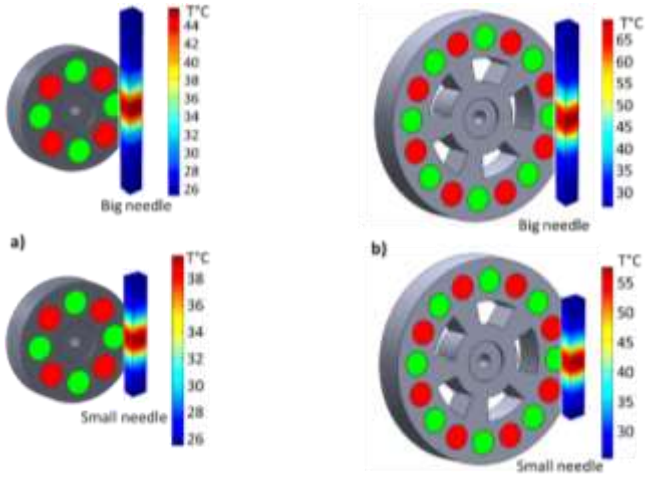

Figure 3-34 Spatial temperature evolution of two needle composites filled with 30% vol. iron oxide using (**a**) an 8-magnet inductor and (**b**) a 16-magnet inductor.

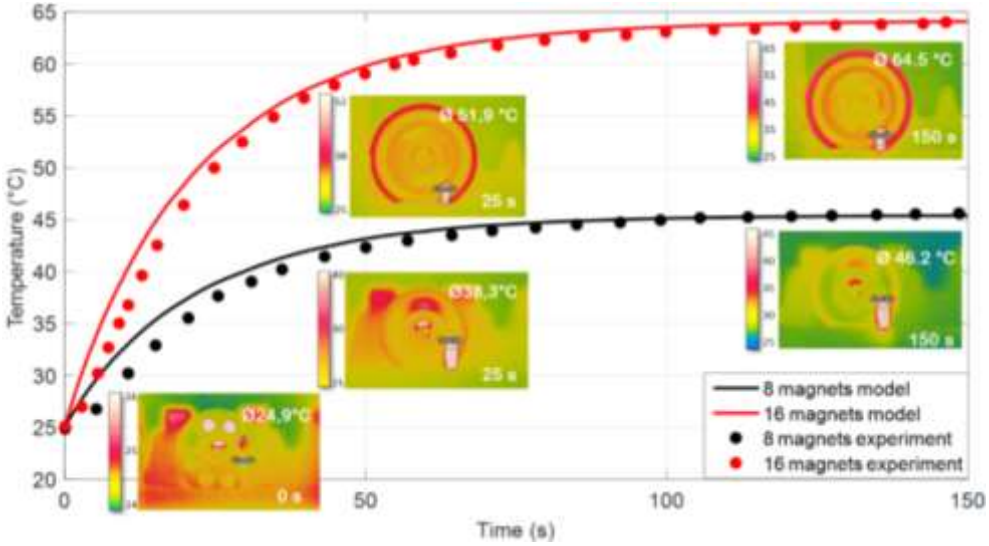

Figure 3-35 Theoretical and experimental temperatures as a function of time for the big needled composites filled with 30% vol. Fe_3O_4excited by two different inductors.

3.7 Summary

This chapter provided a complete analysis on various pertinent parameters that were strongly involved in the LFIH mechanism. For instance, to significantly improve the heating efficiency, the AC magnetic excitation (amplitude and frequency) as well as the Fe_3O_4fraction should be taken into consideration. Experimental and simulation results showed the feasibility of inductively heating the ferromagnetic composite to 100 °C, which is closed to the target temperature imposed by the venous insufficiency procedure. It has been highlighted that the heating effect not only depends on the magnetic excitation and the material fraction, but also on the nature and size of particles, as well as the dimensions of the composite. To fit with medical tools, the ferromagnetic devices were elaborated to a needle-like shape, and great IH improvement was achieved by doubling the number of permanent magnets of inductor. With

the aim of boosting IH performance to fulfill specific requirements of thermal endovenous treatments, the next chapter will investigate on optimization of the material process.

Chapter 4
High Performance Anisotropic Ferromagnetic Composites

As described in the previous section of these manuscript, it seems possible to reach a temperature high enough to achieve varicose veins healing by LFIH of catheters made out of bio compatible magnetic composites. Even if the first results look promising, it is clear that an optimized procedure has to be set up to achieve significant improvements of the current performances. For this, many techniques have been explored. All based on the optimization of factors including the fraction content, the nature, the size, and particles shape. In this chapter, an alternative solution will be proposed. This solution involves to process the ferromagnetic composite under the influence of a constant homogeneous magnetic field, leading to a strong anisotropic behavior coming from particle alignments. Experimental results demonstrate that, by exciting the resulting anisotropic composite along the alignment direction, an enhanced LFIH effect of more than 30% can be observed. Improvements can be noticed in the perpendicular direction as well, meaning that the structured distribution is enough to increase the ferromagnetic properties. Finally, if the composite is flexible, it can be easily used in the medical applications we are targeting (e.g., endovenous thermal catheter, electromagnetic tracking system …)

4.1 Literature review

4.1.1 Anisotropic ferromagnetic composite

Magnetic particles can be incorporated into a polymer body either randomly or in an ordered structure (Figure 4-1). If a uniform magnetic field is applied to the reactive mixture during the curing process, particle chains are formed and get locked into the polymer, leading to anisotropic properties of the resulting composites. These anisotropic properties create preferential directions where the physical properties are magnified. Studying the effect of spatial orientation and position distribution of the inclusions (e.g., ferromagnetic particles, ferromagnetic fibers, etc.) inside the polymer matrix is of real interest. A structured distribution of the magnetic particles can be obtained by processing and curing the composite in the presence of an extern magnetic field (i.e. called magnetophoresis). This leads to particle chain structures formation and to a composite with strong anisotropic properties.

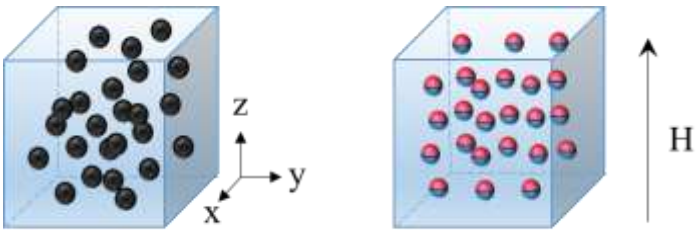

Figure 4-1 Schematic representation of particles: (a) randomly distribution; (b) structured particle distribution

Researchers have demonstrated that the orientation and the distribution of the inclusions in a polymer matrix are strongly dependent on their electromagnetic properties such as the relative permeability, the magneto-mechanical coupling [106][80], and so on [107][108]. An improvement of the mechanical properties (stiffness, Young modulus, etc.) has been observed via magnetophoresis [109]. In [12], the particle chains observed in the composite allow giant deformational effects, high elasticity, anisotropic elastic and swelling properties. .In [110]-[111], authors conclude that compared to non-aligned, aligned specimens present enhanced heating efficiency and increased specific loss power value. Therefore, it is necessary to study the orientation of particles for the low-frequency induction heating effect. The quick responses to the magnetic fields open new opportunities in various applications especially in medical field [112]–[114].

4.1.2 Percolation threshold

In [115], the simulation of the magnetic particle arrangement under an external magnetic field in polymer-based composites has been done. The results indicate that the alignment of the resulting chains is getting poorer with an increase of the particle concentration.

Figure 4-2 shows that magnetic ferrite particles are driven by the magnetic field (0.2 T) to form chain-like structures in liquid epoxy resin [115]. Particles are moving and form short chains first, then these short chains merge together and tend to align to the field direction. In the composites, when the particle volume fraction is below 20% or above 40%., the directionality becomes less apparent (Figure 4-2). Short chains in low-filled composites are oriented directly parallel to the applied magnetic field. For the high-filled composites, the chains tend to form directly a network-like structure, consequence of the small distances separating the particles.

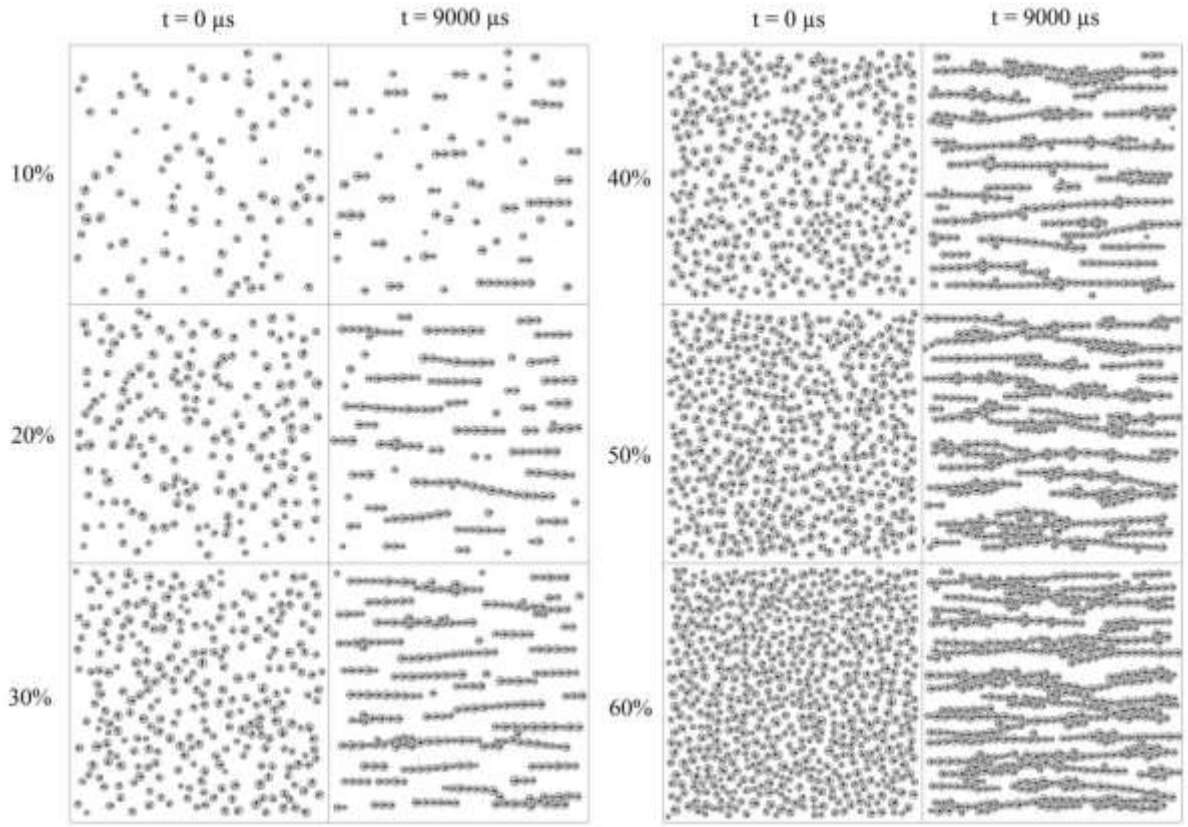

Figure 4-2 Simulation images of magnetic particle arrangement obtained by magnetophoresis of 0.2 T amplitude along the horizontal direction [115].

Figure 4-3 shows simulation results obtained for 40% volume fraction particle composite under different level of magnetophoresis. Chains are formed faster under higher magnetic fields. Finally, after 2400 us, the particles' arrangement is almost the same and this whatever the amplitude of the magnetic field.

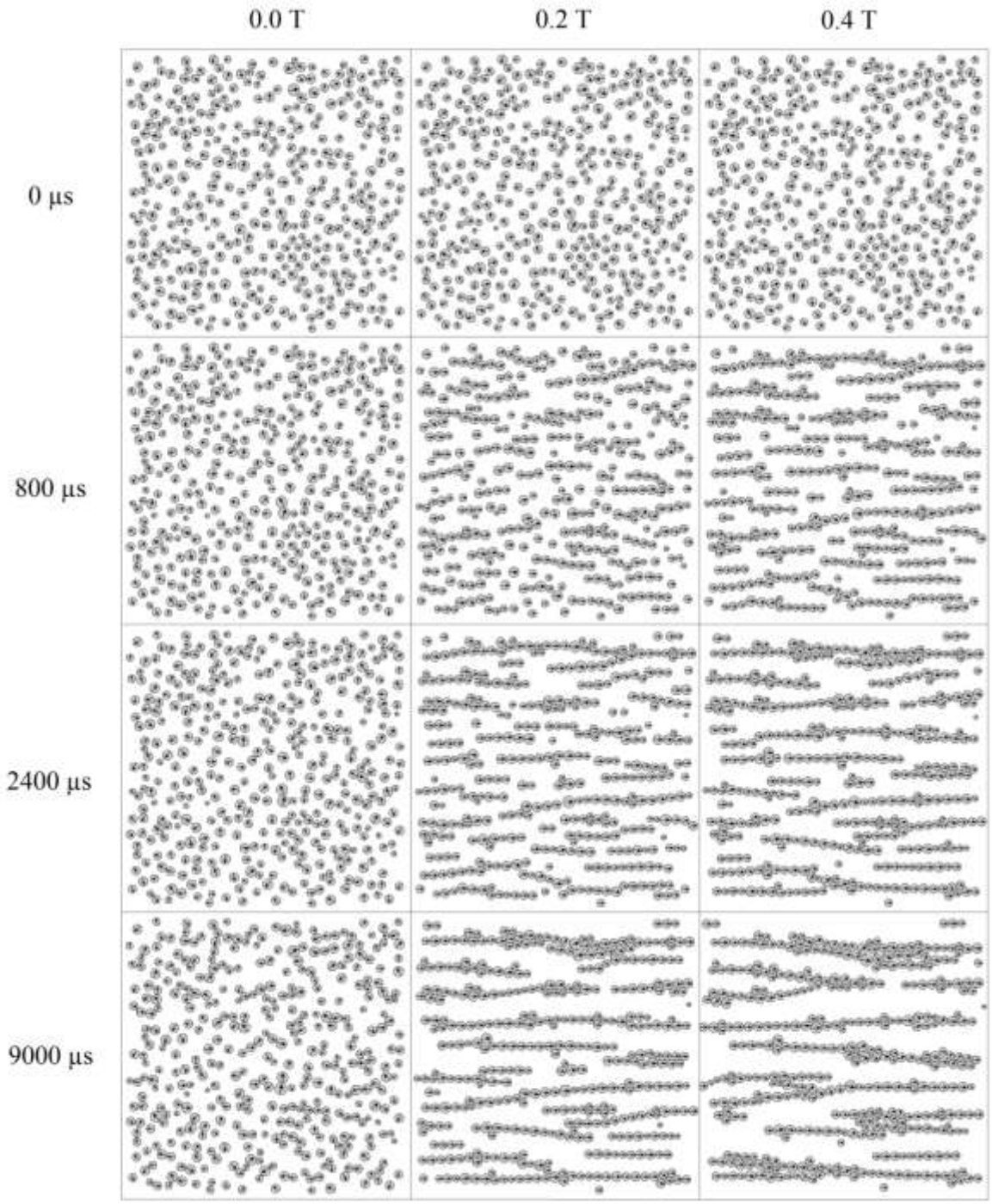

Figure 4-3 Simulation images of random and aligned composites filled with 40% of ferrite particles. Magnetophoresis is performed in the horizontal direction [115].

According to the above explanation, to obtain an anisotropic magnetic behavior, the particle volume fraction has to be limited below 40% volume fraction. In the literature, magnetic fields of different amplitude are used (ranging from 0.02T to 0.8T) to create particle chains during the composites fabrication process, the strength mainly depending on the uncured polymer material's viscosity.

4.1.3 Processing methods

Alignments in ferromagnetic particle chains can be obtained via magnetophoresis during the printing or the curing processes. According to the scientific literature, different methods have already been tested to apply a stable and homogeneous magnetic field to the composite during the fabrication process:

a) In [109], magnetorheological elastomer (MRE) samples are cured in a disk-shaped mold placed in the center of a coil (Figure 4-4-a), generating an 800 mT magnetic field. The temperature is maintained roughly equal to 150 °C for approximately 15 minutes. Cylindrical samples are cut from the original disk using standard water jet cutting technology. Clear formation of particle chain structures inside the MRE samples were observed, such as strong anisotropic properties.

b) A pair of electromagnets (Figure 4-4-b) is employed to provide a uniform DC magnetic field B = 400 mT in [12]. A mixture made out of iron oxide particles (Fe3O4) and poly(dimethylsiloxane) composites (PDMS) is poured into a cubic shape mold. The mold is positioned between two electromagnets during the cross-linking polymerization process. Particle chains are clearly observed and strongly reflected in the anisotropic properties of the resulting samples.

c) In [116], authors slowly move a permanent magnet (Figure 4-4-c), with the main-field axis in the perpendicular direction of the substrate surface. These movements immediately occur after the dispersion drop, and they induce formations of defect-free superlattices with a very high degree of orientation order. The magnetic field strength is tuned by varying the permanent magnet's position.

d) A set of 3 inches diameter Helmholtz coil (Figure 4-4-d) is used in [70] to provide a perfectly-known magnetic field. Its direction is set thanks to a rotating controlled platform. Dry Ni nanowires are mixed with uncured PDMS (Sylgard 184, Dow Corning) by stirring and ultra-sonication processes. Once the vacuum is degassed done, the mixture is placed between the two Helmholtz coils to align the nanowires. The cured composite is cut to get cubic samples. According to the authors, the magnetic alignment provides highly effective improvements to the nano-composites ferromagnetic properties.

e) Researchers in [117] built composites using 3D-printing technology. Particles' direction and orientation are arranged during the printing process (Figure 4-4-e). An electromagnet is placed around the dispensing nozzle to apply the magnetic field. The printing polymer (silicone rubber matrix) contains NdFeB particles and fumed silica nanoparticles. Once the printing process is completed, the printed structure is cured at 120 °C for 1 h. Eventually, the authors successfully 3D-print complex ferromagnetic volumes, including particles alignment.

f) Finally, it is explained in [118] that the magnetic field strength is not the only parameter influencing the alignment of the particles. The particles' magnetic properties, their geometries, their shapes, the filling density have to be considered as well. Simulations are provided to corroborate the experimental observations. The increase of the filling density leads to a sharp decrease in the magnetic alignments, mostly due to the mechanical friction forces. Improvements can be obtained by the addition of a lubricant.

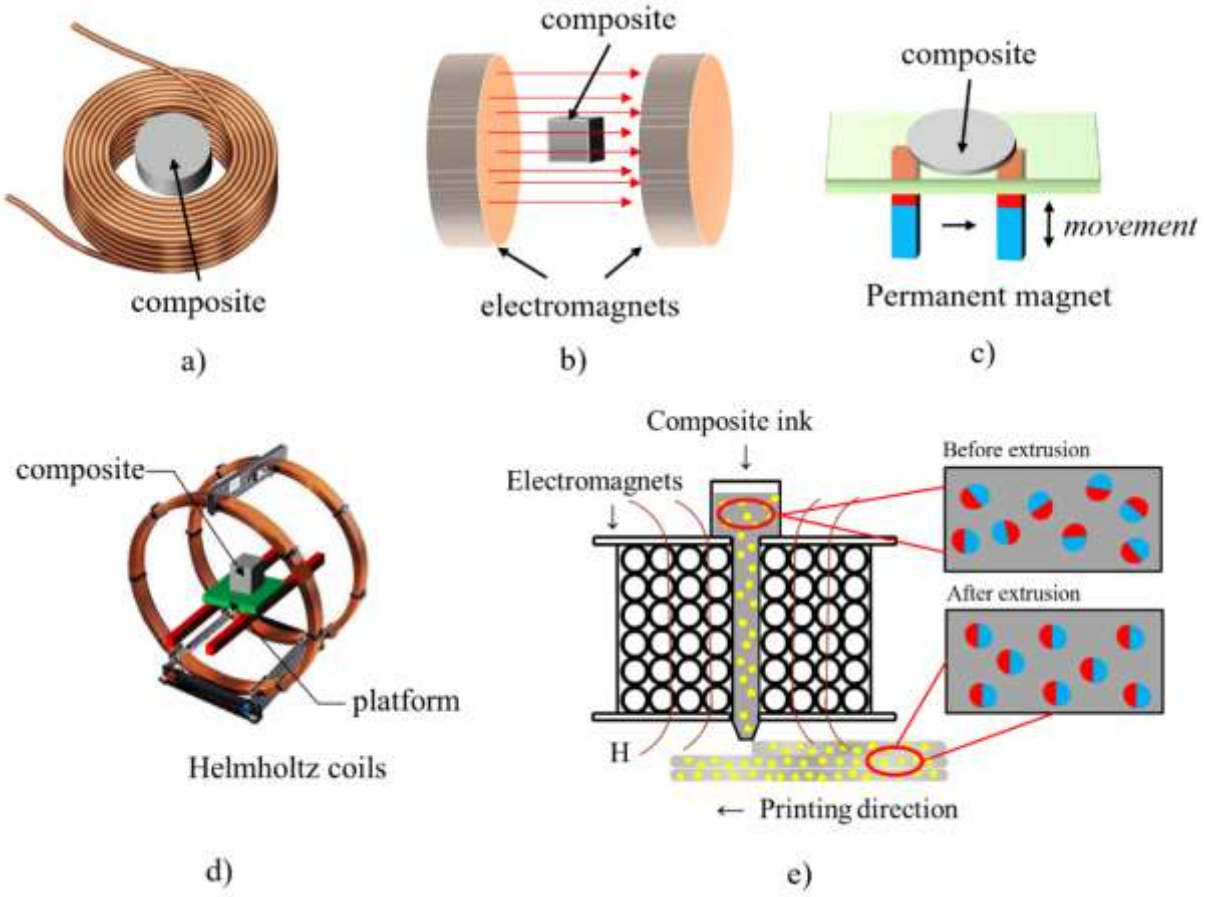

Figure 4-4. Illustration of the different methods proposed in the literature to provide a stable magnetic field during the curing step.

Figure 4-4 gives an overall 2D/3D illustration of all the solutions described above. All these solutions can be used to build our ferromagnetic composites. The solution we opted for is described in the following section, the selection criteria were basically: the simplicity and the homogeneity of the magnetic field in the sample area. Eventually, the constant magnetic field has to be easily tunable.

4.2 Fabrication process

4.2.1 Material selection

As described in subsection 1.5.2 - Matrix material, to observe some arrangements of the ferromagnetic particles inside the polymer matrix under the influence of an external magnetic field, the polymer must be quasi liquid with a limited viscosity. The polymer enables particle diffusion and alignment (even under low amplitude magnetic field) during the fabrication process, just before curing. The ideal polymer must be thermosetting and turn into a solid state once the process over. As detailed in [72] PDMS-based elastomers show a stretchable behavior under high temperature and a mechanical stability over a temperature range of -45 to 200°C. PDMS (SYLGARD™184 Silicone Elastomer) is the best option to be the polymer matrix for our anisotropic composites.

As we want to develop medical applications, biocompatible spherical powder (5 μm diameter) of Fe_3O_4 (SIGMA-ALDRICH) has been selected.

4.2.2 Material preparation

The fabrication of the ferromagnetic composite is based on a simple casting method. Fe_3O_4 spherical particles powder are mixed to the polymer based silicone elastomer. The stirring process is performed for 20 minutes. The particles are scattered in the solution by ultrasound treatment (Hielscher Ultrasonic Processor UP400S) with powerful impulsions during a few minutes in order to get a perfectly homogeneous distribution. The volume fraction of Fe_3O_4 tested, varies from 5% to 35% with a 5% increment. Additive encapsulants are added into the solution with a 1: 10 mass mix ratio and this under constant stirring. Due to both the Ultrasonic processing and the constant stirring, the resulting mixture contains air bubbles, a vacuum treatment performed is thus required subsequently to eliminate them. Afterwards, the solution is placed in a vacuum machine (Memmert V0 400 Vacuum) (<25 Pa, 25°C, for 20 minutes) until it reaches a full disappearance of the bubbles. The resulting mixture is poured into a cubic-shaped mold. Finally, the samples are cured in the oven (Memmert V0 400 drying oven) at 60°C for 4 hours. Figure 4-5 describes the whole fabrication process, which leads to relatively well balanced particle distribution and consequently isotropic ferromagnetic properties.

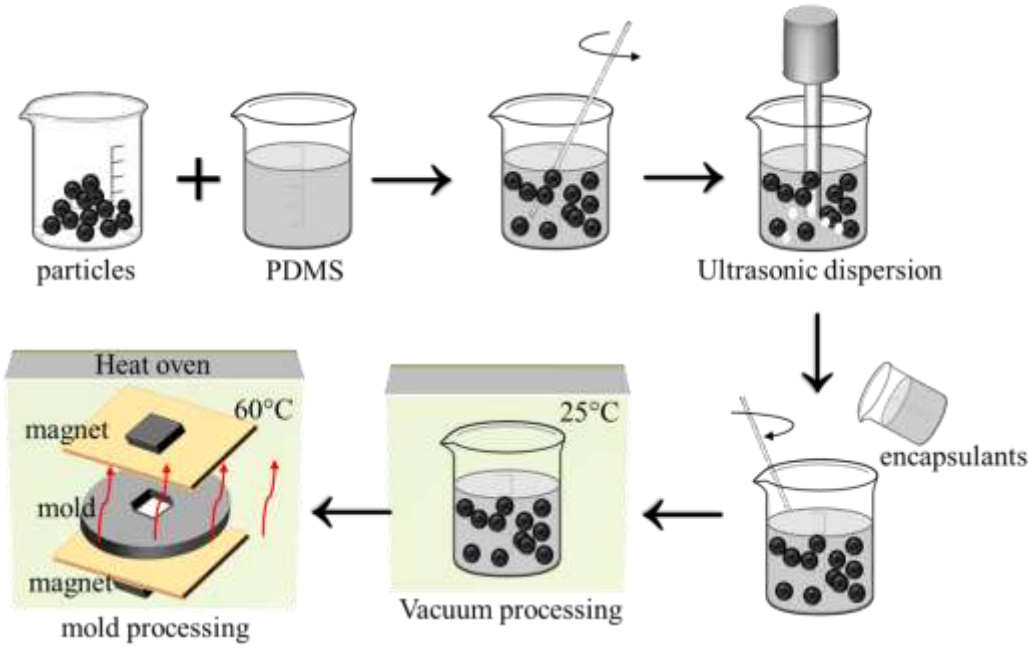

Figure 4-5 Fabrication process of anisotropic ferromagnetic composites

To create alignment and orders in the particle distribution, a 5×5×5 mm^3 cubic-shaped mold filled with the PDMS solution is placed between two strong permanent magnets as illustrated in Figure 4-6. A thin layer of Teflon is inserted between the magnet and the sample to facilitate the demolding step. During the cross-linking process, the whole set is put inside the oven at 60°C. Because of the strong magnetic field, particle chains are formed and remain locked into the elastomer (supposed along z-direction). The amplitude of the constant magnetic field submitted to the ferromagnetic composite is easily tunable by changing the mold's thickness (as described in Subsection Chapter 4.3.1).

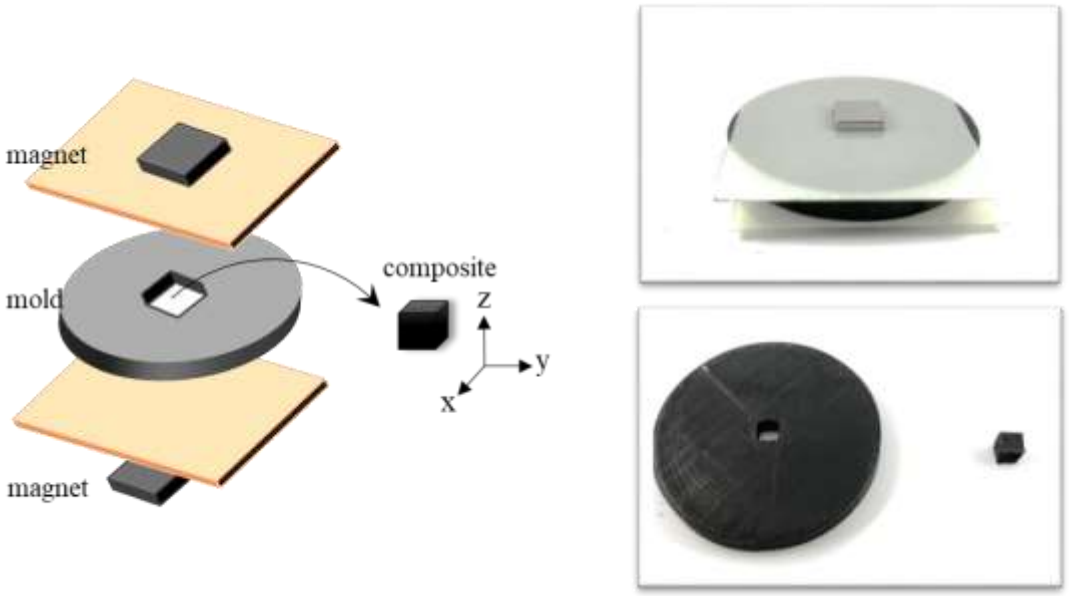

Figure 4-6. Overall 3D view and photos of both cubic mold and the cubic sample.

The above casting method makes it possible to fabricate composites of different shapes and dimensions by simply changing the 3D printed mold. In Chapter 4.3.1, cylinder shape (Ø15 mm) specimens are used for the characterization of the magnetic field excitation (distribution, amplitudes …). For the rest of this chapter cubic shape (5×5×5 mm^3) specimens are more adequate and will be used to characterize the anisotropic behavior in the three x, y and z axis

4.3 Characterization methods

4.3.1 Characterization of the magnetic excitation

The selected permanent magnets are 10×10×2 mm^3 (Q-10-10-02-N from @Supermagnete). According to the mold thickness, they can be spaced apart from 1 to 5mm. A combined approach including experimental and simulation results is used to check on the magnetic field amplitude and to confirm its relative homogeneous distribution in the sample area. A set of characterization from the high-precision tesla-meter (FW-Bell 5080) is carried out to establish the magnetic field distribution on the surface of the permanent magnet (Figure 4-7).

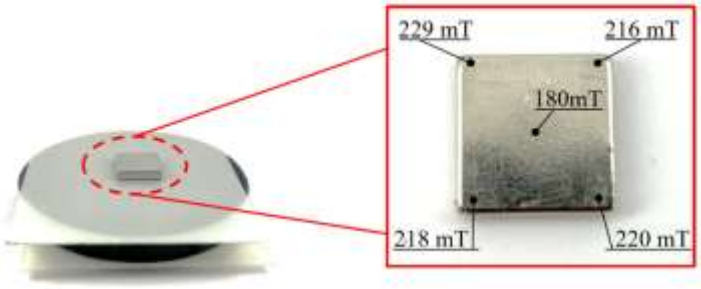

Figure 4-7. Magnetic field measurement on the permanent magnet surface.

These experimental results are used as parameters for the @Comsol model proposed in Figure 4-8 . This simulation results are proposed to check the amplitude and the uniformity of the magnetic field provided by the permanent magnets in the sample area. The permanent magnets are defined through a flux conservation element and with a 160 $kA.m^{-1}$ in the y direction. For the first simulation tested depicted in Figure 4-9(a), the space gap corresponding to the mold thickness is set to 5 mm. In the sample area, the magnetic induction field B varies from 80 mT to 99 mT, with slightly increasing values when approaching the permanent magnets. The influence of the space gap between the permanent magnets to the distribution of magnetic field is highlighted by varying the space gap value from 5mm down to 1mm. According to the resulting 3D graphs of Figure 4-9(a)-(d), a quasi-linear relation can be obtained between the distance and the magnetic field amplitude (Figure 4-10). Also and as envisaged in Figure 4-9, the smaller the space gap, the more uniform the magnetic field distribution.

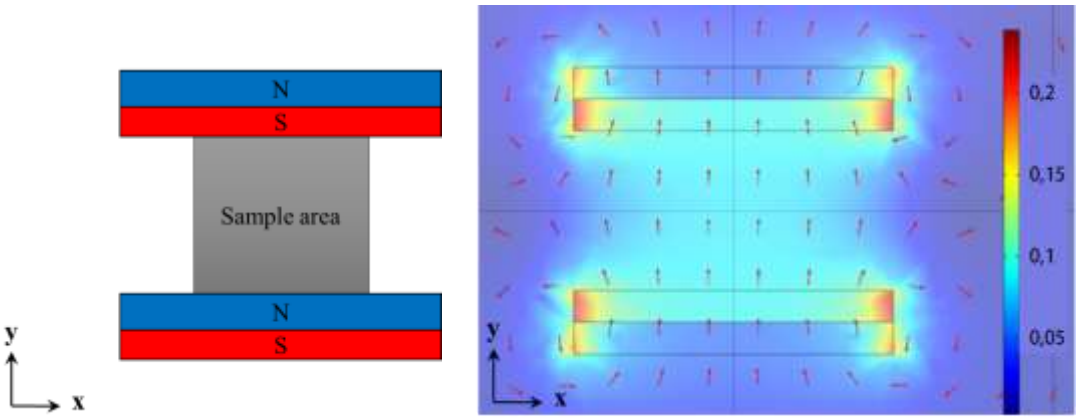

(a) (b)

Figure 4-8. Magnetic field driven by two permanent magnets. (a) Setup design for performing anisotropy composite. (b) Overall 3D view of magnetic distribution based Comsol simulation

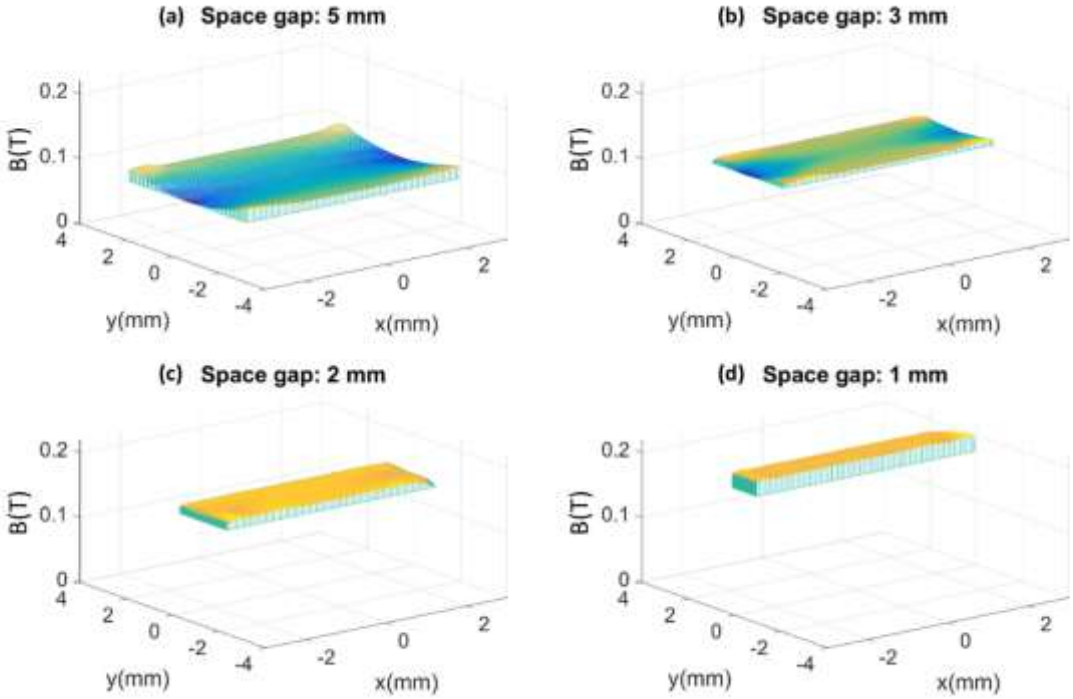

Figure 4-9. Magnetic field distribution in the sample area with space gap of: (a) 5 mm, (b) 3 mm, (c) 2 mm, (d) 1 mm.

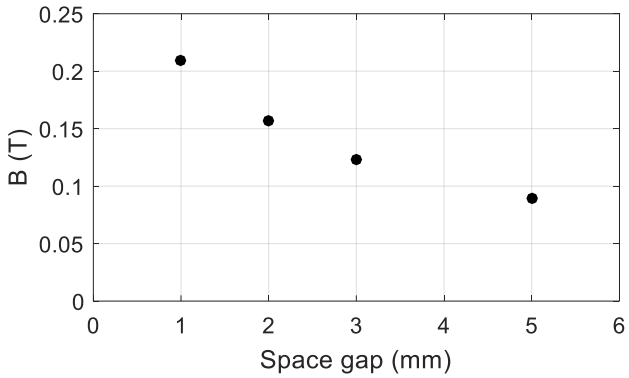

Figure 4-10. Average induction level as a function of the two permanent magnets space gap.

In order to assess the effect of the space gap to the heat generation properties, cylinder-shaped PDMS-based composites with different thickness from 1 mm to 5 mm has been fabricated. All these cylinder-shaped samples exhibit a 15 mm diameter, and were elaborated with a 10% vol. of Fe_3O_4 particles. The experimental setup will be described in the next Subsection 3.1. In every tested cases, the magnetic excitation is imposed in the particle chains direction, i.e. along the revolution axis of the cylinder specimens (z-axis). Due to the z-axis revolution symmetry, cylinder-shaped composite seems to be the most adequate choices for this test. The temperature variations as a function of time under an alternative magnetic field of 2.3 kHz frequency and 160 kA/m amplitude are displayed in Figure 4-11(a). The observation of Figure 4-11(a)-(c) leads to the following conclusions:

a) Whatever the thickness, the oriented samples always exhibit a stronger thermal variation compared to the un-oriented (Figure 4-11(a)).

b) The thicker samples show higher steady state temperatures (Figure 4-11(b)). Under constant magnetic excitations, the heat generation should be linearly linked to the sample volume as the particle distribution is homogeneous. However, slight discrepancy has been recorded where a linear relationship between the heating temperature and the thickness is not perfectly verified. This phenomenon is probably due to thermal exchanges linked to the ratio surface/volume. This ratio is lower for thicker samples.

c) Quite logically, the temperature difference (ΔT) between the oriented and the un-oriented samples decreases with the space gap distance (Figure 4-11(c)). A larger space gap means a lower magnetic field amplitude during the curing process as illustrated Figure 4-10. Above 5 mm space gap, the induced magnetic field between the two permanent magnets significantly reduces and its amplitude can be somewhat fluctuated (i.e. not perfectly stable), resulting in irregular particle alignments. This

leads to very small temperature differences between the isotropic and the anisotropic composites (especially for the 3 mm and 5 mm thick where only 2°C is observed. 6°C and 4°C are obtained for the 1mm and the 2mm, respectively.

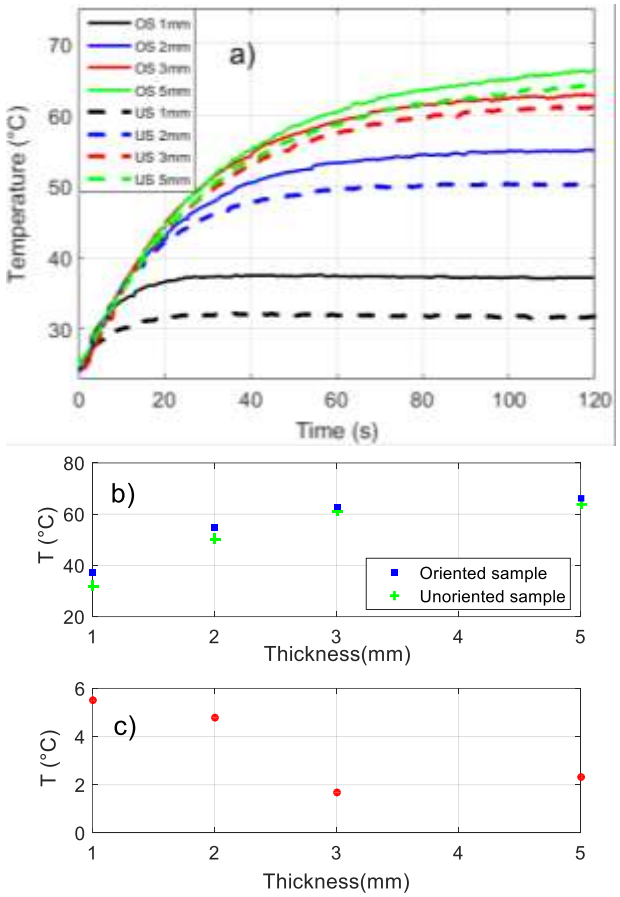

Figure 4-11. (a) Temperature variations as a function of time for oriented samples (OS) and un-oriented samples (US) with different thickness of 1, 2 and 3 mm. (b) Steady-state temperature as a function of the thickness. (c) Steady-state temperature difference between oriented and un-oriented samples as a function of the thickness.

4.3.2 Particles distribution

Scanning Electron Microscopic (SEM) images are used to investigate the particle distribution of the ferromagnetic composite filled with 5% vol. Fe_3O_4 particles. The cubic samples are cut into small slices to fit the SEM geometrical requirements. The thickness of all the samples observed is set to 5 mm. The color balance is an efficient indictor to identify the particles from the polymer base. As illustrated in Figure 4-12, the white spots stands for the Fe_3O_4 particles while the black background is the PDMS matrix. First observations clearly show strong alignments (along z-axis) in the magnetic field direction (cf. Figure 4-12). These qualitative observations are confirmed quantitatively from the directionality histogram from the @imageJ software (cf. Figure 4-13 and Figure 4-14).

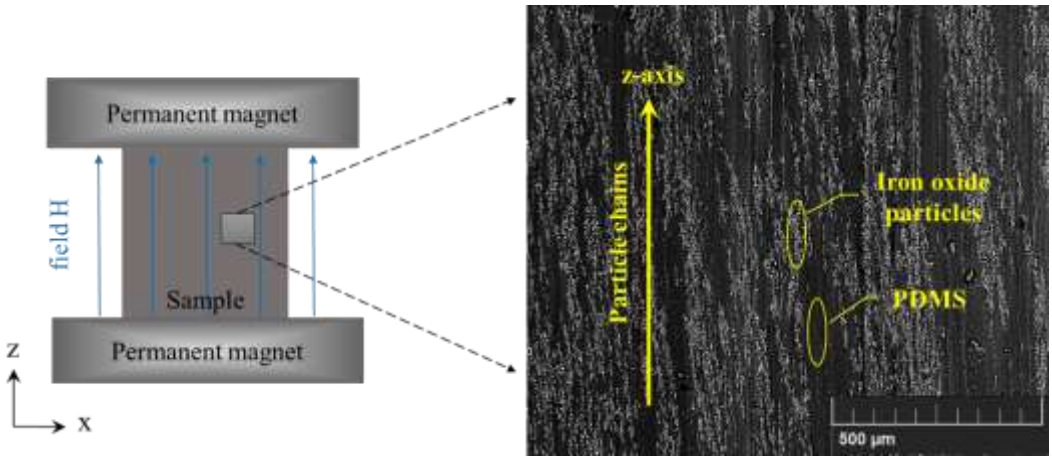

Figure 4-12. SEM image of anisotropy composite-based micro-structure.

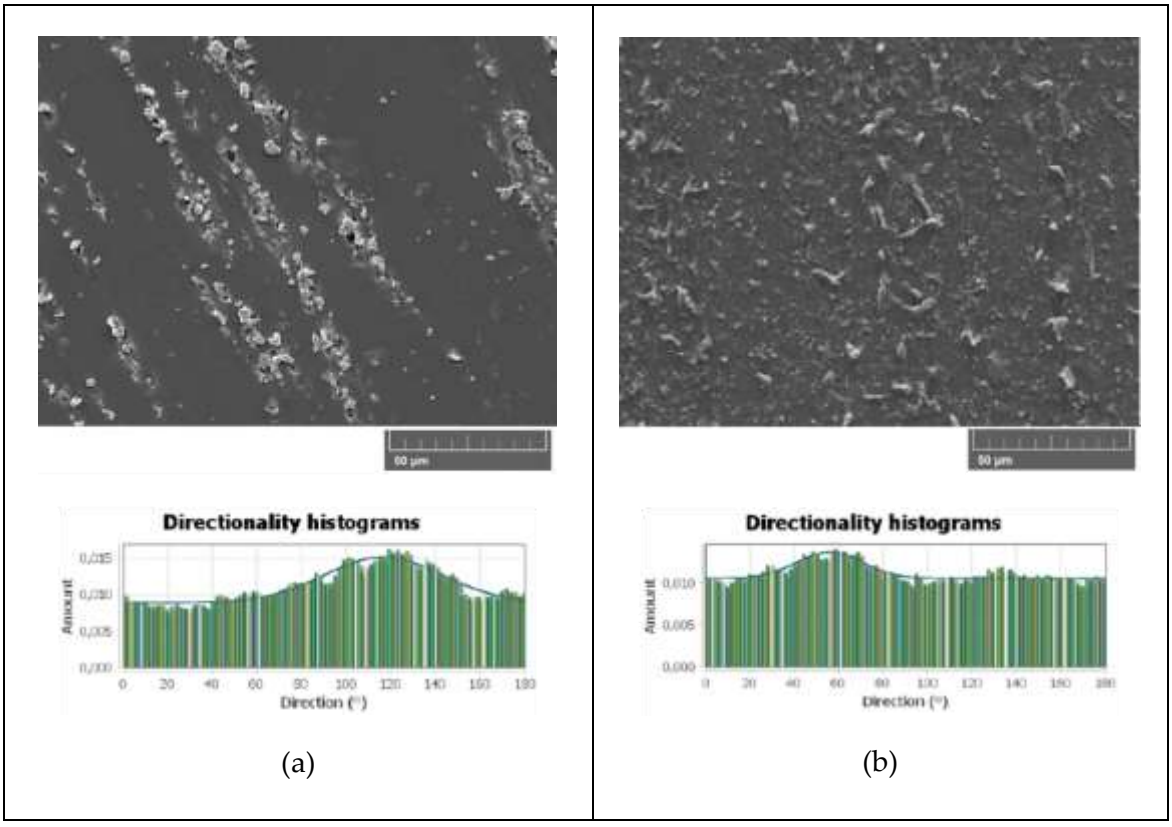

(a) (b)

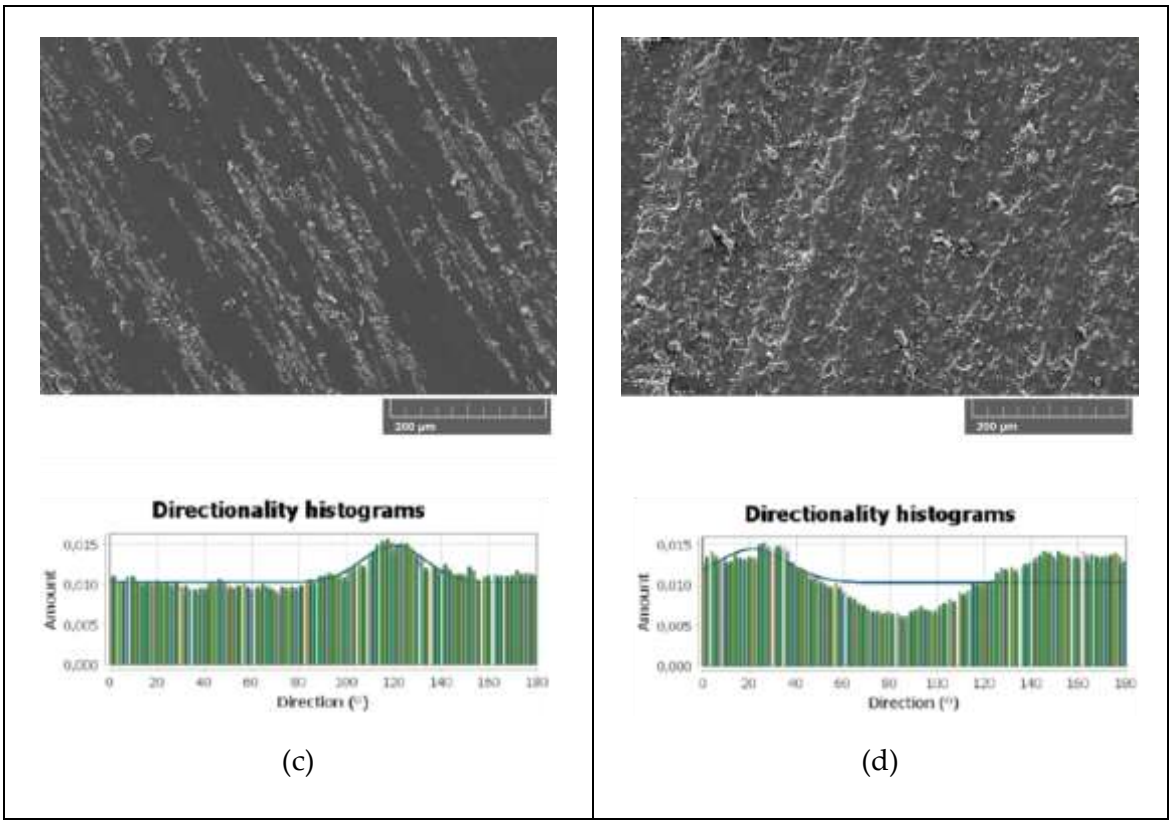

Figure 4-13. SEM images and directionality histogram of (a) oriented sample with magnification of x420; (b) un-oriented sample with magnification of x420; (c) oriented sample with magnification of x120; (d) un-oriented sample with magnification of x120.

Figure 4-13 depicts oriented and un-oriented composites with 5% Fe_3O_4 particle volume fraction,. Two observation scales are proposed, including magnification of x420 times (Figure 4-13 (a)-(b)) and x120 times (Figure 4-13 (c)-(d)). Anisotropic behavior can be visibly confirmed on the oriented samples tested (Figure 4-13). Clear alignments can be observed as confirmed from the directionality histograms. The directionality indicator is based on the Fourier spectrum analysis. Structures with a preferred orientation generate a periodic pattern at +90° orientation in the Fourier transform of the image. Images with completely isotropic content are expected to give a flat histogram, whereas images in which there is a preferred orientation are expected to give a histogram with a peak at that orientation (i.e. 120°). The directionality histogram depends on the magnification of SEM images, especially when the particles are randomly dispersed (Figure 4-13(b) and (d)). For the well aligned particles (Figure 4-13(a) and (c)), we can observed a directionality histogram slightly varying with a privileged orientation for both scales close to 120° (i.e. corresponding to the peak value).

A much clearer preferred orientation can be observed on the directionality histogram of the 5% vol. Fe_3O_4 particle volume fraction (Figure 4-14 (a)). Oppositely, the directionality of the sample with higher filler content (15% vol., Figure 4-14 (b)) is not so obvious. This is probably due to the blurred distinction between the black and the white areas. Finally, the overall

observation of the SEM images and of their directionality histograms clearly show a strong structured distribution of the ferromagnetic particles, confirming our expectations.

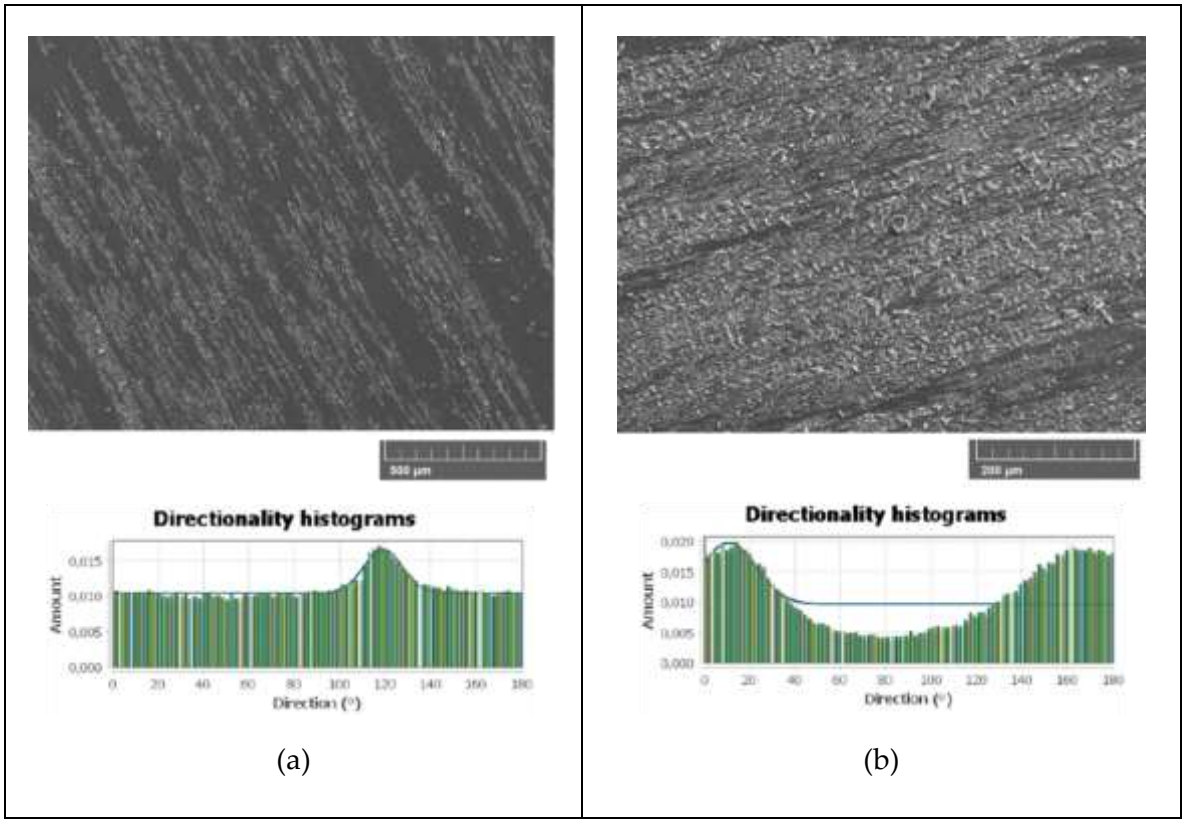

Figure 4-14. (a) Large window SEM and directionality histogram of 5% vol. Fe_3O_4 oriented composite. (b) SEM and directionality histogram of 15% vol. Fe_3O_4.

4.3.3 Permeability characterization

The magnetic permeability of a specimen can be determined based on the measurement of its inductance (see subsection 2.3.2). Considering the relative magnetic permeability of the pure PDMS as one, the composite permeability of same geometry specimens can be given by:

$$\mu_r = \frac{L_{composite}}{L_{polymer}} \qquad \text{Equation 2-5}$$

where $L_{composite}$ and $L_{polymer}$ denoted the composite and the pure PDMS inductances, respectively.

A high precision LCR meter (E4980A Keysight) has been used to record the inductance value of the cubic-shaped pure-PDMS and composite-based samples. Both oriented and un-oriented composites are elaborated with 30% vol. vol. iron oxide particles. All samples are manually wired with a 10 turns coil in a single layer, and been measured under a low frequency range (20Hz to 1MHz). The direction of the magnetic field applied on the oriented composite can be set as z-axis or x, y-axis, depending on how it is wired (see Figure 4-15a). As expected in Figure 4-15b, the anisotropic cube exhibits higher relative permeability on the z-axis than on the x and

y-axis, corresponding to 25% improvement. Also, the oriented sample always has higher permeability than the un-oriented sample, which is coherent to the result of Figure 4-20.

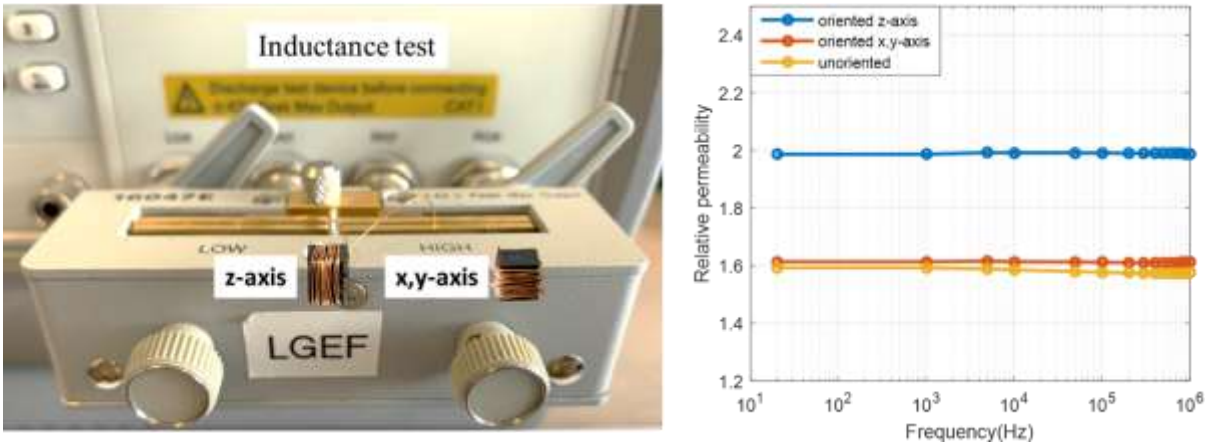

(a) (b)

Figure 4-15. Test bench used for determination of permeability: (a) Inductance measurement based LCR meter. (b) Relative permeability of random sample and oriented samples (z-axis and x, y-axis) as a function frequency.

The inductance value has also been checked for different particle size composites (50-100nm, 5um and 50um Fe_3O_4 particles), both for isotropic and anisotropic composites. Figure 4-16 shows the relative permeability of the un-oriented and oriented samples both in z-axis. Regardless of the particle size, the oriented samples always have higher permeabilities than the un-oriented ones. Additionally, the 50 μm size particle composite has the highest permeability (and this whatever the polymer matrix nature).

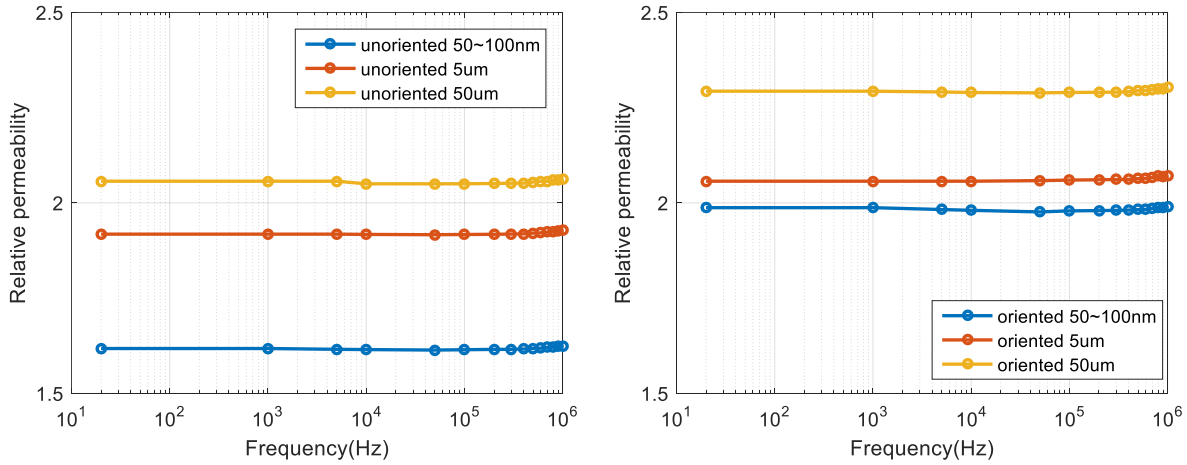

(**a**) (**b**)

Figure 4-16 Permeability of (a) un-oriented and (b) oriented Fe_3O_4 @PDMS composites in particle size of 50-100nm, 5um and 50um.

4.3.4 Hysteresis behavior

The Hysteresis behavior of the isotropic and the anisotropic Fe_3O_4 @PDMS composites (5 μm diameter, 30% vol. fraction) has been characterized with the lab-built electromagnet (Figure 2-12). The electromagnet is power supplied by a power amplifier (P CR-WE Series AC Power Supply, @KIKUSUI). The measures are all carried out at 1Hz and 40 kA/m of magnetic excitation. The resulting hysteresis cycle of the 30% vol. Fe_3O_4 @PDMS composites are illustrated in Figure 4-17, excited in the alignment-induced axis direction. It is clear that under the same experimental conditions, the anisotropic Fe_3O_4 @PDMS composites has a larger hysteresis loop than the isotropic one (stronger magnetic answer). The energy density and the relative permeabiliy of the isotropic and of the anisotropic composites are shown in Tableau 4-1. The results confirm the stronger magnetic behavior of the anisotropic composite.

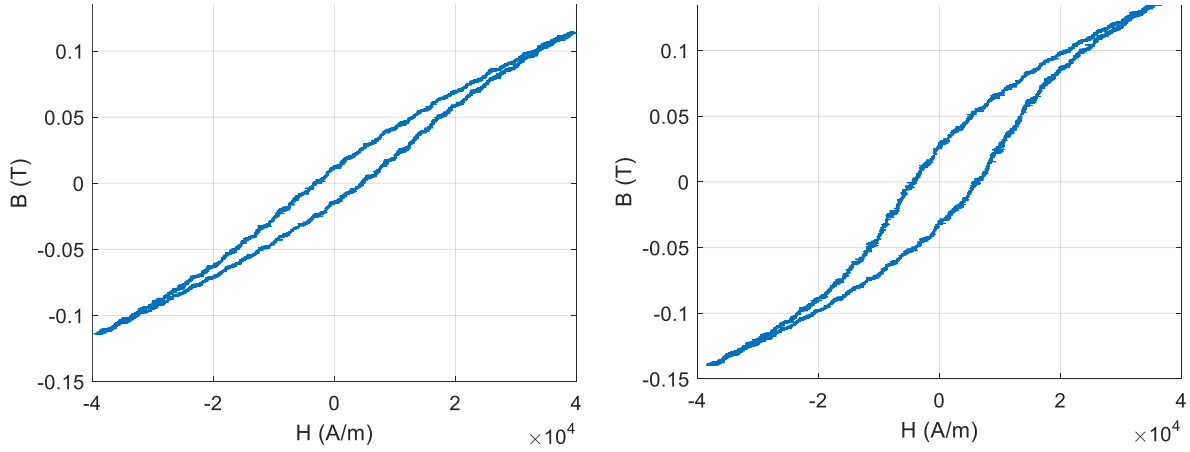

(a) (b)

Figure 4-17 Hysteresis cycle of (a) un-oriented Fe_3O_4 @PDMS composite, and (b) oriented Fe_3O_4 @PDMS composite under magnetic field of 1Hz frequency and 40 kA/m.

Tableau 4-1 The coefficient of hysteresis loop in one cycle period for Fe_3O_4@PDMS composites

	Density energy(J/m3)	Relative permeability μr
Isotropic Fe_3O_4@PDMS	0.0012	2.3975
Anisotropic Fe_3O_4@PDMS	0.0020	3.1595

4.4 LFIH effect of oriented magnetic composites

Figure 4-18performs the IH test where the composite induced by an AC magnetic excitation along the particle alignment direction (z-axis). The induction heating results of anisotropic

samples in different directions can be obtained by simply changing the direction excited by the magnetic field.

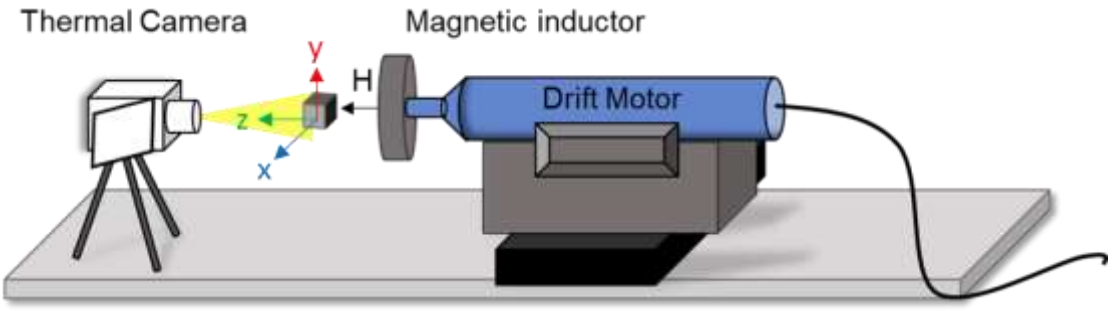

Figure 4-18. The LFIH measurement as a function of the anisotropy sample.

Figure 4-19 displays the temperature variations as functions of time for both the oriented and un-oriented samples, which is induced by an AC magnetic excitation along the z-axis direction. The volume fractions of iron oxide particles ranged from 5% vol. to 35% vol. Whatever the particle fraction, the oriented samples always generate higher induced heat. From the micro-scale point of view, the aligned particle chains clearly drive the magnetic lines and give rise to improved IH response. It can be found that both isotropic and anisotropic composites lead to increasing temperature response as the typical first-order system.

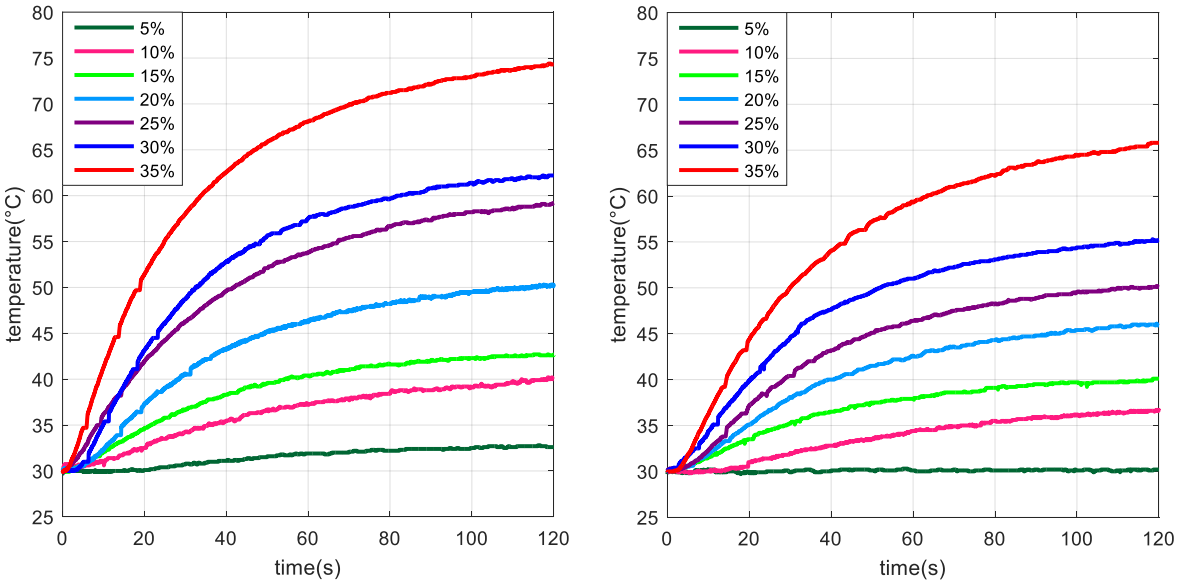

Figure 4-19. Temperature versus time plot for increasing particles volume fraction samples. a) Z-axis of oriented composite; b) Z-axis of un-oriented composite.

Figure 4-20(a) depicts the steady state temperature obtained after around 120 seconds of different volume fraction samples under the 2.3 kHz alternating magnetic field. In order to

better understand the impact of anisotropic properties on IH performance, three directions of magnetic source are applied on both aligned and random composites. As expected, both x- and y-axis responses of the oriented samples exhibit very similar IH results, which is therefore represented by only one curve (cf. blue line) on Figure 4-20(a), for a sake of simplicity. Obviously, these samples exhibit higher temperature response in z-axis applied magnetic field, reflecting their anisotropy of being directionally independent. Conversely, for every direction, the un-oriented samples lead to similar level of induced heat (cf. black line as displayed Figure 4-20(a), confirming their isotropic ferromagnetic behaviors.

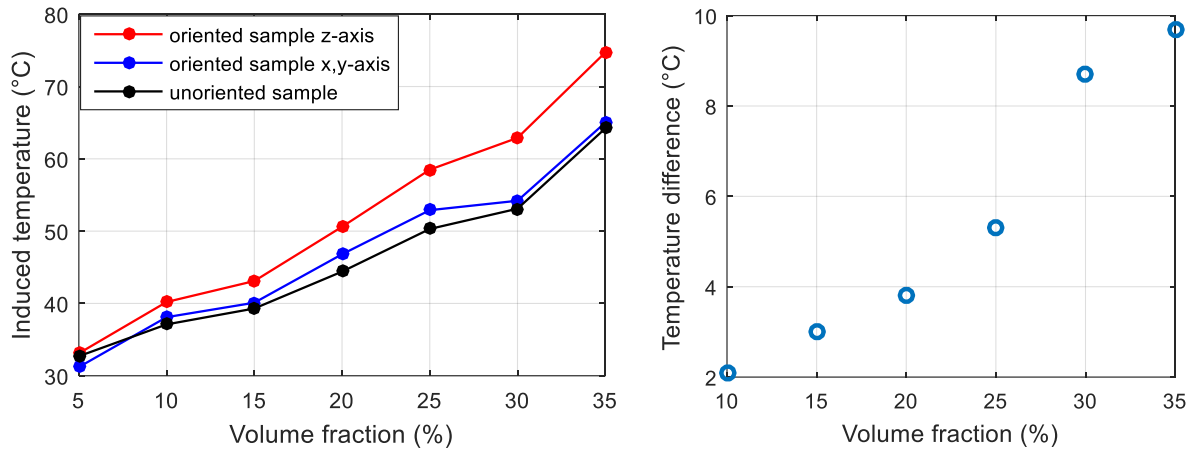

(**a**) (**b**)

Figure 4-20. (a) Steady state temperature as a function of particles volume fraction for both aligned and random composites subjected by different orientations of magnetic field. (b) Temperature difference between the z-axis (preferred orientation) and the x, y-axis of the anisotropic samples.

Surprisingly, regardless of which direction driven by alternating magnetic source, the oriented samples always show higher temperature response than the un-oriented ones. These experimental situations have been voluntarily reproduced many times and similar results have always been observed. This tends to say that an ordered structure is enough to improve the ferromagnetic behavior. Figure 4-20(b) depicts the steady state temperature difference between the z-axis and the x, y-axis of the oriented samples. Quite intuitively, this difference becomes larger by increasing the particle volume fraction.

Concerning the thermal transfer dynamic that can be highlighted in Figure 4-21(a), 120 seconds are required by the 35 vol.% oriented sample to reach its steady state regime (65 °C) in x, y-axis, whereas just 43 seconds in the z-axis, i.e. almost 3 times faster. Here we define a time response ratio (R) characterizing the thermal conversion dynamic performances, which can be given by:

$$R = \frac{t_{x,y-axis}}{t_{z-axis}} \qquad \text{Equation 4-1}$$

where $t_{x,y-axis}$ and t_{z-axis} respectively denote to time necessary for the oriented sample to achieve the steady state value in x, y-direction, and z-direction.

Obviously in Figure 4-21(b), an increase of the volume fraction leads to an improvement of the response time. The higher is the volume fraction the larger is the difference between the thermal time constants of both the oriented and un-oriented samples (Figure 4-21 (b)).

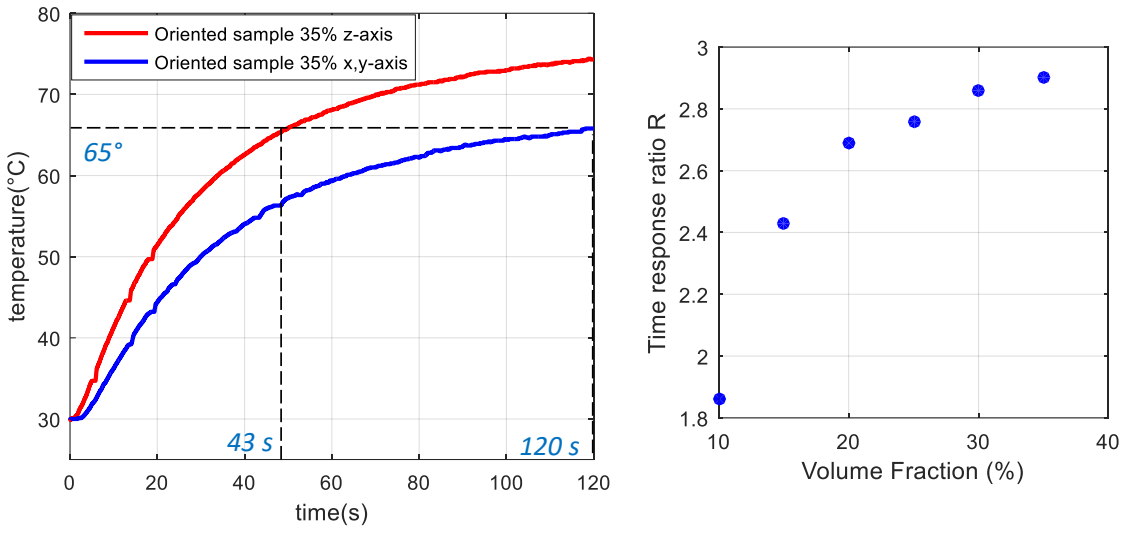

(**a**) (**b**)

Figure 4-21. (a) Temperature as a function of time, comparison easy axis/other axis. (b) Time response ratio R between z-axis and x, y-axis of oriented samples as a function of particle volume fraction.

4.5 Application towards tracking system based electromagnetic sensor

The improvement of the anisotropic composite magnetic permeability opens another perspective for smart sensor designs in medical applications, like electromagnetic tracking (EMT) system used in endovascular procedures. EMT are of great potential for assisting physicians in precision placement of instruments during minimally-invasive interventions, since it is not limited by the line-of-sight restrictions of traditional optical tracking.

Figure 4-22 illustrates a working principal of the EMT device used in vascular procedure. The system composes of three principal components such as: 1) reference magnetic field generated by an emitter electromagnet which is outside the patient's body; 2) a receiver sensor implemented in the guidewire tip that is introduced inside the patient's vein; and 3) tracking system based electronic circuit (Digital signal processing, Microcontroller unit). According to the Lenz's law, when the receiver sensor moves in the space subjected by an alternating magnetic field, a voltage proportional to the vectorial of the cross sectional winding area (S) and the intensity of the magnetic field (B), is induced in every winding. Thus, the resulting

voltage (e) of the N-turn coil is proportional to the varying magnetic flux (Φ) that can be expressed as:

$$e = -N\frac{d\Phi}{dt} = -N\frac{d(\vec{B} \times \vec{S})}{dt} \qquad \text{Equation 4-2}$$

This induced voltage immediately gives the measurement of rotation versus the reference emitter electromagnet and the position in relation with the modulus of the emitting vector. Therefore, the EMT system can accurately calculate both position and orientation of the tip guidewire. In order to detect more than one dimension (e.g. 3 translations and 3 rotations), multiple coil sensors oriented orthogonally to each other may be used[55].

For a given magnetic field, the sensor response may be improved by several ways: 1) increasing the surface (S); 2) increasing the turn number (N); and 3) using a ferromagnetic core with high magnetic permeability. The first solution is not applicable as the sensor dimension is limited by the diameter of the veins. The second solution risks to reduce the flexibility of the coil sensor, impeding its movement particularly in angulations and tortuous anatomies. The third solution, as a result, seems to be an interesting option. Nonetheless, most of ferromagnetic materials with high permeability is not flexible. Therefore, ferromagnetic composite is chosen instead and it can be implemented at the guidewire tip of the medical tool (see Figure 4-22). By choosing an adequate fraction of the magnetic particles, it is possible to achieve the best tradeoff between the mechanical and the magnetic properties of the coil sensor. The flexibility of our PDMS composite doped with iron oxide powder is confirmed by Figure 4-23. Moreover, by structuring the particles distribution, anisotropic sample gives rise to 25% increase in permeability (cf. Figure 4-15 (b)), leading to enhanced device sensitivity.

Assuming a linear relationship between the induced magnetic and the magnetic field, the Figure of Merit (FoM) of the sensing device can be defined as:

$$FoM = \frac{\mu_0 \mu_r}{Y} N \qquad \text{Equation 4-3}$$

where μ_0 is vacuum permeability (i.e. $4\pi . 10^{-7}$ H/m), μ_r is the relative permeability of the material, and Y denotes its Young modulus. The Young modulus is integrated in the FoM by taking into account the flexibility of the sensors. Finally, for a given magnetic generator, improvement of the FoM is equivalent to find the best compromise of the material parameters including magnetic and mechanical properties.

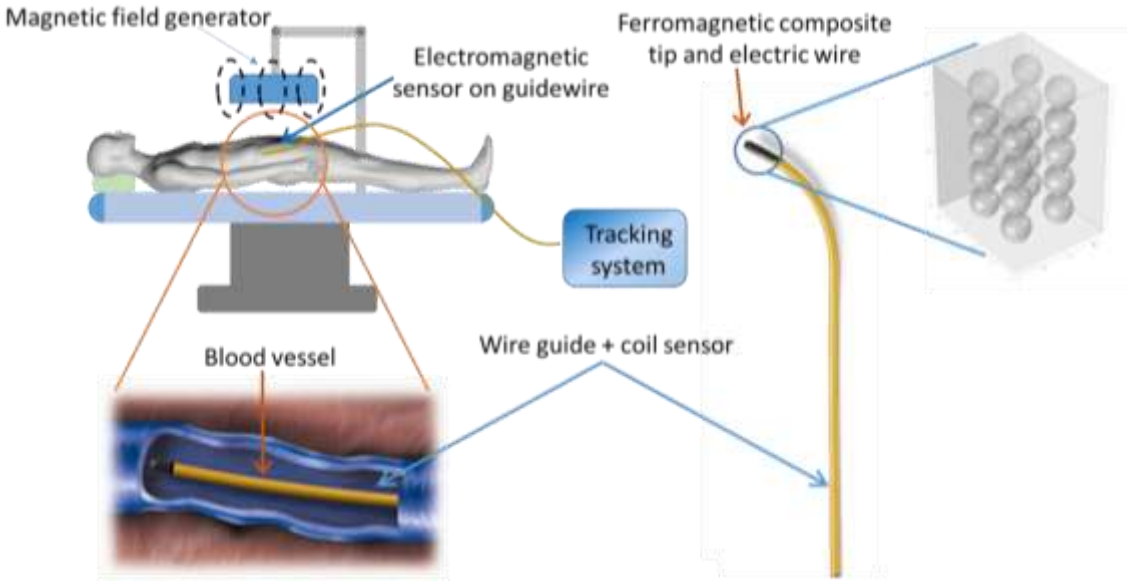

Figure 4-22 Working principal of electromagnetic tracking based ferromagnetic composite

Figure 4-23. Flexible ferromagnetic composite based PDMS polymer elaborated with 30% Fe_3O_4 particles

4.6 Summary

In this chapter, we proposed to improve the conversion properties of ferromagnetic composites by creating an anisotropic structure thanks to particle alignments. 3D @Comsol simulations have allowed to check the relative homogeneity of the magnetic excitation subjected to the sample area throughout the curing stage. Just as expected, SEM images confirmed particle alignments in chain-like structure along the filed direction. Eventually, oriented samples excited in the easy direction exhibit steady state temperatures equal to 75°C when they are limited to 63°C for the un-oriented ones. Coupling this observation and the time constants comparison leads to an increasing of the magneto/thermal conversion performances of approximately 30%. This part of work revealed that higher anisotropic behaviors of the fabricated composites was effectively achieved based on magnetiphoretic process. Our next objective focusses on optimization of material formulation so as to be adaptable to 3D printer.

Chapter 5
3D Printed Flexible Composites

In this chapter, a commercial extrusion 3D printer was explored to process magnetic pastes into desired 3D structures, which has the advantages of time and material efficient. The magnetic pastes formulated in our laboratory was based on the mixture between iron oxide micro particles and the PMDS polymer. By testing the magnetic powder/polymer matrix composition, we produced pastes that are compatible with the 3D printer and can be processed into flexible ferromagnetic samples. The design optimization together with the characterizations of composites were investigated. The LFIH effect, magnetic, and thermal properties of both isotropic and anisotropic composites were then compared. Our development is highly interesting in healthcare applications such as endovascular ablation for varicose treatment, electromagnetic tracking for surgery navigation or medical imaging, and so on.

5.1 Literature review

Additive manufacturing (AM), or more commonly known as three-dimensional (3D) printing technologies, has been demonstrated as an effective pathway to fabricate functional polymer composites. Geometric flexibility, controlled anisotropic properties, and advanced functionality of the printed composites open up opportunities for different applications. The printing of polymers, ceramics and metals is the most promising research topic for more and more applications. In industries such as automotive and aerospace, 3D printing technology is used to make critical fixture parts [119]. In application of wireless sensor, this approach enables researchers to produce unique sensors with integrated wireless capabilities. Printing polymers on PCB control panel can generate functional electronic components, such as wireless embedded sensors and integrated battery holders [120]. In medical field, 3D printing technology is opening the door to unforeseen advancements for life-saving devices. For example, seamless medical carts, anatomical models, and custom surgical tools [121].

5.1.1 External field-assisted magnetic particle alignment

Magnetic materials play an important role for electrical and electronic devices including computer hard disk drives, motors, sensors, and consumer electronics [122]. AM of these materials could change the way engineers develop and test their designs. Magnetic 3D printing process under external filed excitation is still rather limited today, although researchers are actively looking into the issue. Actually, fabricating by 3D printing technology and apply external stimulate to samples during printing, the researcher work falls under the 4D printing domain. The use of external fields to control the directionality or orientation of particles or fibers introduced into polymeric matrices have been sparingly investigated over the past decade [123]. External fields such as flow field, electrical field, magnetic field, and acoustic field have been introduced to precisely control the particles or fibers distribution in polymer matrix during the printing process.

Acoustic forces, promoted by ultrasonic standing waves, have been used for noncontact particle manipulation. As reported on [124], an acoustic field was integrated into the 3D printing system to pattern different micro particles into dense parallel curves or networks in the liquid resin. As indicated, acoustophoresis has the advantages of full particle placement control, no imposed manufacturing constraints, and no material shape or specific physical property requirements. In [125], samples were printed with acoustically leaded alignment of magnetite particles for electronic applications.

There are many researchers dealt with magnetic particle alignment using electric field. Chengxun Liu *et al.* provided a method for manipulating magnetic or magnetizable objects in a matrix [126], which was based on a combination of both magnetophoresis and dielectrophoresis actuation. Md AAM *et al.* successfully manipulated the Barium Hexaferrite nanoparticles in PDMS under simultaneous electric and magnetic fields. This method gave

raise to improved dielectric properties as opposed to the one just employing the magnetic alignment [127]. As far as we learnt from literatures, none of study has yet been addressed the manipulation of magnetic particles under dielectrophoresis via 3D printing process. It was probably because of complex setup implementation where high voltage is needed. For magnetic particle alignment, magnetophoresis appear more effective for particle alignment because of its compactness, easier integration, and higher energy density.

Magnetic particle alignment via magnetophoresis during the 3D printing process promotes the creation parts with high magnetic performance. In [128], researchers performed a magnetic excitation of 10mT during printing process to Co-based nanoparticle ink. A study reported on [129] allowed to achieve printed magnetic ink consisting of UV-curable polyurethane-acrylate (UV-PUA) and reinforced metallic particles. These metallic particles were oriented under magnetic field created by a rotating neodymium permanent magnet. Local orientation has been achieved by using masks of desired patterns during the curing process. As reported in [130], magnetic particles were dispensing into the resin vat and the particles alignment were controlled by the motion path of a magnet beneath the resin vat. Then the digital UV light was used for solidification.

The external magnetic field also applied for the programing of shape memory material. Researchers presented a magnetic multimaterial direct ink writing (DIW) technique for the complex structural integration of photocurable composites contained magnetized neodymium−iron-boron (NdFeB) microparticles. Composites were magnetized under a 1.5 T impulsive magnetic field during the printing [131]. This kind of programmable shape memory composite can stimulate by the cooperative of magnetic field and temperature change after printing, thus showing a multimodal shape configuration. In [132] researchers reported a novel shape memory material (Fe3O4 and NdFeB particles in an amorphous shape memory polymer matrix) magnetized with a desired magnetic profile under an impulse magnetic field ($\approx$1.5 T). After magnetized, with the help of induction heating created by particles under a high frequency magnetic field, the material will deform significantly. Moreover, the magnetization profile of the shape memory material can be reprogrammed for reconfigurable shape transformation by remagnetization.

5.1.2 3D printing of PDMS-based magnetic composites

Many research teams studied the PDMS based magnetic composites. The most popular application including the soft actuators and microfluidic devices utilized the embedded magnetic particles such as Fe_3O_4, neodymium-iron-boron (NdFeB) and paraseodymium-iron-boron (PrFeB) [133]–[137]. However, few of them tried to fabricate these materials using the AM technology. It has proved challenging to 3D print PDMS in complex structures due to its low elastic modulus and usually needs support during the printing process. Although the low viscosity of PDMS facilitates deposition from a printer nozzle, the relatively long gelation time

results in the inflow of PDMS and shape fidelity loss. The low elastic modulus of the pre- cured PDMS and its deformation under gravity still restricts the formation of high precision 3D geometries [138]. To solve such problems, different methods were explored to maintain high print fidelity. For example:

- Advanced Solutions, Inc. is now demonstrating PDMS bio-printing by blending siloxane polymers SE 1700 and Sylgard 184. SE 1700 is a shear-thinning and high viscosity polymer, which enables shape fidelity post-printing. Sylgard 184, with lower viscosity, is blended with SE 1700 to enhance the ink's ability.
- T. J. Hinton *et al*. introduced the 3D printing of PDMS pre-polymer within Carbopol gel support [138]. Thus, combined with the immiscibility of PDMS in Carbopol, it confines the PDMS prepolymer within the support for the curing process to maintain dimensional stability.
- F. Liu *et al*. proposed using a 3D extrusion printer to fabricate artificial magnetic cilium consisting of PDMS doped with iron particles to apply micro-actuators [139]. It was indicated that the concentration of iron particles could influence the modulus of elasticity. The higher the iron concentration, the higher the modulus of elasticity.

The methods described above, no matter adding a blender or applying a UV system for helping curing process or curing layer by layer, the aim is to avoid the paste flowing and keep the print fidelity. In AM of elastomer-particle composites, it is better to increase the viscosity so that the paste can hold on to the shape during the short printing time.

There are many commercialized available inkjet printing equipment like the MultiJet (3D Systems, Rock Hill, South Carolina, United States), PolyJet devices (Stratasys, Eden Prairie, Minnesota, United States) [140]. Hyrel 3D printer (System 30M, US), and so on. In this study, we opt for the Hyrel 3D printer, which can process hybrid material systems via multi-extruder and offer flexibility in feed materials. The Hyrel system 30M can achieve feature sizes below 50 μm by using a lead-screw driven system. The programmable pumping system precisely controls the volume of deposited ink. Particularly, the Hyrel printer is modulable, open source code, cost effective and easy use.

Several teams also employed Hydrel 3D printer to fabricate ferromagnetic composite. For instance, Y. Yan *et al*. successfully printed the magnetic core and conductive winding by the Hydrel multi-extruder paste-extrusion 3D printer [141]. Also in [142] and [143], a nanosilver paste and a UV-curable NiCuZn ferrite paste were applied to the Hyrel printer in order to perform 3D soft ferrite magnetic components. To the best of our knowledge, none of these investigations have yet dealt with anisotropic material through 3D Hyrel printer. Here we report extrusion-based printing technique with magnetic alignment capability. Fe_3O_4@PDMS composite with and without magnetophoresis are printed; their magnetic and thermal properties are compared. Our results suggest that in the alignment-induced preferred direction, an increase in permeability and LFIH are observed.

5.2 Material preparation and 3D printing process

The whole process consist of three main steps: 1) mixing the magnetic powder with the polymer to form a 3D printing paste, 2) extruding the paste layer by layer to get the desired object and 3) polymerization process. Aligned anisotropy can be obtained by applying an external field during the printing operation.

5.2.1 Printing paste preparation

The lab-fabricated magnetic paste (Fe_3O_4 @PDMS) was evaluated to serve as feedstock for the printer. To fabricate compatible paste, the fraction of particles has to be taken into consideration. Actually, the main difficulty in the elaboration of the magnetic paste is to find the right proportions to mix. As described in subsection Chapter 4.1.2, the particle volume fraction of is limit at 40% so as not to excess the percolation threshold. On a one hand, increase particle fraction results in higher viscosity and helps the printing paste maintain geometric fidelity during AM [139][144][145]. On the other hand, the particle fraction is restricted by clogging issues happening in the printing nozzle. To achieve a good balance between material and process, we added little by little the particles until getting the solution viscous enough for printing. In experiment, printing paste elaborated with 30% vol. of Fe_3O_4 powder were chosen. Actually, above the particle volume fraction of 30%, the solution becomes extremely dense and inhomogeneous, increasing probability of clogged nozzle.

The ferromagnetic paste preparation is similar to the one of the casting method. As described in Figure 5-1, 5-μm Fe_3O_4 spherical particles are mixed to the PDMS polymer base. The stirring process is performed for 20 minutes. The particles are scattered in the solution by ultrasound treatment (Hielscher Ultrasonic Processor UP400S) with powerful impulsions for a few minutes in order to get a perfectly homogeneous distribution. Polymer base and curing agent were combined in a 10:1 ratio. The mixture is then is placed in a vacuum machine (Memmert V0 400 Vacuum) (< 25 Pa, 25°C, for 20 minutes) until it reaches a full disappearance of the bubbles.

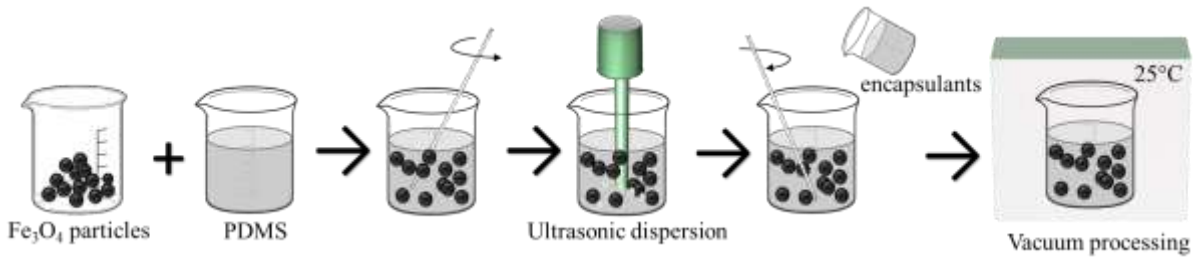

Figure 5-1 Printing paste preparation.

5.2.2 3D printing process

The printing setup consists of a modular head SDS extruder (cold flow at room temperature) and a glass platform, enabling it to be translated in 3 directions. The syringe pump extruder has a standard ink reservoir of 30 ml that can print fluids in desired patterns and shapes using adequate nozzle diameters. In our study, the syringe, which is capable of retraction and tunable speed movements, is equipped with a stainless steel nozzle tip (Nordson EFD, Precision stainless steel tip ID 7018107) whose inner diameter equals 0.84 mm.

Repetrel controlling software is used to run most of the Hyrel equipment, which allows generating GCODE from various 3D designs (e.g., .stl file, text file, etc.) and other system control functions. For instance, the desired shapes and size of sample could be built by Computer Assitant Design (CAD) software. The models are fed into Slice 3r, creating the 3D models into G-code (Figure 5-2). The composite is then printed on top of a substrate that lies on the print bed (Figure 5-3 a).

Several relevant parameters affect the printing quality, including the printing height per layer, the material flow rate, and the pressure control. After several adjustments, the best material flow rate and the pressure controls have been chosen equal to 300 pulse/µl and 0.8 (1 is the default), respectively.

Figure 5-2 3D printing process flow chart.

After the printing process, the sample and its underlying substrate are placed into the oven (Memmert V0 400 drying oven) at 100°C during 35 mn for polymerization (Figure 5-3 b).

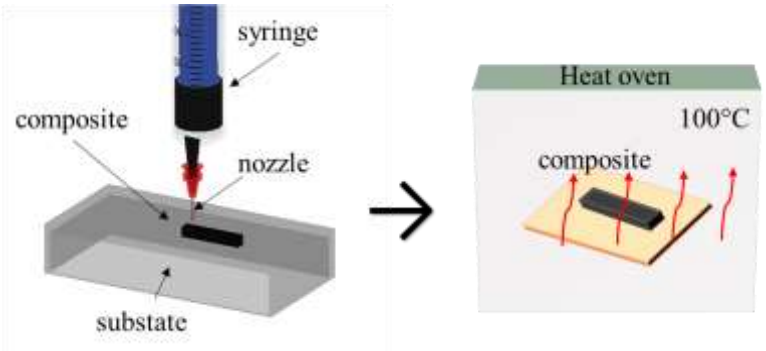

a) 3D Printing setup b) Polymerization processing

Figure 5-3 How to make 3D printed composite

5.2.3 Printed pattern letters based isotropic ferromagnetic composite

Figure 5-4(a) demonstrates a feasibility of printing the iron-oxide-powder paste into a letter pattern, which is deposited on a substrate made of high-temperature-resistant paper. IH result of the printed sample is confirmed through thermal camera image displayed in Figure 5-4(b). To achieve high accuracy of temperature recording, it must be taken into account that the emission coefficient of the substrate is approximately 0.9. Interestingly, the temperature of the "N" and "S" letters at the center is lower compared to "I" and "A" letters at the two sides. This result is consistent with the magnetic inductor's circular design. The magnetic field is stronger at the periphery (position of 8 permanent magnets) than at the center (containing no magnet).

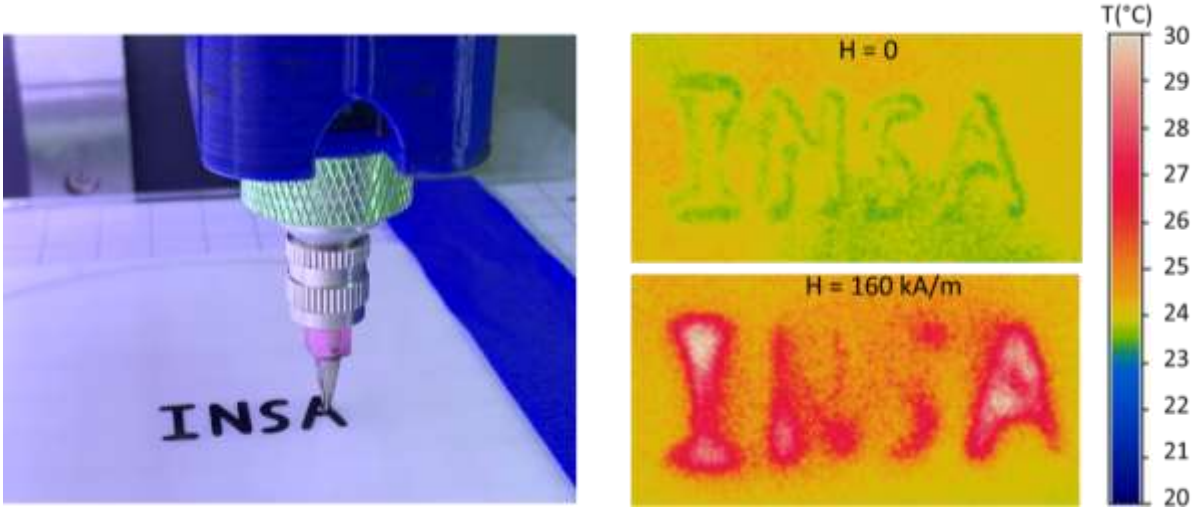

(**a**) (**b**)

Figure 5-4. LFIH result of printed ferromagnetic composite: a) Injection of PDMS + 15% Fe3O4 solution from printer nozzle; b) IH observation through a thermal camera.

To enhance the induced temperature, it is possible to increase the pattern thickness, which is normally proportional to the number of printing layers applied to it. After each layer, the sample is quickly heated by an electrical hot dryer (Memmert V0 400 drying oven), and finally, the multilayer-pattern is put in the oven at 100°C for 35 min to evaporate residues and solvent completely. As expected in Figure 5-5, the temperature change linearly increases as a function of the sample thickness. This result agrees with the one reported on previous works where heat power density is considered proportional to the sample volume.

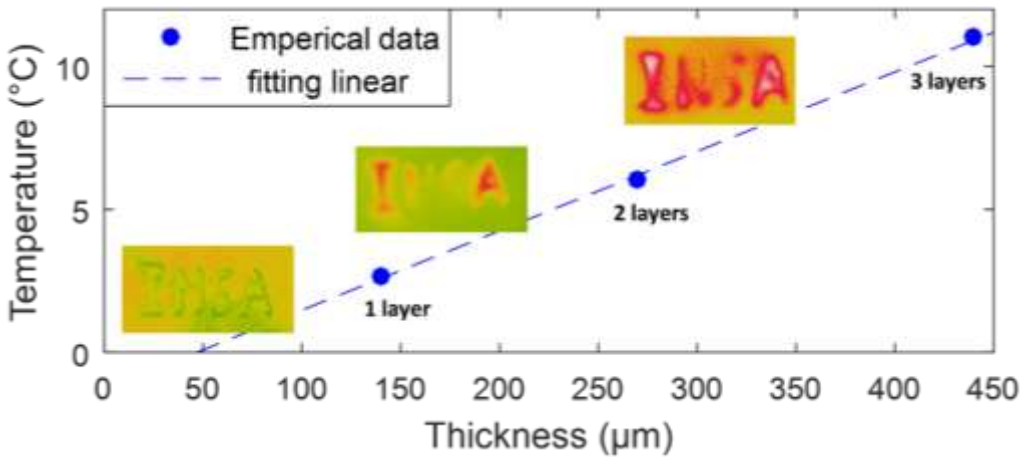

Figure 5-5. Temperature change versus thickness of printed letter pattern.

Eventually, Figure 5-6 confirms that the selected material based PDMS elastomer leads to the creation of flexible ferromagnetic composites, whatever fabrication process is chosen, either casting method or printing technology. This property is critical for medical tool design. The smart guidewire used to treat superficial venous insufficiency or magnetically track a find location should be flexible enough to be easily navigated inside the vessels.

Preliminary result highlighted a reliability of the home-made material, which is demonstrated as compatible to AM. It encourages us to go further for the development of magnetic composites that can be 3D printed with various sizes and shapes. Actually, the number of printing passes can be varied to rapidly prototype magnetic films in different thicknesses or more complex structures in different dimensions. Another aspect dedicated to anisotropic material whose properties are directionally dependent is also the main concern of this research. To print the oriented composite, the particles are kept in chain-like structure by applying an external magnetic field via permanent magnets. Next work will focus on enhancing the 3D printing setup by bringing magnetic source close to the platform, making it possible to align particles during curing and printing stages.

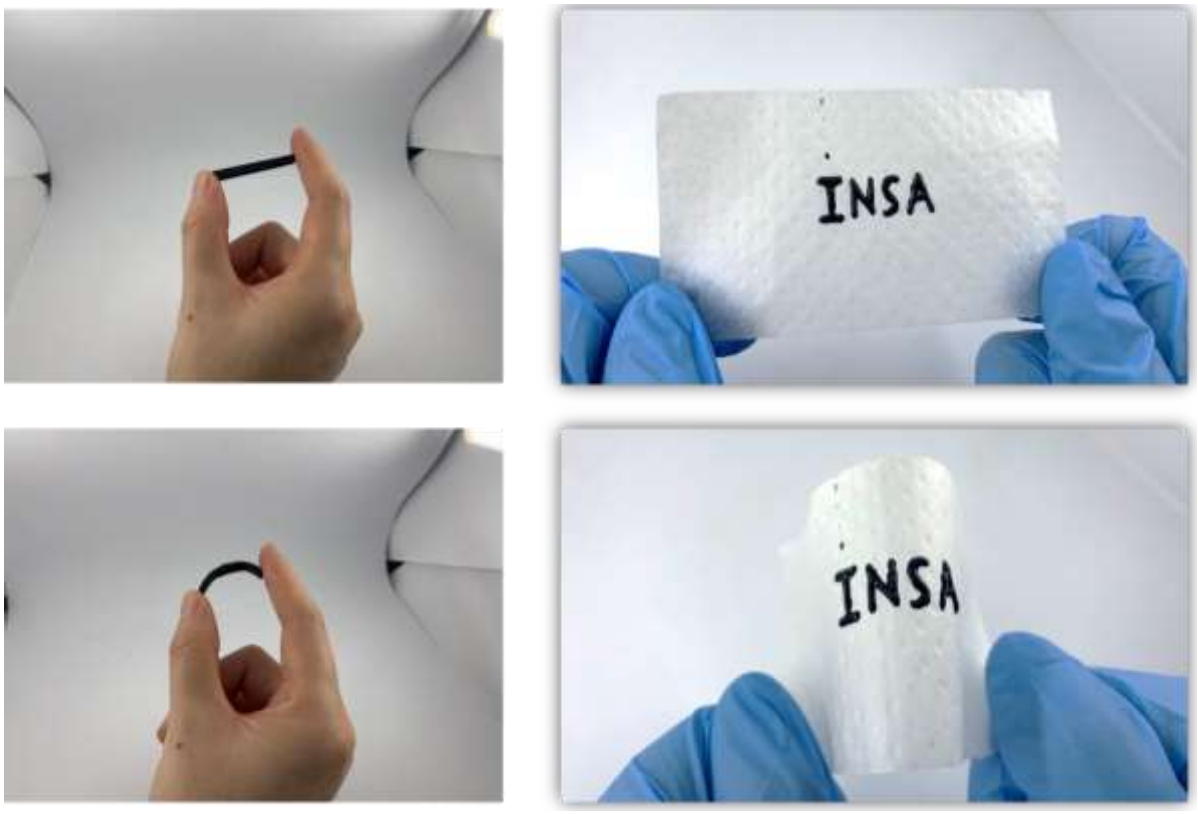

(a) (b)

Figure 5-6. Flexible ferromagnetic composite based PDMS polymer elaborated with 30% iron oxide particles: (a) Sample using casting method; (b) Pattern letters using printing technology.

5.3 Magnet array excitation

In this section, the extrusion-based printing technique with magnetic alignment capability is demonstrated. According to the literatures stated in subsection 4.1, alignment of ferromagnetic particles can be performed dielectrophoresis, magnetophoresis, and acoustophoresis. In this study, we use magnetophoresis to control the particle distribution during the printing process. This method leads to easy implementation, as the magnetic source can be performed via compact equipment like permanent magnets or electromagnetic coils. Furthermore, magnetic field have strong effect to the iron-oxide, allowing the successful alignment of the particles with moderate field amplitude. Using another source like electric power, it needs high amplifier supply (usually very cumbersome) to create sufficient electric filed exerted on the sample. Typically, an electric field of several kV/cm is necessary to obtain satisfactory anisotropic behavior. Accordingly, complicated setup is required, especially when printing process is carried out under high voltage application.

5.3.1 Setup design

To design our setup, permanent magnet is used as it has further advantages than electromagnets. Firstly, neither input energy nor cooling power is required [146]. Secondly, due to the limitation of printing space in 3D printer, permanent magnet array could provide easier working condition. The magnetic source is built based on array of five identical cubic magnets. Three configuration are carried out, comprising a) vertical array, b) horizontal array, and c) Halbach array (see Figure 5-7).

Halbach array is a special arrangement of permanent magnets that allows improving the magnetic field on one side of the array while canceling it on the other side [147]. This is the reason why this design is sometime refered to as ”one-sided flux” [148]. The effect is accomplished by orienting the magnets so that their poles are out of phase, typically by 90 degrees. This orientation essentially re-routes the magnetic field below the structure (the “non-working” surface) to the plane above the structure (the “working” surface), strengthening the magnetic field of the working surface and reducing the field of the non-working surface to nearly zero.

Changing polarity of the applied magnetic field can affect ferromagnetic domains in printed composites. In this way, various geometric 3D structures with tunable magnetic properties can be achieved. It is expected in Figure 5-7(a) that the vertical array with all of the north poles pointing up would provide an equivalent magnetic field on above and underneath of the array. Similarly, the horizontal in Figure 5-7(b) array would have an equal strength magnetic field on either side of the magnet. The Halbach array in Figure 5-7 (c) would give an enhanced magnetic field above, while the field underneath would cancel.

In the next subsection, Comsol simulation will be conducted to illustrate the magnetic field mapping generated by these three configurations. As all magnets are identical, study is first investigated on the model of one magnet.

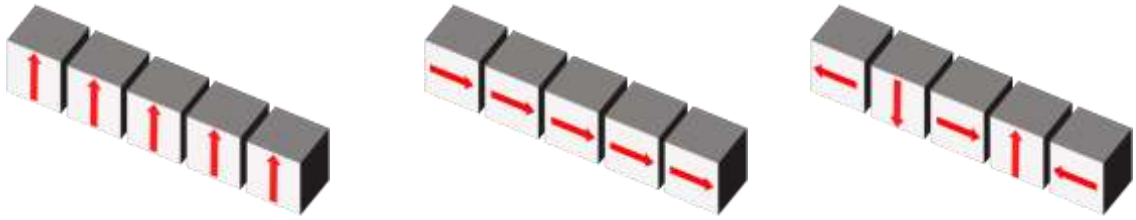

(**a**) (**b**) (c)

Figure 5-7 Schematic diagram of magnetic source: (a) Vertical array with north up; (b) Horizontal array with north side; and (c) Halbach array.

5.3.2 Magnetic field distribution based Comsol simulation

The magnetic fields mapping of a single permanent magnet (cubic shape with 10 mm side length) were simulated using the finite-element methods of @Comsol software. Through the detection of the Hall sensor probe (Figure 5-8 (a)), the average magnetic flux density is measured as 480mT, corresponding to a magnetization of 950 kA/m. This value is fed to the Comsol module, allowing to display the magnetic field distribution of the permanent magnet (cf. Figure 5-8(b)).

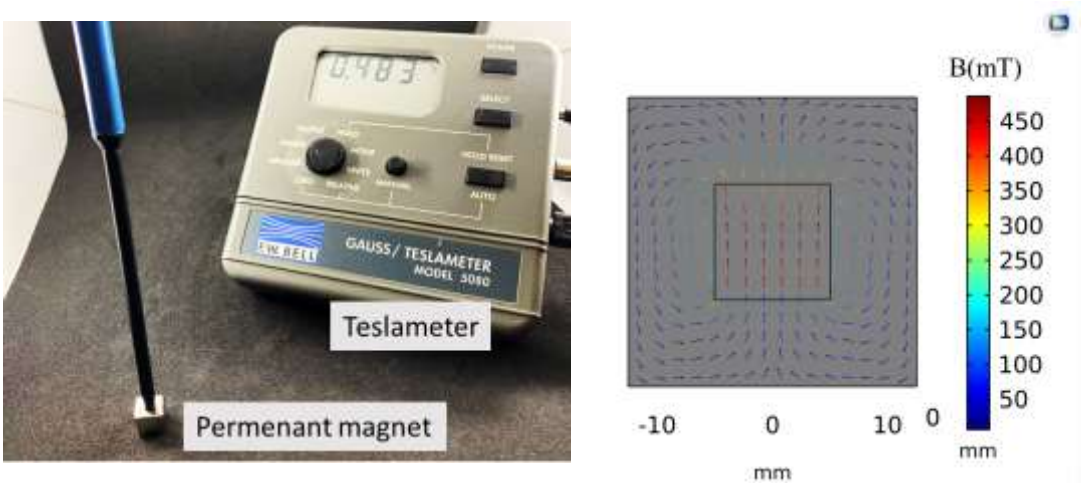

(a) (b)

Figure 5-8 Magnetic flux density of a single permanent magnet: (a) measured by hall probe; and (b) Simulation using Comsol software.

The simulation results of the flux density (*B*) along the symmetry z-axis for the three configurations are performed in Figure 5-9. As expected, the magnetic strength of the vertical and horizontal arrays is equally strong on the top and bottom of the magnet. The configuration in Figure 5-9 (a) indicates a perfect vertical directionality of the filed vectors, which is uniform and consistent for a large zone. Figure 5-9 (b) highlights the symmetric property of the magnetic field lines with respect to the (xOy) plan, which explains why the filed vectors are horizontal above and underneath the plan. In contrast, the Halbach array in Figure 5-9 (c) shows different behavior between the two sides. Both simulation and measurement have confirmed strong field on the top while a fairly weak field on the bottom. Inversely to the horizontal array where the horizontal direction is clearly shown, the one of the Halbach is just obvious at the center of the magnet surface.

Figure 5-10 displays the empirical measure and the simulation results of the magnetic flux density, which drastically decreases with the increasing distance from the array surface. Good coherent between experiment and theoretical results is achieved, reflecting high reliability of the Comsol model. At any distance, the vertical array leads to the highest magnetic strength, which is probably manifested by its uniform and consistence directionality. The horizontal

array, on the other hand, exhibits very weak value, i.e. 9 times lower than the vertical array. As expected, the Halbach array shows a difference between the above and the underneath. Actually, it allow to boost the magnetic strength above the surface, making its amplitude closed to the one of the vertical configuration. Surprisingly, the magnetic field underneath is not totally canceled itself as predicted the Halbach model[146]. This effect could be originated from the small gap existed among the magnets. To some extends, the above field of Halbach array is an improvement of the horizontal array field. However, the Halbach array manifests somewhat inhomogeneity in the field direction, and only on the center, the directionality is considered horizontal. It is therefore necessary to print the sample as close as possible to the center of the magnet array since the field gradients increase with the increasing distance from the symmetry axis. Consequently, an undesired force acts on the magnetic particle, which leads to unfavorable magnetization of the sample [149].

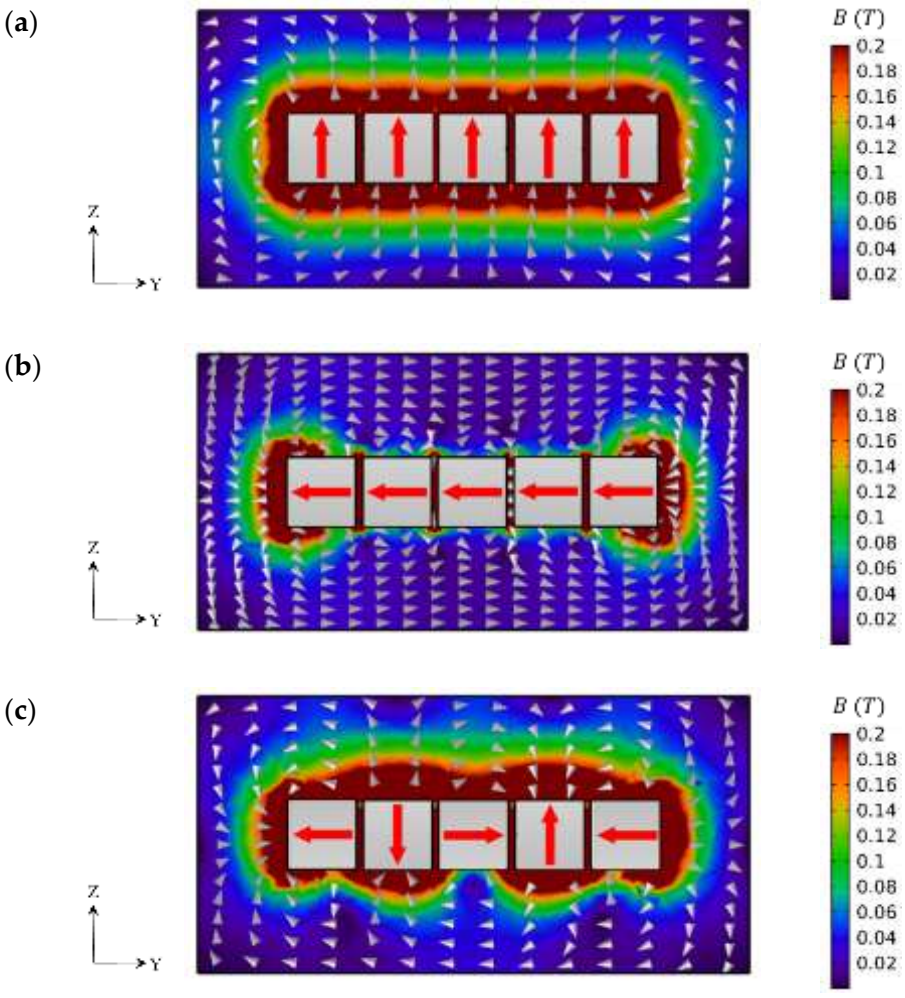

Figure 5-9 Magnetic field distribution of (a) vertical array; (b) horizontal array; and (c) Halbach array.

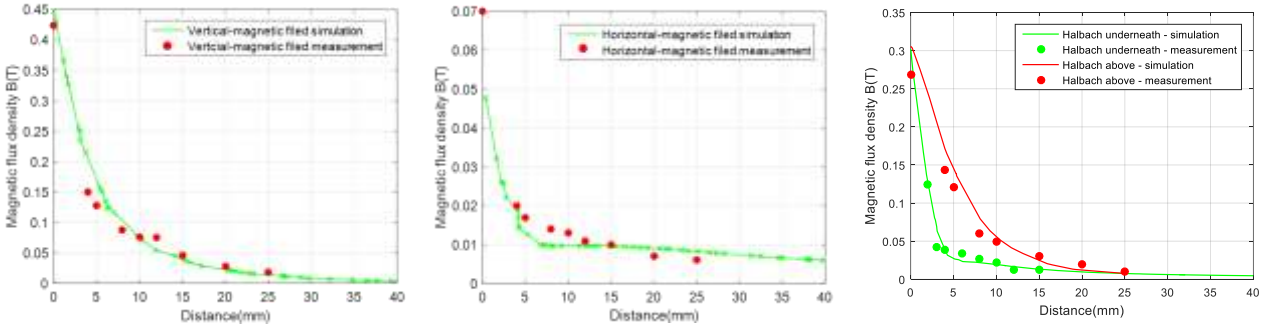

(a) (b) (c)

Figure 5-10 Magnetic flux density (B) versus z-distance of (a) vertical array; (b) horizontal array; and (c) Halbach array.

5.3.3 Setup implementation on 3D printer

Figure 5-11 shows the customized magnetic source that consists of the magnet array embedded into a home-made substrate. The substrate was 3D printed using FDM (fused deposition modeling) technique. Continuous filament of PLA thermoplastic (Polymaker PolyPlus PLA) is fed to the commercialized printer (FlashForge - Creator Pro), allowing to obtain desired size and shape of the substrate. By adjusting its thickness, it is possible to control the distance between the magnet array and the printed composite. Therefore, the desired magnetic field applied on the sample can be achieved.

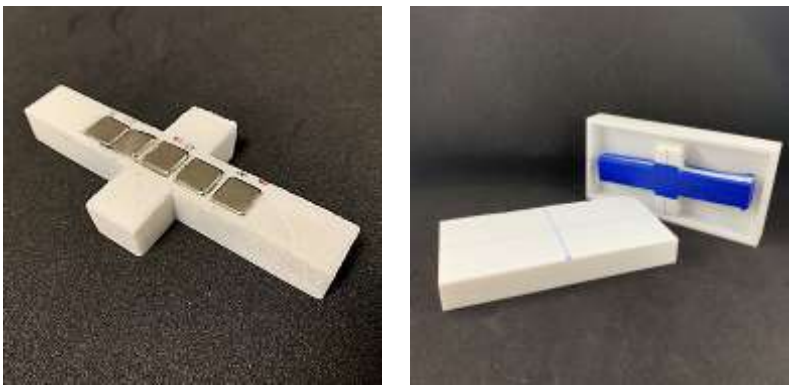

Figure 5-11 Customized magnetic source including magnet array embedded into plastic substrate

Figure 5-12 illustrates the whole 3D printing setup. The magnetic array was placed below the extruder nozzle so as to deliver a magnetic field to the printed samples. The printing process of the isotropic material was previously described in subsection 5.2.2. Similar steps are conducted to the anisotropic sample, with an addition of the external filed under which the particles can orient itself. The advantage of this approach is that the printer configuration does not require any modifications, only the permanent magnet has to be attached to the printing bed.

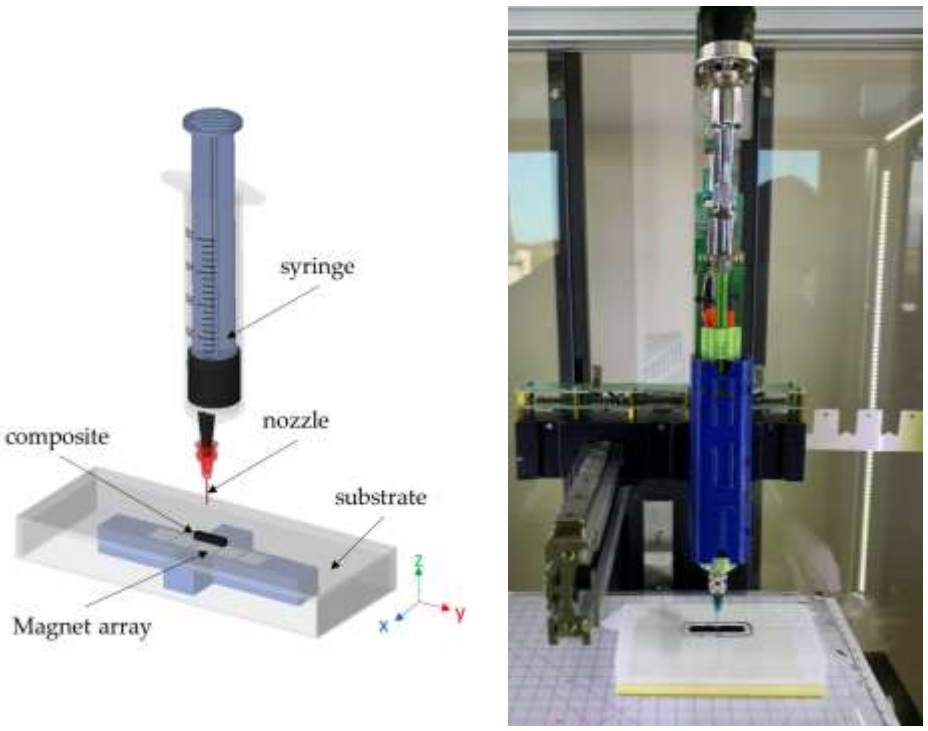

(a) (b)

Figure 5-12 (a) Schematic and (b) physical image of 3D printing set up.

5.4 Optimization of 3D printing anisotropic composites

The goal of this section is to perform magnetic anisotropic composite with the help of the test bench described above. As the printing manipulation is subjected to the magnetic field, optimization of the printer setup becomes the main concern.

5.4.1 Optimization of magnetic field level

The 30% vol. Fe_3O_4@PDMS composites were excited with or without magnetic field. In case of magnetic field application, a set of configurations are investigated such as vertical array, horizontal array, and Halbach array. The filed level does not only depend on the chosen configuration but also on the distance between the magnetic source and the printed sample. Short distance leads to strong magnetic flux density (B) but makes the printing process complicated because of strong interaction between the permanent magnets and the ferromagnetic composite. Consequently, the trajectory of the extruded paste could be modified, resulting in deformed shape of the printed samples. Long distance, on the other hand, decreases drastically the magnetic strength and therefore can affect to the alignment of ferromagnetic particles. Here we opted for three distances (4mm, 8mm, and 12mm) to perform the needle shaped composites printed with dimension of 33×5×4 mm^3. In each case, the magnetic flux density (B) as well as the mass (M) of the sample were assessed. All values were available in Table 5-1. It is noted that B was measured above the magnet array, i.e.

corresponding to the working area of the printing manufacture. To improve the accuracy of the mass measurement, we take the average value obtained from three samples fabricated at the same condition. The sample printed without magnetic field is chosen as reference, which can be compared with other oriented samples.

Figure 5-13 graphically illustrated the results of Table 5-1. It can be seen in Figure 5-13 (a) that the evolution of B as a function of the distance and of the magnets configuration is coherent to the analyses of subsection 5.3.2. Actually, the vertical array and the Halbach array leads to similar good magnetic performance while it is very weak in the case of horizontal array. As B substantially drops with the distance, a significant fall in magnetic strength from 4 mm to 8 mm has been observed. Nonetheless, only somewhat decrease occurs from 8 mm to 12 mm. This explains why in Figure 5-13 (b), the average mass of the anisotropic composites is very similar when being set at these two distances. Contrarily to the case of 4mm, the printing paste is affected by strong magnetic field, resulting in significant loss of mass with respect to the one of the referenced sample. The distance at above 8mm is more suitable for the AM thanks to its high mass fidelity under whatever magnet array configuration. Even with the most optimized working condition, small variation of mass still exists, which is due to inevitable factors manifesting during the printing procedure. For instance, we all know that the syringe movement was automatically controlled by a precise stepper motor, but whether the paste can be output continuously depends on the particles dispersion within the PDMS matrix. Indeed, the aggregation of particles could cause the clogging issue, provoking a small deviation of the printed sample. Finally, for the best trade-off between the magnetic performance and the printing quality, we opt for a distance of 8 mm between the magnet array and the printing bed.

Table 5-1 Measured values of the magnetic flux density (B) and the average mass (M) of 30% vol. Fe_3O_4@PDMS composites printed at various distances from the array surface.

Distance	Without magnetic field (mT)		Vertical array (mT)		Horizontal array (mT)		Halbach array (mT)	
	B (mT)	M (g)	B (mT)	M (g)	B (mT)	M (g)	B (mT)	M (g)
4mm	0	1.423	150	1.117	20	1.117	143	1.303
8mm	0	1.459	88	1.462	14	1.462	60	1.437
12mm	0	1.425	75	1.432	11	1.432	45	1.436

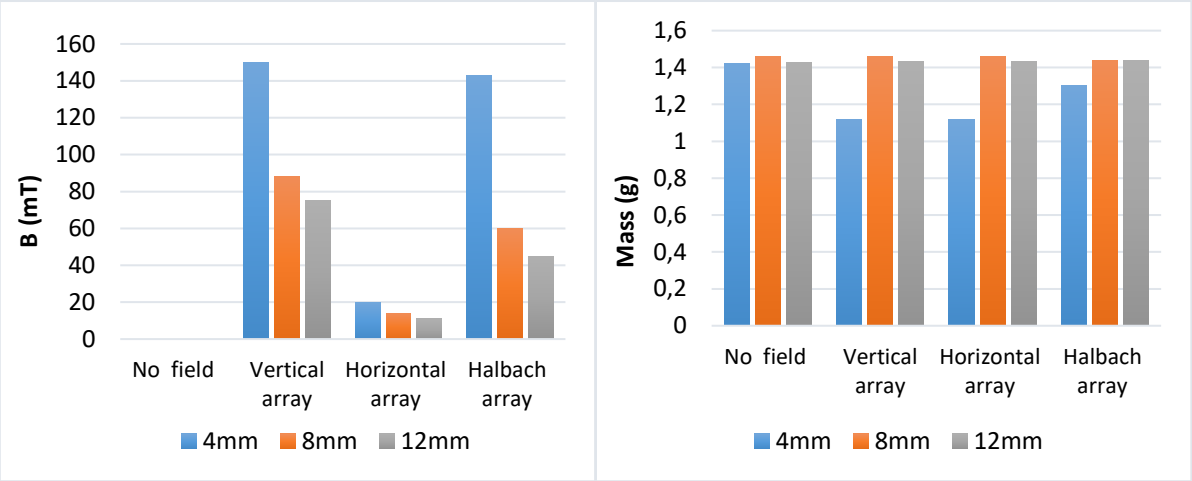

Figure 5-13 Distance influence of a) the magnetic flux density; and b) the mass for the printed composites under 4 setup configurations.

5.4.2 Optimization of the printer nozzle

In subsection 5.2.3, we printed the isotropic pattern letters with the stainless steel nozzle, here referred to as PSS tip. When the printing platform was subjected to an external magnetic source, the nozzle, containing about 50% of ferrite, would be somehow attracted by the magnets; especially when they get closed together. With the aim of decreasing the magnetic effect to the nozzle, a plastic tip with the same inner diameter of 0.84mm (Smoothflow tapered tip ID 7018158, here referred to as STT) has been used to replace the PSS tip (see Figure 5-14). The following result allows to verify whether or not the type of nozzle could affect the sample performance in terms of heating temperature and magnetic permeability. Figure 5-15 shows a comparison between the PSS and the STT tip, with which the needle-shaped composites was performed.

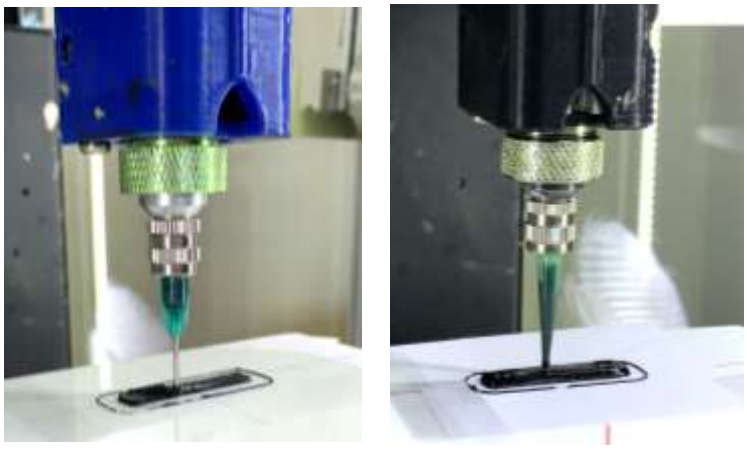

(a) (b)

Figure 5-14 Inject syringe attached with (a) stainless steel tip (PSS); and (b) plastic tip (STT).

The results revealed that both temperature response (Figure 5-15 (a)) and magnetic permeability (Figure 5-15 (b)) of the oriented samples substantially enhances as opposed to the one randomly dispersed. Interestingly, the Halbach and the horizontal arrays leads to better responses compared to the vertical configuration. This behavior is probably originated from the thermal and magnetic anisotropies, which will be thoroughly detailed in the next subsection 5.5. To some extents, the final temperature of LFIH test as well as the relative permeability slightly improve with the STT tip. This is certainly due to the fact that it less interacts with the magnetic field than the PSS tip.

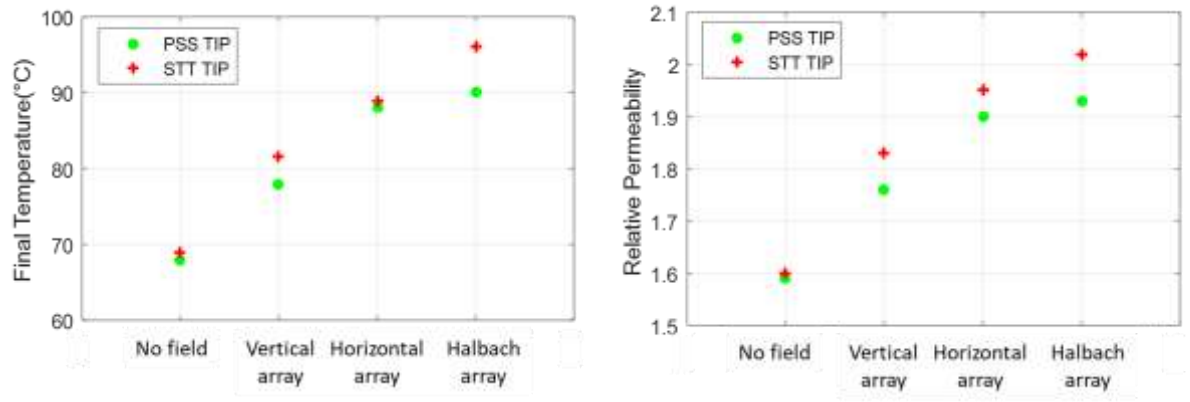

(a) (b)

Figure 5-15 Comparison of samples' properties printed with PSS tip and STT tip: (a) heating temperature difference of LFIH test; (b) relative permeability

5.4.3 Optimization of magnetic field direction

Figure 5-16 shows the needle-shaped composites subjected to different configurations of an external magnetic field. All samples, printed by the STT tip nozzle, are set at the same distance of 8mm from the magnet array. Whatever direction of magnetic field excitation, the outer surface of the oriented sample could form irregular contours as the extruding ink is disturbed by the field lines. In spite of the same material dispersion and fraction, the three magnetic sources do not give out similar sample's appearance. In other words, the printing quality definitively depends on the field direction.

Actually, the sample in Figure 5-16 (b) printed under vertical field (~ 88 mT) has the worst outer shape with extremely rough surface. Conversely, the horizontal field (~ 14 mT) leads to much better result because of not only its weaker magnitude (7-fold less) but also, and in particular, its direction. Indeed, the attractive force between the magnets and the oriented particles is maximal when it is in the vertical direction. On the other hand, if the magnetic force acts parallel to the contact surface (shear force) as in the horizontal setup, its value becomes much smaller (approximately of 15-25% of the maximum force [150]). This behavior was

clearly shown on Figure 5-9 : the field is maximal above and underneath in the vertical array whereas in the horizontal one, it is more significant in the two sides. Thus, the horizontal configuration allows to achieve anisotropic composite with satisfactory appearance, i.e. similar to the un-oriented sample. It is noteworthy in Figure 5-16 (d) that the Halbach array leads to intermediary shape quality compared to the other configurations. The surface of the sample is not so regular: smooth on the center and rough on the both sides. This look can be explained based on the Comsol simulation described on Figure 5-9. Indeed, the magnetic field above the Halbach array is only homogenous in direction and magnitude (~ 60 mT) within 10mm around the center. As demonstrated, the direction is perfectly horizontal in the center while almost vertical in the both sides.

(a) (b) (**c**) (d)

Figure 5-16 Samples printed with STT tip under 4 configurations: (a) without magnetophoresis; and with magnetophoresis consisting of (b) vertical array; (c) horizontal array; and (d) Halbach array

The above results let to a conclusion that the horizontal magnetic field is the best configuration for significantly reducing the fidelity loss of the sample shape. There is still a lot to improve in terms of material and processing. For the future research, it is worth to develop UV curable feedstock. For example, add photo-initiator to PDMS or directly use photosensitive resin to replace it. Providing the printing sample UV light makes a possibility to achieve curing at the same time. This will enhance the shape fidelity so as to reach the goal of printing complex parts. Besides, other technique should be taken into consideration to avoid clogging from agglomeration of particles in the printing tip. For instance, mounts a magnetic shield on the printing tip, or add auxiliary dispersant (e.g., chloroform) [151] during feedstock preparation step to get a better dispersion of particles.

The next section reports on characterization, through which we aim to figure out how the printing process itself affects the thermal and magnetic anisotropies of the sample. The effect of magnetic alignment has been investigated as well in both cubic and needle shaped samples.

5.5 Characterization of IH and magnetic properties

In this section, two types of samples were made: cubic and needle shaped, printed with and without a magnetic alignment field, whose magnitude depends on the selected alignment configuration. The cubic shape (5×5×5 mm^3) is firstly investigated as it is more adequate for

testing anisotropy in three directions (x-, y-, and z-axis). The needle shape (33×5×4 mm^3), which fits better to application of varicose treatment, will be presented next.

5.5.1 Cubic-shaped composites

To design the anisotropic cuboid composites, the horizontal array and the Halbach array are used to drive the magnetic field along y-axis. The vertical configuration is not adaptable to print such a small sample size, as the working space of the printing nozzle is extremely close to the center where the magnetic field is the strongest (cf. Figure 5-17). It can be observed in Figure 5-17 that the Halbach array allows to achieve samples printed in proper shape as the horizontal array. This, gain, allows to confirm the field homogeneity at the center of the Halbach array.

Figure 5-17 Cubic-shape samples printed under the two types of horizontal magnetic field.

The sample's magnetic permeability can be determined based on the measurement of its inductance via the LCR impedance meter (see subsection 2.3.2). All samples are manually wired with 10 turns in a single layer and have been measured under the low-frequency range (20Hz to 1MHz). Figure 3-19 shows how to measure the permeability in different x-, y-, and z-axes, which are determined by the direction of the induced flux density ($B_{induced}$). $B_{induced}$ is resulted from a current (I) delivered by the impedance mater that flows through the wire.

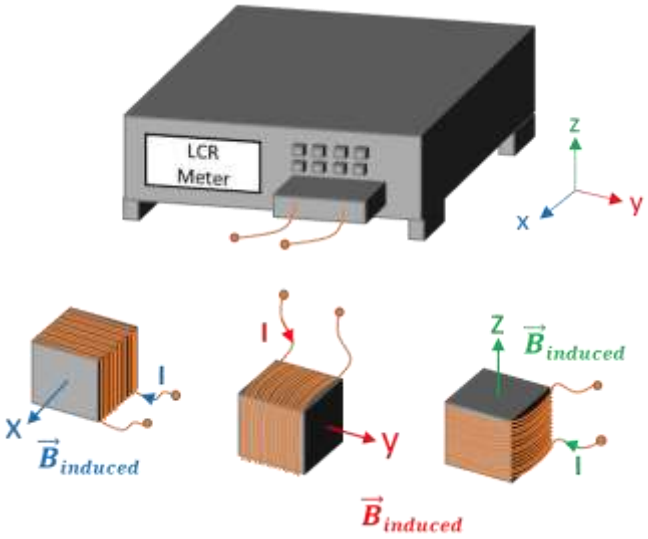

Figure 5-18 Permeability test in 3 directions: (a) x-axis; (b) y-axis; and (c) z-axis

The relative permeability of the 30% vol. Fe_3O_4@PDMS composites under various configuration are compared in Figure 5-19. The results allows to conclude that:

- Whatever magnetic field configuration, the relative permeability is almost constant under the low-frequency range.
- The un-oriented sample exhibits the lowest relative permeability in each axis. Its magnetic isotropic is confirmed by the fact that the permeability is the same for all directions. Only one curve (black color) has been displayed in Figure 5-19 to avoid overlap.
- The orientation of magnetic particles enhances the permeability along the x- and y-axes, but more significant in the easy direction (y-axis). Inversely, no improvement along the z-axis.
- The Halbach array leads to higher relative permeability in the y-axis than the horizontal array. It is contrary to the case of the x-axis. Accordingly, the cubic sample printed under the Halbach array has stronger anisotropic behavior, which is due to larger change in magnetic strength between the x- and y-axes. This property is probably manifested by the unsymmetrical and irregular field distribution driven by the Halbach configuration.

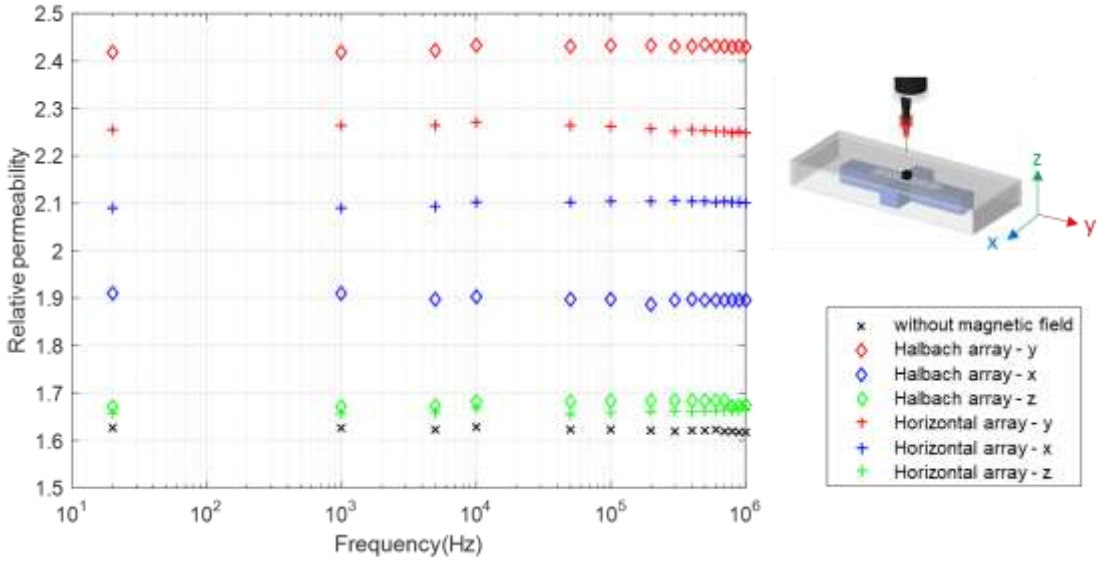

Figure 5-19 Relative permeability of printed cubic sample in different axis.

The LFIH test results of the printed cubic samples under horizontal array and Halbach array are shown in Figure 5-20. Experimental test bench was described in Figure 3-1 (chapter 3.1.1) where the 16-magnet inductor were used to generate a 4200-Hz magnetic field. It is expecting that the temperature response is the most significant in the preferred direction (y-axis) and the lowest in the z-direction, regardless of which magnetophoretic configuration is used during printing process. This behavior faithfully matches the permeability response as illustrated in Figure 5-19. Surprisingly, the Halbach array does not show a considerable improvement in IH effect for all directions, even along the easy y-axis. The result indicates that moderate amplitude generated by magnetophoresis is sufficient to perform anisotropy. Experiment demonstrates only 5% to 10% enhancement in temperature and permeability against 4-folds increase of magnetic strength (60 mT in the Halbach array versus 14 mT in the horizontal array). On a one hand, low filed level is enough to successfully magnetize particles. On the other hand, the direction of the external filed excitation is a key factor to favor anisotropy, either in magnetic or thermal test. In reality, exciting samples with the magnetic field collinear to the preferred direction, to some extent, gives raise to significant enhancement in relative permeability (50% increase), and temperature (30% increase) as well.

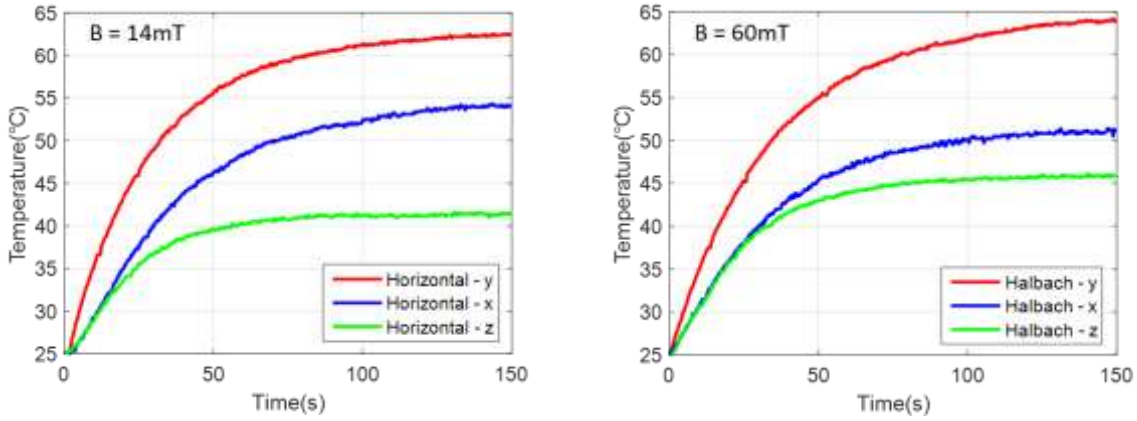

(a) (b)

Figure 5-20 Time evolution of temperature measured on cubic samples subjected to magnetophoresis using (a) horizontal array; and (b) Halbach array.

In sum, magnetic alignment, which orients the easy axes of magnetic particles in the same direction as the applied field, sustainably increases permeability and IH effect. In the next subsection, we focus on characterization of the needle-shape composites, whose dimension in the three directions are not identical as in case of the cubic shape. It will be reveal that the sample's geometry, to some extents, could affect to the anisotropic thermal exchange.

5.5.2 Needle-shaped composites

This study aims to confirm that the effect of magnetic orientation is also seen in the low frequency IH and permeability measurements performed on needle-shaped samples. Here we investigate on the experimental characterization of the four samples depicted in Figure 5-16, which are subjected to the four configurations used in the printing process. As described in Figure 5-21 (a), the permeability is measured along the alignment-induced preferred direction (y-axis). This explains why the composites printed under the horizontal magnetic field gives higher permeability value than the one printed under the vertical axis (Figure 5-21). Evidently, the sample fabricated without magnetophoresis has the lowest relative permeability. In contrast, those printed under a magnetic field either in horizontal direction (y-axis) or in vertical direction (z-axis), exhibit anisotropy with enhancement of magnetic permeability. As observed, the anisotropic response is the most obvious in the case of the Halbach array with an increase of approximately 30% with respect to the un-oriented sample.

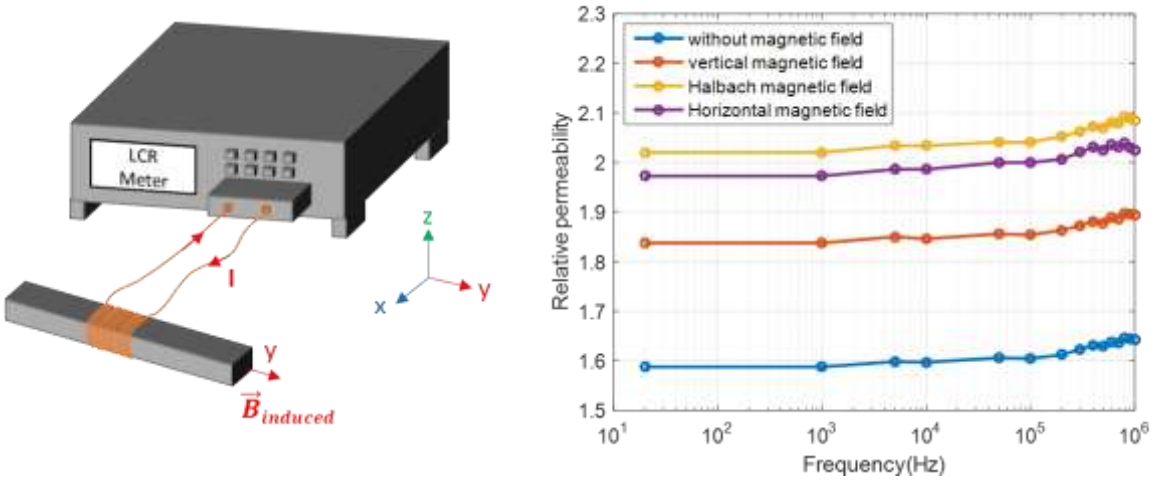

(a) (b)

Figure 5-21 (a) Permeability test in y-axis direction; (b) Relative permeability versus frequency of un-oriented and oriented samples with and without magnetiphoretic process.

Figure 5-22 (a) performs the IH test where the composite induced by an AC magnetic excitation along the thickness direction (z-axis). The temperature variations as functions of time for the three oriented samples and the un-oriented one are displayed in Figure 5-22 (b). Based on these results, some conclusions are outlined as following:

- Alignment of particles during AM induces anisotropy of the composite. This is manifested by its significant enhancement in IH effect as opposed to the one of the isotropic sample. An increase of around 35 % has been achieved with the most optimized magnetophoresis.
- The sample printed under the Halbach magnetic source has the highest final temperature of around 95°C. This value is getting closer to the target temperature imposed by medical use.
- Based on the best trade-off between the IH performance and the shape fidelity via 3D printing, the horizontal array seems to be the best choice with final temperature near to 90°C.
- Time constant of more than one minute is still an issue in LFIH, while endovenous ablation needs much faster temperature response of 4 - 5 seconds. Significant improvements in terms of process, material, and experimental setup are challenging but nonetheless will be one of most priorities in our future development.
- According to the previous analyses (subsection 5.5.1 and 4.4), the sample printed using the vertical array would show the best temperature response, since the magnetic field generated by the 16-magnet inductor has the same direction to the preferred z-axis (see Figure 5-22 (a)). However, the result in Figure 5-22 (b) indicates the contrary. In reality,

the composites printed under the horizontal magnetic field reveals higher anisotropic behavior. The only reason can explain this discrepancy is based on the difference of sample's geometric. This study deals with the needle-shaped composite with dimensions not equal in the three direction. As opposed to the cuboid sample, the needle one has much greater length/width ratio that further contribute to the thermal anisotropy at the lateral surfaces. Such an effect maybe masked in the cuboid sample because of its small size and particular geometry. This issue will be clarified in the following discussion.

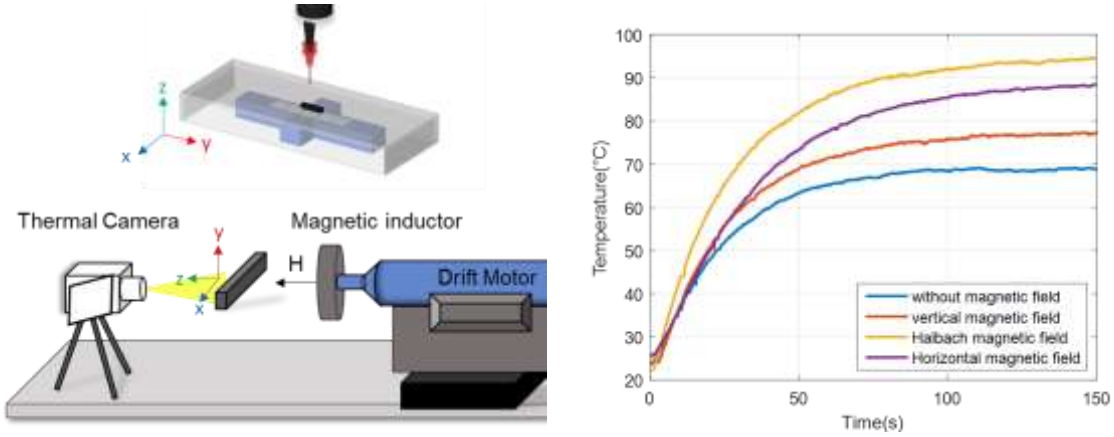

(a) (b)

Figure 5-22 (a) IH test in z-axis direction; (b) Temperature versus time plot for sample printed under different magnetophoretic conditions.

Thermal conductivity of composite could be increased by optimizing the physical contacts between adjacent particles in polymer matrix. According to [152][153], one of simple methods involving in alignment of particles, which enhances the generation of successful pathways for heat conduction (Figure 5-23 (a)). As seen in Figure 5-23 (b), particle arranged in horizontal direction contributes to the increase in thermal conductivity along that direction. This facilitates heat dissipation on the two side surfaces. Similarly, the heat dissipation on the composites filled with particle vertical chains occurs easier in the above and bottom surfaces. It is obvious that composites with vertically aligned particles lead to larger "easy" surfaces of heat dissipation compared to those with the horizontal direction. Actually, the higher are the "easy" surfaces, the higher are the thermal exchanges induced by radiation and convection. A significant length/width ratio of the needled sample favors the thermal exchanges in the vertical direction, resulting in lower temperature with respect to the one in the horizontal direction.

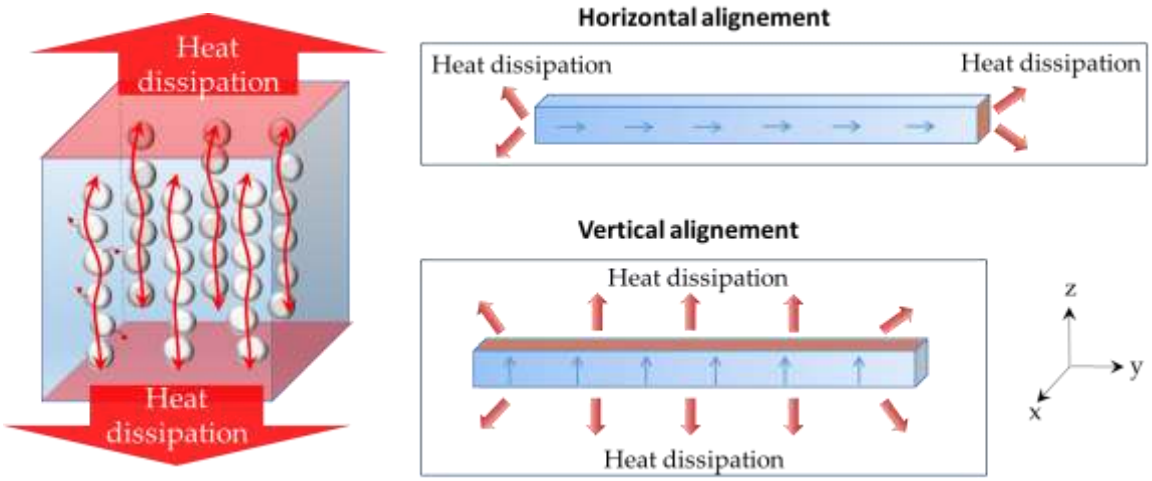

(a) (b)

Figure 5-23 (a) Thermal conductance pathways generated by particle chain-like structure; (b) Heat dissipation of composites aligned in z-axis and y-axis .

In order to confirm the contribution of the pathway for the improvement in thermal conductivity, empirical measure is carried out on a cuboid sample (18mm side length) via a Thermal Conductivity Analyser (TCi Thermal Conductivity Analyzer). The technique consists in using a unilateral interfacial thermal reflectance sensor that applies a constant heat source to the sample (Figure 5-24). The instantaneous measurement of thermal conduction ensures a detailed overview of the heat transfer properties of the samples [154]. For a better comparison, two kind of tested composites are chosen, including random distributed sample, and anisotropic sample aligned in z-axis (Figure 5-23 (a)). From the measurement of the thermal conductivity (λ) and the effusivity (e), it is possible to induce the specific heat capacity (C_p) of the composites that can be given by:

$$C_p = \frac{e^2}{\lambda \rho} \qquad \text{Equation 5-1}$$

where ρ is the mass density.

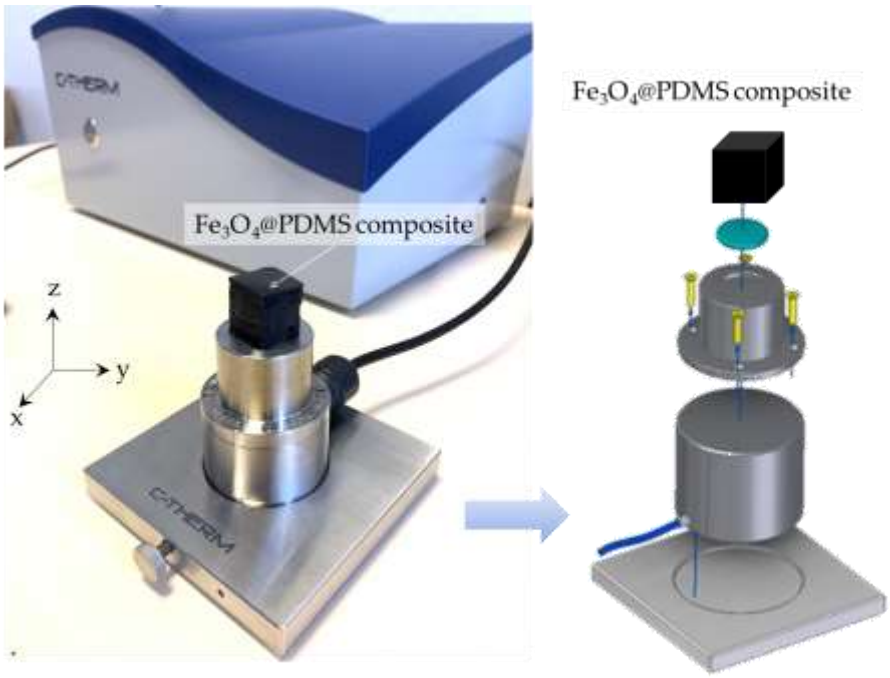

Figure 5-24 Measurement via thermal conductivity analyzer[154]

The results of λ and C_p are shown in Table 5-2. Due to the particle agglomeration in vertical direction, the randomly distributed composite has different values on z-axis and x,y axis. Two major mechanisms lead to the agglomeration of particles in the sample. The first one is related to Brownian motion, occurring when particles collide and stick together as a result of their random. This phenome is more obvious in the case of nano particles. Another mechanism, in particular, that leads to the agglomeration of particles is known as gravitational agglomeration, which is dependent on the size of the particles and their terminal velocity[155]. The slowly settling particles are caught by the more rapidly settling particles, leading to the formation of clusters. The clustering of particles has an effect on material properties (thermal, mechanical, electric, etc.). During the fabrication process, microparticles in downward is inevitable and the degree of agglomeration is settled principally by gravitational force.

As expected for the oriented sample (cf. Table 5-2), the thermal conductivity increases around 58% in the z-axis compared to the one of the random sample. The increase thermal conductivity stems from easy straight pathway generated by the particle chains. Regarding the specific heat capacity, a slight increase of approximately 10% in the z-axis has been obtained, meaning that a little higher amount of energy is needed to heat the sample on that direction. The alignment of particles results in an anisotropic behavior, i.e. more obvious on the thermal conduction than the heat capacity.

Table 5-2 Thermal conductivity and specific heat capacity of the random and oriented composites measured in different direction

	Thermal Conductivity λ (W/mK)		Specific heat capacity C_P (J/kgK)	
	z-axis	x,y -axis	z-axis	x,y-aixs
Randomly distributed cubic sample	0.47	0.65	659.32	708.47
Oriented cubic sample (aligned in z-axis)	0.74	0.6	723.34	695.82

Finally, all these results are very encouraging, confirming high potential of ferromagnetic composites for LFIH application. The developed material is biocompatible, flexible, and adaptable to AM; making it possible to be 3D printed in different size and shape that matches varicose vein treatment. Particle alignment during fabrication clearly shows enhancement in thermal and magnetic anisotropy. Future works aims to improve the material and process in order to achieve the target temperature of 120°C as well as faster response time.

Another issue which also attracts surgeon's interest is that whether or not varicose veins could be treated with lower temperature. Experimental measurement is carried to determine the melting temperature of the human veins. Thanks to the medical staff working with us, we had the opportunity of testing living blood vessels collected from surgical interventions. The preliminary results obtained from differential scanning calorimetry (DSC) tend to confirm a transition effect between 110°C and 120°C (cf. Figure 1-12). This transition is also confirmed from visual observation since we can witness the blood vessel starting to melt. However, electrocoagulation as required by the varicose treatment is probably happening at lower temperature.

Most of current commercialized devices dedicated to the endovenous thermal ablation work with an imposed temperature of 120°C, which corresponds to the melting temperature of the vein. However, based on the clinical protocol, the duration of such a temperature must be very short, around 4-5 seconds in order not to melt the vein and damage the surrounding tissue. The principal of the endovascular technique is to close up the varicose vein, not to melt it. As a result, the heating device can go up to 120°C, but not the vein. Even surgeons, no one knows whether an application of lower temperature (i.e. around 100°C) with a longer duration could be effectiveness for the procedure. Further in-vitro test will be carried out to confirm this concern. In any way, lowering the temperature is certainly safer for human's tissue and thus of high benefit for patients.

5.6 Summary

This chapter reported on construction and optimization of magnetophoresis via AM process. Based on 3D printing technology, desired shapes and sizes of 30% vol. Fe_3O_4@PDMS

composites were successfully fabricated with effective cost and time. Magnetic particles did not simply mix with the polymer but formed chain-like structure under a magnetic field applied during the printing stage. The chain-like structure is useful for providing anisotropic magnetic and thermal properties to the sample. Using these anisotropies, not only we can improve the relative permeability, but also the IH effect. Such enhancements are particularly of high benefit for medical uses such as electromagnetic tracking system, varicose treatment device, and so on.

Printing paste composed of other magnetic particles with high shape anisotropy, such as flake shape or rod-like shape, can be further investigated to achieve better alignment effects. As a next step, the results motivate the development of a customized setup capable of aligning the particles during printing by applying a variable external magnetic field in the desired direction. After successfully implementing this design, complex structures with special magnetic capabilities should be printable. This would be a breakthrough in the development and manufacturing of ferromagnetic composites with varying local magnetization directions.

General Conclusion

This research reported on the Low Frequency Induction Heating (LFIH) effect on ferromagnetic composites, which has high potential for medical use. It was demonstrated that the heating behavior could be affected by diverse factors, including :

- parameters related to the materials (e.g. content, nature, size of the magnetic particles; dimension of composite, dispersion and structuration of the iron powder within the polymer matrix, thermal conductivity and specific heat of both polymer and fillers, etc.);
- parameters related to the external magnetic excitation (e.g. frequency, amplitude, and direction);
- parameters related to the external environment (e.g. heat dissipation, thermal exchange).

Firstly, optimization of the above parameters to reach the target temperature (120°) was the key objective of the thesis. Experimental and simulation results showed the feasibility of our device, enabling to heat the Fe_3O_4@ABS composite to 100°C. Accordingly, improving material and process led to satisfactory temperature that was closed to requirement of the venous insufficiency procedure. Furthermore, to fit with medical tools, the ferromagnetic devices were elaborated to a needle-like shape that is small enough to navigate inside the vessels. Great LFIH enhancement has been achieved, even though lots of issue should be taken into consideration to match the medical interests. These initial results, however, were very encouraging, confirming a possibility to generate substantial temperature increase based on low-frequency magnetic field. To the best of our knowledge, this is the first time LFIH approach has been demonstrated to be high potential for minimally-invasive therapies. Most recent researches based IH related to medical application (e.g. hyperthermia cancer treatment) required extremely high power supply up to a few MHz, involving very complex system where accurate power converters and control design become mandatory.

Secondly, improvement of the magnetic-thermal conversion of ferromagnetic composites was obtained by performing an anisotropic structure. Samples were fabricated based on the casting method. The particles were aligned within PMDS matrix by application of a constant magnetic field during curing stage. 3D @Comsol simulations allowed to check the relative homogeneity of the magnetic excitation field in the sample area. Just as expected, SEM images showed strong particle alignments of the anisotropic composites. Eventually, oriented samples excited in the easy direction gave rise to 20% increase in temperatures as opposed to the un-oriented ones. Coupling this observation and the time constants comparison led to an enhancement of magneto/thermal power conversion of approximately 30%. This study revealed that higher anisotropic behaviors of the fabricated composites was effectively achieved based on the alignment of the ferromagnetic particles.

Thirdly, we kept our work on optimization of material formulation so as to be adaptable to 3D printer. Such an advancement in additive manufacturing (AM) made a possibility to get miniaturized heating or sensing elements. This allowed to facilitate their integration in medical instruments like electromagnetic tracking system or endovenous thermal ablative tool. Desired shapes and sizes of 30% vol. Fe_3O_4@PDMS composites were successfully 3D printed with effective cost and time. The needle-shaped sample built under the optimized magnetic strength and direction results in improved temperature of around 95°C. It was revealed that printing material through magnetophoresis has shown high benefit to enhance anisotropy. However, it could make the printing process difficult because of attractive force between the magnets and the paste, provoking shape fidelity loss. Based on the best trade-off between the IH performance and the shape fidelity, the horizontal field direction was considered to be the best configuration.

Finally, several aspects would be considered in our future research direction. Some of them are cited as below:

- using other forms of magnetic particles with higher shape anisotropy;
- getting a better dispersion of particles to avoid clogging nozzle;
- customizing special shape and size of ferromagnetic catheter tips for patients who have varicose veins treated;
- developing and manufacturing ferromagnetic composites with varying local magnetization directions;
- building UV curable feedstock so as to cure sample during printing stage;
- enhancing IH setup with higher magnetic frequency (e.g. a few tens of kHz) in order to achieve the desired temperature with faster time constant;
- designing anisotropic materials with a more complex structure so as to get multi magnetic sensors embedded into electromagnetic tracking system.

Last but not least, to confirm the reliability of the proposed approach for real clinical environments, further *in vitro* and *in vivo* tests are under consideration for future exploration. The next step is to compare the long-term efficacy and the risk-benefit ratio of the LFIH method with those of existing endovenous techniques. To sum up, the thesis work not only confirmed high performance of anisotropic ferromagnetic composites, but also paved the way for a new technique of varicose treatment based LFIH effect.

References

[1] A. Aharoni, *Introduction to the theory of ferromagnetism*. Oxford University Press, 2000.

[2] R. C. Smith and C. L. Hom, "Domain Wall Theory for Ferroelectric Hysteresis," *J. Intell. Mater. Syst. Struct.*, vol. 10, no. 3, pp. 195–213, 1999.

[3] P. Gaunt, "Ferromagnetic domain wall pinning by a random array of inhomogeneities," *Philos. Mag. B Phys. Condens. Matter; Stat. Mech. Electron. Opt. Magn. Prop.*, vol. 48, no. 3, pp. 261–276, Sep. 1983.

[4] T. J. Yang, V. Gopalan, P. J. Swart, and U. Mohideen, "Direct Observation of Pinning and Bowing of a Single Ferroelectric Domain Wall," *Phys. Rev. Lett.*, vol. 82, no. 20, pp. 4106–4109, May 1999.

[5] A. Hubert and R. Schäfer, "Introduction," in *Magnetic Domains*, Berlin, Heidelberg: Springer Berlin Heidelberg, 2008, pp. 1–10.

[6] J. P. A. Bastos and N. Sadowski, *Magnetic materials and 3D finite element modeling*. 2013.

[7] D. Ribbenfjärd, *Electromagnetic transformer modelling including the ferromagnetic core*. Skolan för elektro- och systemteknik, Kungliga Tekniska högskolan, 2010.

[8] R. Hergt *et al.*, "Physical limits of hyperthermia using magnetite fine particles," *IEEE Transactions on Magnetics*, vol. 34, no. 5 pt 2. pp. 3745–3754, 1998.

[9] S. Kasap and P. Capper, *Springer Handbook of Electronic and Photonic Materials*. 2007.

[10] G. H. Goldsztein, F. Broner, and S. H. Strogatz, "Dynamical hysteresis without static hysteresis: scaling laws and asymptotic expansions," *SIAM J. Appl. Math.*, vol. 57, no. 4, pp. 1163–1187, 1997.

[11] K. P. Lee, A. Gopalan, S. Komathi, and D. Raghupathy, "Polyaniline-based nanocomposites: Preparation, properties and applications," in *Physical Properties and Applications of Polymer Nanocomposites*, Woodhead Publishing, 2010, pp. 187–243.

[12] Filipcsei G Csetneki I Szilágyi A Zrínyi M, "Magnetic Field-Responsive Smart Polymer Composites," *Adv. Comput. Simul. Approaches Soft Matter Sci. I*, no. May, pp. 85–98, 2008.

[13] M. Zrínyi, L. Barsi, and A. Büki, "Deformation of ferrogels induced by nonuniform magnetic fields," *J. Chem. Phys.*, vol. 104, no. 21, pp. 8750–8756, 1996.

[14] C. BELLAN and G. BOSSIS, "Field Dependence of Viscoelastic Properties of Mr Elastomers," *Int. J. Mod. Phys. B*, vol. 16, no. 17n18, pp. 2447–2453, 2002.

[15] G. V. Stepanov, D. Y. Borin, Y. L. Raikher, P. V. Melenev, and N. S. Perov, "Motion of ferroparticles inside the polymeric matrix in magnetoactive elastomers," *J. Phys. Condens. Matter*, vol. 20, no. 20, 2008.

[16] J. Ma, J. Hu, Z. Li, and C. W. Nan, "Recent progress in multiferroic magnetoelectric composites: From bulk to thin films," *Adv. Mater.*, vol. 23, no. 9, pp. 1062–1087, 2011.

[17] L. H. Reddy, J. L. Arias, J. Nicolas, and P. Couvreur, "Magnetic Nanoparticles : Design and Characterization , Toxicity and Biocompatibility , Pharmaceutical and Biomedical Applications," 2012.

[18] M. Y. Razzaq, M. Anhalt, L. Frormann, and B. Weidenfeller, "Thermal, electrical and magnetic studies of magnetite filled polyurethane shape memory polymers," *Mater. Sci. Eng. A*, vol. 444, no. 1–2, pp. 227–235, 2007.

[19] C. C. Corten, M. W. Urban, and F. Shelby, “Repairing polymers using an oscillating magnetic field,” *Adv. Mater.*, vol. 21, no. 48, pp. 2784–2787, 2010.

[20] B. J. Adzima, C. J. Kloxin, and C. N. Bowman, “Externally triggered healing of a thermoreversible covalent network via self-limited hysteresis heating,” *Adv. Mater.*, vol. 22, no. 25, pp. 2784–2787, 2010.

[21] G. Li and D. Nettles, “Thermomechanical characterization of a shape memory polymer based self-repairing syntactic foam,” *Polymer (Guildf).*, vol. 51, no. 3, pp. 755–762, 2010.

[22] C. Bárcena, A. K. Sra, and J. Gao, “Applications of magnetic nanoparticles in medicine: magnetic fluid hyperthermia,” *Nanoscale Magn. Mater. Appl.*, vol. 28, no. 3, pp. 591–626, 2009.

[23] R. E. Rosensweig, “Heating magnetic fluid with alternating magnetic field,” *J. Magn. Magn. Mater.*, vol. 252, pp. 370–374, 2002.

[24] L. Michael, C. Wilhelm, J. Siaugue, O. Horner, J. Bacri, and F. Gazeau, “Magnetically induced hyperthermia : size-dependent heating power of γ -Fe2O3 nanoparticles,” *J. Phys. Condens. Matter*, vol. 204133, 2008.

[25] R. Hergt, S. Dutz, and M. Zeisberger, “Validity limits of the Neel relaxation model of magnetic nanoparticles for hyperthermia,” *J. Phys. Condens. Matter*, vol. 015706, pp. 1–6, 2010.

[26] B. Ducharne, M. Q. Le, G. Sebald, P. J. Cottinet, D. Guyomar, and Y. Hebrard, “Characterization and modeling of magnetic domain wall dynamics using reconstituted hysteresis loops from Barkhausen noise,” *J. Magn. Magn. Mater.*, vol. 432, pp. 231–238, 2017.

[27] O. Lucia *et al.*, “Induction Heating Technology and Its Applications : Past Developments , Current Technology , and Future Challenges,” *IEEE Trans. Ind. Electron.*, vol. 61 (n°5)., pp. 2509–2520, 2015.

[28] R. L. C. Valery Rudnev, Don Loveless, *Handbook of Induction Heating - - Google Livres*. 2002.

[29] J. Acero *et al.*, “The domestic induction heating appliance: An overview of recent research,” *Conf. Proc. - IEEE Appl. Power Electron. Conf. Expo. - APEC*, pp. 651–657, 2008.

[30] K. M. PATEL, “An Overview of Applications of Induction Heating,” *Int. J. Electr. Eng. Technol.*, vol. 10, no. 2, pp. 81–85, 2019.

[31] P. R. Stauffer, T. C. Cetas, and R. C. Jones, “Magnetic Induction Heating of Ferromagnetic Implants for Inducing Localized Hyperthermia in Deep-Seated Tumors,” *IEEE Trans. Biomed. Eng.*, vol. BME-31, no. 2, pp. 235–251, 1984.

[32] C. S. S. R. Kumar and F. Mohammad, “Magnetic nanomaterials for hyperthermia-based therapy and controlled drug delivery,” *Adv. Drug Deliv. Rev.*, vol. 63, no. 9, pp. 789–808, 2011.

[33] P. Das, M. Colombo, and D. Prosperi, “Recent advances in magnetic fluid hyperthermia for cancer therapy,” *Colloids Surfaces B Biointerfaces*, vol. 174, no. October 2018, pp. 42–55, 2019.

[34] F. O. R. Limiting and E. To, *INTERNATIONAL COMMISSION ON NON-IONIZING RADIATION PROTECTION ICNIRP GUIDELINES FOR LIMITING EXPOSURE TO TIME - VARYING*, vol. 74, no. 4. 1999.

[35] E. Technology, “Portable cancer treatment system using induction heating,” Aalborg University, Denmark, 2012.

[36] B. J. Knauf, D. P. Webb, C. Liu, and P. P. Conway, “Low frequency induction heating for the sealing of plastic microfluidic systems,” *Microfluid. Nanofluidics*, vol. 9, no. 2–3, pp. 243–252, 2010.

[37] B. J. Knauf, D. P. Webb, C. Liu, and P. P. Conway, “Plastic packaging using low frequency induction heating (LFIH) for microsystems,” *10th Electron. Packag. Technol. Conf. EPTC 2008*,

pp. 172–180, 2008.

[38] “Low Frequency Heating Systems | Inductoheat Inc.” [Online]. Available: https://inductoheat.com/products/low-frequency-induction-heating/. [Accessed: 19-Mar-2021].

[39] Y. Iguchi, Atsushi, Kitamizo-cho Otsuka, “Low-frequency electromagnetic induction heater,” EP0383272A2, 2009.

[40] Z. Xiang *et al.*, “Induction heating-based low-frequency alternating magnetic field: High potential of ferromagnetic composites for medical applications,” *Mater. Des.*, vol. 174, p. 107804, 2019.

[41] H. Hydration, “The Water In You,” *The USGS Water Science School*. pp. 13–38, 2010.

[42] C. Carroll *et al.*, “Clinical effectiveness and cost-effectiveness of minimally invasive techniques to manage varicose veins: A systematic review and economic evaluation,” *Health Technol. Assess. (Rockv).*, vol. 17, no. 48, 2013.

[43] M. Arora, “Management of varicose veins,” *JK Sci.*, vol. 19, pp. 185–189, 2015.

[44] R. R. V. D. B. O. S. Rotterdam, J. Guex, H. Partsch, and C. Allegra, “Endovenous thermal ablation for varicose veins: strengths and weaknesses,” *Phlebolymphology*, vol. 19, no. 4, pp. 163–169, 2012.

[45] M. P. Goldman and S. Amiry, “Closure of the Greater Saphenous Vein with Endoluminal Radiofrequency Thermal Heating of the Vein Wall in Combination with Ambulatory Phlebectomy : 50 Patients with More Than 6-Month Follow-up,” *Dermatologic Surg.*, vol. 28, no. 1, pp. 29–31, 2002.

[46] J.-J. Liu, F. L.-H., X. D.-C., L. X., D. Z.-H., and F. W.-G., “The endovenous laser treatment for patients with varicose veins,” *Pakistan J. Med. Sci.*, vol. 32, no. 1, pp. 55–58, 2016.

[47] D. Grinberg, S. Siddique, M. Le, R. Liang, J. Capsal, and P. Cottinet, “4D Printing Based Piezoelectric Composite for Medical Applications,” pp. 1–7, 2018.

[48] Z. Xiang, B. Gupta, M. Q. Le, P. J. Cottinet, and B. Ducharne, “Hysteresis model of 3D printed magnetic particles based polymer composite materials,” in *2018 IEEE International Magnetic Conference, INTERMAG 2018*, 2018.

[49] L. H. Rasmussen, M. Lawaetz, L. Bjoern, B. Vennits, A. Blemings, and B. Eklof, “Randomized clinical trial comparing endovenous laser ablation, radiofrequency ablation, foam sclerotherapy and surgical stripping for great saphenous varicose veins,” *Br. J. Surg.*, vol. 98, no. 8, pp. 1079–1087, 2011.

[50] T. G. Poder, J. F. Fisette, S. K. Bédard, and M. A. Despatis, “Is radiofrequency ablation of varicose veins a valuable option? A systematic review of the literature with a cost analysis,” *Can. J. Surg.*, vol. 61, no. 2, pp. 128–138, 2018.

[51] S. Condino *et al.*, “Simultaneous tracking of catheters and guidewires: Comparison to standard fluoroscopic guidance for arterial cannulation,” *Eur. J. Vasc. Endovasc. Surg.*, vol. 47, no. 1, pp. 53–60, 2014.

[52] C. Nafis, V. Jensen, L. Beauregard, and P. Anderson, “Method for estimating dynamic EM tracking accuracy of surgical navigation tools,” in *Medical Imaging 2006: Visualization, Image-Guided Procedures, and Display*, 2006, vol. 6141, no. 61410, p. 61410K.

[53] Z. Yaniv, E. Wilson, D. Lindisch, and K. Cleary, “Electromagnetic tracking in the clinical environment,” *Med. Phys.*, vol. 36, no. 3, pp. 876–892, 2009.

[54] K. Schicho *et al.*, “Stability of miniature electromagnetic tracking systems,” *Phys. Med. Biol.*, vol.

50, no. 9, pp. 2089–2098, 2005.

[55] A. M. Franz, T. Haidegger, W. Birkfellner, K. Cleary, T. M. Peters, and L. Maier-Hein, “Electromagnetic tracking in medicine -A review of technology, validation, and applications,” *IEEE Trans. Med. Imaging*, vol. 33, no. 8, pp. 1702–1725, 2014.

[56] M. Nagel, M. Hoheisel, R. Petzold, W. A. Kalender, and U. H. W. Krause, “Needle and catheter navigation using electromagnetic tracking for computer-assisted C-arm CT interventions,” in *Medical Imaging 2007: Visualization and Image-Guided Procedures*, 2007, vol. 6509, p. 65090J.

[57] J. B. Hummel *et al.*, “Design and application of an assessment protocol for electromagnetic tracking systems,” *Med. Phys.*, vol. 32, no. 7, pp. 2371–2379, 2005.

[58] J. Thevenot *et al.*, “Magnetic responsive polymer composite materials To cite this version : HAL Id : hal-00926554 Chem Soc Rev,” vol. 42, no. 17, 2018.

[59] F. H. C. Crick and A. F. W. Hughes, “The physical properties of cytoplasm. A study by means of the magnetic particle method Part I. Experimental,” *Exp. Cell Res.*, vol. 1, no. 1, pp. 37–80, Jan. 1950.

[60] E. Duguet, S. Vasseur, S. Mornet, and J.-M. Devoisselle, “Magnetic nanoparticles and their applications in medicine,” *Nanomedicine*, vol. 1, no. 2, pp. 157–168, 2006.

[61] D. L. Zhao, H. L. Zhang, X. W. Zeng, Q. S. Xia, and J. T. Tang, “Inductive heat property of Fe3O4/polymer composite nanoparticles in an ac magnetic field for localized hyperthermia,” *Biomed. Mater.*, vol. 1, no. 4, pp. 198–201, 2006.

[62] W. Gan *et al.*, “Magnetic Wood as an Effective Induction Heating Material: Magnetocaloric Effect and Thermal Insulation,” *Adv. Mater. Interfaces*, vol. 4, no. 22, pp. 1–9, 2017.

[63] A. Seki *et al.*, “Study of the heating characteristics and mechanisms of magnetic nanoparticles over a wide range of frequencies and amplitudes of an alternating magnetic field,” in *Journal of Physics: Conference Series*, 2014, vol. 521, no. 1.

[64] Z. Xiang, K. Jakkpat, B. Ducharne, and J. Capsal, “Enhancing the Low-Frequency Induction Heating Effect of Magnetic Composites for Medical Applications,” pp. 1–16, 2020.

[65] NIIR Board of Consultants & Engineers, “Handbook On Printing Technology (offset, Flexo, Gravure, Screen, Digital, 3d Printing) 3rd Revised Edition by Niir Board Of Consultants & Engineers, ISBN: 9788178331768 | NPCS,” *Asia Pacific Business Press Inc.*, 2017. [Online]. Available: https://www.niir.org/books/book/handbook-on-printing-technology-offset-flexo-gravure-screen-digital-3d-printing-3rd-revised-edition/isbn-9788178331768/zb,,49,a,1b,0,a/index.html. [Accessed: 13-Jul-2018].

[66] S. G. Thibaut Cadiou, Frederic Demoly, “A hybrid additive manufacturing platform based on fused filament fabrication and direct ink writing techniques for multi-material 3D printing,” *Int. J. Adv. Manuf. Technol.*, 2021.

[67] M. Nikzad, S. H. Masood, and I. Sbarski, “Thermo-mechanical properties of a highly filled polymeric composites for Fused Deposition Modeling,” *Materials and Design*, vol. 32, no. 6. pp. 3448–3456, 2011.

[68] Y. Wang, F. Castles, and P. S. Grant, “3D printing of NiZn ferrite/ABS magnetic composites for electromagnetic devices,” in *Materials Research Society Symposium Proceedings*, 2015, vol. 1788, pp. 29–35.

[69] B. Khatri, K. Lappe, D. Noetzel, K. Pursche, and T. Hanemann, “A 3D-Printable Polymer-Metal Soft-Magnetic Functional Composite—Development and Characterization,” *Materials (Basel).*, vol. 11, no. 2, p. 189, 2018.

[70] L. Sun, K. Keshoju, and H. Xing, “Magnetic field mediated nanowire alignment in liquids for nanocomposite synthesis,” *Nanotechnology*, vol. 19, no. 40, 2008.

[71] Z. Xiang *et al.*, “Enhancing the Low-Frequency Induction Heating Effect of Magnetic Composites for Medical Applications,” *Polym. 2020, Vol. 12, Page 386*, vol. 12, no. 2, p. 386, Feb. 2020.

[72] S. H. Jeong, S. Zhang, K. Hjort, J. Hilborn, and Z. Wu, “PDMS-Based Elastomer Tuned Soft , Stretchable , and Sticky for Epidermal Electronics S3-PDMS,” *Adv. Mater.*, vol. 28, no. 28, 2016.

[73] B. Khatri, K. Lappe, D. Noetzel, K. Pursche, and T. Hanemann, “A 3D-Printable Polymer-Metal Soft-Magnetic Functional Composite—Development and Characterization.” 2018.

[74] D. S. McLachlan, M. Blaszkiewicz, and R. E. Newnham, “Electrical Resistivity of Composites,” *J. Am. Ceram. Soc.*, vol. 73, no. 8, pp. 2187–2203, Aug. 1990.

[75] F. Terman, “Terman - Radio Engineers Handbook - 1943.pdf,” *Radio Engineers’ Handbook*. p. 90, 1943.

[76] Z. Szabó and J. Füzi, “Equivalence of Magnetic Metamaterials and Composites in the View of Effective Medium Theories,” *IEEE Trans. Magn.*, vol. 50, no. 4, 2014.

[77] I. Tsukerman, “Classical and non-classical effective medium theories : New perspectives,” *Phys. Lett. A*, vol. 1, pp. 1–6, 2017.

[78] O. Rybin, “Microwave effective medium theory for two-component magnetic metamaterials,” *Int. J. Appl. Electromagn. Mech.*, vol. 35, pp. 93–101, 2011.

[79] J. H. Paterson, R. Devine, and A. D. R. Phelps, “Complex permeability of soft magnetic ferrite/polyester resin composites at frequencies above 1 MHz,” *J. Magn. Magn. Mater.*, vol. 196, pp. 394–396, 1999.

[80] T. Liu, P. H. Zhou, L. J. Deng, and W. Tang, “Spatial orientation and position distribution effect on the effective permeability of composites consisting of aligned flakes,” vol. 114904, 2009.

[81] Q. Li, Y. Chen, and V. G. Harris, “Particle-size distribution modified effective medium theory and validation by magneto-dielectric Co-Ti substituted BaM ferrite composites,” *J. Magn. Magn. Mater.*, vol. 453, pp. 44–47, 2018.

[82] D. W. Schubert, S. Werner, I. Hahn, and V. Solovieva, “Effect of particle size and size distribution on the permeability of soft magnetic liquid silicone rubber composites,” *Compos. Sci. Technol.*, vol. 177, no. April, pp. 26–33, 2019.

[83] M. Anhalt, “Systematic investigation of particle size dependence of magnetic properties in soft magnetic composites,” *J. Magn. Magn. Mater.*, vol. 320, no. 14, pp. 366–369, 2008.

[84] D. Hasegawa, H. Yang, T. Ogawa, and M. Takahashi, “Challenge of ultra high frequency limit of permeability for magnetic nanoparticle assembly with organic polymer-Application of superparamagnetism,” *J. Magn. Magn. Mater.*, vol. 321, no. 7, pp. 746–749, 2009.

[85] X. Wang, R. Gong, P. Li, L. Liu, and W. Cheng, “Effects of aspect ratio and particle size on the microwave properties of Fe-Cr-Si-Al alloy flakes,” *Mater. Sci. Eng. A*, vol. 466, no. 1–2, pp. 178–182, 2007.

[86] A. Hilal, “Magnetic components modeling including thermal effects for DC-DC converters virtual prototyping,” 2015.

[87] L. Rivière, N. Caussé, A. Lonjon, É. Dantras, and C. Lacabanne, “Specific heat capacity and thermal conductivity of PEEK/Ag nanoparticles composites determined by Modulated-Temperature Differential Scanning Calorimetry,” *Polym. Degrad. Stab.*, vol. 127, pp. 98–104, 2016.

[88] B. Budiansky, “Thermal and Thermoelastic Properties of Isotropic Composites,” *J. Compos.*

Mater., vol. 4, no. 3, pp. 286–295, 1970.

[89] Maxwell JC, "A Treatise on Electricity & Magnetism - Volume 2 : James Clerk Maxwell : Free Download, Borrow, and Streaming : Internet Archive," *New York*, 1954. [Online]. Available: https://archive.org/details/ATreatiseOnElectricityMagnetism-Volume2/page/n363/mode/2up. [Accessed: 05-Apr-2020].

[90] T. Bayerl, R. Schledjewski, and P. Mitschang, "Induction heating of thermoplastic materials by particulate heating promoters," *Polym. Polym. Compos.*, vol. 20, no. 4, pp. 333–342, 2012.

[91] P. D. Pfister and Y. Perriard, "Very-high-speed slotless permanent-magnet motors: Analytical modeling, optimization, design, and torque measurement methods," *IEEE Trans. Ind. Electron.*, vol. 57, no. 1, pp. 296–303, 2010.

[92] "Side-by-side comparison of High-Speed Dental Handpiece Attachments | Dentalcompare.com." [Online]. Available: https://www.dentalcompare.com/Restorative-Dentistry/5149-Dental-Handpiece-Attachments/Compare/?compare=34229,3132945,3132954,3082130&catid=5149. [Accessed: 08-Nov-2020].

[93] Q. Li, C. W. Kartikowati, S. Horie, T. Ogi, T. Iwaki, and K. Okuyama, "Correlation between particle size/domain structure and magnetic properties of highly crystalline Fe3O4 nanoparticles," *Sci. Rep.*, vol. 7, no. 1, Dec. 2017.

[94] V. V. Mody, A. Singh, and B. Wesley, "Basics of magnetic nanoparticles for their application in the field of magnetic fluid hyperthermia," *Eur. J. Nanomedicine*, vol. 5, no. 1, pp. 11–21, 2013.

[95] T. S. Srivatsan and R. A. Varin, "Processing and Fabrication of Advanced Materials XII: Preface," in *Processing and Fabrication of Advanced Materials XII*, 2003.

[96] D. L. Leslie-Pelecky and R. D. Rieke, "Magnetic properties of nanostructured materials," *Chem. Mater.*, vol. 8, no. 8, pp. 1770–1783, 1996.

[97] D. Kim, N. Lee, M. Park, B. H. Kim, K. An, and T. Hyeon, "Synthesis of Uniform Ferrimagnetic Magnetite Nanocubes," *J. Am. Chem. Soc.*, pp. 454–455, 2009.

[98] Q. Li, C. W. Kartikowati, S. Horie, T. Ogi, T. Iwaki, and K. Okuyama, "Correlation between particle size/domain structure and magnetic properties of highly crystalline Fe3O4 nanoparticles," *Sci. Rep.*, vol. 7, no. 1, 2017.

[99] *Biosensors Based on Nanomaterials and Nanodevices*. 2017.

[100] Y. Yang *et al.*, "Self-healing of electrical damage in polymers using superparamagnetic nanoparticles," *Nat. Nanotechnol.*, vol. 14, no. 2, pp. 151–155, 2019.

[101] K. Gibson, M. Meissner, and D. Wright, "Great saphenous vein diameter does not correlate with worsening quality of life scores in patients with great saphenous vein incompetence," *J. Vasc. Surg.*, vol. 56, no. 6, pp. 1634–1641, 2012.

[102] A. Yasim, E. Eroglu, O. Bozoglan, B. Mese, M. Acipayam, and H. Kara, "A new non-tumescent endovenous ablation method for varicose vein treatment: Early results of N-butyl cyanoacrylate (VariClose®)," *Phlebology*, vol. 32, no. 3, pp. 194–199, 2017.

[103] *March 2008 MSAC application 1113 Assessment report*, no. March. 2008.

[104] L. M. A. Viarengo, J. Potério-Filho, G. M. B. Potério, F. H. Menezes, and G. V. Meirelles, "Endovenous laser treatment for varicose veins in patients with active ulcers: Measurement of intravenous and perivenous temperatures during the procedure," *Dermatologic Surg.*, vol. 33, no. 10, pp. 1234–1241, 2007.

[105] C. García-Madrid, J. Ó. Pastor Manrique, F. Gómez Blasco, and E. Sala Planell, "New Advances in the Treatment of Varicose Veins: Endovenous Radiofrequency VNUS Closure®," *Cirugía*

Española (English Ed., vol. 89, no. 7, pp. 420–426, 2011.

[106] T. Fiske, H. S. Gokturk, R. Yazici, and D. M. Kalyon, "Effects of Flow Induced Orientation of Ferromagnetic Injection Molded Composites," *Polym. Eng. Sci.*, vol. 37, no. 5, pp. 826–837, 1997.

[107] M. Le *et al.*, "Enhanced magnetoelectric effect for flexible current sensor applications Enhanced magnetoelectric effect for flexible current sensor applications," *J. Appl. Phys.*, vol. 115, no. 19, pp. 0–10, 2014.

[108] D. Guyomar, D. F. Matei, B. Guiffard, Q. Le, and R. Belouadah, "Magnetoelectricity in polyurethane films loaded with different magnetic particles," *Mater. Lett.*, vol. 63, no. 6–7, pp. 611–613, 2009.

[109] K. Danas, S. V. Kankanala, and N. Triantafyllidis, "Experiments and modeling of iron-particle-filled magnetorheological elastomers," *J. Mech. Phys. Solids*, vol. 60, no. 1, pp. 120–138, Jan. 2012.

[110] E. Myrovali *et al.*, "Arrangement at the nanoscale: Effect on magnetic particle hyperthermia," *Sci. Rep.*, vol. 6, no. November, pp. 1–11, 2016.

[111] K. Simeonidis, M. P. Morales, M. Marciello, M. Angelakeris, O. Chubykalo-fesenko, and D. Serantes, "In-situ particles reorientation during magnetic hyperthermia application : Shape matters twice," *Nat. Publ. Gr.*, no. December, pp. 1–11, 2016.

[112] L. C. J. Pereira, J. T. Coutinho, I. M. M. Ferreira, C. M. M. N. Jo, and P. Borges, "Iron oxide nanoparticles stabilized with a bilayer of oleic acid for magnetic hyperthermia and MRI applications," *Appl. Surf. Sci.*, vol. 383, 2016.

[113] A. Ito, M. Shinkai, H. Honda, and T. Kobayashi, "Medical Application of Functionalized Magnetic Nanoparticles," *J. Biosci. Bioeng.*, vol. 100, no. 1, pp. 1–11, 2005.

[114] C. Hu, M. Q. Meng, M. Mandal, C. Engineering, and A. B. Tg, "Efficient Magnetic Localization and Orientation Technique for Capsule Endoscopy *," in *2005 IEEE/RSJ International Conference on Intelligent Robots and Systems*, 2005, pp. 628–633.

[115] K. Goc *et al.*, "Influence of magnetic field-aided filler orientation on structure and transport properties of ferrite filled composites," *J. Magn. Magn. Mater.*, vol. 419, pp. 345–353, 2016.

[116] A. Ahniyaz, Y. Sakamoto, and L. Bergstro, "Magnetic field-induced assembly of oriented superlattices from maghemite nanocubes," 2007.

[117] Y. Kim, H. Yuk, R. Zhao, S. A. Chester, and X. Zhao, "Printing ferromagnetic domains for untethered fast-transforming soft materials," *Nature*, vol. 558, no. 7709, pp. 274–279, 2018.

[118] O. A. Golovnia, A. G. Popov, A. N. Sobolev, and G. C. Hadjipanayis, "Alignment of magnetic uniaxial particles in a magnetic field: Simulation," *J. Magn. Magn. Mater.*, vol. 365, pp. 64–69, 2014.

[119] S. Singamneni, Y. LV, A. Hewitt, R. Chalk, W. Thomas, and D. Jordison, "Additive Manufacturing for the Aircraft Industry: A Review," *J. Aeronaut. Aerosp. Eng.*, vol. 08, no. 01, 2019.

[120] M. F. Farooqui, M. A. Karimi, K. N. Salama, and A. Shamim, "3D-Printed Disposable Wireless Sensors with Integrated Microelectronics for Large Area Environmental Monitoring," *Adv. Mater. Technol.*, vol. 2, no. 8, pp. 1–9, 2017.

[121] M. Javaid and A. Haleem, "Additive manufacturing applications in medical cases: A literature based review," *Alexandria J. Med.*, vol. 54, no. 4, pp. 411–422, 2018.

[122] Brett G. Compton *et al.*, "Direct-write 3D-printing of NdFeB bonded magnets," *Mater. Manuf. Process.*, pp. 109–113, 2016.

[123] M. Roy, P. Tran, T. Dickens, and A. Schrand, "Composite Reinforcement Architectures: A Review

of Field-Assisted Additive Manufacturing for Polymers," *J. Compos. Sci.*, vol. 4, no. 1, p. 1, 2019.

[124] L. Lu, X. Tang, S. Hu, and Y. Pan, "Acoustic field-assisted particle patterning for smart polymer composite fabrication in stereolithography," *3D Print. Addit. Manuf.*, vol. 5, no. 2, pp. 151–159, 2018.

[125] G. W. Bishop *et al.*, "Acoustic patterning for 3D embedded electrically conductive wire in stereolithography," *J. Micromechanics Microengineering*.

[126] H. (BE) Chengxun Liu, Leuven (BE); Liesbet Lagae, "Manipulation of magnetic or magnetizable objects using magnetophoresis and dielectrophoresis. Patent No: US8409415B2," 8,409,415 B2, 2013.

[127] Z. O. Md. Abdulla Al Masud, Noel D'Souza, Paris von Lockette, "On the Dielectrophoretic and Magnetic Alignment of Magnetoactive Barium Hexaferrite-PDMS Nanocomposites," *Conf. ASME Conf. Smart Mater. Adapt. Struct. Intell. Syst.*, no. October, 2017.

[128] H. Song *et al.*, "Inkjet printing of magnetic materials with aligned anisotropy," *J. Appl. Phys.*, vol. 115, no. 17, p. 17E308, 2014.

[129] D. Kokkinis, M. Schaffner, and A. R. Studart, "Multimaterial magnetically assisted 3D printing of composite materials," *Nat. Commun.*, vol. 6, 2015.

[130] L. Lu, E. B. Joyee, and Y. Pan, "Correlation between microscale magnetic particle distribution and magnetic-field-responsive performance of three-dimensional printed composites," *J. Micro Nano-Manufacturing*, vol. 6, no. 1, pp. 1–7, 2018.

[131] C. Ma *et al.*, "Magnetic Multimaterial Printing for Multimodal Shape Transformation with Tunable Properties and Shiftable Mechanical Behaviors," *ACS Appl. Mater. Interfaces*, 2020.

[132] Q. Ze *et al.*, "Magnetic Shape Memory Polymers with Integrated Multifunctional Shape Manipulation," *Adv. Mater.*, vol. 32, no. 4, pp. 1–8, 2020.

[133] K. Song and Y. Cha, "Fe3O4-Silicone mixture as flexible actuator," *Materials (Basel).*, vol. 11, no. 5, 2018.

[134] B. A. Darmawan *et al.*, "Simple fabrication of helical-shaped microrobot with NdFeB nanoparticle by self-rolling technique," *Proc. MARSS 2019 4th Int. Conf. Manip. Autom. Robot. Small Scales*, pp. 1–6, 2019.

[135] V. K. Venkiteswaran, L. F. P. Samaniego, J. Sikorski, and S. Misra, "Bio-inspired terrestrial motion of magnetic soft millirobots," *IEEE Robot. Autom. Lett.*, vol. 4, no. 2, pp. 1753–1759, 2019.

[136] F. Pirmoradi, L. Cheng, and M. Chiao, "A magnetic poly(dimethylesiloxane) composite membrane incorporated with uniformly dispersed, coated iron oxide nanoparticles," *J. Micromechanics Microengineering*, vol. 20, no. 1, 2010.

[137] B. A. Evans *et al.*, "A highly tunable silicone-based magnetic elastomer with nanoscale homogeneity," *J. Magn. Magn. Mater.*, vol. 324, no. 4, pp. 501–507, 2012.

[138] T. J. Hinton, A. Hudson, K. Pusch, A. Lee, and A. W. Feinberg, "3D Printing PDMS Elastomer in a Hydrophilic Support Bath via Freeform Reversible Embedding," *ACS Biomater. Sci. Eng.*, vol. 2, no. 10, pp. 1781–1786, 2016.

[139] F. Liu, G. Alici, B. Zhang, S. Beirne, and W. Li, "Fabrication and characterization of a magnetic micro-actuator based on deformable Fe-doped PDMS artificial cilium using 3D printing," *Smart Mater. Struct.*, vol. 24, no. 3, 2015.

[140] Y. L. Yap, C. Wang, S. L. Sing, V. Dikshit, W. Y. Yeong, and J. Wei, "Material jetting additive manufacturing: An experimental study using designed metrological benchmarks," *Precis. Eng.*, vol. 50, pp. 275–285, 2017.

[141] Y. Yan *et al.*, "Additive Manufacturing of Magnetic Components for Heterogeneous Integration," *Proc. - Electron. Components Technol. Conf.*, pp. 324–330, 2017.

[142] L. Liu, T. Ge, Y. Yan, K. D. T. Ngo, and G. Lu, "UV-assisted 3D-printing of Soft Ferrite Magnetic Components for Power Electronics Integration," *2017 Int. Conf. Electron. Packag.*, vol. 1, pp. 4–7, 2017.

[143] L. Liu *et al.*, "Design and Additive Manufacturing of Multi-Permeability Magnetic Cores," *2017 IEEE Energy Convers. Congr. Expo.*, pp. 881–886, 2017.

[144] J. A. Lewis, "Direct ink writing of 3D functional materials," *Adv. Funct. Mater.*, vol. 16, no. 17, pp. 2193–2204, 2006.

[145] M. Ho *et al.*, "Additive Manufacturing with Strontium Hexaferrite-Photoresist Composite," *IEEE Trans. Magn.*, vol. PP, p. 1, 2019.

[146] J. S. Choi and J. Yoo, "Design of a Halbach magnet array based on optimization techniques," *IEEE Trans. Magn.*, vol. 44, no. 10, pp. 2361–2366, 2008.

[147] K. Halbach, "Design of permanent multipole magnets with oriented rare earth cobalt material," *Nucl. Instruments Methods*, vol. 169, no. 1, pp. 1–10, 1980.

[148] J. C. Mallinson, "One-Sided Fluxes — A Magnetic Curiosity?," *IEEE Trans. Magn.*, vol. 9, no. 4, pp. 678–682, 1973.

[149] K. Sonnleitner *et al.*, "3D printing of polymer-bonded anisotropic magnets in an external magnetic field and by a modified production process," *Appl. Phys. Lett.*, vol. 116, no. 9, pp. 3–8, 2020.

[150] Supermagnete.de, "Shear force: Magnetic adhesive force in shear direction - supermagnete." [Online]. Available: https://www.supermagnete.fr/eng/faq/Why-does-my-magnet-not-carry-the-maximum-weight-on-the-wall. [Accessed: 25-Jan-2021].

[151] R. Bayaniahangar, "3D printing of iron oxide incorporation polydimethysiloxane soft magnetic actuator," MICHIGAN TECHNOLOGICAL UNIVERSITY, 2020.

[152] H. Hong, J. U. Kim, and T. Il Kim, "Effective assembly of nano-ceramic materials for high and anisotropic thermal conductivity in a polymer composite," *Polymers (Basel).*, vol. 9, no. 9, 2017.

[153] M. A. Raux, P. A. Hassel, L. Sorvik, P. Mayhew, and H. Hemmen, "An Innovative Way to Make Anisotropic Thermal Interface Materials," *Intersoc. Conf. Therm. Thermomechanical Phenom. Electron. Syst. ITHERM*, vol. 2020-July, pp. 970–974, 2020.

[154] "Dissipateurs Thermiques | Getelec." [Online]. Available: https://www.getelec.com/solutions-cem/dissipateurs-thermiques/. [Accessed: 26-Jan-2021].

[155] A. Singer, Z. Barakat, S. Mohapatra, and S. S. Mohapatra, "Nanoscale Drug-Delivery Systems," in *Nanocarriers for Drug Delivery*, Elsevier, 2019, pp. 395–419.

Thesis publications

Peer-reviewed publications:

1. Xiang, Ziyin, Ducharne, B., Della Schiava, N., Capsal, J. F., Cottinet, P. J., Coativy, G., … Le, M. Q. (2019). "Induction heating-based low-frequency alternating magnetic field: High potential of ferromagnetic composites for medical applications," *Mater. Des.*, vol. 174, p. 107804, 2019.
2. Xiang, Ziyin, Jakkpat, K.-I., Ducharne, B., Capsal, J.-F., Mogniotte, J.-F., Lermusiaux, P., … Le, M. Q. "Enhancing the Low-Frequency Induction Heating Effect of Magnetic Composites for Medical Applications," *Polym. 2020*, Vol. 12, Page 386, vol. 12, no. 2, p. 386, Feb. 2020.
3. Xiang, Z., Le, M. Q., Cottinet, P. J., Griffiths, P., Baeza, G. P., Capsal, J. F., … Ducharne, B, "Development of anisotropic ferromagnetic composites for low-frequency induction heating technology in medical applications," *Mater. Today Chem.*, vol. 19, Mar. 2021.
4. 3D printing of flexible composites via magnetophoresis – toward medical application based low-frequency induction heating effect, in preparation.

Conferences publications:

5. Xiang, Z., Gupta, B., Le, M. Q., Cottinet, P. J., & Ducharne, B. "Hysteresis model of 3D printed magnetic particles based polymer composite materials," in *2018 IEEE International Magnetic Conference, INTERMAG 2018*, 2018.
6. Xiang, Ziyin, Le, M. Q., Cottinet, P., & Ducharne, B. "Low frequency induction heating of 3D printed composites: Toward medical applications," *Conf. 2019 Jt. MMM-Intermag Conf.*, 2019.
7. Xiang, Ziyin, Le, M. Q., Cottinet, P., & Ducharne, B. "Induction heating properties of ferromagnetic composite for varicose veins healing Key words," *15th Int. Conf. Magn. Fluid (ICMF),Paris, Fr.*, pp. 1–2, 2019.

Conferences participation:

- International conference « IEEE International Magnetics Conference (INTERMAG) » and the Conference on Magnetism and Magnetic Materials (MMM). January 2019. Washington DC, USA
- ENHANCE event - Workshop "From Molecular Engineering to Advanced Materials". May 2019. Cologne, German
- 15th International Conference on Magnetic Fluids – ICMF 2019. July, 2019. Paris, France.

FOLIO ADMINISTRATIF

THESE DE L'UNIVERSITE DE LYON OPEREE AU SEIN DE L'INSA LYON

NOM : XIANG DATE de SOUTENANCE : 12 AVRIL 2021

Prénom : Ziyin

TITRE: Low-frequency induction heating effect of ferromagnetic composites

NATURE : Doctorat Numéro d'ordre : 2021LYSEI022

Ecole doctorale : E.E.A.

Spécialité : Electronique - Génie électrique

RESUME : Les composites ferromagnétiques, matrices polymères renforcées de particules ferromagnétiques présentent un potentiel intéressant dans de nombreuses applications médicales. Dans cette thèse, nous nous concentrons particulièrement autour du Chauffage par Induction Basse Fréquence (CIBF) de cathéters ferromagnétiques, une méthode alternative pour l'ablation des varices. L'effet CIBF apparaît dès lors que le composite est exposé à un champ magnétique alternatif. Ce phénomène est principalement dû aux courants de Foucault dits "microscopiques" générés par les mouvements des parois des domaines magnétiques. En introduisant le cathéter à travers la varice endommagée et en l'excitant par un champ magnétique basse fréquence, haute amplitude, il est concevable d'atteindre une température suffisamment élevée pour guérir correctement la zone endommagée sans perturber les zones saines environnantes. Par comparaison aux traitements existants, la méthode CIBF est précise, économique et simple. En transférant la chaleur sans conduction, l'encombrement du cathéter est réduit et le procédé semble applicable même pour des veines très sinueuses.

Des composites ferromagnétiques de différentes formes et fractions volumiques ont été fabriqués et testés grâce à un dispositif expérimental dédié. Différents paramètres (fréquence, pourcentage de particules…) ont été analysés afin d'établir la combinaison présentant la meilleure réponse thermique. Les propriétés physiques (perméabilité, conductivités électrique et thermique) ont également été caractérisées. Un modèle Comsol® combinant comportement ferromagnétique et thermique a été conçu afin d'améliorer la compréhension des phénomènes.

Pour améliorer la conversion, des échantillons anisotropes ont été développés en imposant un champ magnétique statique dans la phase de solidification.

Finalement, une imprimante 3D de type extrusion a été utilisée pour imprimer des échantillons de formes proches de celle d'un cathéter. Des spécimens isotropes et anisotropes ont été imprimés. Les réponses CIBF distinctes et marquées entre les différentes directions testées chez les échantillons anisotropes ouvrent la voie à d'autres applications médicales comme le suivi électromagnétique (navigation chirurgicale).

MOTS-CLÉS : Composites ferromagnétiques, Chauffage par Induction Basse Fréquence, Comportement anisotrope, Caractérisation magnétique, Caractérisation thermique, Applications médicales

Laboratoire (s) de recherche : Laboratoire de Génie Electrique et Ferroélectricité (LGEF) INSA Lyon

Directeur de thèse: DUCHARNE Benjamin

Co-directrice de thèse : LE Minh Quyen

Président de jury : SEBALD Gaël

Composition du jury : DEMOLY Frédéric (rapporteur de thèse), GUIFFARD Benoit (rapporteur de thèse), DANIEL Laurent (examinateur), NARITA Fumio (examinateur), DELLA SHIAVA Nellie (examinatrice), SEBALD Gaël (président), DUCHARNE Benjamin (directeur de thèse), LE Minh Quyen (co-directrice de thèse).